AD-A066 196   AIR FORCE INST OF TECH WRIGHT-PATTERSON AFB OHIO SCH--ETC F/G 7/2
DISCHARGE PROCESSES IN THE OXYGEN PLASMA.(U)
DEC 78 J W DETTMER
UNCLASSIFIED   AFIT/DS/PH/78-3   NL

1 OF 4
AD
A066196

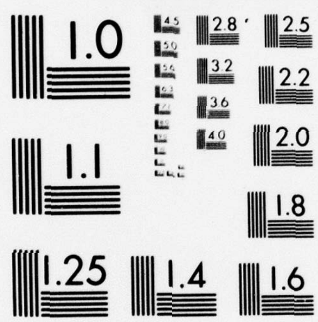

MICROCOPY RESOLUTION TEST CHART
NATIONAL BUREAU OF STANDARDS-1963-A

AFIT/DS/78-3

LEVEL

DISCHARGE PROCESSES IN THE

OXYGEN PLASMA.

DI~~SSERTATION~~

AFIT/DS/PH/78-3

John W. Dettmer
~~Colonel USAF~~

Doctoral thesis,

Dec 78

314p.

Approved for public release; distribution unlimited.

012225

79 03 19 024

AFIT/DS/78-3

DISCHARGE PROCESSES IN THE OXYGEN PLASMA

Dissertation

Presented to the Faculty of the School of Engineering
of the Air Force Institute of Technology
Air University
in Partial Fulfillment of the
Requirements for the Degree of
Doctor of Philosophy

by

John W. Dettmer, B.S., M.S.

Colonel USAF

Approved for public release; distribution unlimited.

AFIT/DS/PH/78-3

DISCHARGE PROCESSES
IN THE
OXYGEN PLASMA

by

John W. Dettmer, B.S., M.S.

Colonel USAF

Approved:

Alan Garscadden — 6th December 1978.
Chairman

Carl T. Case — 27 Nov 1978

Robert L Hengehold — 1 Dec 1978

Ernest A. Dorko — 5 Dec 1978

David A. Lee — 5 December 1978

Accepted:

J.S. Przemieniecki — 7 December 1978
Dean, School of Engineering

Preface

I wish to thank Dr. Alan Garscadden for suggesting the topic of this study and for his encouragement and guidance during its course.

Of the many others at the Aerospace Research Laboratories who have assisted in this work, I would especially like to thank the following: D. Clifford Van Sickle and James Ray for their assistance in constructing and assembling the experimental equipment; Major William Bailey, Captain Michael Stamm, and Lt. William Long for allowing the use of computer programs they had developed and for helping me to adapt them to my purposes; and to Capt. John Prince for helping set up and operate the mass spectrometer equipment.

I also wish to thank Dr. Arthur Phelps of JILA for his recommendations and information on electron impact cross sections and Mr. Walter Wiegand of United Aircraft for his suggestions and listings of chemical reactions.

Finally, I owe a special gratitude to my lovely and patient wife who not only maintained our home and family throughout the period of the study but also typed all of the draft versions of the dissertation.

John W. Dettmer

Contents

Page

List of Figures

List of Figures (Continued)

List of Figures (Continued)

List of Figures (Continued)

List of Figures (Continued)

List of Tables

List of Tables (Continued)

List of Symbols

Symbol	Definition
a_n	Constant of Fourier expansion
A	Area of probe or discharge, depending on use
b_n	Constant of Fourier expansion
c	Speed
C_S	Probe sheath capacitance
D_{AS}	Ambipolar diffusion coefficient of species S
D_S	Diffusion coefficient of species S
$E, \overline{E}$	Electric field
E/N	Reduced electric field
$f_S^{(0)}$	Isotropic electron distribution function of species S
$f_S^{(1)}$	Directed electron distribution function of species S
$F(r)$	Radial profile of electron density
F	Gas flow reduced to standard conditions
F_a	Actual gas flow
g	Relative speed between electrons and neutral particles
I	Electrical current
j	Current density or imaginary number designator, depending on use
k	Wave number or Boltzmann's constant, depending on use
k_x	Rate for process X

List of Symbols (Continued)

Symbol	Definition
K	Thermal conductivity
L	Length of positive column
L_X	Loss due to process X
m_S	Mass of species S
N	Number density of gas or harmonic of Fourier expansion, depending on use
N_S	Number density of species S
N_{SO}	Number density of species S at centerline of the tube
P	Gas pressure
P_M	Power input per molecule
q	Electronic charge
Q	Quality factor
Q_X	Cross section for process X
r	Radius dimension
r_c	Correlation coefficient for least squares approximation
R	Universal gas constant
R_O	Inner radius of discharge tube
R_S	Probe sheath resistance
R_X	Reaction rate for process X
S	Differential scattering cross section
t	Time
T, Tg	Gas temperature

List of Symbols (Continued)

Symbol	Definition
T_o	Gas temperature at the center of the discharge tube
T_S	Temperature of species S
T_W	Temperature of discharge tube wall
U	Energy or electric potential, depending on use
U_X	Thermal energy gain or loss for process X
$\bar{v}_s$	Velocity of species S
$V\phi$	Phase velocity
V	Electric potential or volume, depending on use
V_F	Gas flow velocity
z	Distance along tube axis
α	Intermediate parameter, use dependent on context
α_i	Ionization coefficient
γ	Intermediate parameter, use dependent on context
$\bar{\Gamma}_s$	Flux density of species S
$\bar{\sigma}$	Admittance
$\Delta(\ )$	Change in a parameter
$\mathcal{E}_s$	Characteristic energy of species S
ϵ_o	Permittivity of free space
ϵ_r	Relative permittivity
λ_D	Debye length
λ	Wavelength
λ_s	Sheath thickness

List of Symbols (Continued)

Symbol	Definition
μ_{os}	Reduced mobility coefficient of species S
μ_s	Mobility coefficient of species S
ν	Vibration quantum number
ν_{eN}	Electron-neutral collision frequency
τ_{RES}	Residence time of the gas in the tube
χ	Scattering angle
ψ	Azimuth angle
ω	Frequency

Abstract

The electric glow discharge in oxygen was experimentally studied and mathematically modeled for the parameter space of one to ten torr of pressure and for current densities up to 35 milliamperes per square centimeter. Experimentally it was observed that the oxygen discharge existed in one of two forms: a high-electric-field form or a low-electric-field form. The high field form was present at high currents and low pressures, the low field form at low currents and high pressures. The high field form exhibited stable characteristics while the low field form was observed to be nonstable, exhibiting periodic or aperiodic oscillatory behavior. The periodic oscillations existed only at certain frequencies or modes, and the discharge impedance was a function of the frequency. The optical output of the oscillatory form of the discharge was highly modulated with short duty cycle pulses. The oscillations exhibited a small amount of normal dispersion. The point of transition between forms and the electrical impedance of the forms was unaffected by the addition of an inert gas, argon, to the discharge. Adding an electron-detaching gas, carbon monoxide, increased the low field impedance until the difference between the forms essentially ceased to exist. Mass spectra measurements indicated that the atomic oxygen density increased significantly when the discharge transitioned from

the low to high field forms. Solutions of the Boltzmann transport equation indicated that the electron energy distribution function exhibited a characteristic intermediate between Maxwellian and Druyvesteyn. Chemistry model results showed the dominant positive ion to be O_2^+ and the dominant negative ion to be O^-. The transition from the stable to unstable forms was determined to be related to two criteria: the dominance of the derivative of the attachment coefficient with respect to E/N over that of the ionization coefficient and the equivalence of the negative ion and electron number densities. The former was satisfied for all values of E/N below 67 TD. The later condition was determined to be a function of pressure and accurately predicted the point of transition. The metastable $O_2^*(a^1\Delta)$ was important in the discharge for two reasons. Two step ionization was required in addition to direct ionization to match the experimental electron density measurements. Also, the inclusion of the metastable molecule as the primary electron detacher was required to match the transition points determined by experiment with those determined from the model.

DISCHARGE PROCESSES IN THE OXYGEN PLASMA

I. Introduction

This chapter begins with a statement of the objectives of the study and then describes the general approach that was used to achieve the objectives. Next, in order to provide a background for the reader, the general characteristics and criteria of a plasma are presented; and it is shown that the parameter space covered by the study met the listed criteria. The chapter then focuses on the particular type of plasma that was studied - the electrical glow discharge positive column. Finally the chapter discusses the oxygen positive column: its characteristics, its unique properties, and the theories that have been developed to explain them.

Objectives

The objectives of this study were to investigate the plasma existing in the positive column of an oxygen glow discharge and to determine the physical and chemical processes involved.

Recently there has been a renewed interest in the oxygen plasma, an interest generated by the development of the laser. Oxygen has been postulated and used as both the lasing medium and the pumping medium in electrical and electrical-chemical lasers ~~(Ref 1:9-16, Ref 2:415-416, Ref 3:1-18.~~

over

Ref 4:2243-2245, Ref 5:834-838). Also, there has been a continuing interest in efficient production of ozone (Ref 6:1-4). Effective utilizations of oxygen electric discharges require a knowledge of the oxygen plasma, a plasma which differs from other plasmas in many of its characteristics. For example, electrical glow discharges in oxygen have been observed to exist in two different forms: a low electrical impedance form which exhibits an oscillatory behavior and a high electrical impedance form which is relatively stable. The transition between the two forms occurs as a function of current density and gas pressure. The characteristics of the two forms and the transition phenomenon have been studied for many years, and several different theories have been developed - theories which have not been entirely consistent with each other. Therefore it was a purpose of this study to determine a consistent explanation of the characteristics of the oxygen discharge.

Specifically the study was designed to determine:

1. A consistent set of measurements of the physical properties of the two forms of the oxygen discharge.
2. Measurements of the effects on the discharge of adding inert and electron-detaching gases.
3. The energy distribution function of the electrons.
4. The relative densities of the various charged and neutral species present in the discharge and the dominant chemical and physical processes associated with their productions and losses.

5. A resolution of the role that the metastable molecule O_2 $(a^1\Delta)$ plays in the ionization and electron-detachment processes.

6. An explanation of the two forms of the oxygen discharge and the criteria for transitioning between them.

The study of the oxygen discharge was approached from two different aspects: an experimental investigation and a mathematical modeling. During the experimental phase the observable characteristics of the oxygen positive column were investigated for a gas pressure range of one to ten torr and a current density range of .35 to 35 milliamperes per square centimeter. Experimentally determined were the impedance characteristics, gas temperatures, electric field shapes and dispersion characteristics of the low field oscillations, electron densities, neutral mass spectra, and the effects of adding other selected gases. The modeling phase consisted of a determination of the electron energy distributions and electron-impact pumping rates for reduced field strengths (E/N) from one to one hundred Townsends* and a determination of the steady state charged and neutral species densities over the same reduced field range for initial molecular densities from 3.2×10^{16} to 5.6×10^{17} molecules per cubic centimeter. The results of the experimental phase were used to validate the mathematical models; the results of computations using the mathematical models were then used to develop the

---

*E/N is the Electric Field divided by the density of the neutral species. One Townsend equals 10^{-17} volt-cm^2.

theory of the oxygen plasma.

Background

General Characteristics of a Plasma. (Ref 7:2-8, Ref 8:1-8, Ref 9:1-2, Ref 10:205-246, Ref 11:217-251). The term plasma was first utilized by Irving Langmuir in 1928 to describe the inner region of an electrical discharge. Since then the definition has been broadened to describe a state of matter in which a significant number of the atoms and/or molecules are electrically charged or ionized. Characteristically in a plasma the charged particles arrange themselves in such a manner as to effectively shield externally and internally generated electrostatic fields within a distance of a Debye length, λ_d , and to achieve local charge neutrality over regions greater than a Debye length. For an electron density N at temperature T_e, the Debye length is given by:

$$\lambda_d = 6.9 \cdot \left(\frac{T_e}{N_e}\right)^{\frac{1}{2}} \qquad (1)$$

For a confined plasma the satisfaction of the above criteria requires that the physical dimensions of the confining system be large compared to the Debye length and that there be a sufficient number of electrons within a Debye sphere* to produce shielding. For a cylindrical geometry of radious R_o the plasma criteria are:

---

*Sphere with radius λ_d.

$$\lambda_d < R_o \qquad (2)$$

$$N_e \ll 1.9 \times 10^6 \cdot T_e^3 \qquad (3)$$

For the parameter space of this study the electron temperature varied between 2×10^3 and 4×10^4 °K; the tube radius was .95 cm, and the electron density varied from 10^9 to 10^{11} cm^{-3}. This resulted in a maximum Debye length of .05 cm. Thus, the criteria of equations 2 and 3 were satisfied.

The observable characteristics of a plasma are strong functions of the species that constitute the plasma. Collisions between species play a particularly important role in ionized gases. For a weakly ionized gas (such as used in this study) the dominant collisions are those between charged and neutral species and those between different neutral species; the collisions between charged species can often be neglected. The properties of the species and their collision processes play important roles in the plasma characteristics. Since molecular gases have many more inelastic electron-impact cross sections than atomic gases, plasmas in the molecular gases have very different characteristics from those in the atomic gases. Electronegative gases form stable negative ions upon electron impact; electropositive gases do not. For plasmas in electropositive gases the only charged species that must be considered are the positive ions and the electrons; for plasmas in electronegative gases the negative ions must also be considered. The characteristics of plasmas with three charged species may be expected to differ from those with only two charged species. Because of these factors oxygen is a very interesting gas to study: it is a molecular gas; it forms stable negative ions; its electron collision cross sections have been generally well defined; and it is easily obtained in a highly purified state.

The majority of the universe exists in the plasma state. This includes the stars, which are almost completely ionized because of their high temperatures; this type of plasma is an example of an equilibrium plasma in which the ionization is thermally produced and the temperatures of the neutral and charged species are in equilibrium. The equilibrium plasma is relatively uncommon in laboratory experiments. The usual laboratory techniques involve some nonequilibrium process by which the ionization is maintained by raising some of the charged species to a higher temperature than the neutrals. The most common example of this is the gas discharge in which an electrical potential, applied across a gap, provides the selected excitation of the charged species. If the majority of the ionization is by direct electron impact rather than by thermal channels, the discharge is a glow discharge. The positive column of a glow discharge is a region in which the physical and chemical processes are generally uniform or of a bounded periodic nature. The positive column interfaces on the cathode end of the discharge with the Faraday dark space and on the anode end with the anode glow. Because the processes are well ordered* in the positive column, it provides a convenient medium for the investigation of the plasma characteristics.

The electrical current through the positive column is maintained primarily by the highly mobile electrons. Sufficient ions are created to maintain space charge neutrality. In the uniform column the electric field is constant and of relatively low value compared to other regions of the discharge. However, the electric field is sufficient to raise the electron temperature to as high as $40{,}000^{\circ}K$, while the heavy particles remain within several hundred degrees of room temperature.

The characteristics of the positive column vary with the constituents of the gas, its pressure and temperature, the current density, and the boundary conditions. For example, the light emitted and electric field are dependent on the diameter of the confining tube. Smaller diameters increase diffusion losses, and therefore a higher field is required to sustain the discharge. This results in a more luminous column. The distance between the electrodes essentially determines the length of the column - as the tube length is increased, there is an equivalent increase in the length of the positive column; the other regions of the

---

*Well ordered in the sense that the electric field and charged particle densities are relatively constant in the axial dimension. Refer to Figure 1 for a graphical presentation of these parameters in the glow discharge.

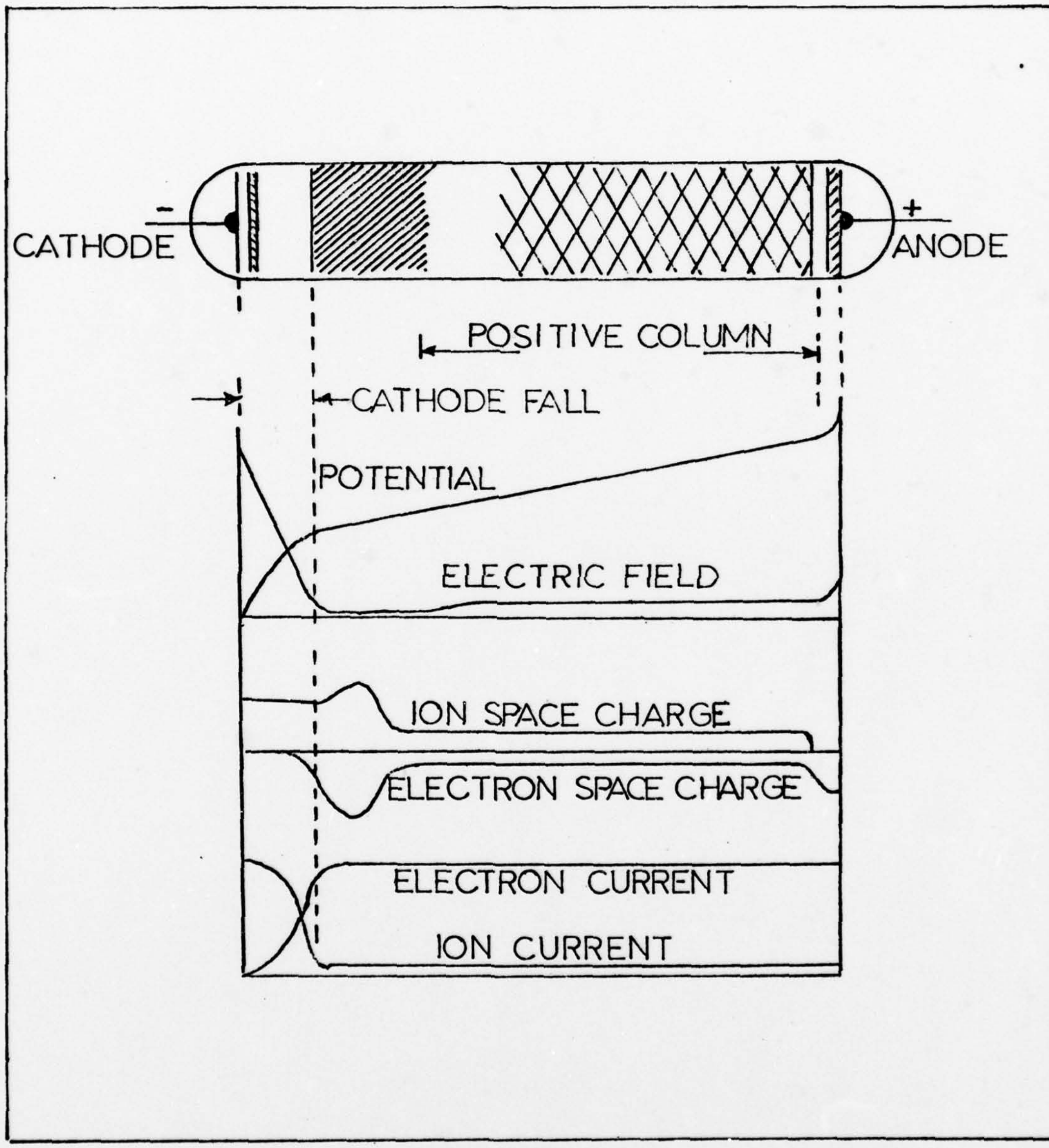

Figure 1. Glow Discharge (From Ref 11:218)

discharge remain constant. As the pressure of the discharge is increased, the effects of collision processes become more important and eventually dominate over the diffusion losses. Gas heating leads to radial density gradients and higher reduced electric fields, E/N, in the center of the column than at the boundary. This is evidenced by the apparent radial constriction of the column as the pressure or current is increased. The electric field in molecular gas discharges is higher than in atomic gas discharges by an order of magnitude. This is caused by the greater number of inelastic loss processes of the molecular gas which dissipate the electron energy into nonionizing channels.

The positive column can be either uniform or oscillatory in its properties. Oscillations appear as alternate dark and bright regions which may be either stationary or may move along the column. Often their motion is so rapid as to result in the appearance of a uniform column.

General Characteristics of the Positive Column in Oxygen. The electrical and optical characteristics of the oxygen positive column are unique; they occupy an intermediate place between the normal electropositive discharges, such as nitrogen or the rare gases, and the strongly electronegative discharges exemplified by iodine (Ref 12:519). This fact has caused the oxygen discharge to be studied by many investigators through the years. However, only recently have the experimental and theoretical techniques been available to fully define and explain the discharge characteristics.

In 1927, Guntherschulze observed that the oxygen positive column existed in two forms: one with a high voltage gradient and a greyish green optical output and another which had a low voltage gradient and was violet in color. The existence of one or the other form was noted to be a function of the pressure and current (Ref 13:763). In 1951, Seeliger and Wichman defined the High field form as the H form and the low field form as the T form*. Their impression of the color difference was that the optical emissions from the H form were blue with a light violet core; whereas in the T form, a grey blue light was emitted (Ref 14:235-244).

Other investigators further defined the electrical and optical characteristics of the column. It was noted that the H form existed at higher currents and lower pressures than the T form. If the pressure was held constant, an increase in current would cause the column to transition from the T to H forms. Holding current constant and increasing pressure would cause it to switch from the H to T forms. Pekarek published a paper in which the existence regions for the two forms were defined (Ref 15:750). Figure 2 depicts these regions. The occurances of the T and H forms were not necessarily exclusive; they have both been observed in the column at the same time. When both forms were present, they were axially separated with the H portion always situated on the

---

*H and T had their origins in the German words for High and Low: Hoch and Tief.

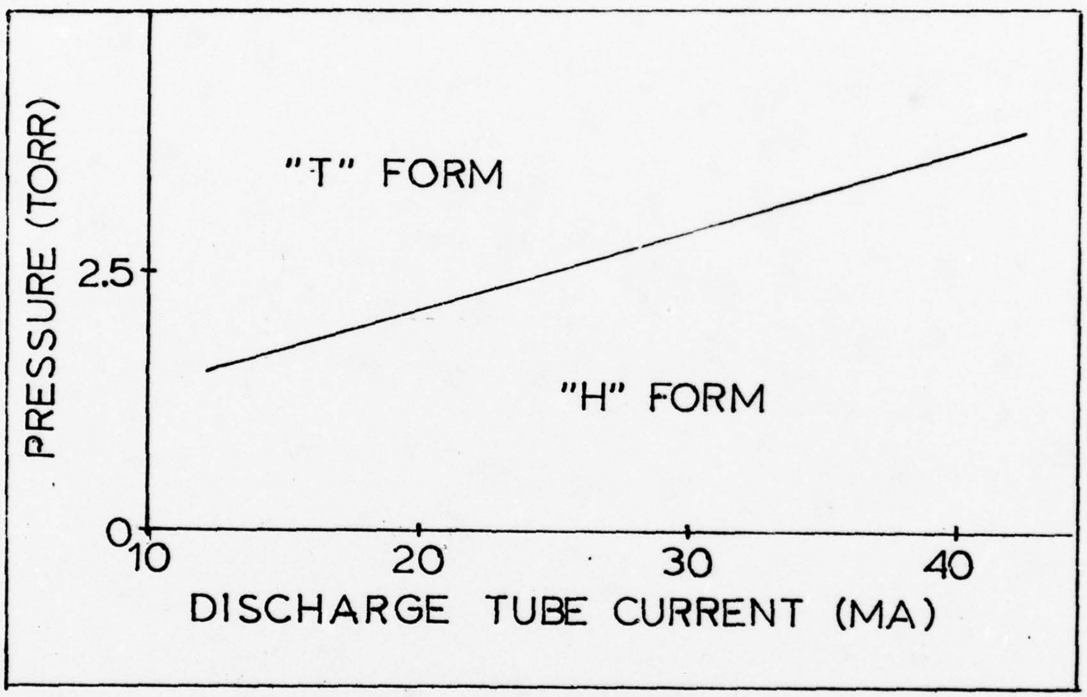

Figure 2. H-T Forms Existence Regions (From Ref. 15:750)

anode side of the column and the T portion on the cathode side. As these parameters were swept through the transition region from the H form to the T form, it was observed that the T form appeared at the cathode face of the positive column and progressed to the anode. Conversely when the parameters were swept from their T form to H form values, the H form started at the anode and progressed to the cathode. Also, the transition between the forms exhibited a hysteresis effect. At any position in the positive column, if either the discharge current or gas pressure was swept, the transition between the forms was dependent on the direction of the sweep (Ref 16:305-317, Ref 17:3.1.5.1). This hysteresis effect is shown in Figure 3.

Of the two forms it is the T form which is considered to differ from other molecular gases; the voltage gradient in this form is anomalously low when compared with other molecular gases (Ref 17:3.1.5.1). Practically all of the investigators have noted that the T form is oscillatory, with the oscillations traveling from the cathode to the anode. These oscillations have been noted as either being periodic or aperiodic depending on the discharge parameters (Ref 18: 11-13). The H form has generally been noted as homogeneous with a gradient typical of other molecular gases; this has led to it being described as the normal form of the oxygen discharge. Sabadil, however, has noted that under certain conditions the H form can also be oscillatory with low amplitude moving or stationary strata (Ref 16:13-18).

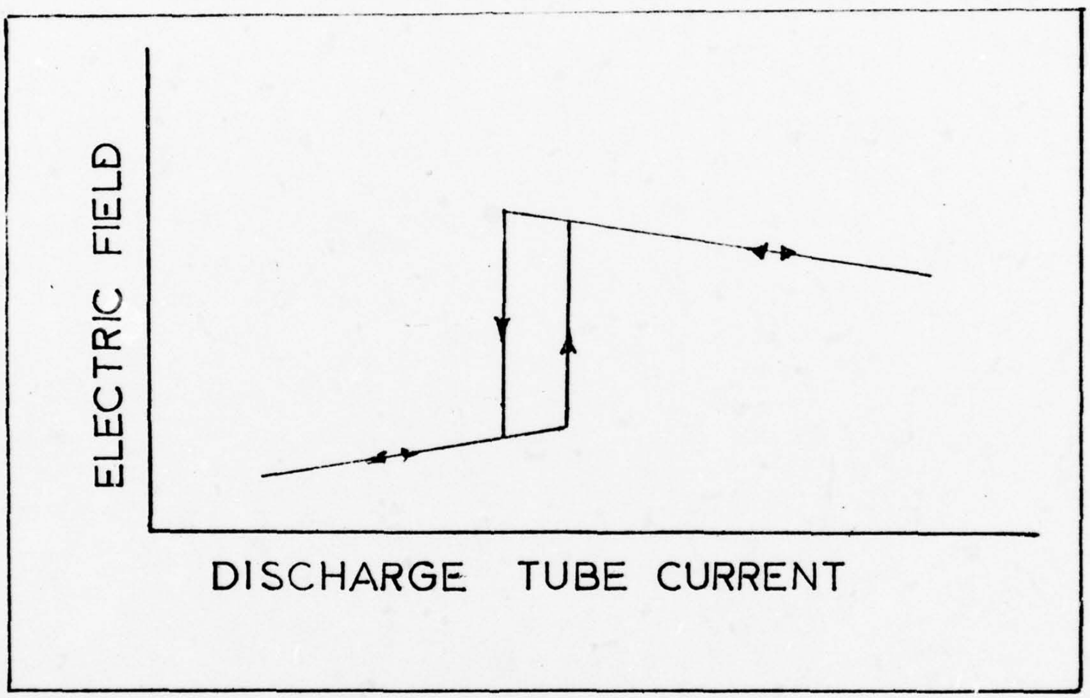

Figure 3. Hysteresis Effect

Species in the Oxygen Positive Column. The concentration of atomic oxygen and ozone have been observed to be functions of the form of the discharge. Ozone has been claimed only to exist in the T form and not in the H form (Ref 14:235-244, Ref 19:1). On the other hand the concentration of atomic oxygen has been determined to be much greater in the H form than in the T form. This was initially determined by analysis of the optical output of the column; the molecular band structure dominated in the T form and the atomic line structure in the H form (Ref 14:235-244, Ref 15:749). Theoretical estimates of up to 8% dissociation have been made (Ref 12:520). The major source of atomic oxygen has been postulated to be from electron impact excitation of the ground state oxygen molecule to the repulsive vibrational levels of the $B^3\Sigma_u^-$ electronic state:

$$e + O_2(X^3\Sigma_g^-, \nu \leq 2) \rightarrow e + O_2(B^3\Sigma_u^-, \nu \geq 11) \rightarrow e + 2O$$

The excitation to the dissociative vibrational levels is caused by the offset between the potential energy curves of these two electronic states and the fact that it is a sudden collision, and consequently the Franck-Condon principle applies (Ref 20:510-511, Ref 21:11). Figure 4 is the term diagram for oxygen and is included to illustrate the potential energy offsets. Depending on the pressure, atomic oxygen was postulated to be lost by diffusion to the walls, where recombination takes place, or by collisional processes. The collisional processes were favored due to the low recombination

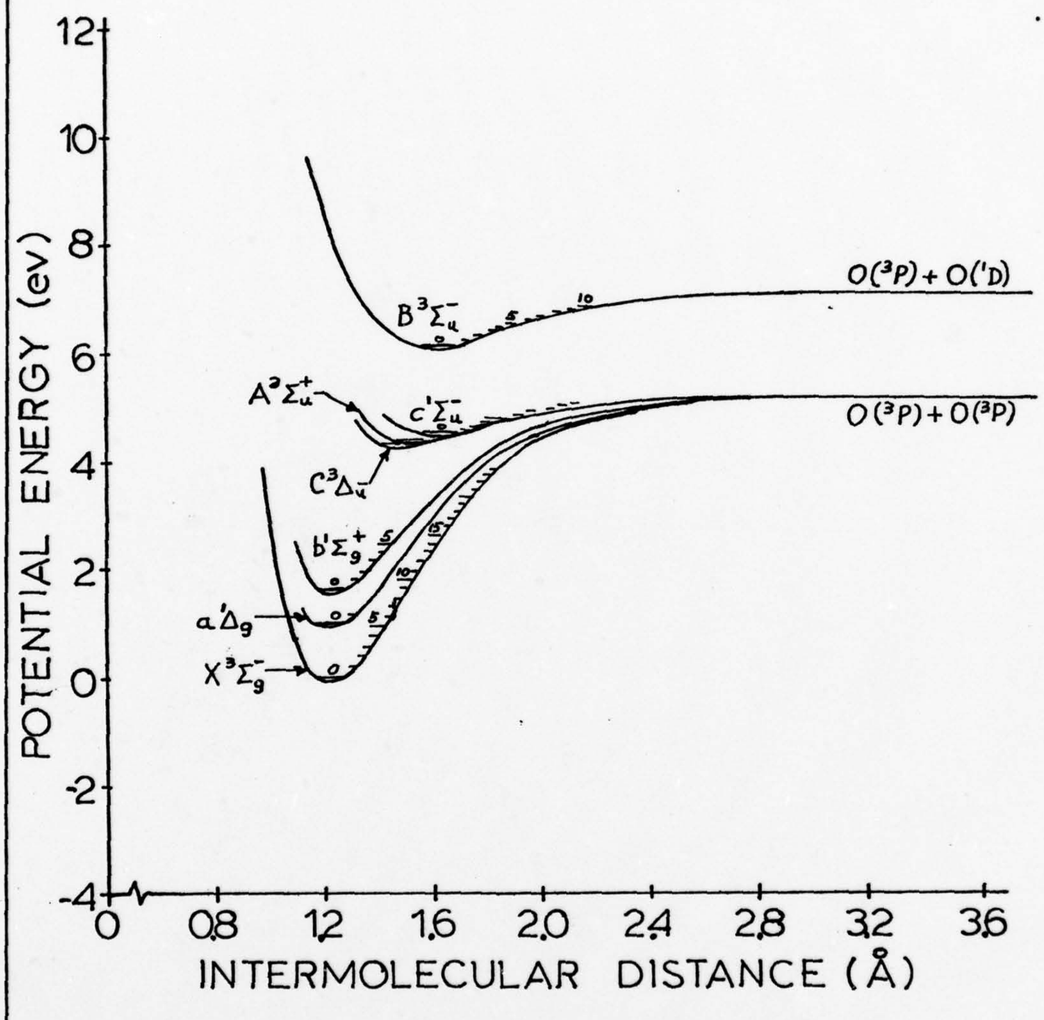

Figure 4. Term Diagram for Oxygen (From Ref. 79)

rate at the wall* and the resulting flat radial profile (Ref 22:3.1.5.9, Ref 23:235-251).

Because of the electronegative nature of oxygen, the oxygen plasma is a three component plasma consisting of three types of charge carriers: electrons, positive ions, and negative ions. In the glow discharge the predominant positive ion was reported to be O_2^+ (Ref 24:820, Ref 12:520, Ref 19: 8-9). At PR_o = .18, P = .04 torr and j = 60 uA/cm^2, Thompson reported a molecular ion to atomic ion ratio of 70 to 1 (Ref 12:519). At a pressure of 2.5 torr, the ratio of O_2^+ to O^+ depended on the discharge form; in the H form, O_2^+ overwhelmingly dominated; and in the T form, the ratio was approximately 2 to 1 (Ref 19:8-9). The predominant negative ion was determined to be O^- (Ref 25:1068, Ref 26:299-308, Ref 24: 820). For the .04 torr observation referenced previously, Thompson reported a ratio of 10 to 1 for the O^- to O_2^- ion (Ref 12:519). The main production mechanism for the O^- ion was postulated to be the dissociative attachment process: $e + O_2 \rightarrow O^- + O$ (Ref 24:820, Ref 23:235-251). In a three component plasma with a large concentration of negative ions, ambipolar diffusion was considered to be a weak process; and the radial electric field was reported to be very low. A weak ambipolar diffusion process reduces the radial loss to the walls of the negative ions and requires that the dominant loss be collisional (Ref 24:818, Ref 22:3.1.5.9, Ref 23:

*Estimated at 10^{-4} for pyrex (Ref 23:234-251).

235-251). The associative detachment process $O^- + O \rightarrow O_2 + e$ was suggested as the major loss mechanism for the atomic negative ion (Ref 12:522, Ref 27:53-66, Ref 24:821, Ref 22:3. 1.5.9). The molecular negative ion O_2- was claimed to be primarily formed by the charge exchange process with O^-: $O^- + O_2 \rightarrow O_2^- + O$ (Ref 12:522). Under certain conditions in the discharge, the negative ion concentration has been determined to dominate the electron concentration by up to 20 to 1 (Ref 24:818).

There are two low-lying metastable states of molecular oxygen: the O_2 $(a^1\Delta)$ and O_2 $(b^1\Sigma)$ states. The role that these states play in the characteristics of the oxygen plasma has been unresolved. There are investigators who postulated that ionization from these metastable levels must play an important and necessary role in the oxygen discharge in order to match experimentally observed ionization rates (Ref 17: 3.1.5.1, Ref 19:2). Other investigators discounted stepwize ionization as insignificant when compared to direct processes, since the energy difference between the ground and metastable states are small compared to the ionization energy (Ref 12: 520, Ref 27:53-66).

Oscillatory Behavior in the Oxygen Discharge. The oscillations in the T form of the oxygen discharge have been claimed to differ from those found in N_2, H_2, or noble gas discharges. The oxygen oscillations are very highly modulated and have been observed to exist in the T portion of the column when both forms are present (Ref 15:750-751, Ref 16:

305-317, Ref 26:299-308). The oscillations in other gases are typically less modulated and appear in the total column. The oxygen oscillations were observed to be forward waves moving from cathode to anode (Ref 16:305-317) with a velocity approximately that of the negative ion drift (Ref 23:235-251). This velocity was on the order 10^5 to 10^6 cm/sec, and the frequency was between 10 KHz and 1 MHz (Ref 18:11, Ref 29: 85, Ref 15:751). The oscillations have been reported as dispersionless, i.e., the velocity was independent of frequency (Ref 16:305-317).

The oscillation frequency in the T form was found to vary with the parameters of the discharge (Ref 28:409-420). As the current, the length of the column, the pressure, the anode diameter, or the tube diameter was increased, the frequency decreased (Ref 16:305-317, Ref 28:409-420). The amplitude of the oscillations was observed to be inversely related to the frequency (Ref 28:409-420).

The oscillations in the T form are not always periodic; for certain conditions of current and pressure, they have been found to be aperiodic or noiselike. The aperiodic T form has been observed to have a slightly lower gradient than the periodic one (Ref 18:12). It was possible to use external modulation of the column to synchronize the column to one of its periodic modes of oscillation (Ref 26:299-308).

The oscillations in the H form were noted to be similar to those found in N_2, H_2, and noble gas discharges (Ref 23: 235-251). The H form oscillations have been observed to move in the forward direction, backward direction, or to remain stationary (Ref 16:305-317). Sabadil's observations were on discharges with pressures in the .1 to .35 torr range. Other investigators, whose investigations were normally in higher pressure discharges, failed to determine any oscillations in the H form.

Theories Regarding the Two Forms of the Oxygen Discharge. The characteristics of the H form of the oxygen discharge were observed to be very similar to other molecular gases; therefore, it was generally acknowledged that this is the normal form of the discharge, and it generally exhibits two-component-plasma characteristics. It is the T form that was listed as abnormal, and several theories have been developed to explain the characteristics of this form and the reason it exists in only a portion of the pressure-current parameter space.

In a 1966 article Sabadil noted that the T form oscillations showed no dispersion and that the velocity of the oscillations was independent of the discharge current and tube diameter and that there was no indication of damping by ion-neutral collisions. This led him to postulate that the oscillations were ionic sound waves resulting from an ionization-recombination instability. Based on previously published data on the recombination rates and ion densities, he was able to calculate a positive ion-negative ion recombination time constant which agreed with his T oscillation period within an order of magnitude (Ref 16:305-317). In a follow-on paper in 1968, Sabadil noted that the coefficient for the recombination process between the negative and positive ions in oxygen was inversely related to the gas temperature ($Kr \sim Tg^{-5/2}$). Experiments with various oxygen discharges at temperatures between $-170^{o}C$ and $+300^{o}C$ indicated very slight changes in the oscillation period over the temperature range. This led Sabadil to abandon the ionization-recombination theory for the oscillations (Ref 26:299-308).

In a 1968 paper Sabadil noted the similarity between the Funn-Effect instabilities that occur in gallium arsenide semiconductors and the oscillations in the T form of the oxygen discharge. In the semiconductor, differential negative mobility* arises due to the transfer of electrons from a high mobility central valley in the conduction band to satellite valleys which are at a higher energy but where the mobility is lower. For the oxygen discharge the atomic negative ion O^- was suggested as the low mobility charge carrier and the electron as the high mobility carrier. To exhibit this effect the production of low mobility carriers must depend on some process which has an energy threshold. For GaAs this threshold is the energy difference between the central and satellite valleys of the conduction band; for oxygen this threshold is the minimum energy associated with the dissociative attachment process - approximately 4.4 ev. For both the semiconductor and the oxygen discharge, under certain

*As a function of the electric field

conditions the charge carrier distribution becomes unstable; and there are established high and low field domains which propagate from cathode to anode. The Sabadil paper proposed a qualitative model of transitioning from the low field to the high field domain but failed to describe a mechanism for the converse (Ref 26:299-308).

In a 1974 report Nighan and Wiegand developed a theoretical model of the causes and conditions for instabilities in molecular discharges, particularly discharges in which negative ion processes play a significant role. Their analysis indicated that the oscillations in the T form of the O_2 discharge were a manifestation of an ionization instability caused by the dissociative attachment process. The occurrence of this instability was stated to be a function of the electron temperature dependence of the attachment coefficient, the electron temperature dependence of the ionization coefficient, and the relative magnitude of the negative ions and electrons. Specifically, a necessary condition for the instability to occur is that the following inequality be true:

$$\frac{\delta Ka}{\delta Te} > \frac{\delta Ki}{\delta Te} \qquad (4)$$

where Ka is the attachment coefficient for the process: $e + O_2 \rightarrow O^- + O$, Ki is the direct ionization coefficient; and Te is the electron temperature. The dominance of the attachment temperature dependence over that of ionization allows for an inverse relationship between disturbances in electron temperature and electron density, thereby providing a positive feedback path in the electron kinetics. A sufficient condition for the oscillations to occur is that the negative ion concentration must be significant compared to the electron concentration. This requires that detachment processes play a minor role. The transition from the T form to the H form was postulated to occur when the detaching species concentration increases to the point where the detachment process dominates the negative ion balance equations. For the pure oxygen discharge the dominant detaching species was suggested to be either the neutral atom 0 or the metastable neutral molecule 0_2 $(a^1\Delta)$. The buildup of another stable negative ion 0_3- by the process: $0^- + 0_2 + M \rightarrow 0_3^- + M$ was considered as the method of delaying the transition from the T to H forms. These two trends tend to explain the current and pressure dependence of the transition between the forms of the oxygen discharge (Ref 30:1-40).

II. GENERAL EXPERIMENTAL SETUP

The general setup described in this chapter was utilized throughout the experimental phase of this study. With one exception, only minor changes were made in progressing from one experiment to another. The one exception was the discharge tube; a different design was utilized for the mass spectra experiments. The general setup was designed to provide the necessities of the experiments: controllable pressure, gas flow, gas mixture, D.C. electrical power with variable potential and current, and cooling for the discharge tube. The following sections describe the discharge tube design and the systems employed in the general experimental setup.

Discharge Tube (Figure 5)

The discharge tube was constructed entirely of quartz. This material was chosen over glass due to its high softening temperature and low electrical dissipation factor at microwave frequencies; the latter characteristic was required for the electron density measurements. With the exception of the anode region, the tube was jacketed for cooling purposes. The inside diameter of the inside tube was 19mm with the exception of the cathode region. In this region the diameter was increased to 25mm to accommodate the large cathode. The length between the column edges of the anode and cathode was 505mm. Ground taper joints were installed every

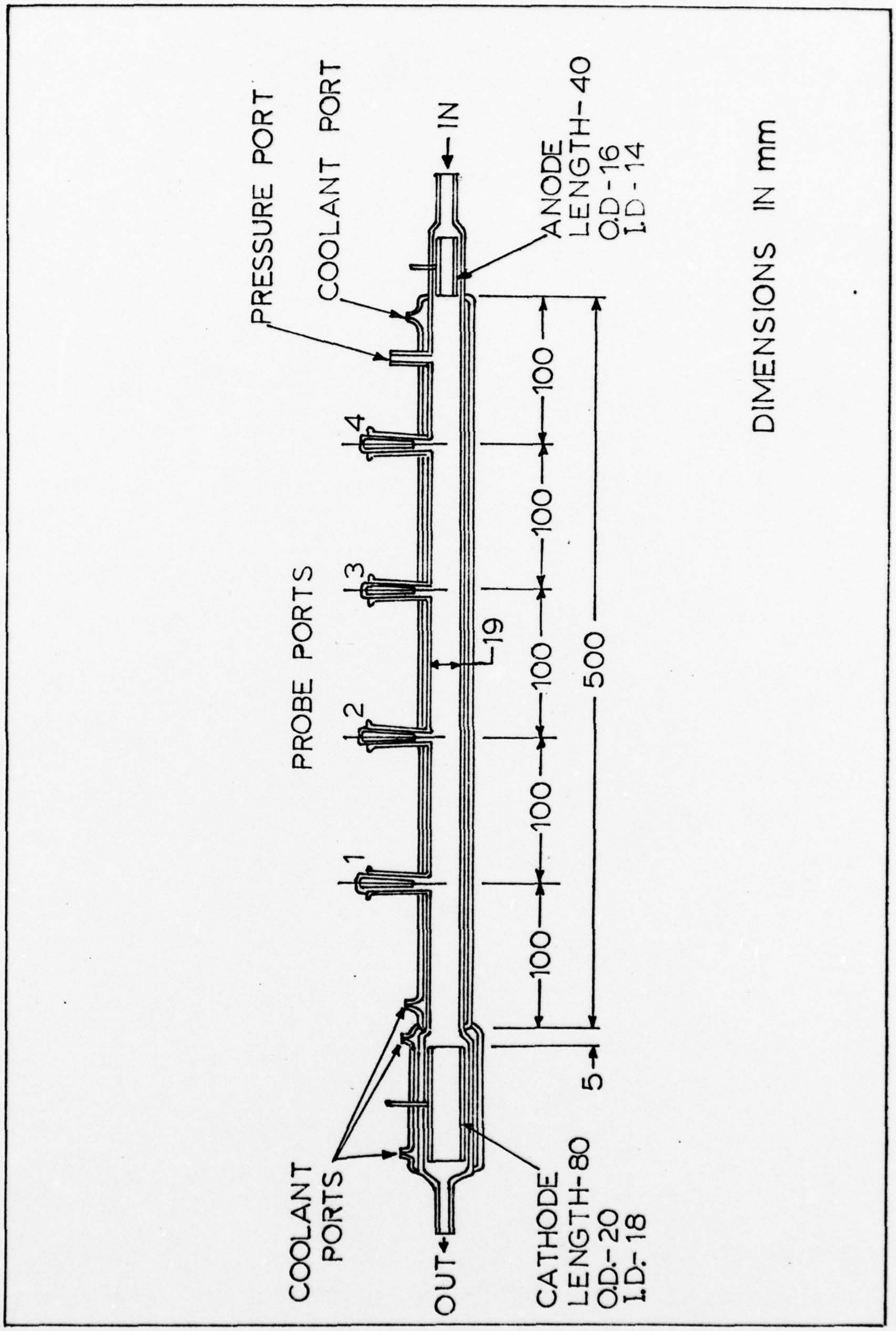

Figure 5. Discharge Tube

100mm along the column to allow probes to be inserted into the tube. During the majority of the experimentation, electric field probes were inserted into the taper joints. These probes consisted of .25mm diameter platinum wire encapsulated in glass, except for 2mm at the end near the center of the tube. For the plasma temperature experiment, a thermocouple was inserted through one of the taper joints.

The electrodes, anode and cathode, were constructed of oxygen-free copper to minimize water vapors. The lead pins were constructed of Kovar. An epoxy substrate was used to mechanically support and to seal the pins at the points where they passed through the glass. During the break-in period for the tube, these substrate joints had to be thermally cycled several times before they formed good mechanical and vacuum seals. The electrodes were broken-in by a gradual increase in discharge current to slowly create an even oxidation of the surfaces. Too fast a break-in caused localized heavy oxidation which resulted in surface flaking and surface unevenness. In order to avoid flaking at high currents,the cathode design had to be as massive as the tube design would allow. An 80mm long by 20mm diameter hollow cylinder was experimentally determined to be sufficient for currents to 100ma. The anode size was relatively insensitive to discharge current. Therefore a smaller design, 40mm long by 16mm diameter hollow cylinder, was used for this electrode.

Gas System (Figure 6)

Throughout the experimentation the primary gas used was oxygen. Other gases - helium, argon, or carbon monoxide - were used to initiate the discharge and as additives to the oxygen. Power supply limitations precluded discharge initiation in pure oxygen. All the gases used were ultra high purity and were dispensed from size A bottles.

The portion of the gas system upstream of the discharge tube was constructed of stainless steel components, with the exception of a short section of tygon tubing connecting the mixing chamber to the tube itself. The portion of the system between the pressure regulators and the flow controlling needle valves was maintained at a small positive pressure relative to ambient to minimize the effect of small leaks should they occur. High and low range flowmeters in the oxygen and additive gas lines allowed mixing to one part in five hundred and measurement of the gas flow. The flow and mixtures were controlled by needle valves in each line. Mixing occurred in a chamber filled with small diameter glass beads.

Downstream of the discharge tube, coarse and fine needle-valves were used to precisely control system pressure. A large capacity, 17.7 CFM Duo-Seal #1397, mechanical vacuum pump was used to maintain system vacuum. A 6.5 Cu.Ft. glass-lined water tank was used as a ballast for the system to smooth pump pulses.

System pressure was measured near the anode end of

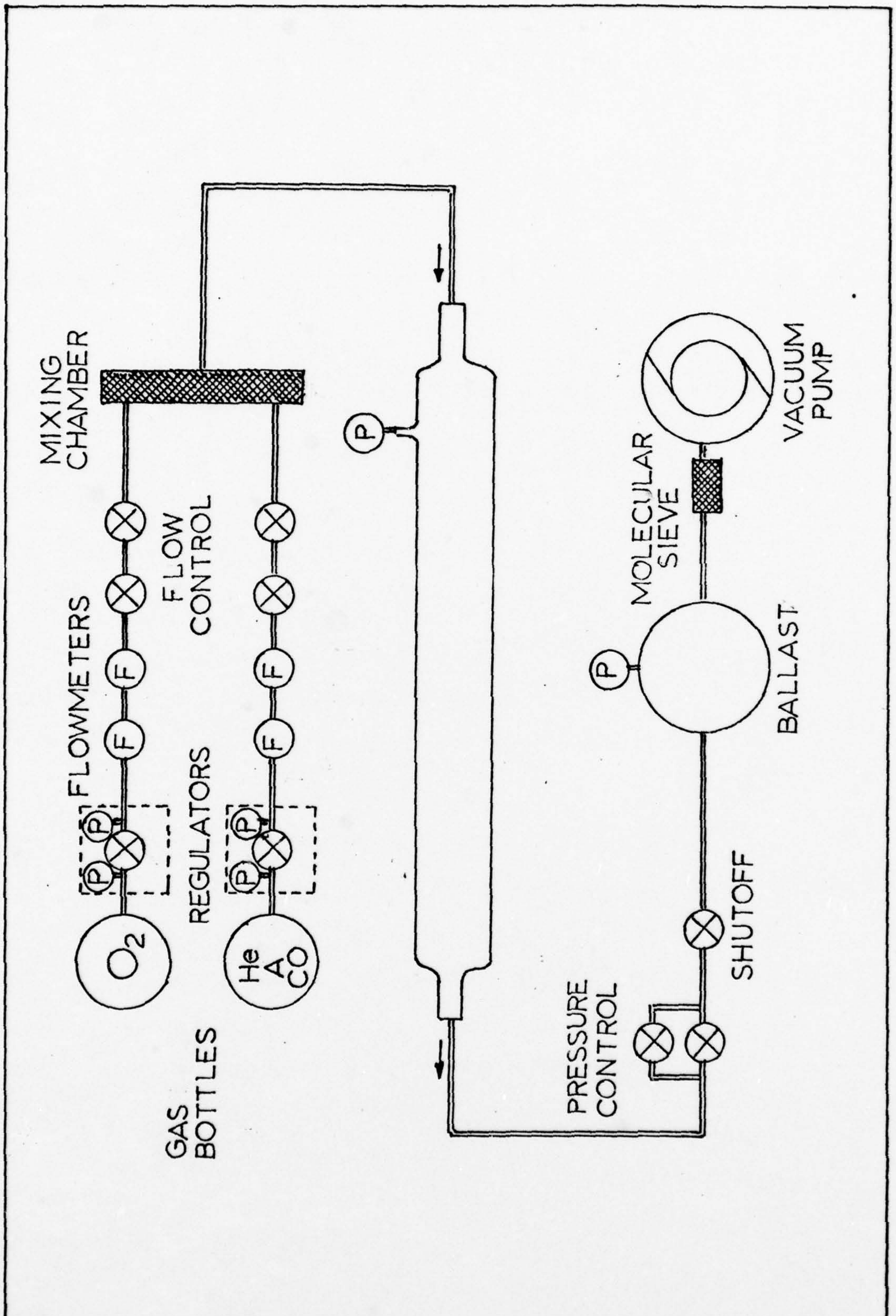

Figure 6. Gas System Schematic

the discharge tube by a Baratron capacitance manometer system. Both absolute and relative 100 torr heads were utilized during different phases of the experimentation.

The overall gas system was capable of operating at a minimum pressure of one micron with no flow. During operations with a discharge the pressure was adjusted to between one and ten torr in the tube. A positive flow was maintained throughout all experiments to minimize the buildup of contaminants in the discharge volume that could have resulted from small leaks or from out-gassing. Flows ranged between 10 and 500 SCCM.

Electrical System (Figure 7)

The electrical power for the discharge was provided by a Spellman Model HP5PN500SRX power supply. This supply was capable of providing a regulated voltage between zero and five kilovolts D.C. or a regulated current between zero and five hundred m.a. The current-regulating circuit of the Spellman was not capable of responding to the rapid change of impedance of the oxygen discharge during transition between the high and low field forms. Therefore, a custom-built, fast-reaction, current-regulator was placed in series between the Spellman power supply and the discharge; and the Spellman power supply was operated in the constant voltage mode. The current regulator was capable of being controlled manually, by a motor driven sweep, or by an electronic signal of arbitrary waveform. Pulses were used

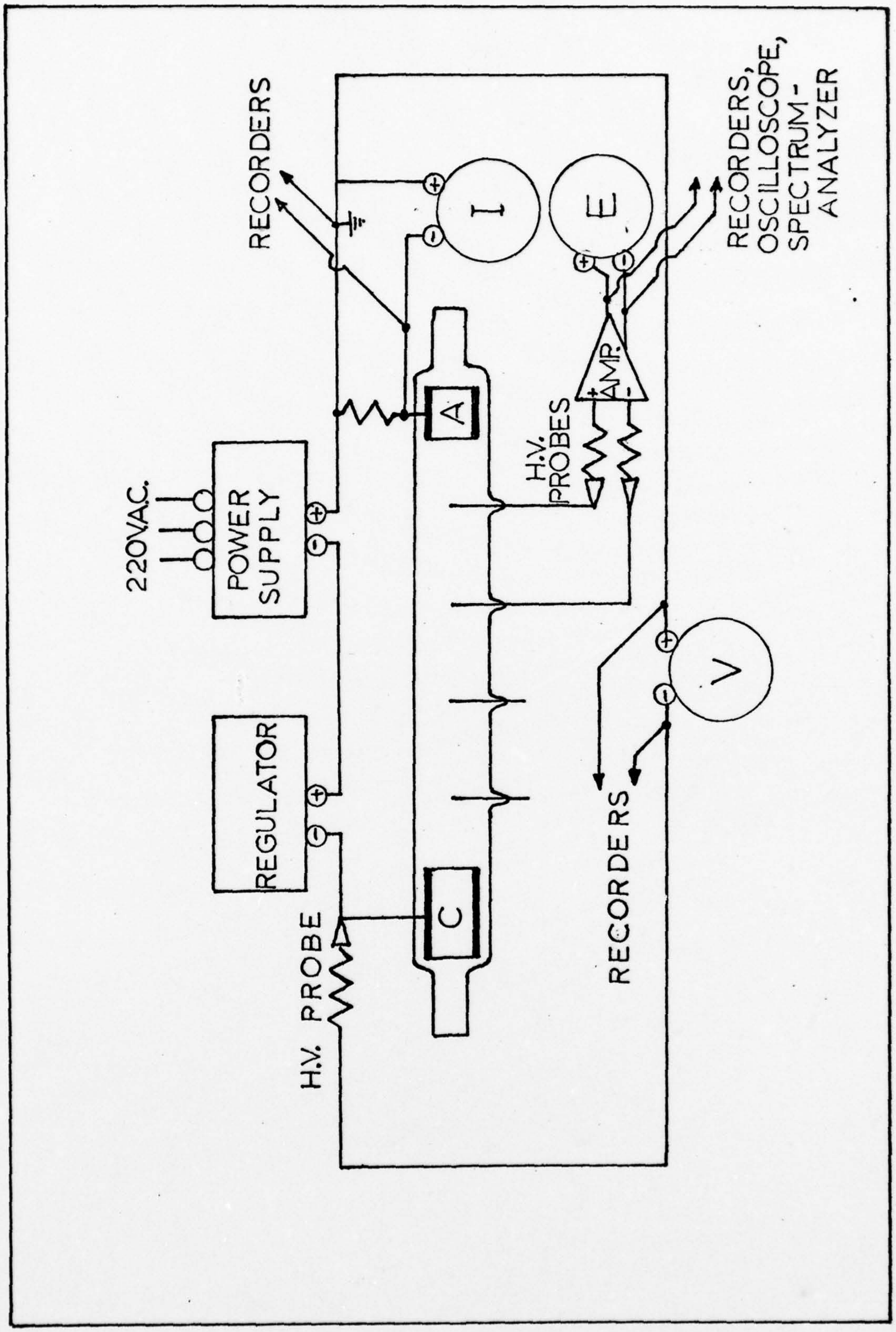

Figure 7. Electrical Schematic

during one experiment to synchronize the oscillations. The utilization of a good current regulator was key to removing the external circuit effects from the discharge characteristics. The custom regulator used in this study outperformed any commercially available at the time.

The current through the discharge tube and the potential across the tube were monitored on digital voltmeters and recorded on a Hewlett Packard 7004A x-y recorder. The electric field was determined from the potential difference between probes inserted in two ports of the discharge tube. Two systems for measuring the electric field were utilized during various phases of the experimentation. A laboratory-constructed differential amplifier system with an input impedance in excess of 10^{10} ohms was used for D.C. and low frequency measurements. For high frequency measurements of the oscillatory electric fields, frequency compensated Tektronix probes with input impedances of 10^{9} ohms were used in conjunction with a Tektronix 1A7A differential amplifier. The outputs of these systems were variously connected to a digital voltmeter, a Hewlett-Packard 7004B x-y recorder, a Tektronix 555 oscilloscope, and/or a Hewlett-Packard 8556A spectrum analyzer.

Cooling System (Figure 8)

It was observed early in the experimentation that the oxygen discharge ran very hot; a significant portion of the input energy was converted to heat. In order to insure

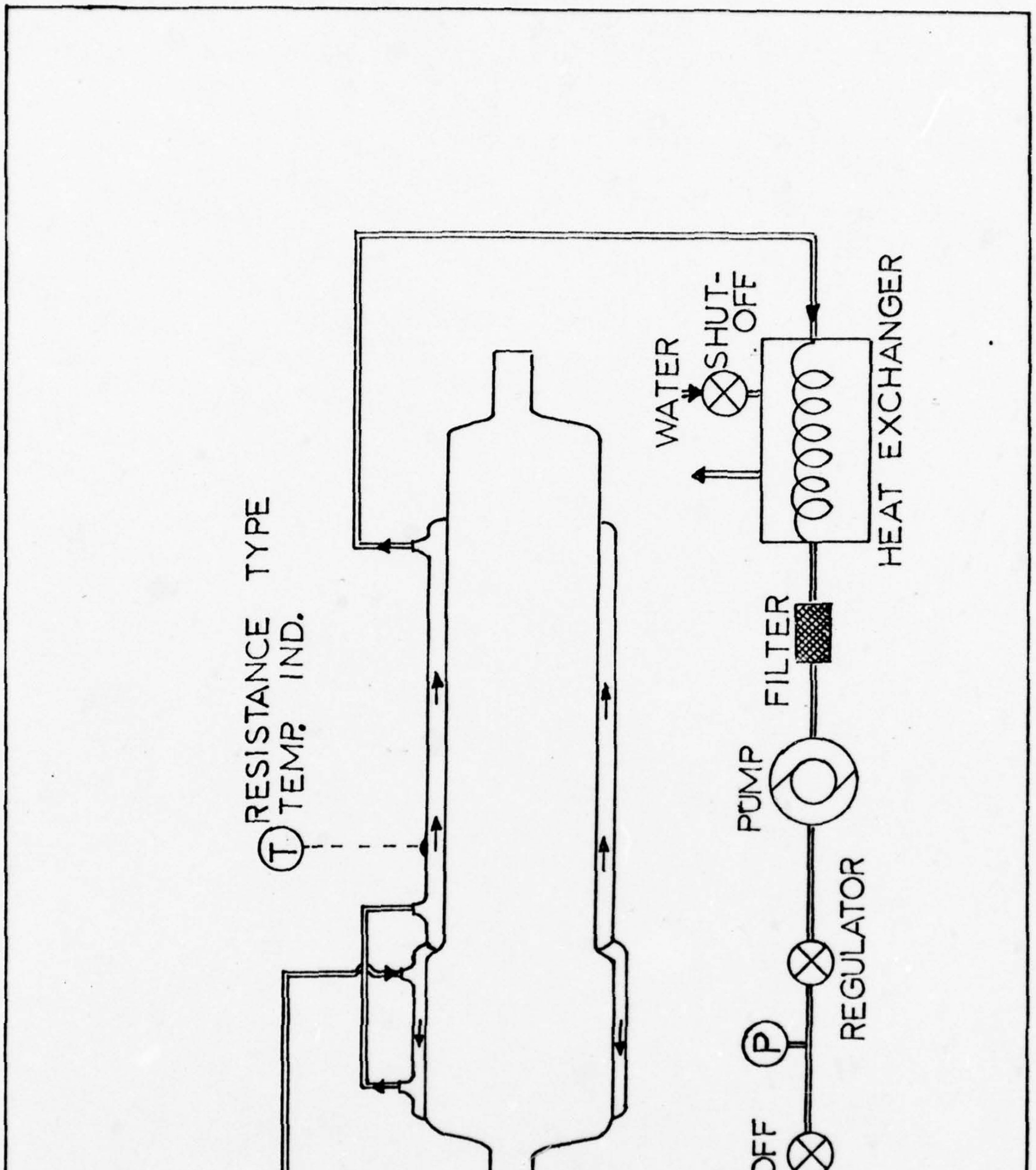

Figure 8. Cooling System Schematic

experimental repeatability and to protect the discharge tube, a cooling system was utilized to maintain the discharge tube wall temperature near that of tap water. Carbon tetrachloride was utilized as the coolant due to its low dissipation factor at microwave frequencies; this was important for the electron density experiment.

The coolant was pumped through the tube at a pressure of approximately five to ten psi. After passing through the tube, the heat was removed from the carbon-tetrachloride in a water-cooled heat exchanger. The system was so efficient that the outside wall of the outer jacket never exceeded a temperature of $18^{o}C$, as measured by a platinum resistance probe taped to the tube.

III. Impedance Characteristics

This chapter is the first in which experimental results are presented. It covers the measurements of the electrical impedance of the oxygen discharges both with and without additive gases. Electrical impedance experiments are relatively easy to perform, and they tell a lot about the overall characteristics of a particular plasma. However, it is very difficult to determine from these results the explanations of the characteristics. In this chapter both quantitative and qualitative results are presented. Some of these are explained in future chapters after further experimentation or modeling.

The chapter starts with a brief explanation of the factors that determine the impedance of a discharge. This is followed by a description of the experimental techniques used. Then the experimental results are presented. Specifically, the discharge potential and electric field values are depicted as functions of current and pressure for pure oxygen, oxygen plus argon, and oxygen plus carbon monoxide. Also, mappings of the high and low field forms of the discharge and the effects of inert and detaching additive gases are presented.

Theory

When an electric field is applied to a plasma, the charged particles are accelerated in a direction parallel or anti-parallel to the field. The charged particle current density, $\bar{j}$, can be determined from:

$$\bar{j} = q \cdot \left(\sum_i N_i \cdot \bar{V}_i - N_e \cdot \bar{V}_e \right) \qquad (5)$$

where q is the electronic charge, N_i and N_e are the ion and electron number densities; and $\bar{V}_i$ and $\bar{V}_e$ are the ion and electron drift velocities. Due to its high mobility the electron is the major contributor to the current flow in a discharge. The electron drift velocity can be calculated from:

$$\bar{V}_e = - \frac{\bar{E}}{m_e \cdot \nu_{eN}} \qquad (6)$$

This relationship combines the effect of the accelerating force, the electric field ($\bar{E}$), and the effects of the decelerating force, the frequency of electron-neutral collisions (ν_{eN}). Combining the above equations and disregarding the ion current leads to the following relationship for the plasma impedance:

$$\bar{j} = \left(\frac{q \cdot N_e}{m_e \cdot \nu_{eN}} \right) \cdot \bar{E} \qquad (7)$$

The discharge current versus voltage relationship can be determined from the above equation by integrating the current density throughout the cross section of the discharge and the electric field along the length of the discharge.

In equation 7 the electron number density and effective collision frequency are complex functions of the electric field, gas temperature, gas pressure, collisional cross sections of the constituent species, and the discharge tube geometry. Although the theoretical determination of the impedance is complicated, the measurement of the discharge impedance is normally an elementary experiment. However, in the case of oxygen, the measurement of the impedance in the transition regions is complicated by the requirement for a very good current regulator. Previous low-field-form investigations without good current regulation are subject to the suspicion of the discharge acting as a circuit element in an oscillatory circuit rather than just exhibiting positive column oscillations.

Experimental Setup/Technique

The general experimental setup described in Chapter II was utilized during the determination of the discharge impedance characteristics. X-Y recorders were used for recording the tube potential and electric field as functions of the discharge current. The discharge current was slowly swept from both low to high current and from high to low, thus allowing the hysteresis effects to be displayed. The electric field was measured by probes inserted through ports 3 and 4.

The gases were flowed through the tube at rates calculated to maintain a constant residence time regardless of pressure. Temperature effects were not taken into account. The flow was adjusted according to the following relation:

$$F = P \cdot 6.78 \tag{8}$$

where F is the gas flow in standard cc per min. The velocity of the gas in the tube Vg was:

$$V_g = \frac{F_a}{\pi \cdot R_o^2} \tag{9}$$

where F_a is the actual gas flow in cc per sec and is determined by:

$$F_a = 4.32 \times 10^{-2} \cdot \left(\frac{T \cdot F}{P}\right) \tag{10}$$

The residue time of the gas in the tube, τ_{res} , was:

$$\tau_{res} = \frac{L}{V_g} \tag{11}$$

where L is the length of the discharge. For T = 300°K, L = 50.5 cm, R_o= .95 cm: Vg = 31.02 cm/sec, τ res = 1.63 sec.

Experimental Results

Pressure Effects and Hysteresis. Figures 9, 10, and 11 depict the tube potential and electric field variations as functions of the tube current. These figures depict typical curves for the parameters specified. Experimental repeatibility was good between runs, especially in regard to the potential and electric field values. The greatest variation occurred in the current values at which the discharge transitioned between forms. Generally this variation was less than 10% for the high current transition. The low current transition variation was greater. However, it is postulated that this variation was due to the reduced stability of the current regulator at low currents and the high negative impedance of the discharge. Often, at or near the point of the low current transition, the regulator would begin to oscillate; and the discharge would extinguish. It was impossible to map this transition at pressures in excess of 6 torr.

Figure 9 depicts the potential variation as a function of current at various pressures. The high current transition between the high and low field forms was a very strong function of both current and pressure; the low current transition was a strong function of current only. The transition between the forms was very rapid at any one axial position in the tube. The two forms often existed in the tube at the same time. When this occurred the high field form existed on the anode side of the positive column and the low field form on the cathode side. Discontinuities in the tube often provided the interface between the two forms when they coincided in the column. This simultaneous existence of the two forms is illustrated by the stair-stepped nature of the transitions in figure 9. As different axial sections

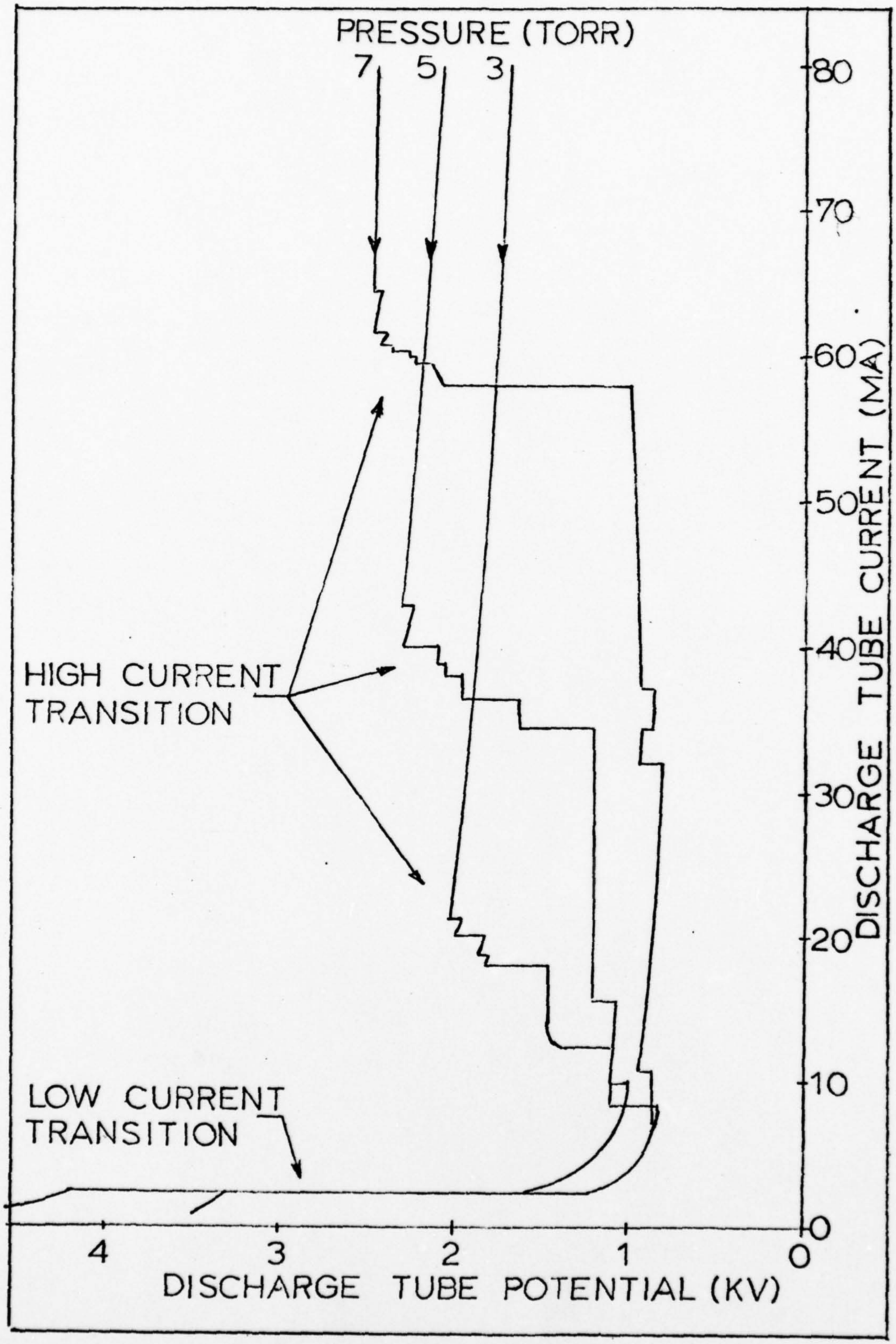

Figure 9. Pressure Effects on Discharge Impedance

of the tube transitioned, the potential trace stepped to a new value. Often the electric field probes acted as the spatial discontinuities for the interfaces between the forms.

In the high field form the discharge was stable; there were no perceivable oscillations or random behavior. In the low field form, however, there were large amplitude oscillations and/or noiselike behavior. This was observed from oscilloscope and spectrum analyzer traces of the tube current. In the low field form there was considerable jumping among different potential values as the current was swept. This is shown only on the 7 torr trace of Figure 9 but appeared on all the raw data. The difference between the low field potentials was small and was related to the frequency of oscillation. As the oscillation frequency jumped between different stable and/or astable modes, the potential would jump.

Figure 10 depicts the hysteresis nature of the transition. The discharge tended to stay in the form in which it existed. The high current transition always exhibited a predictable hysteresis phenomenon. The low current transition did not; the limitations of the experiment equipment precluded a predictable mapping of this transition.

Figure 11 is a typical electric field variation for the discharge. The transitions of the electric field tracked those of the tube potential. Due to the fact the electric field measurements encompassed only a small section of the axial length of the tube, the stair-stepping during

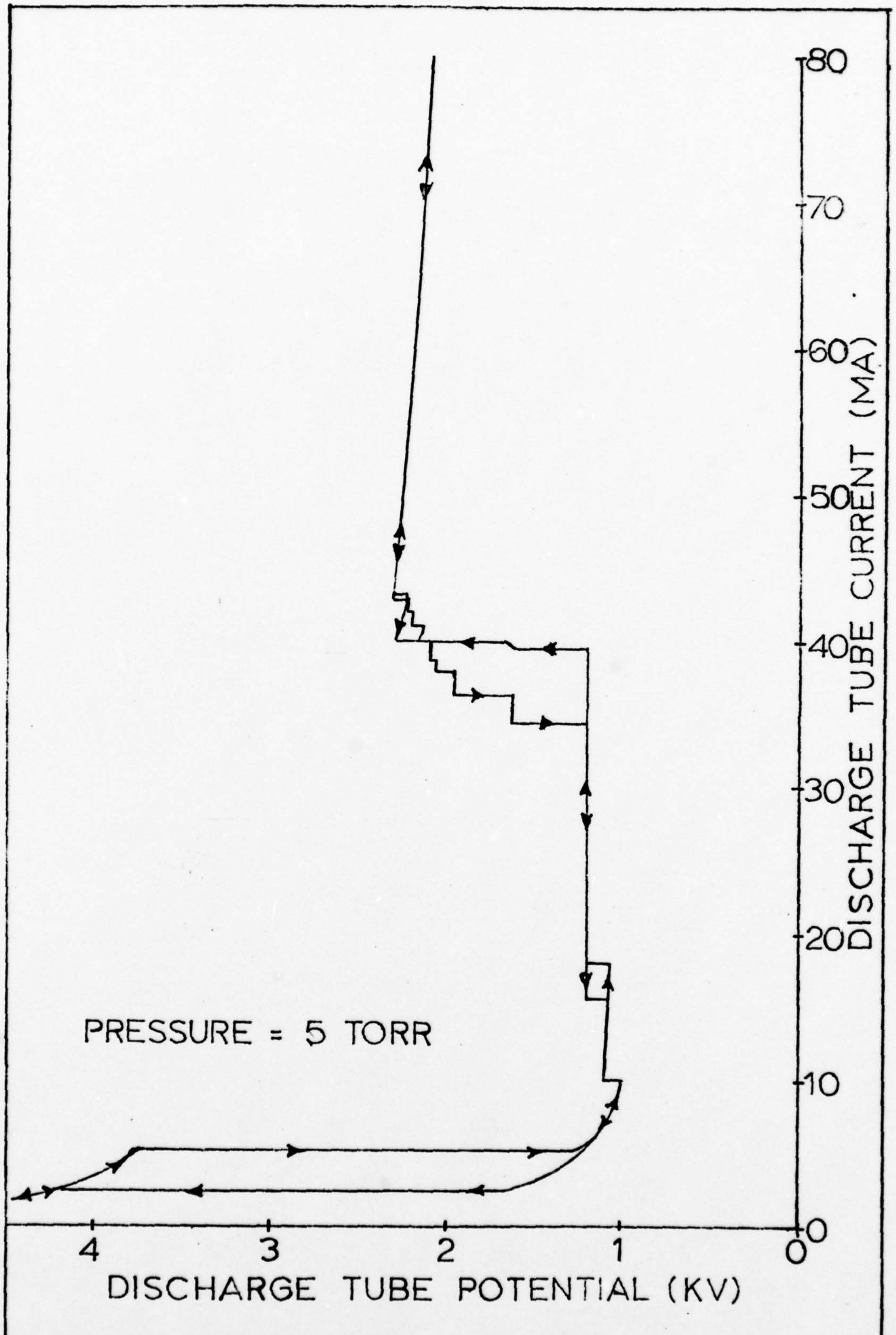

Figure 10. Hysteresis of Discharge Impedance

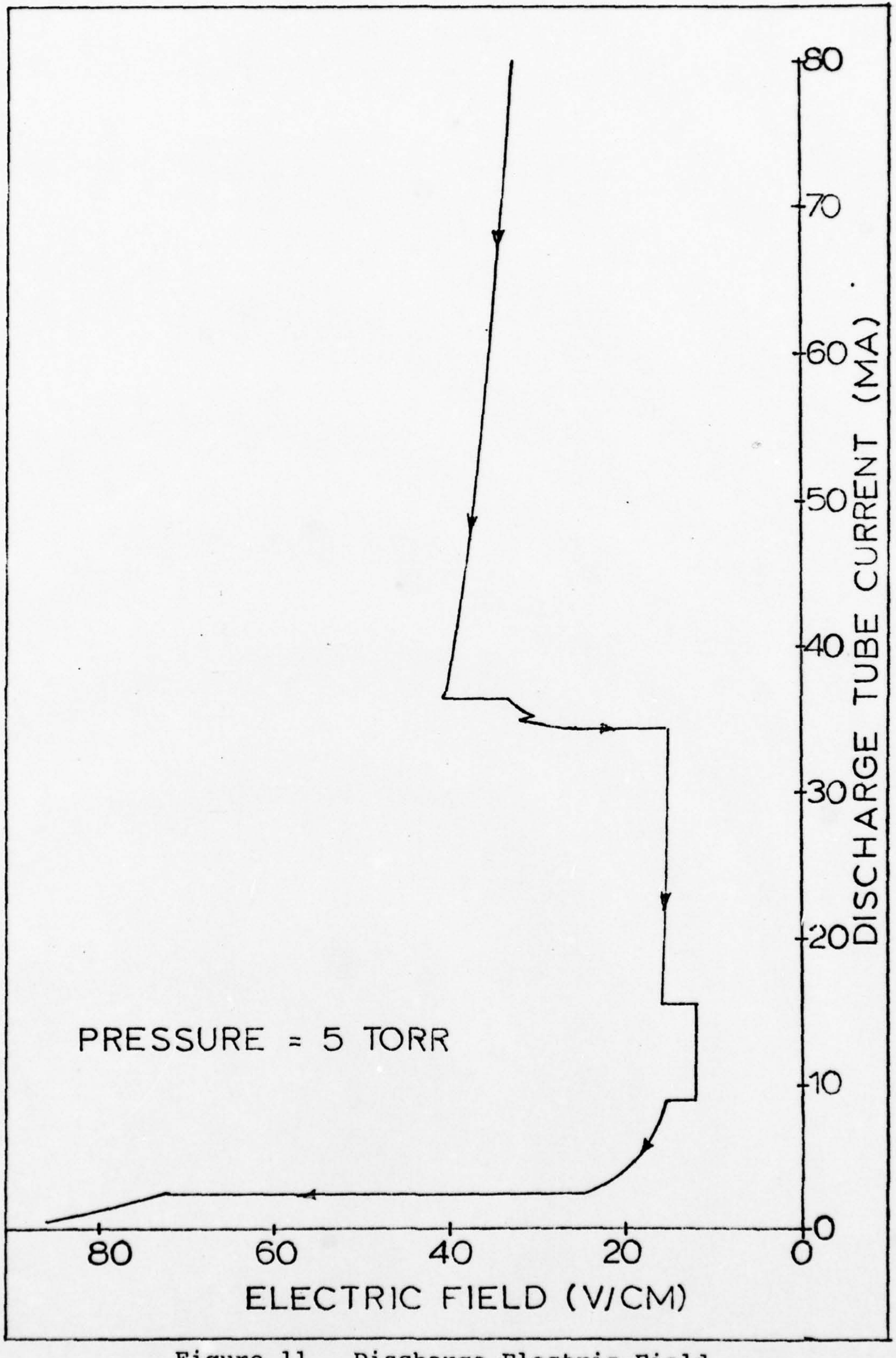

Figure 11. Discharge Electric Field

transition was much less evident. Usually only two steps were included in the spatial span between the two electric field probes.

Existence Regions. Figure 12 is a plot of the existence regions for the high and low field forms as functions of the discharge current and pressure. The transition points were taken from the electric field-vs-current traces. During a high current-to-low current sweep, transition was considered to have taken place when the first portion of the region between the two probes transitioned. For the low-to-high sweep the final transition was used for the transition point. Points from several different experimental runs were plotted, and a least squares power curve fit was made. The resulting boundary curves for the high current transitions showed good correlation (r_c^2 = .96 to .98) with the data; the low current transitions were poorly correlated. The experimental results of Pekarek are shown for comparison* (Ref 15: 750).

Flow Effects. An experiment was conducted to determine the effects of gas flow rate on the characteristics of the discharge. Flow rate was varied over approximately an order of magnitude. It was observed that the impedances in the low and high field forms of the discharge did not vary significantly as functions of the flow rate. However, the

---

*A direct comparison is difficult to make. Pekarek's experiments were conducted with a nonflowing gas in an uncooled discharge tube.

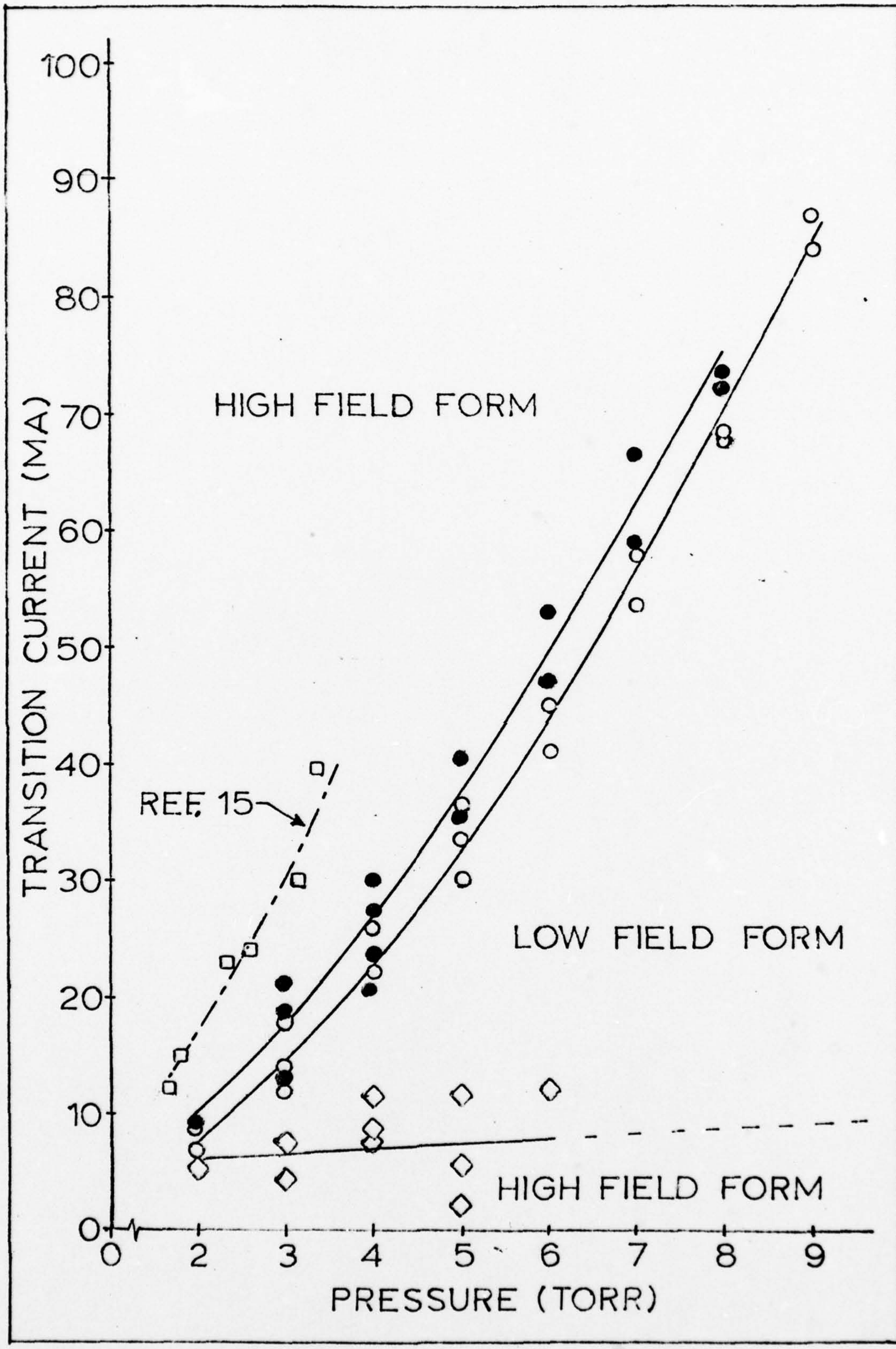

Figure 12. Existence Regions

point of transition between the forms did change. Figure 13 depicts the low-to-high and high-to-low transition points as functions of the flow rate. As shown on the figure the transitions occurred at lower currents, and the hysteresis became more pronounced as the flow was increased.

Effects of Additives. Other gases were mixed with the oxygen to determine the effect on the discharge characteristics. Carbon monoxide and argon were chosen as the additive gases - carbon monoxide because it is a strong detacher of the electron from the O^- ion (Ref. 31:597-599) and argon because it is inert and should have only minor effects on the characteristics. During the experimentation the oxygen flow was set at a high rate*, and the mix percentage was controlled by adjustment of the additive gas flow rate. The partial pressure of the oxygen was maintained constant while the total pressure was allowed to vary with the additive. The mixture percentages specified in figures 14 through 17 refer to volume and were calculated by dividing the additive flow rate by the oxygen flow rate.

Figure 14 depicts the effect of the addition of argon on the impedance characteristics of the discharge. As shown in the figure the effect was minor. The impedances of the high and low field forms remained basically unchanged. The transition point between the two forms was slightly effected,

---

*400-500 sccm, depending on the vacuum system's ability to maintain the desired pressure.

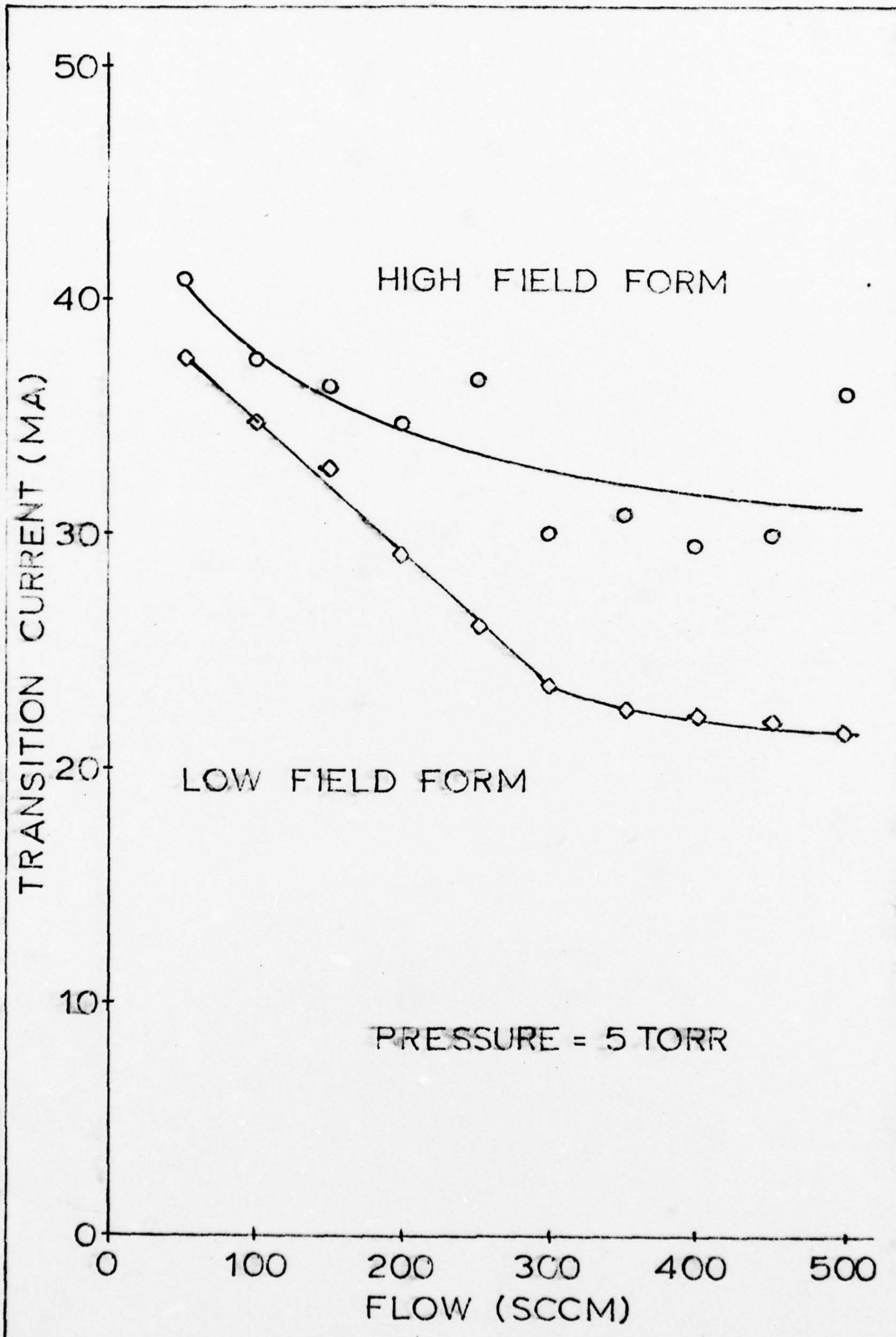

Figure 13. Effects of Flow on Transition

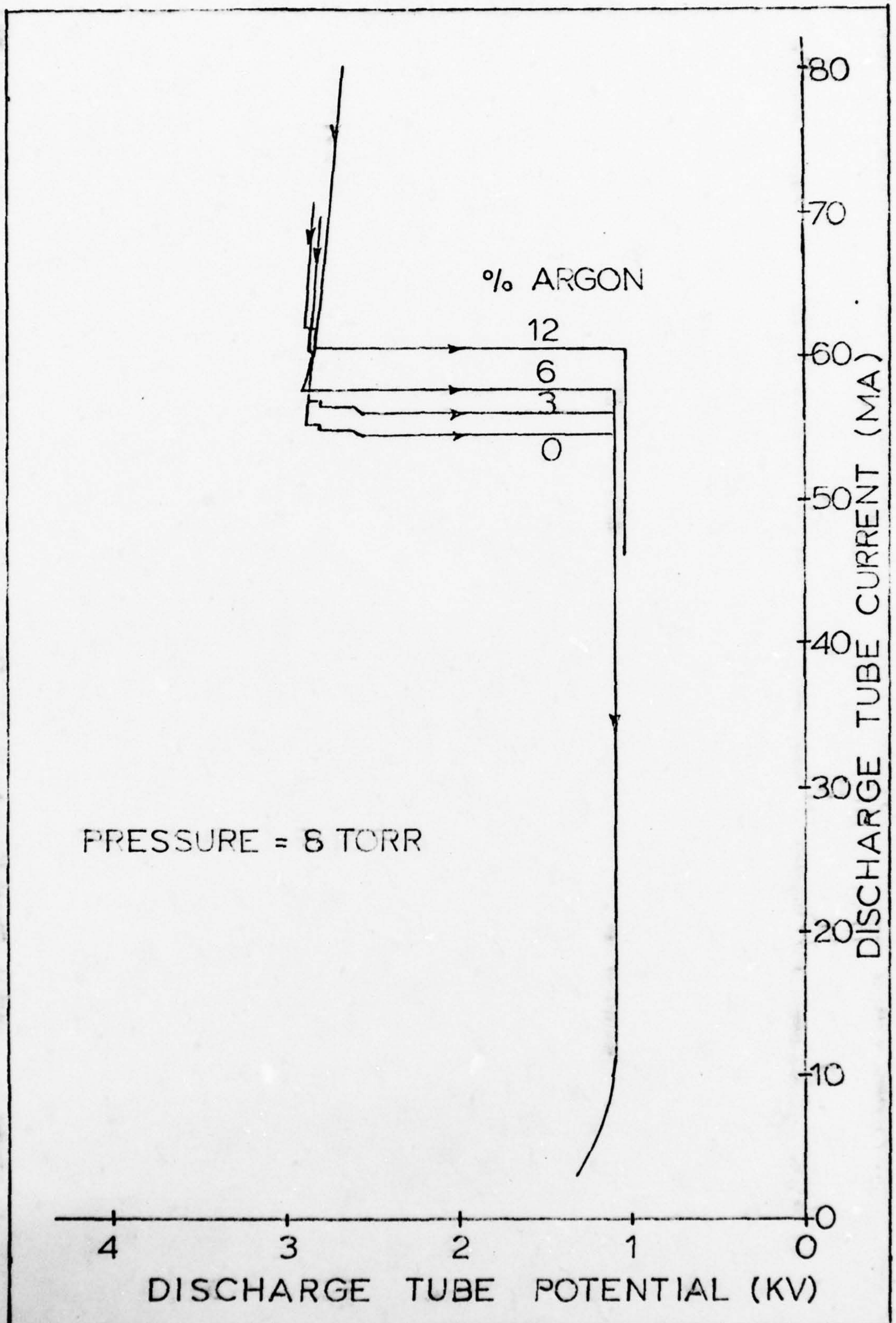

Figure 14. Argon Additive Effects on Discharge Impedance

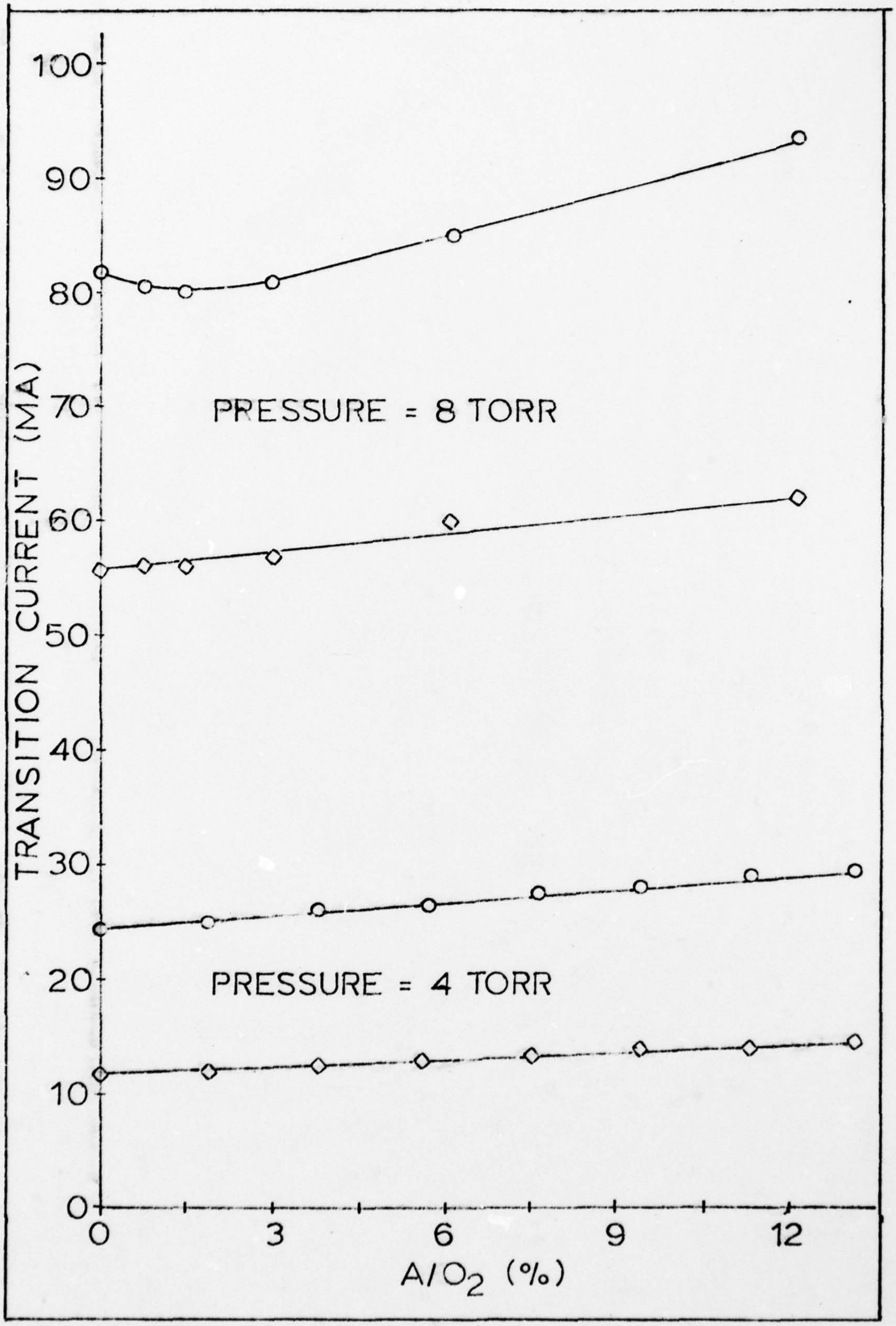

Figure 15. Argon Additive Effects on Transition

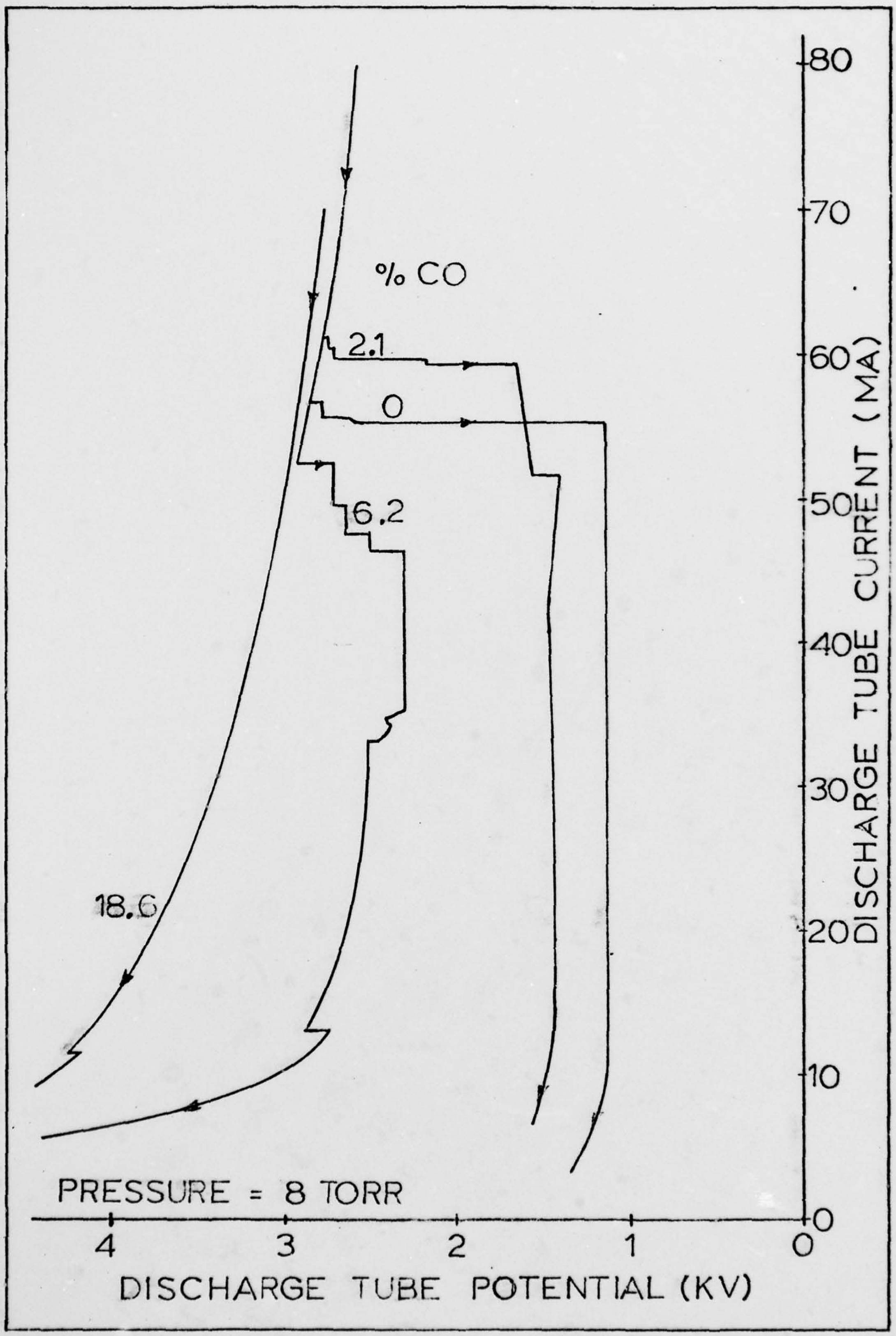

Figure 16. CO Additive Effects on Discharge Impedance

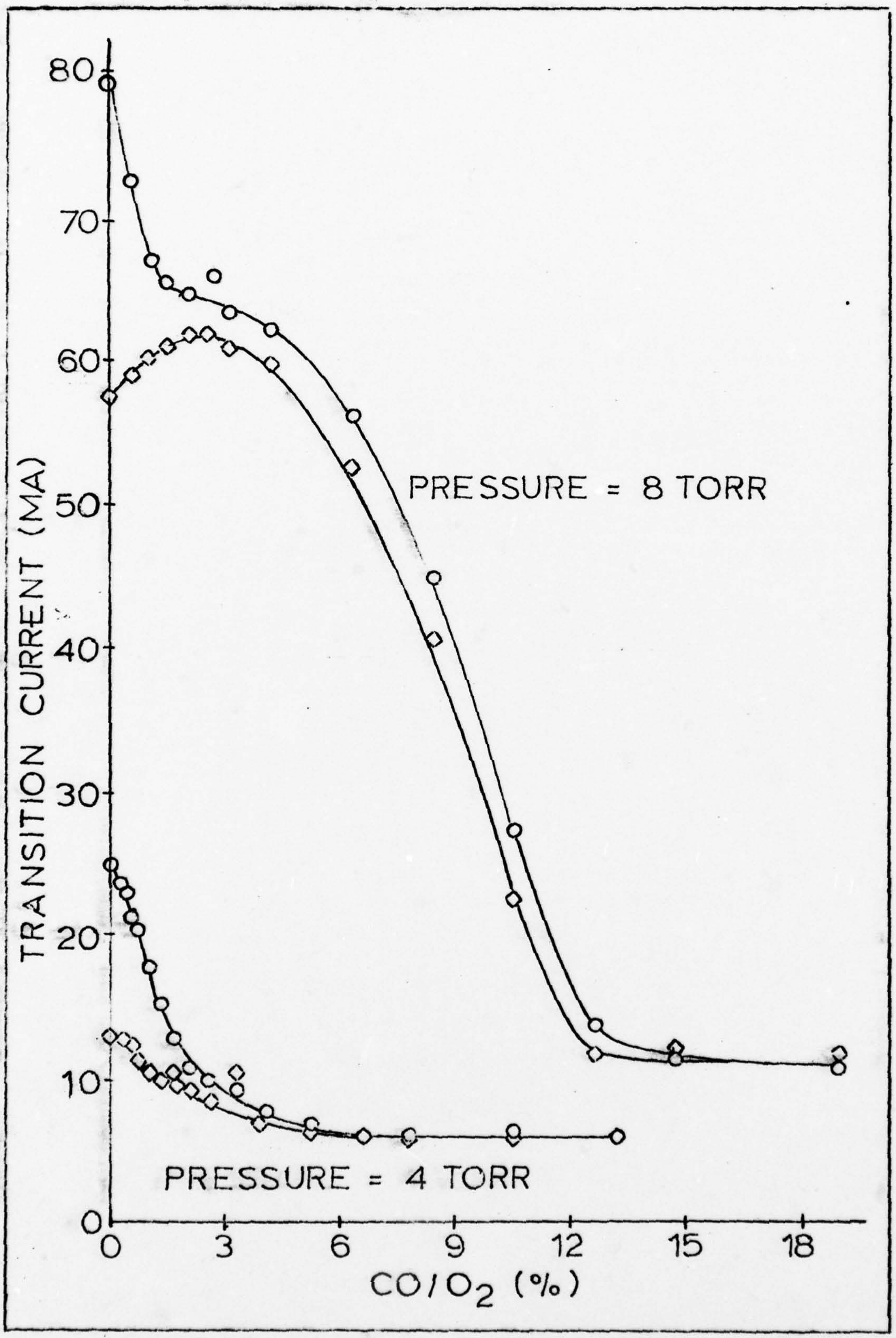

Figure 17. CO Additive Effects on Transition

as depicted in figure 15.

The effect of carbon monoxide on the discharge was much more pronounced, as depicted in figure 16. As carbon monoxide was added, the DC impedance of the low field form increased to the point where the difference between the two forms essentially ceased to exist. The transition between the two forms generally decreased to lower currents, and the hysteresis became less pronounced as the additive was increased. Figure 17 depicts the carbon monoxide effect on the transition point. For both the 4 and 8 torr experimental runs there was no mixture that completely eliminated the transition; however, as illustrated by the 18.6% run in figure 16, the difference in impedance across the transition was minor.

IV. Discharge Heating and Gas Temperature

The number density of the neutral particles N is one of the key parameters of a partially ionized gas. This parameter, used in conjunction with the electric field, was required for comparison of the experimental results of this study with the modeling results and with other experiments. The number density was calculated by using the perfect gas law*:

$$N = \frac{P}{R \cdot T} \tag{12}$$

The determination of the pressure, P, was easy; the determination of the temperature, T, was very difficult.

This chapter addresses the determination of the gas temperature. In the first portion of the chapter a relationship for the radial and axial gas temperature is determined using the assumption that all the input energy is deposited in gas heating. Next the setup used to experimentally determine the gas temperature is presented. This is followed by the experimental results. Finally, these results are used to develop a relationship between gas temperature, input electrical power, and gas pressure. Once determined, this relationship was used in reducing all of the experimental data. As an example, the relationship between E/N and

---

*Valid for the pressures used in this study.

current is presented for various pressures.

Theoretical Determination of Gas Temperature

The following analysis is based on the assumptions that all of the electrical energy input ends up in gas heating and that the heating is uniform in the axial and radial directions. The first assumption is obviously not true;. some of the energy goes into excitations which decay into optical channels* or into long-lived metastable levels which flow out of the tube before decaying. The second assumption for the radial direction is good for the low field form where all of the experimental measurements were made. Thompson has shown that the energy pumping species, the electrons, have a generally constant density profile when the negative ion to electron concentration ratio is high, as is true of the low field form of the discharge (Ref 20:514). Due to oscillations the axial heating is definitely not uniform at any one point of time. Time averaging, however, should allow this assumption to be reasonably good.

The theoretical determination of the gas temperature is based on balancing the rates of energy gain and losses. Consider the incremental volume between the two concentric cylinders of figure 18.

---

*This is a very small amount as evidenced by the limited optical output from the discharge.

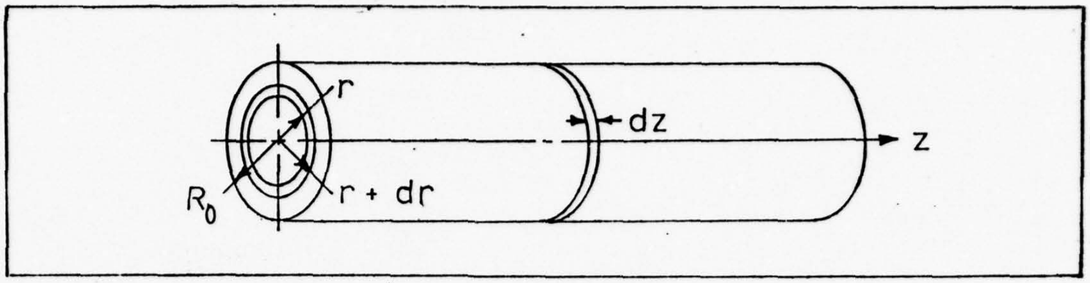

Figure 18. Geometry for Temperature Determination

The energy rate balance equation is*:

$$\dot{U}_g = \left(\dot{U}_{co} - \dot{U}_{ci}\right) + \left(\dot{U}_{Fo} - \dot{U}_{Fi}\right) \tag{13}$$

Rate of energy gain in the volume; Net radial conduction loss; Net flow loss

The energy gain from the electric field is:

$$\dot{U}_g = \frac{.478 \cdot E \cdot I \cdot r \cdot dr}{R_o^2} \quad (\text{cal sec}^{-1}) \tag{14}$$

The radial conduction of energy into or out of a cylindrical surface with height dz is:

$$\dot{U}_c = K \cdot \int \overline{\nabla T} \cdot \overline{dA} = 2 \cdot \pi \cdot K \cdot r \cdot dz \cdot \frac{\partial T}{\partial r} \tag{15}$$

Where K is the thermal conduction coefficient for the gas. Using the first two terms of a Taylor series expansion to relate the temperature at r + dr to the temperature at r, the net rate of radial conduction loss is:

---

*Axial conduction was assumed to be small compared to flow.

$$\dot{U}_{co} - \dot{U}_{ci} = -2 \cdot \pi \cdot K \cdot dr \cdot dz \cdot \frac{\partial}{\partial r}\left(r \cdot \frac{\partial T}{\partial r}\right) \tag{16}$$

The axial flow of energy into or out of the concentric circular areas is:

$$\dot{U}_F = \frac{5}{2} \cdot N \cdot k \cdot T \cdot \pi \cdot r \cdot dr \cdot V_g \tag{17}$$

where k is Boltzmann's constant. The net rate of axial flow loss is:

$$\dot{U}_{FO} - \dot{U}_{Fi} = \frac{5}{2} \cdot N \cdot k \cdot \pi \cdot r \cdot dr \cdot V_g \cdot \frac{\partial T}{\partial z} \cdot dz \tag{18}$$

where the first two terms of a Taylor series expansion were used to relate the temperature at z + dz to the temperature at z. Equation 12 was used to determine the value of N; and equations 8, 9 and 10 were used to determine the value of Vg. After substituting these equations into equation 18 and combining it with equations 14 and 16 into equation 13:

$$.530 \cdot E \cdot I = -\frac{3.88 \times 10^{-4}}{r} \cdot \frac{\partial}{\partial r}\left(r \cdot \frac{\partial T}{\partial r}\right) + 2.6 \times 10^{-5} \cdot P \cdot \frac{\partial T}{\partial z} \tag{19}$$

where the value of 6.18×10^{-5} cal/(sec)(cm^2)(^{o}c/cm) was used for K (Ref 32:E-2). In solving equation 19 for T, it was assumed that the radial and axial functional relationships of temperature are separable.

$$T(r,z) = T(r) \cdot T(z) \tag{20}$$

T(r) represents the radial profile at any position z; T(z) is the axial temperature at r = o. Substituting equation 20 into equation 19:

$$.530 \cdot E \cdot I = -3.88 \times 10^{-4} \cdot \frac{T_o(z)}{r} \cdot \frac{\partial}{\partial r}\left(r \cdot \frac{\partial T(r)}{\partial r}\right) + 2.6 \times 10^{-5} \cdot P \cdot T(r) \cdot \frac{\partial T_o(z)}{\partial z} \tag{21}$$

The solution for the radial profile is a parabolic function:

$$T(r) = 1 + \frac{r^2}{R_o^2} \cdot \left(\frac{T_w}{T_o(z)} - 1\right) \tag{22}$$

where Tw is the wall temperature and it was assumed to be constant. The solution for the axial dependence is an exponential:

$$T_o(z) = T_w + 3.08 \times 10^{2} \cdot E \cdot I \cdot \left(1 - \mathrm{EXP}\left\{\frac{-66.1 \cdot Z}{P}\right\}\right) \tag{23}$$

where it was assumed that the gas entered the tube at z = o with temperature $T_o(z)$ = Tw. For any significant axial position along the positive column, the exponential term in equation 23 is negligible and can be neglected.* Therefore, the centerline temperature can be calculated by:

---

*Experiments were run with an order of magnitude change in flow rate. No appreciable effects on the centerline temperature were noted.

$$T_o(z) = T_w + 3.08 \times 10^2 \cdot E \cdot I \quad (24)$$

The average temperature can be calculated by combining equations 22 and 24 and integrating over the radius of the tube.

$$\langle T \rangle = T_w + 2.05 \times 10^2 \cdot E \cdot I \quad (25)$$

Experimental Determination of Gas Temperature

Experimental Setup. The general experimental setup described in Chapter II was utilized with one addition: a small thermocouple was inserted into port number two in such a position that it could be used to measure centerline temperature. An additional identical thermocouple was immersed in ice water and was utilized as a reference. The potential difference between the two junctions was read out from a digital voltmeter and was used to determine the gas temperature.

Experimental Results. Runs were made at pressures between two and nine torr. Only readings in the low field form were possible. When the discharge transitioned to the high field form, the probe would begin to glow, and the temperature reading would rapidly increase to a value above the theoretical maximum. This incandescence was possibly caused by the recombination of atomic oxygen at the probe surface.

The raw data at any one pressure was insufficient to allow temperature prediction for the total range of power inputs experienced at that pressure. It was important that all of the data, for all pressures, be utilized to allow analytic interpolation and reasonable extrapolation to cover the full parameter space. The data was reduced to a relationship of centerline temperature rise* as functions of power input per molecule and system pressure. The wall temperature was measured throughout the experiment and averaged $290^{\circ}K$ with very little variation. The centerline temperature rise was calculated from:

$$\Delta Tc = T \text{ thermocouple} - 290^{\circ}K \tag{26}$$

The power input per molecule was calculated from:

$$P_M = \frac{E \cdot I}{\langle N \rangle} \cdot \frac{1}{\pi \cdot R_o^2} \tag{27}$$

where equation 12 was used to calculate the average gas density, $\langle N \rangle$.

$$\langle N \rangle = \frac{9.66 \times 10^{18} \cdot P}{\langle T \rangle} \tag{28}$$

The experimental relationship between temperature rise, ΔT_c, to reduced power input is depicted in figure 19.

<u>Analytic Relationship for Gas Temperature</u>. The shapes

---

*Centerline temperature rise was the difference between the measured centerline temperature and the measured wall temperature.

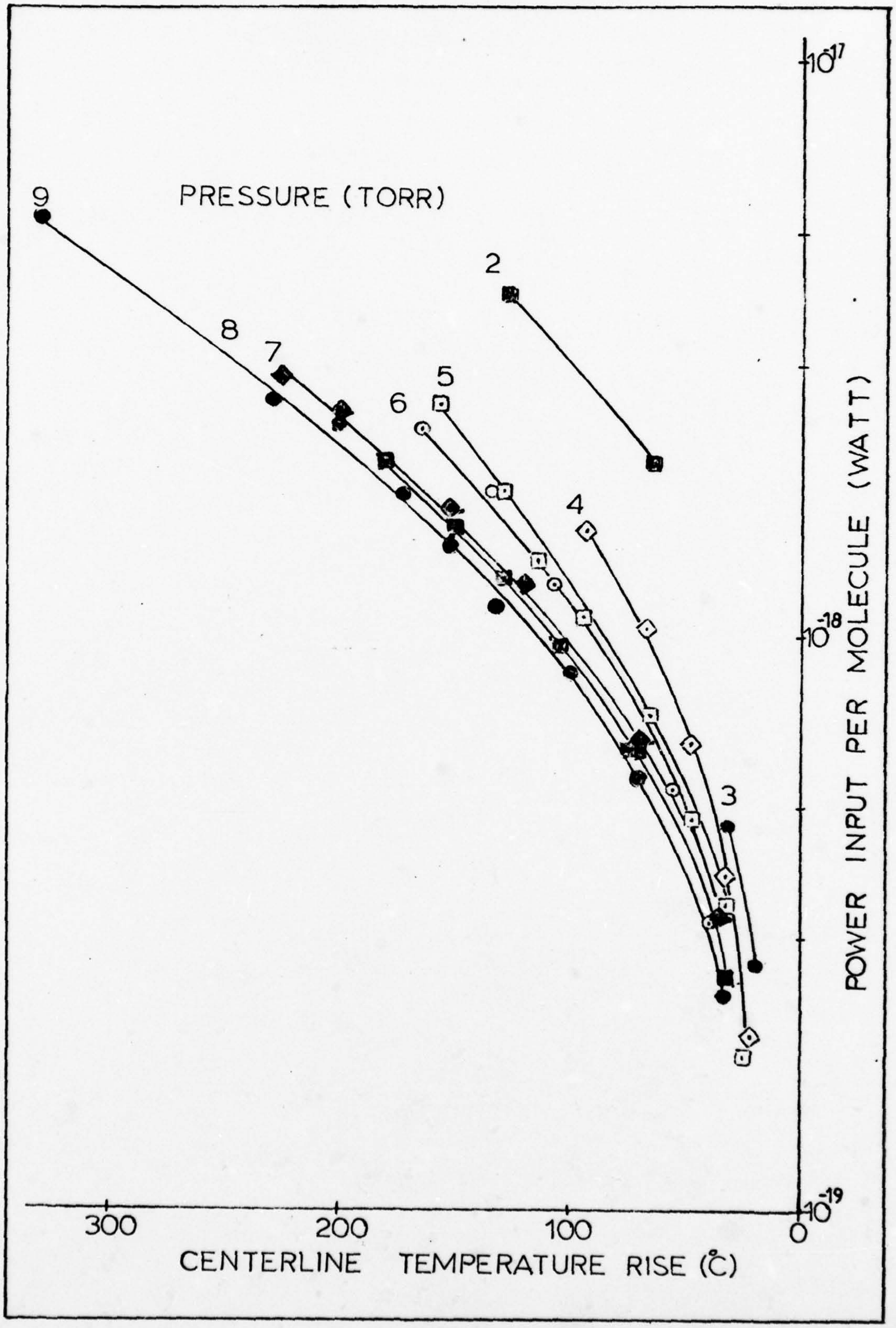

Figure 19. Experimental Temperature Rise

of the curves in figure 19 indicated that an analytic expression for centerline temperature rise could be developed from independent functions of reduced power input and pressure.

$$\Delta T_c = f(P_M) \cdot g(P) \tag{29}$$

The reduced power input function, Pm, was fit to a power curve and the pressure function, P, to a quadratic. The following relation was determined to fit all of the data with good correlation (r_c^2 = .99):

$$\Delta T_c = \left(3.23 + 21.1 \cdot P - 1.05 \cdot P^2\right) \cdot \left(P_M\right)^{0.769} \tag{30}$$

Equations 25, 27, and 28 were used for the determination of Pm. Equation 30 is transcendental and was solved by iterative computations.

Figure 20 depicts the results calculated for 9, 6 and 3 torr using the above expression. Also, the theoretical maximum temperature and the experimental data are plotted. It is to be noted that the calculated curves show initially a negative second derivative, due possibly to an increase in the amount of energy going into nonheating channels as the power input is increased. As the power input is increased further, however, the second derivative becomes positive. This is possibly caused by the rapidly decreasing gas density as the temperature rises.

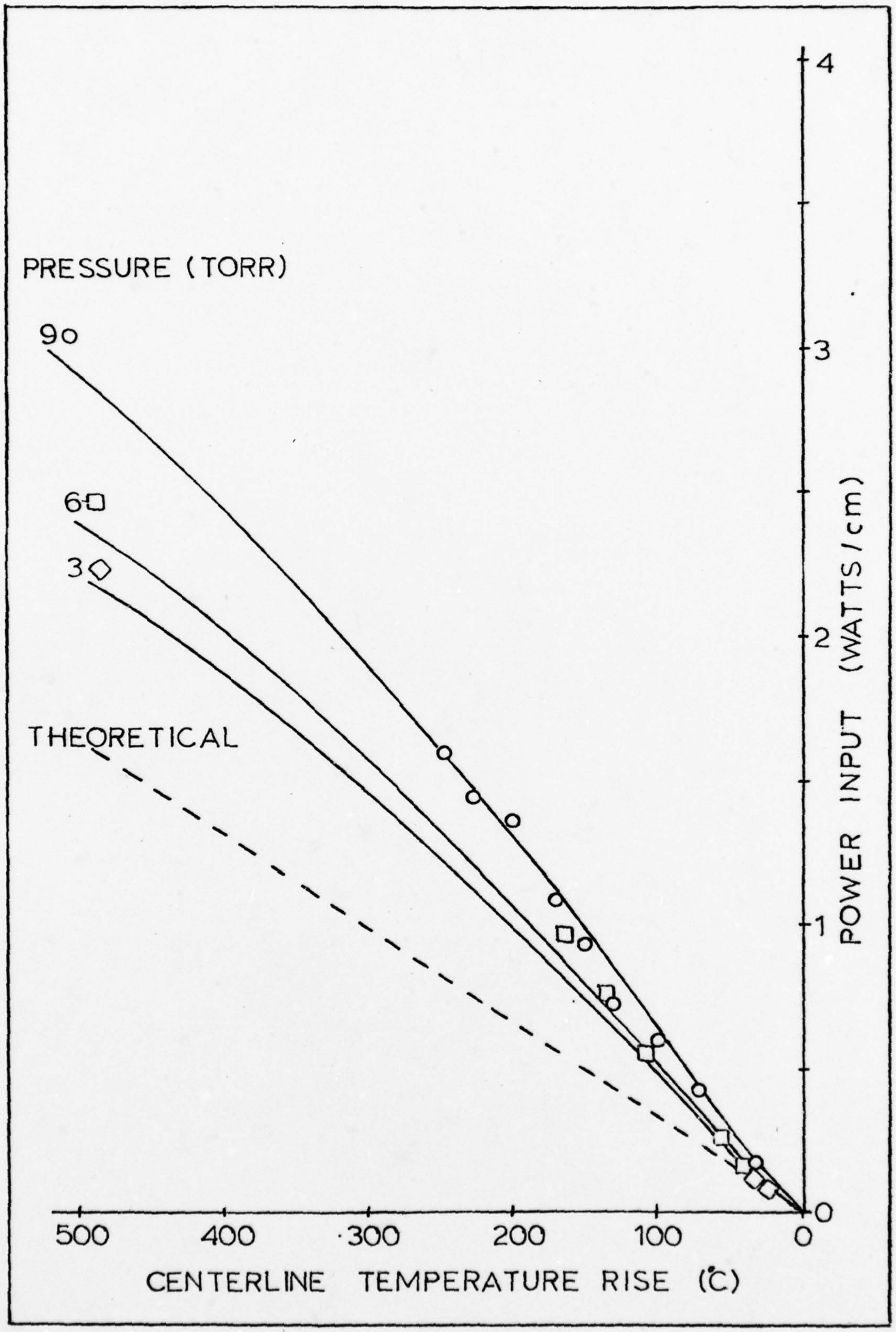

Figure 20. Analytic Temperature Rise

Reduced Electric Field Variation

The analytical expression for the temperature rise in the discharge, equation 30, was used in equation 28 to calculate the gas density, (N), as a function of input power and pressure. This calculation was used to determine the reduced electric field, (E/N), as functions of pressure and current. Figure 21 depicts these relationships for three pressures: 8, 6 and 4 torr. The current sweep was from high-to-low.

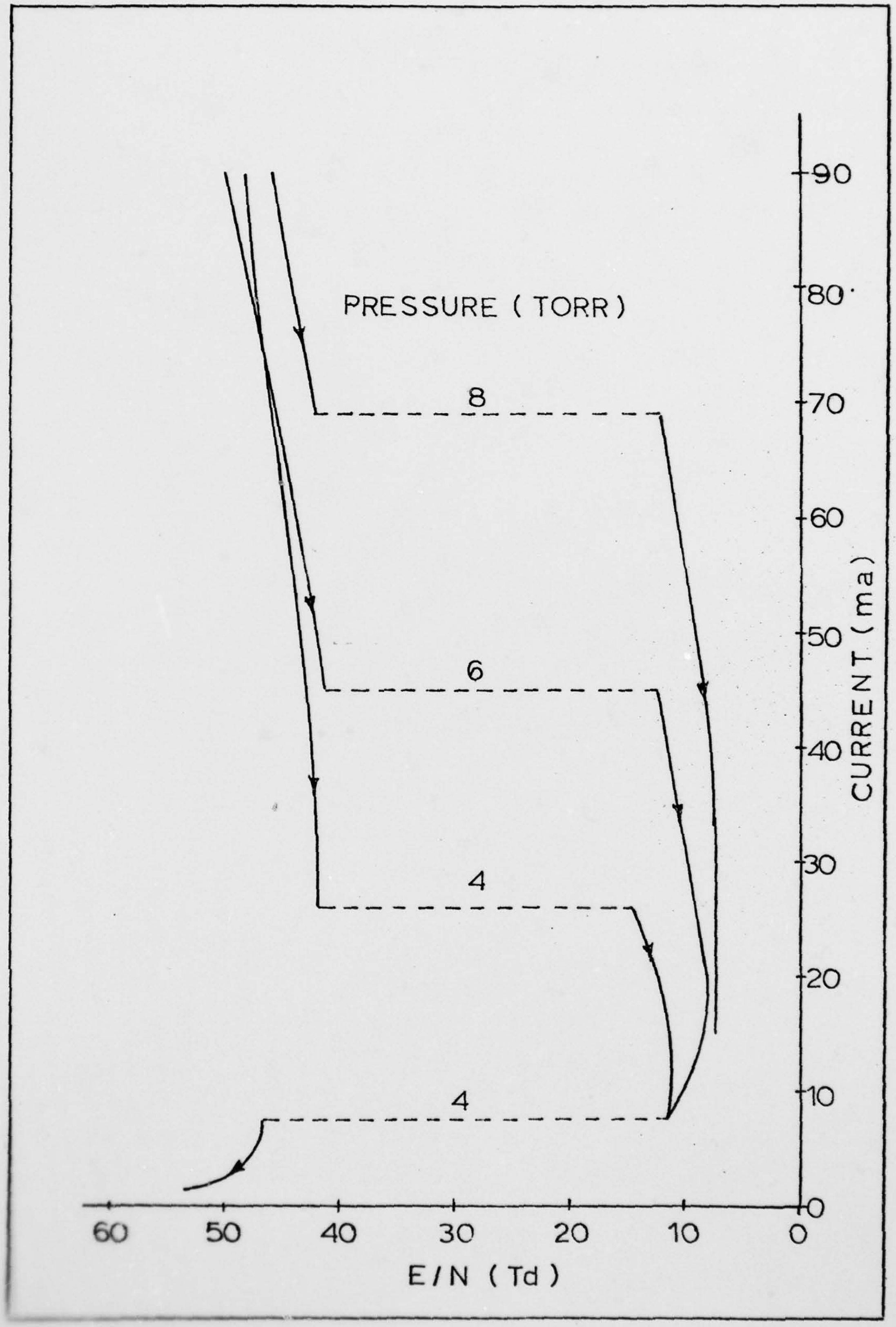

Figure 21. E/N Variation

V. Low Field Oscillations

The unique characteristics of its low field form sets the oxygen plasma apart from the plasmas of other gases. This chapter reports the results of experiments that investigated the oscillations that existed in the low field form. The results of these measurements were not used in validating the models, since the models were limited to only the high field form of the discharge. These experiments were run to provide a better insight into the oxygen plasma.

Two aspects of the low field oscillations were investigated. First the dispersion* was determined for various pressures and discharge electrical currents. Secondly, the nonsteady electric field was measured as a function of the same parameters.

Dispersion of the Oscillations

Experimental Setup and Procedure. In order to determine the characteristics of the low field oscillations, the experimental setup depicted in figure 22 was used in conjunction with the general experimental setup described in Chapter II. A function generator operating in a pulse mode was utilized to pulse the current regulator at the frequency of interest. The low field oscillations were locked into a

---

*Functional relationship between the wave number, k, and the oscillation frequency, ω.

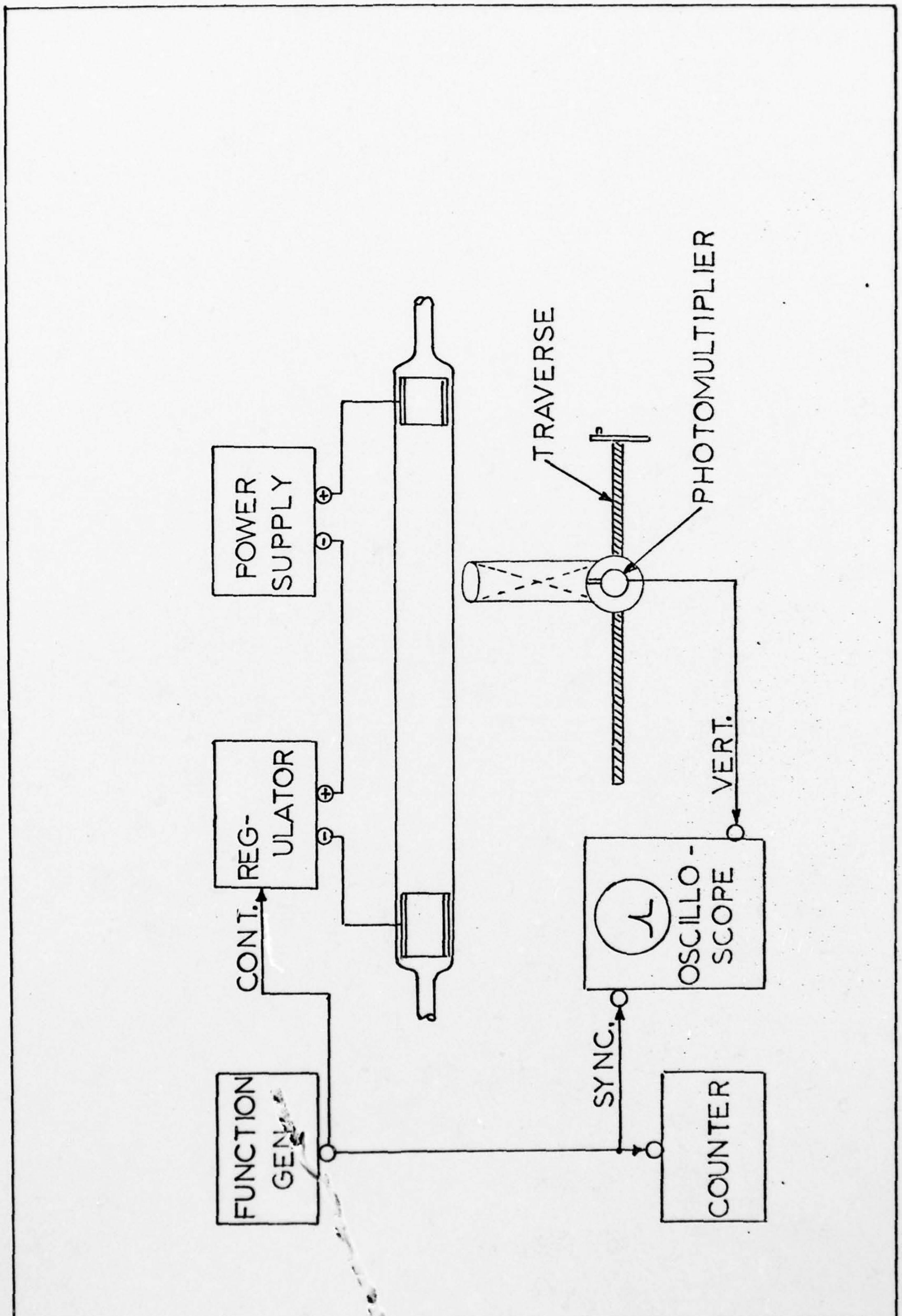

Figure 22. Dispersion Measurement Setup

single frequency stable mode by this method. The output of the function generator was also connected to a frequency counter for a backup determination of the oscillation frequencies.

A photomultiplier tube was mounted inside a casing with a narrow input slit. The optical output from the discharge was focused on the slit. A Gaertner micrometer traverse was used to move and accurately measure the position of the photomultiplier along the length of the discharge. The output of the photomultiplier was used in conjunction with the variable time delay feature of the oscilloscope to accurately determine the time between oscillation pulses. This was the primary method of determining the oscillation frequencies. The wavelengths of the oscillations were determined by synchronizing the oscilloscope to the function generator and using the traverse to determine the distance between pulse peaks.

Experiment Results. The output from the photomultiplier showed that the oscillations consisted of very short pulses of light with a relatively long dark period between pulses. This large intensity ratio indicated a high level of modulation. Figure 23 depicts a typical photomultiplier output signal.

Figures 24 and 25 are the dispersion characteristics for pressures of 4 and 8 torr respectively. The observed oscillation frequencies ranged from 20KHz to 90KHz. This falls within the 2 to 100KHz range reported by other

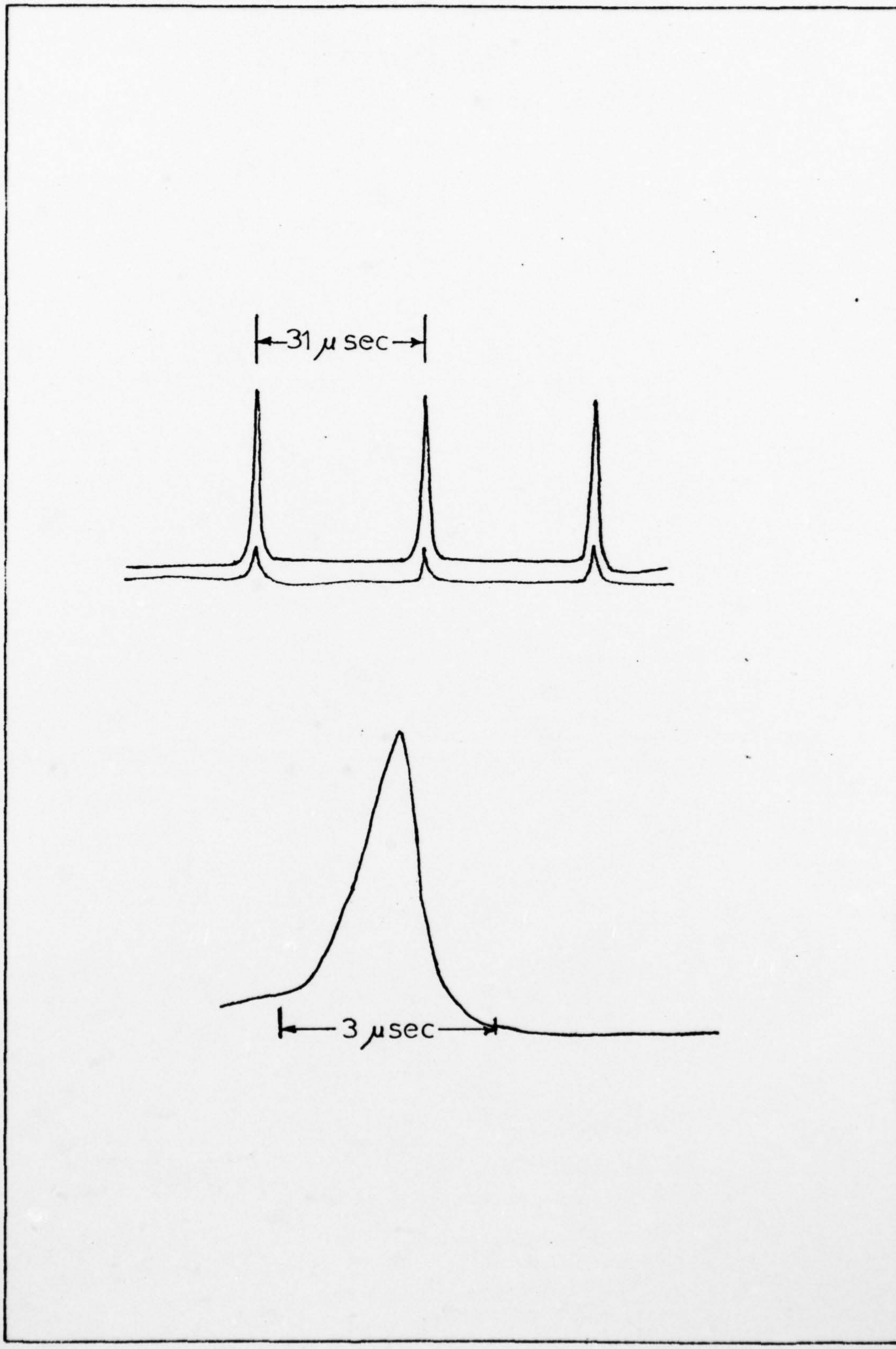

Figure 23. Typical Photomultiplier Output

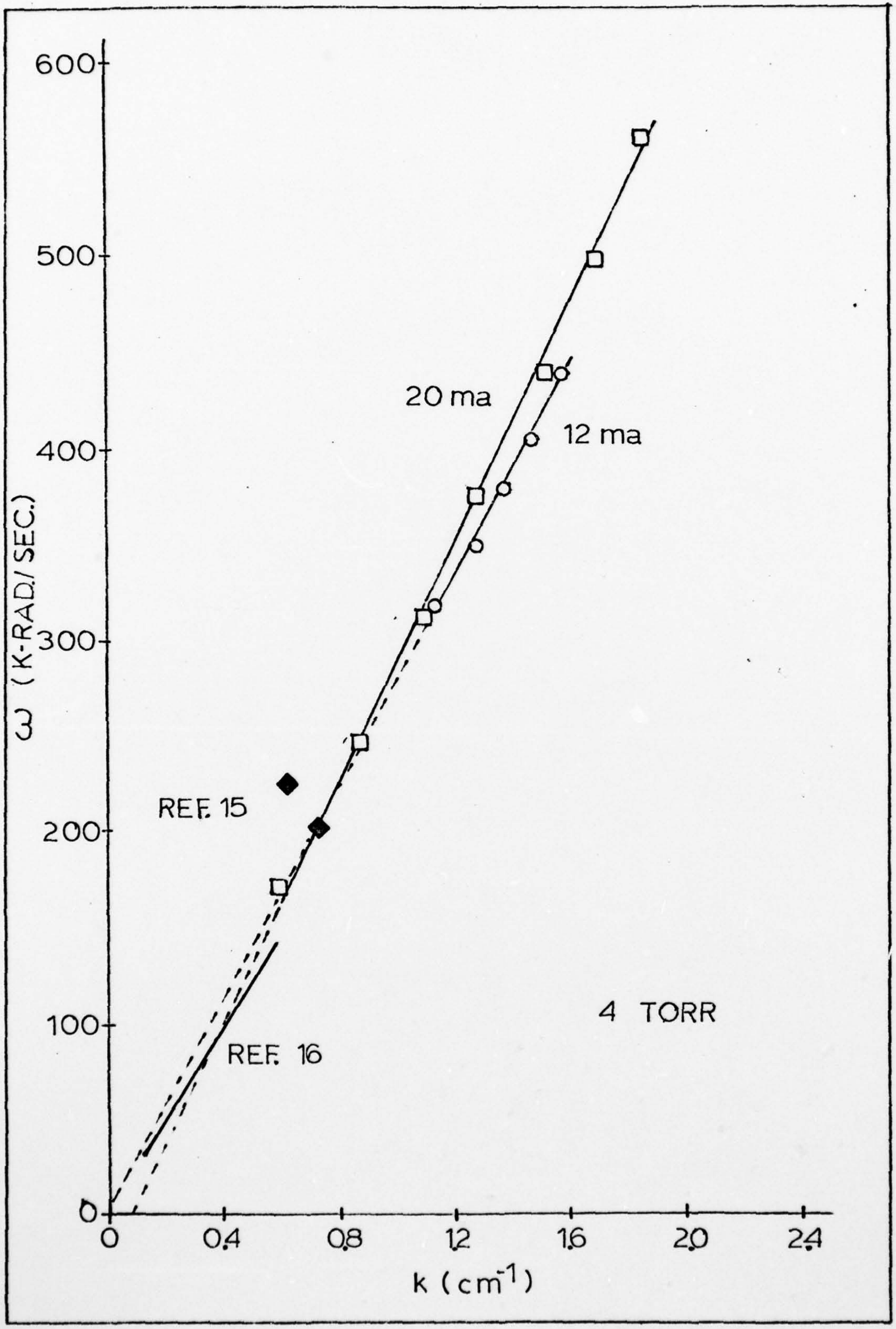

Figure 24. Dispersion Characteristics for 4 Torr

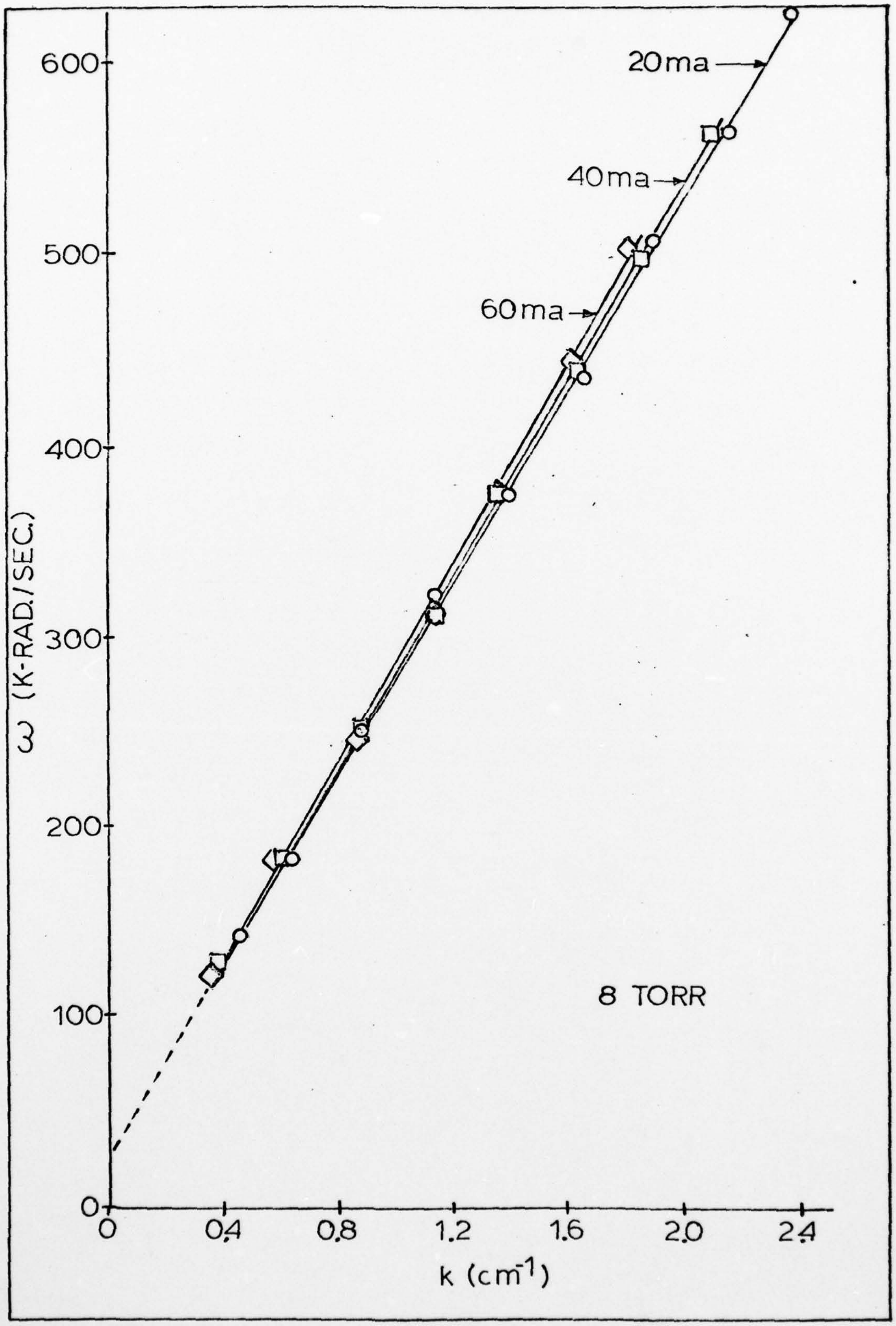

Figure 25. Dispersion Characteristics for 8 Torr

investigators (Ref 15:751, Ref 18:11, Ref 29:85, Ref 16:305-317). For comparison the results of Pekarek's experiments at 2 torr in a 0.9 cm radius tube (Ref 15:749-753) and Sabadil's experiments at .65 to 3.2 torr in a 2.5 cm radius tube (Ref 16:305-317) are shown in figure 24. As indicated by the positive-value intercepts of the dispersion curves with the ω axis, the oscillations observed during this study usually exhibited a small amount of normal dispersion.* The phase velocities varied between 2.6 x 10^5 cm/sec and 3.5 x 10^5 cm/sec and the group velocities between 2.5 x 10^5 cm/sec and 3.1 x 10^5 cm/sec. Sabadil's results indicated the oscillations to be dispersionless with a velocity of 2.4 x 10^5 cm/sec for observations between .65 and 3.2 torr (Ref 16: 305-317). Pekarek's observed velocities varied between 2.7 and 3.6 x 10^5 cm/sec. Since the smount of dispersion determined by this study was so small and exhibited some scatter, the experimental evidence is considered to be indicative but not conclusive in contradicting Sabadil's nondispersion observations.

As stated in Chapter III, it was observed that the voltage across the tube in the low field form would jump back and forth between several different values and that these values were related to the oscillation frequency. Figures 26 and 27 depict the variation in tube voltage with changes in the oscillation frequency. It is to be noted

---

*The phase velocity decreased with increasing frequency.

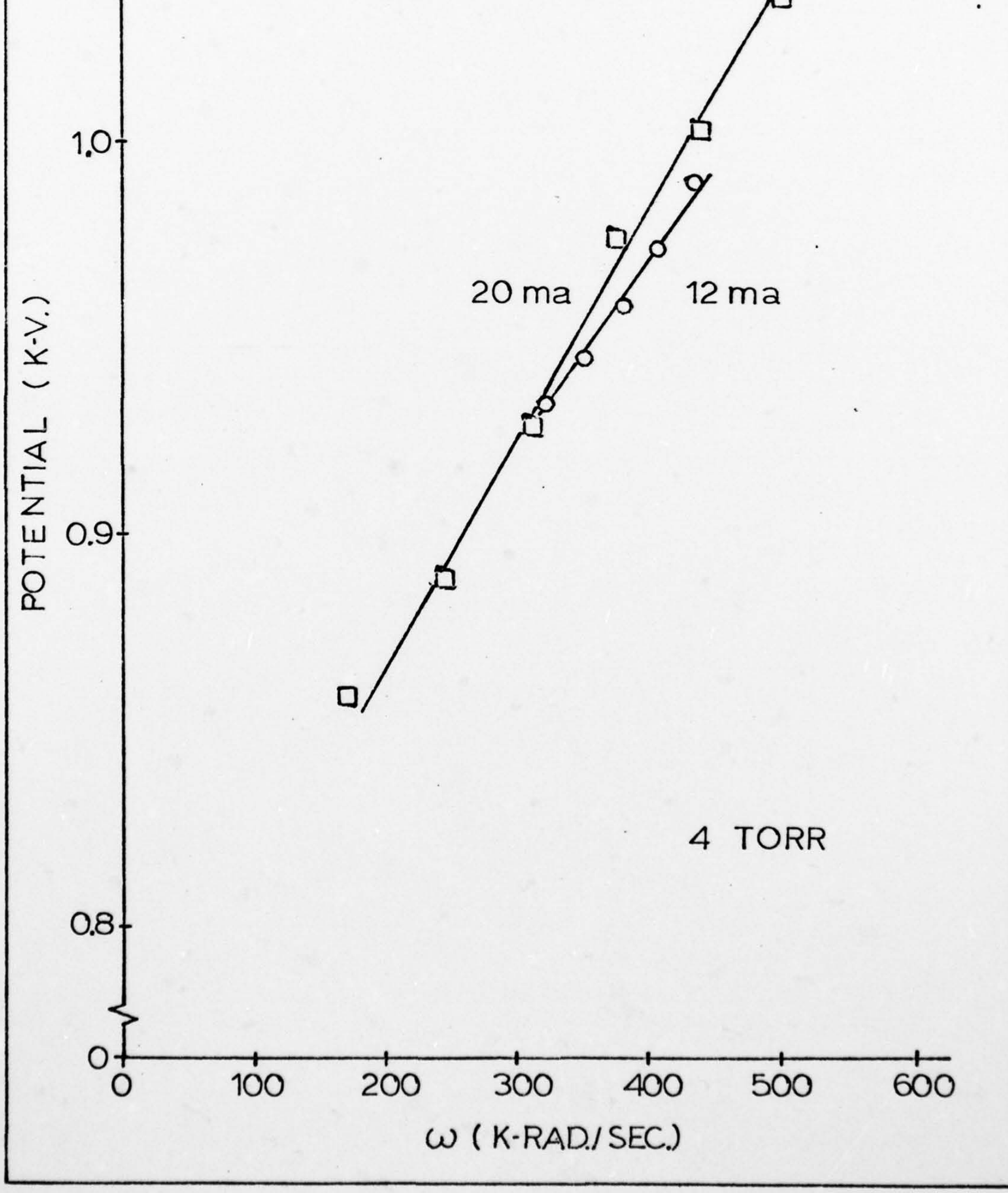

Figure 26. Potential Variations at 4 Torr

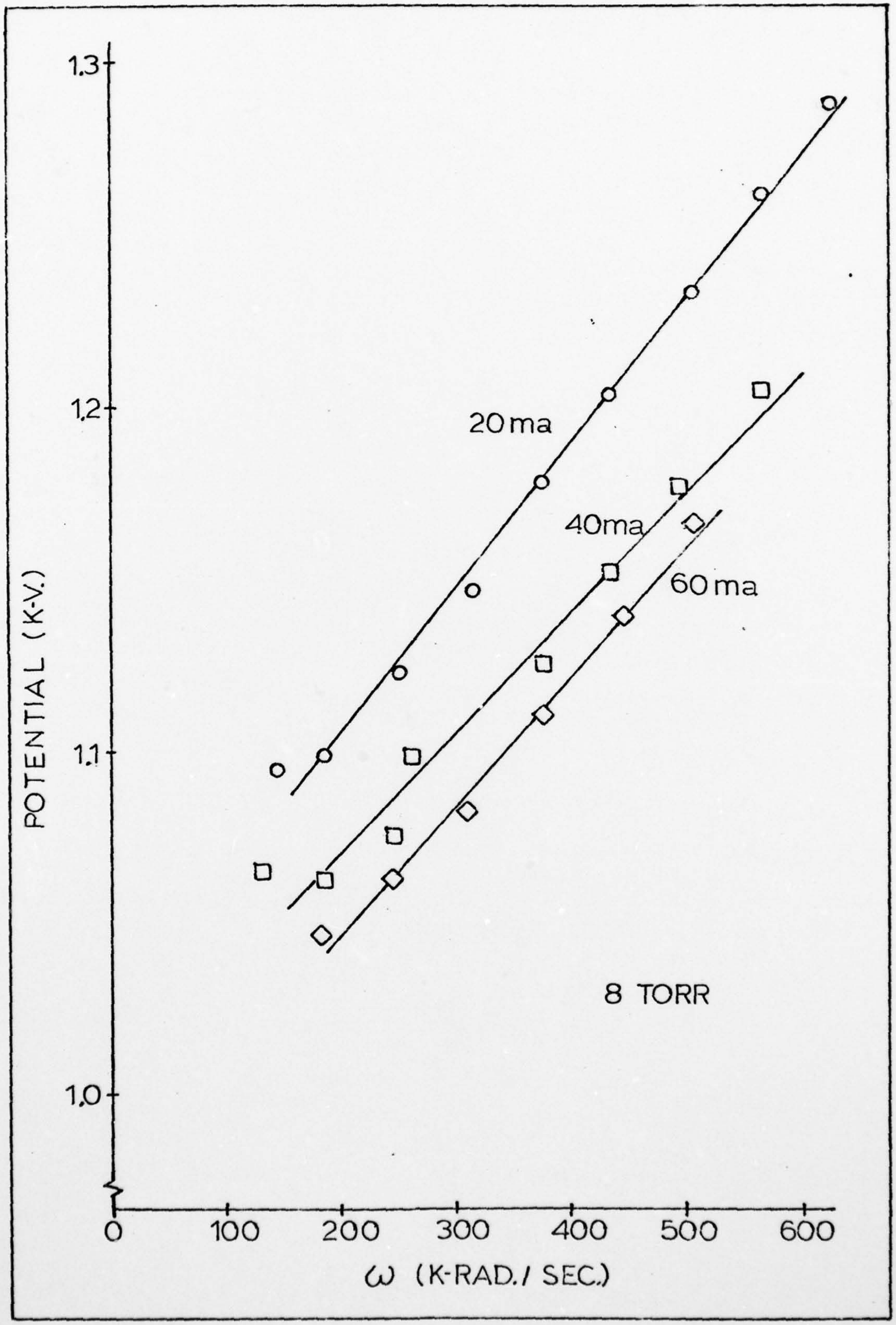

Figure 27. Potential Variations at 8 Torr

that it was possible to lock the oscillations only into certain stable modes, as indicated by the data points. Frequencies of oscillation between these stable modes were impossible to achieve. Therefore, the lines are drawn on the figures only to indicate the trend of the data.

Electric Field Shape

Experiment Theory. The objective of the experiment was to measure the electric field variations in the low field form of the discharge. To do so a method was required to transform the observable measurements of potential difference into a determination of the electric field. At any axial point, z, in the discharge the potential referenced to one of the electrodes can be represented by a Fourier series expansion:

$$V(z,t) = \frac{a_o(z)}{2} + \sum_{N=1}^{\infty}\Big(a_N(z)\cdot \cos\{N\cdot\omega\cdot t - k_N\cdot z\} + b_N(z)\cdot \sin\{N\cdot\omega\cdot t - k_N\cdot z\}\Big) \tag{31}$$

The electric field, E, evaluated at an arbitrary point z = o is:

$$E(z,t) = \left.\frac{\partial V(z,t)}{\partial z}\right|_{z=o} \tag{32}$$

$$E(z,t) = \frac{1}{2}\cdot\frac{da_o}{dz} + \sum_{N=1}^{\infty}\left[\left(\frac{da_N}{dz} - k_N\cdot b_N\right)\cdot \cos\{N\cdot\omega\cdot t\} + \left(\frac{db_N}{dz} + k_N\cdot a_N\right)\cdot \sin\{N\cdot\omega\cdot t\}\right] \quad (33)$$

Assume that:

$$\left|\frac{da_N}{dz}\right| < \left|k_N\cdot a_N\right| \quad (34)$$

$$\left|\frac{db_N}{dz}\right| < \left|k_N\cdot b_N\right| \quad (35)$$

This assumption is valid if the oscillation electric field pulse does not change with position. In the region of measurement in the discharge the optical pulse shape did not change significantly as a function of position, which is consistent with the assumption. The electric field evaluated at an arbitrary point z = o is therefore:

$$E(z,t) = \frac{1}{2}\cdot\frac{da_o}{dz} + \sum_{N=1}^{\infty}\left(-k_N\cdot b_N\cdot \cos\{N\cdot\omega\cdot t\} + k_N\cdot a_N\cdot \sin\{N\cdot\omega\cdot t\}\right) \quad (36)$$

One method of determining the electric field is to use two axially separated probes located in the plasma and measuring the potential difference. This method has serious disadvantages if the probes are separated by distances greater than the wavelength of any of the significant harmonics. For the range of wavelengths observed in this experiment, the distance between the probes would have had to have been less than .3mm to faithfully reproduce just the fundamental frequency.

The method that was utilized involved a time derivative of the signal from a single probe referenced to an electrode of the discharge. Taking a time derivative of equation 31 at an arbitrary point, z = o, yields:

$$\frac{dV}{dt} = \sum_{N=1}^{\infty}\left(-N\cdot\omega\cdot a_N\cdot \mathrm{SIN}\{N\cdot\omega\cdot t\} + N\cdot\omega\cdot b_N\cdot \mathrm{COS}\{N\cdot\omega\cdot t\}\right) \quad (37)$$

If the medium is dispersionless, or very nearly so:

$$K_N = \frac{N\cdot\omega}{V_\phi} \quad (38)$$

where V_ϕ is the phase velocity of the oscillations. Therefore:

$$\frac{dV}{dt} = -V_\phi\cdot\sum_{N=1}^{\infty}\left(-K_N\cdot b_N\cdot \mathrm{COS}\{N\cdot\omega\cdot t\} + K_N\cdot a_N\cdot \mathrm{SIN}\{N\cdot\omega\cdot t\}\right) \quad (39)$$

The optical dispersion experiments reported previously in this chapter showed that the oscillations were just slightly dispersive.* The maximum variation in phase velocity at any one pressure and current was less than 23% over a frequency variation of 4.1 to 1.

In measuring the potential in the discharge, the characteristics of the interaction of the probe with the plasma had to be considered. Any object immersed in a plasma will develop a sheath around it. This sheath can be considered to present a parallel resistance and capacitance coupling between the probe and the plasma. A rigorous analysis of the coupling for a cylindrical probe is very complex and is beyond the scope of this study. However, a simplified analysis can be used to determine if this coupling is important in determining the overall measurements. Consider the electrical circuit of figure 28.

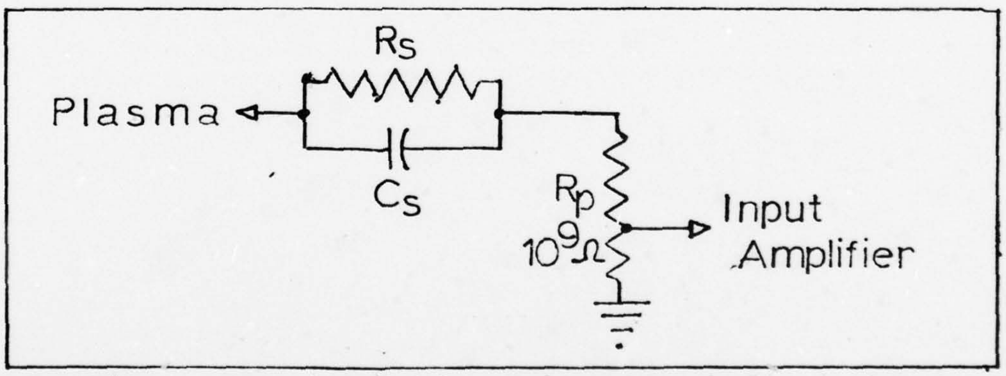

Figure 28. Equivalent Circuit of Plasma Sheath

Rs and Cs are the sheath resistance and capacitance

---

*Refer to figures 24 and 25.

AD-A066 196 AIR FORCE INST OF TECH WRIGHT-PATTERSON AFB OHIO SCH--ETC F/G 7/2
DISCHARGE PROCESSES IN THE OXYGEN PLASMA.(U)
DEC 78 J W DETTMER
UNCLASSIFIED AFIT/DS/PH/78-3 NL

2 OF 4
AD
A066196

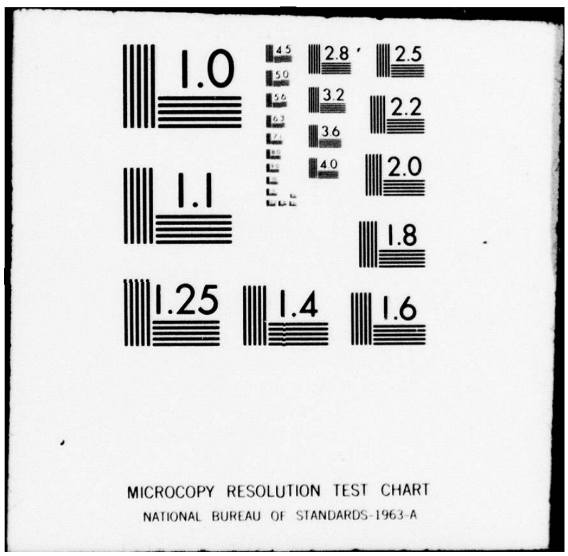
1.0
1.1
1.25
1.4
1.6
1.8
2.0
2.2
2.5
2.8
3.2
3.6
4.0
4.5
5.0
5.6
6.3
MICROCOPY RESOLUTION TEST CHART
NATIONAL BUREAU OF STANDARDS-1963-A

respectively. For a probe operating at the floating potential, where no current is being drawn from the plasma, the plasma dynamic resistance can be approximated by (Ref 9:142-143):

$$R_s = \left|\frac{dV_P}{dI}\right|_{I=0} = \frac{k \cdot T_e}{q} \cdot \frac{4}{A \cdot q \cdot N_e \cdot \langle V \rangle_i} \qquad (40) \cdot$$

where A = area of the probe = 1.6 x 10^{-2} cm^2

$\langle V \rangle_i$ = mean velocity of the ions

$\langle V \rangle_i = \left(\frac{3 \cdot k \cdot T_i}{m_i}\right)^{\frac{1}{2}}$ = 4.8 x 10^4 cm/sec for molecular oxygen ions at $300^{o}K$

Ne = 10^{10} $\frac{\text{electrons}}{\text{cm } 3}$ for low field form

Te = 2 x 10^4 ^{o}K for low field form

Rs = 6 x 10^6 ohms

The capacitance can be approximated by (Ref 9:128-129, Ref 33:21):

$$C_s \approx \frac{A \cdot \epsilon_o}{\lambda_s} \qquad (41)$$

where λ s = sheath thickness $\approx \lambda_D \approx$ 10^{-2} cm

Cs = 1.4 x 10^{-13} farad

The combination of Rs and Cs had a time constant equivalent to approximately 2 x 10^5 hertz. Even at this frequency and higher, their values had little effect on the overall measurements due to the high impedance of the probe.

Experimental Setup. Figure 29 illustrates the setup

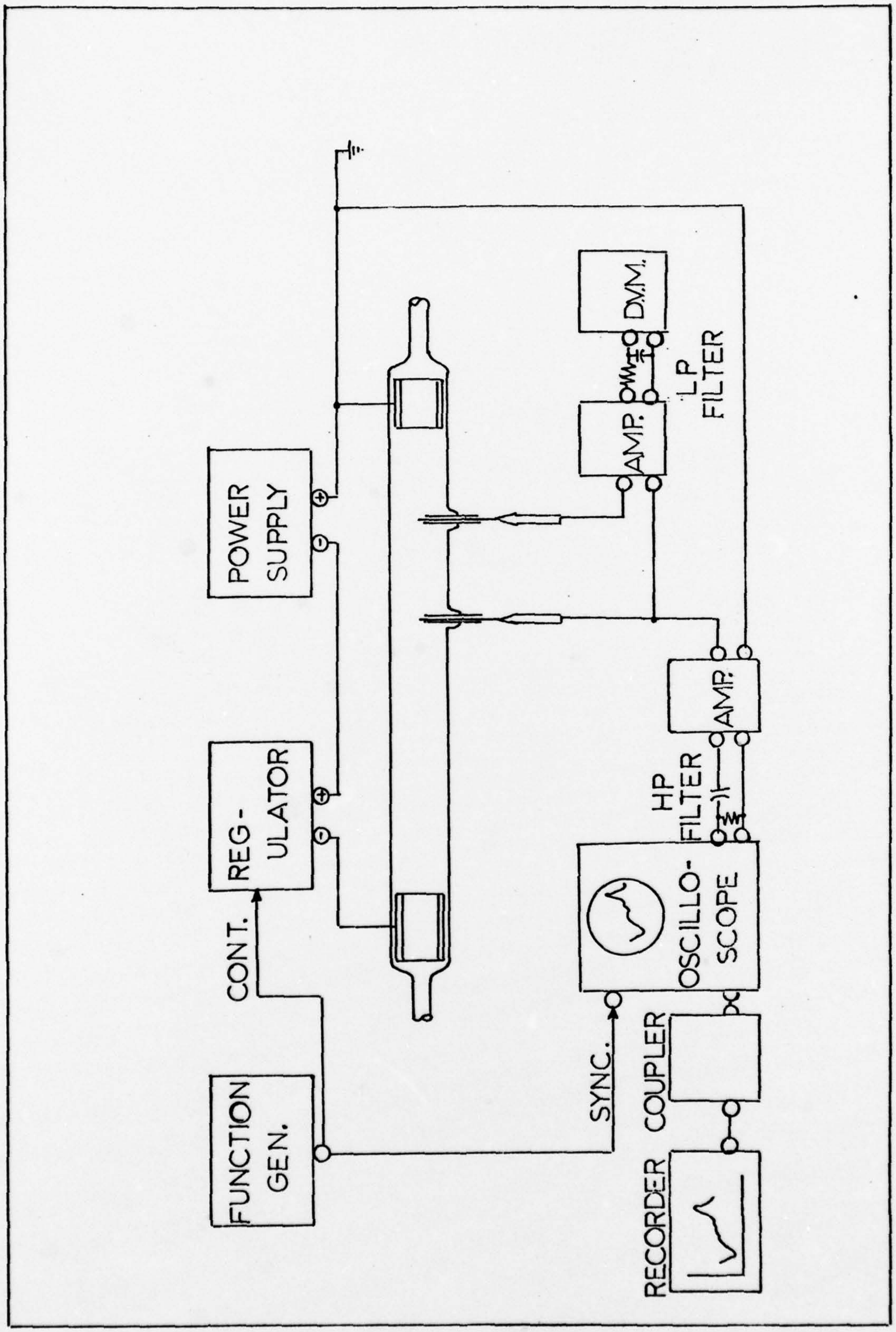

Figure 29. Electric Field Measurement Setup

utilized to measure the time dependent electric field in the low field form of the discharge. To determine the steady (d.c.) portion of the field, the differential voltage between two probes was passed through a low pass filter and displayed on a digital voltmeter. The varying (a.c.) portion of the field was determined by differentiating the potential of one of the probes referenced to ground. A simple resistor and capacitor differentiator was constructed and calibrated for the purpose. The output of the differentiator was connected to the vertical axis of a Tektronix 555 oscilloscope; the horizontal trace was synchronized to the oscillation frequency. The deflection plates of the oscilloscope were connected through a Tektronix coupler to a HP70043 x-y recorder to provide a permanent record.

Experimental Results. Figures 30 and 31 depict electric field shapes at the four different port locations for two different discharge currents. The d.c. values of the field, determined from the potential differences between two probes, were added to the a.c. shapes determined at the specified probe. Therefore, the a.c. values were measured at a single port, and the d.c. values were averaged over the region between two ports (10cm). This resulted in an inaccuracy which is evidenced by the electric field trace passing below the zero line on some of the traces. E/N values corresponding to the electric field values are listed in parenthesis on each of the traces. The reduced electric field was determined utilizing equation 30.

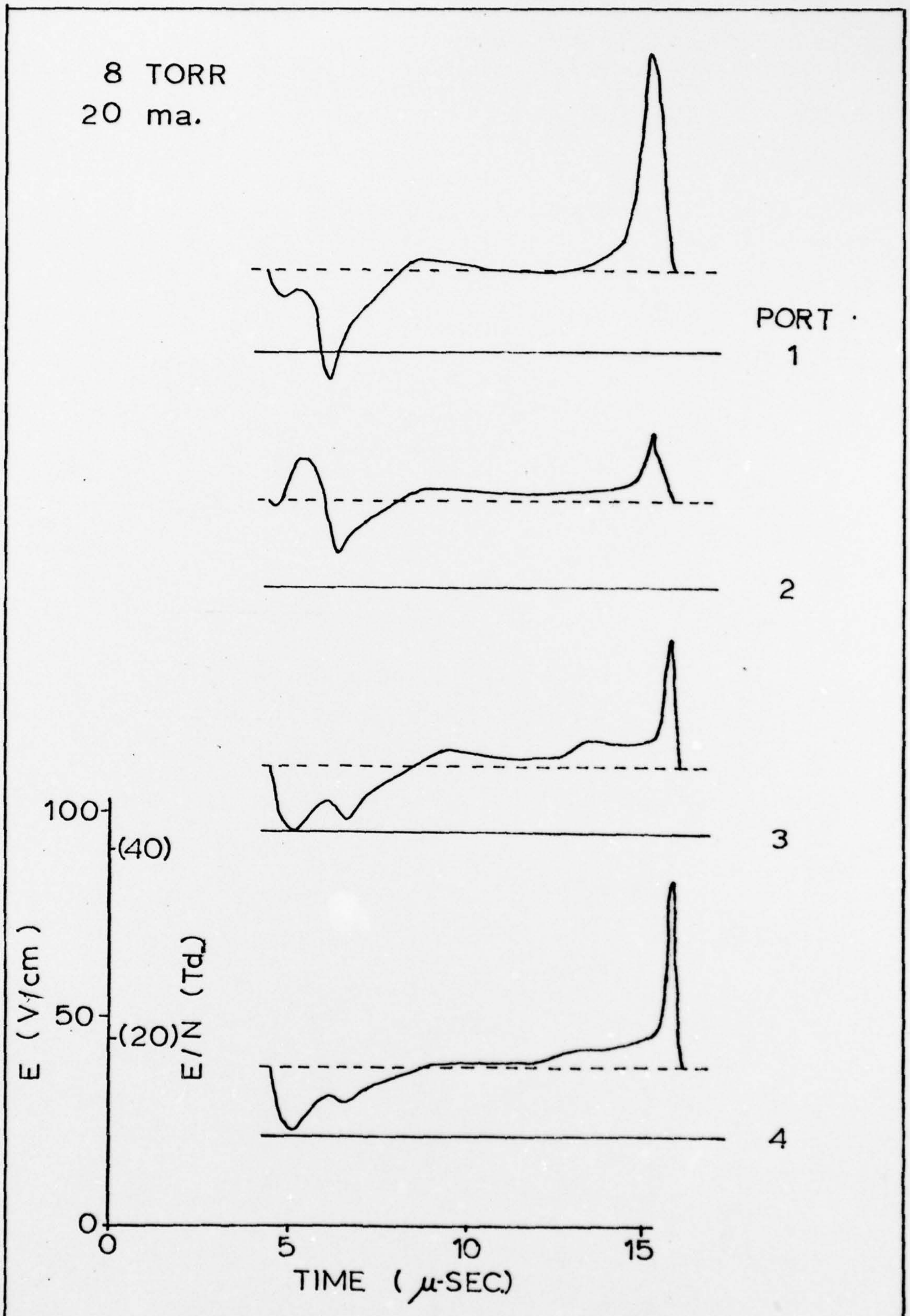

Figure 30. Electric Field Shape

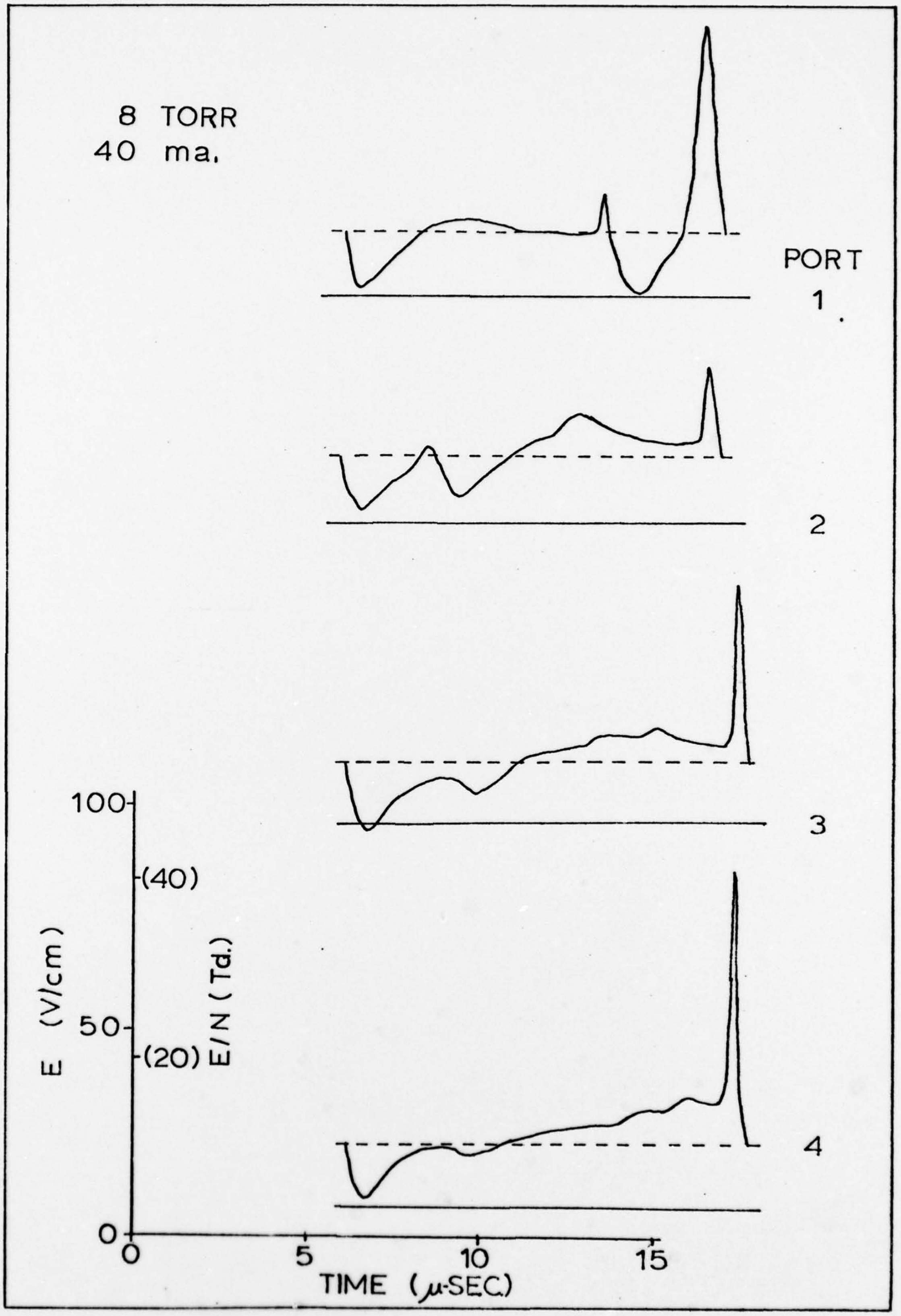

Figure 31. Electric Field Shape

VI. Electron Density

The number of free electrons in a plasma determines many of the characteristics of that plasma. For example - since the electrons are the principal electric current carriers, their density is a key parameter in determining the impedance of a discharge.* Also, the relative density of electrons to negative ions is one factor in determining the stability of a discharge.** Therefore, to describe a discharge it is necessary to have a knowledge of the electron density. The objective of the experiments described in this section was to determine the number density of electrons in an oxygen discharge by utilizing a microwave cavity. The results of these experiments were compared to values calculated from current continuity equations and were used then to validate the computer modeling.

The chapter starts with a description of the theory associated with the utilization of a microwave cavity for electron density measurements. Next, the experimental setup and procedures are described. This section is followed by the calculations of the factors used to determine the electron density values from the changes in the cavity resonant frequency and quality factor.

---

*Refer to equation 7.

**This aspect is discussed further in Chapter X.

Finally, the experimental results are presented along with electron density values calculated from simple current continuity relationships.

Experiment Theory

A conventional method of determining plasma electron densities and collision frequencies consists of measuring the changes of resonant frequency and quality factor* of a microwave cavity caused by the introduction of the plasma (Ref 35:196). The basic measurable characteristics of a cavity (resonant frequency, wo, and quality factor, Q) are not only functions of the physical dimensions but also of the properties of the medium contained within it. If the changes in these measurables are sufficiently small when a plasma is introduced into the cavity, perturbation theory can be used and the following relations utilized** (Ref 36:441):

$$\frac{\Delta\omega}{\omega} = \frac{1}{2\cdot\epsilon_o\cdot\omega_o}\cdot\frac{\int_{V'} \sigma_i \cdot E^2\cdot dV}{\int_V \epsilon_r \cdot E^2\cdot dV} \tag{42}$$

---

*The quality factor is a measure of the losses of a cavity. It can be defined as a ratio of the energy stored in the cavity to the energy loss per cycle (Ref 34:146).

**Slater did not include the relative permittivity in the normalization integral. Due to the particular geometry of this experiment, it must be added to account for the highly dielectric quartz tubes and carbon tetrachloride coolant.

$$\Delta\left(\frac{1}{Q}\right) = \frac{1}{\epsilon_o \cdot \omega_o} \cdot \frac{\int_{V'} \sigma_r \cdot E^2 \cdot dV}{\int_V \epsilon_r \cdot E^2 \cdot dV} \tag{43}$$

where:

ω_o = resonant frequency of the cavity without the plasma

ω_P = resonant frequency of the cavity with the plasma

$\Delta\omega = \omega_P - \omega_o$

Q_O = quality of the cavity without the plasma

Q_P = quality of the cavity with the plasma

$\Delta\left(\frac{1}{Q}\right) = \frac{1}{Q_P} - \frac{1}{Q_o}$

V = cavity volume including the plasma interaction region

V' = plasma interaction portion of the cavity volume

$\sigma_r + j\sigma_i$ = complex plasma admittance

ϵ_r = relative permittivity of dielectrics in the bore

E = electric field

The validity of the perturbation theory is based on the electron density being low enough to permit interaction of the electromagnetic field with the plasma electrons (Ref 35:196):

$$N_e < \frac{m_e \cdot \epsilon_o \cdot \omega_P^2}{q^2} \tag{44}$$

where Me and q are the mass and charge on the electron respectively. As the electron density, Ne, approaches the value on the right hand side of the inequality 44 the plasma begins to shield its interior from the externally applied electric field; and the theory becomes invalid. Additionally, the pressure should be sufficiently low that (Ref 35: 196):

$$\nu_{eN} < \omega_P \tag{45}$$

A high value of collision frequency, ν en, could result in the lowering of the cavity, Q, to the point where higher order cavity modes may be excited.

Based on the assumption of a Lorentz gas model*, the complex admittance can be expressed as (Ref 8:194):

$$\sigma_r + j\sigma_i = \frac{N_e \cdot q^2 \cdot \nu_{eN}}{m_e \cdot (\nu_{eN}^2 + \omega_P^2)} - j \cdot \frac{N_e \cdot q^2 \cdot \omega_P}{m_e \cdot (\nu_{eN}^2 + \omega_P^2)} \tag{46}$$

Substituting equation 46 into 42 and 43:

$$\frac{\Delta\omega}{\omega_o} = \frac{q^2 \cdot \omega_P}{2 \cdot \epsilon_o \cdot \omega_o \cdot m_e (\nu_{eN}^2 + \omega_P^2)} \cdot \frac{\int_{V'} N_e \cdot E^2 \cdot dV}{\int_V \epsilon_r \cdot E^2 \cdot dV} \tag{47}$$

$$\Delta\left(\frac{1}{Q}\right) = \frac{q^2 \cdot \nu_{eN}}{\epsilon_o \cdot \omega_o \cdot m_e (\nu_{eN}^2 + \omega_P^2)} \cdot \frac{\int_{V'} N_e \cdot E^2 \cdot dV}{\int_V \epsilon_r \cdot E^2 \cdot dV} \tag{48}$$

---

*A Lorentz gas is a plasma in which the electron and ion number densities are less than the neutrals; only the electrons participate in the phenomena of interest; electron-neutral collisions are the only collisions of concern; and the neutrals are assumed to have infinite mass (Ref 8:191).

Solving these equations for electron density and collision frequency:

$$\int_{V'} N_e \cdot E^2 \cdot dV = \frac{2 \cdot \Delta\omega \cdot \epsilon_o \cdot \omega_o \cdot m_e}{q^2} \cdot \left[1 + \left(\frac{\Delta\left(\frac{1}{Q}\right) \cdot \omega_P}{2 \cdot \Delta\omega}\right)^2\right] \cdot \int_V \epsilon_r \cdot E^2 \cdot dV \tag{49}$$

$$\nu_{eN} = \Delta\left(\frac{1}{Q}\right) \cdot \frac{\omega_P^2}{2 \cdot \Delta\omega} \tag{50}$$

The difficulty in solving equation 49 lies in evaluating the integrals. Some knowledge of the spatial variations of the electric field and of the electron number densities is required. These integrals are evaluated in a following section of this chapter.

<u>Experimental Setup</u>

Figure 32 depicts the setup utilized to determine the change in cavity resonance and the quality factor as functions of discharge pressure and current (Ref 37:2-3, Ref 38: 1-6). The output from a microwave sweep frequency oscillator was fed through a splitter and directional coupler to a toroidal cavity. The latter was mounted concentric to the discharge tube between probe ports numbers three and four. A portion of the microwave oscillator output was taken from the splitter and fed into an absorption wavemeter. A detector was then utilized to measure the strength of the signal;

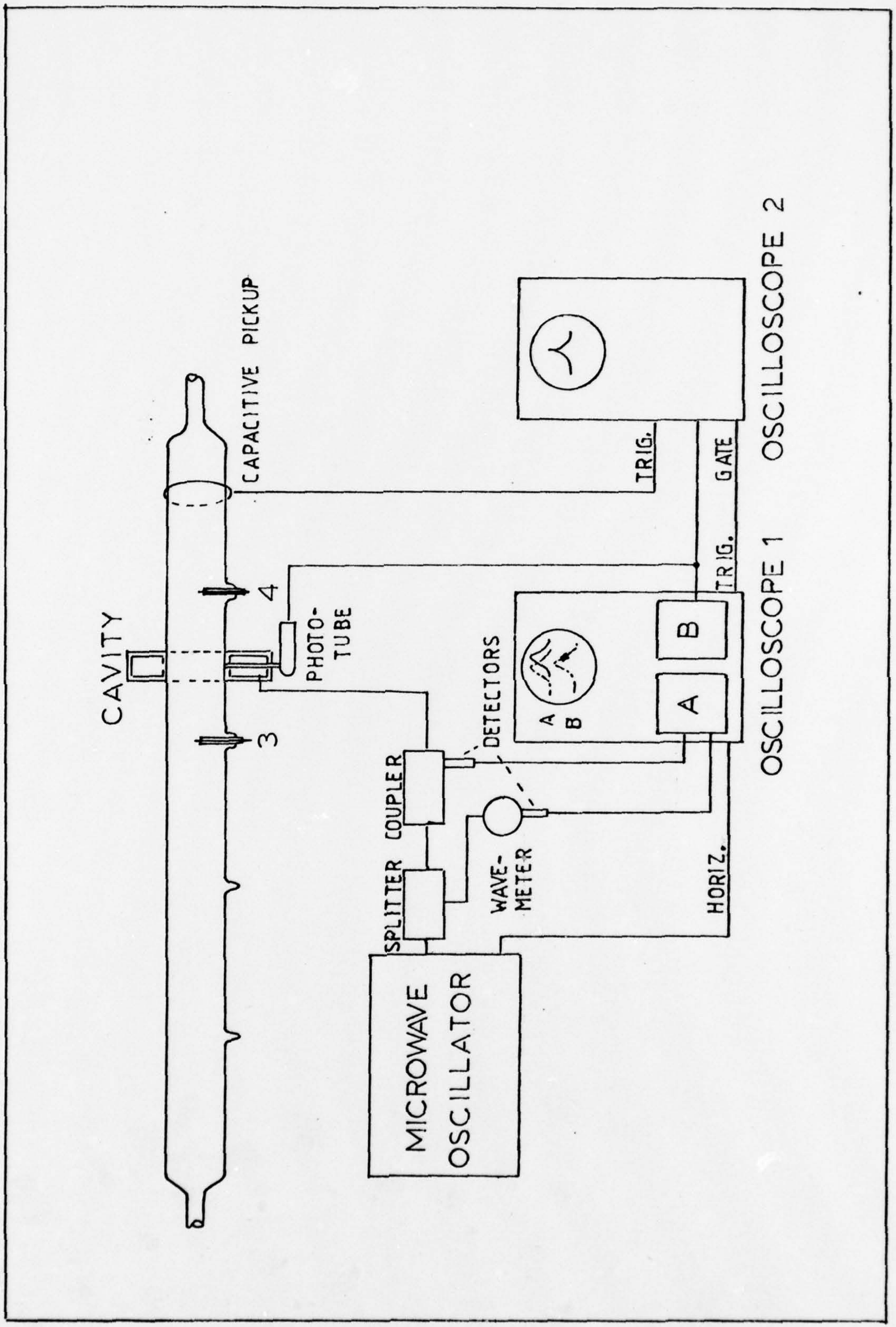

Figure 32. Electron Density Experimental Setup

its output was connected to one input of a differential amplifier. The reflected energy from the cavity was passed through the directional coupler to another detector; its output was connected to the other channel of the differential amplifier. The output of the differential amplifier controlled the vertical axis of one beam (A) of a dual beam oscilloscope (1); the horizontal axis was driven by the sweep signal output from the microwave sweep oscillator. Therefore, the beam "A" trace depicted the cavity response versus frequency of the cavity resonance. The narrow resonance of the tunable wavemeter provided a mark on the trace which permitted the accurate determination of the resonant frequency and Q of the cavity.

The setup described in the previous paragraph was sufficient for determining the characteristics of the non-oscillatory high field form of the discharge. However, the varying electron densities of the low field form caused the "A" trace to jitter excessively, thus negating the capability of measuring anything but the average values. To measure the characteristics of the discharge at any desired phase point of an oscillation, the experimental setup was modified to highlight the portion of the "A" trace that corresponds to that phase point. A small diameter quartz rod, acting as a light pipe, was passed through the cavity to the discharge tube, thus connecting the optical signal of the plasma at the center of the cavity to a photomultiplier tube. The output of the tube was used to control the vertical axis of oscilloscope 2 and the "B" trace of oscilloscope 1. The horizontal axis of oscilloscope 2 was driven by its internal sweep which was synchronized through an adjustable delay to a capacitive pick-up looped around the discharge tube. The horizontal axis of the "B" trace of oscilloscope 1 was driven by one of the sweep oscillators in the scope; this oscillator was synchronized to the gate output of oscilloscope 2, thus assuring that the output of the photomultiplier was centered on the trace. The other sweep of oscilloscope 1 was operated in a delayed mode and was used to intensify both the "A" and "B" traces. Therefore, using the delay control of oscilloscope 1, a particular phase point could be selected on the "B" trace; and the corresponding resonance curve on the "A" trace would be intensified. For all runs in the low field form, the electron density measurements were made at the peak and minimum points of the optical output. Figure 33 depicts a typical oscilloscope 1 trace acquired during a low field measurement.

Determination of Cavity/Plasma Coupling

The early microwave cavities utilized for measuring plasma parameters were of cylindrical design. This type of resonator, although easy to analyze, was restricted to relatively long thin discharge tubes for which the tube diameter was smaller than either the length or diameter of the cavity. The results of such measurements represented the values averaged over an axial length of the discharge which was

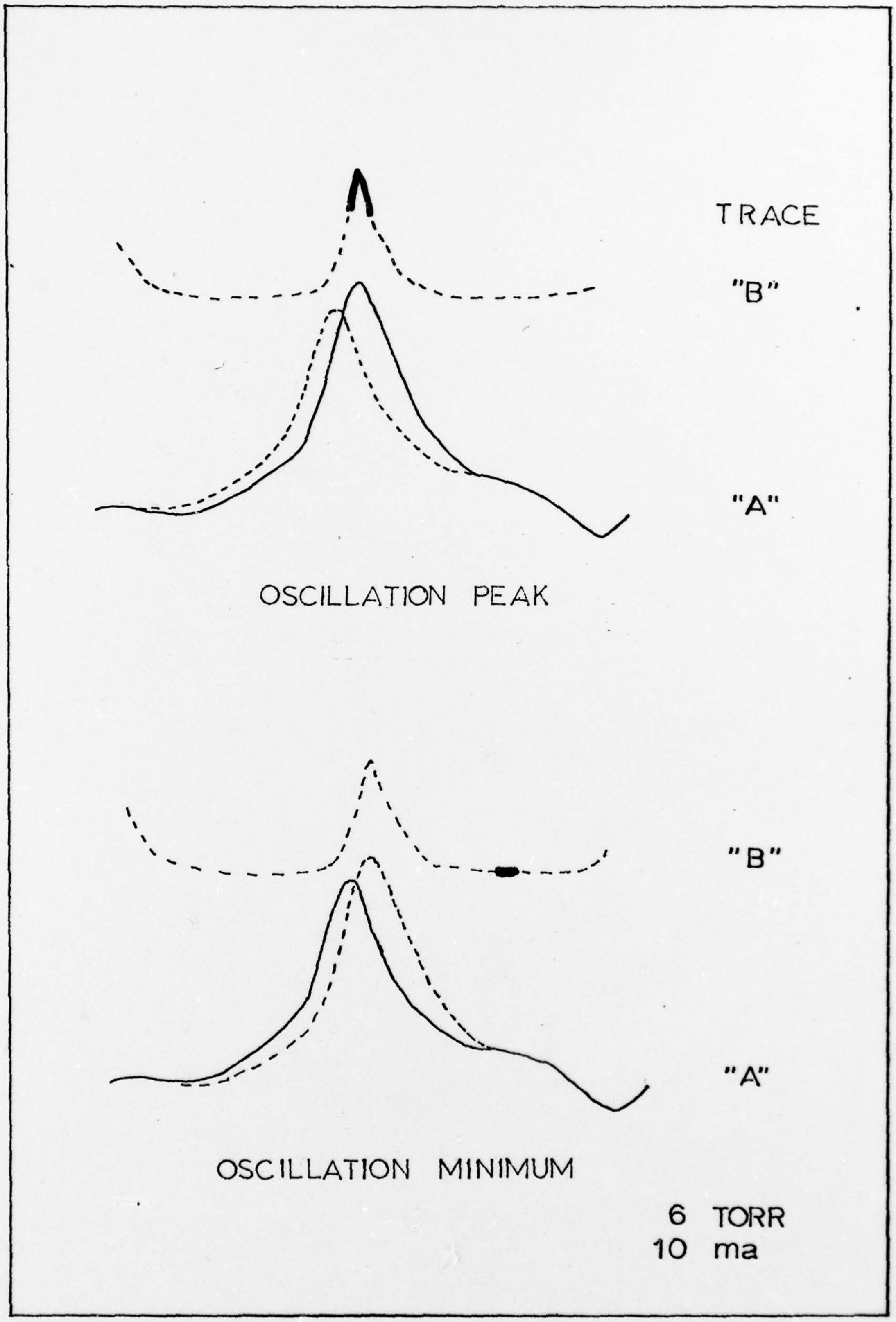

Figure 33. Sample Resonance Traces

several times the diameter of the discharge tube; thus, the cylindrical cavity was incapable of providing the spatial resolution necessary to investigate oscillatory plasmas.

Toroidal resonators, however, do not exhibit such a restriction*. Due to the small region of interaction between the cavity and the plasma, the length of the measured plasma region can be less than the diameter of the discharge tube. This factor made the toroidal cavity the device of choice for measuring the parameters of an oscillatory column. The disadvantage associated with the toroidal cavity was the difficulty of analysis (Ref 39:3979, Ref 40:48-49).

The analysis of the toroidal cavity leads to the evaluation of the integrals:

$$\int_V \epsilon_r \cdot E^2 \cdot dV \tag{51}$$

$$\int_{V'} N_e \cdot E^2 \cdot dV \tag{52}$$

The analysis of integral 51 was not trivial but was straightforward. Its value was determined by the geometry of the cavity and discharge tube; the accuracy of the calculation depended on the method of evaluation and the assumptions

---

*The toroidal resonator used in this study was not the conventional toroidal resonator but a special design originated by M.V. Sicha to give good spatial resolution (Ref 41: 256). Figure 35 illustrates the cross section of the resonator.

that went into that method. The analysis of integral 52 would have been impossible if assumptions had not been made concerning the spatial distribution of the electron density. In order to evaluate this integral and treat it as a linear function of the electron density, the electron spatial density was assumed to vary between two different profiles. For the two-component-plasma the electron density was assumed to have a Bessel profile in the radial direction and a uniform profile in the axial direction (Ref 11:241):

$$N_e = N_{eo} \cdot J_o \left\{ \frac{2.4 \cdot r}{R_o} \right\} \tag{53}$$

For the three-component-plasma the radial and axial profiles were both assumed to be uniform. The radial uniformity was shown to be good for oxygen plasmas in which the negative ion to electron densities ratio was greater than ten (Ref 24:819-820). The axial uniformity assumption was reasonable for the minimum of the oscillation; however, it greatly reduced the accuracy of the measurement of the electron density at the peak of the oscillations. For example - using the electrical field trace of figures 30 and 31 and ports numbers three and four and the measured phase velocity of figure 25, the axial extent of the oscillation minimum was 29mm; and the peak was 1.3mm*. Therefore, the measurement at the oscillation peak must be considered as an averaged

---

*As compared to a cavity gap of 1.6mm.

value; all other values should be actual.

The calculation of the integrals 51 and 52 was based on the assumption that the electric field pattern set up by the pole tips of the resonator was quasi-stationary. With this assumption the resonator was treated as a capacitor formed by the pole tips in parallel with a coaxial line (Ref 40:49). This method of analyzing the toroidal cavity and its interaction with the plasma was realistic as long as the gap width was small compared to the discharge tube diameter. For a gap width that was 7% of the tube diameter, Sicha showed excellent agreement between theory and experiment (Ref 39:3984-3989). For the cavity utilized in this study the gap width was also 7% of the tube diameter.

In computing the normalizing integral 51 the method of Sicha was employed (Ref 40:50-56). The resonator space was divided into four sections: the slot between the pole tips forming the capacitor, the stray field space (caused by the capacitor) inside the cavity, the coaxial line approximation of the cavity itself, and the bore where the discharge tube and plasma were introduced.

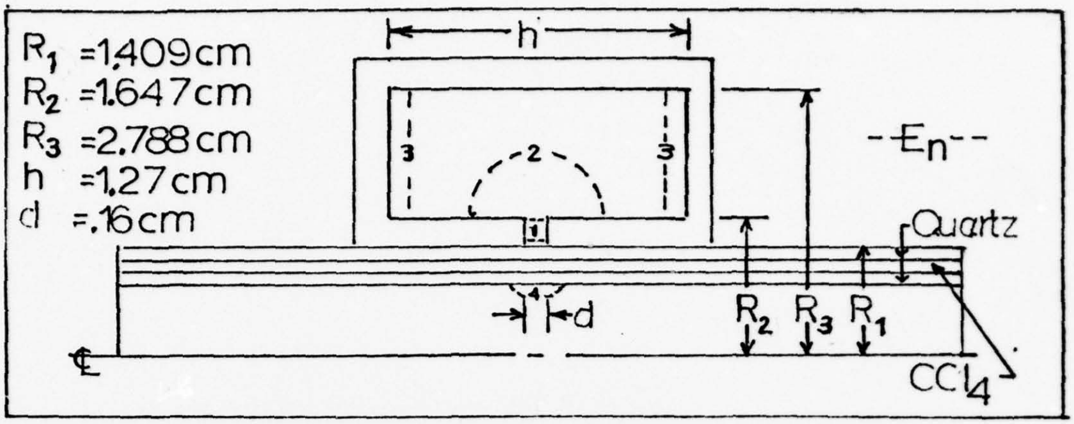

Figure 34. Cavity Cross Section

Integral 51 was determined by summing the integrals for each of these spaces*:

$$\int_V \epsilon_r \cdot E^2 \cdot dV = \underbrace{\int_{V_P} \epsilon_{r_P} \cdot E_1^2 \cdot dV}_{\text{between pole tips}} + \underbrace{\int_{V_c} \epsilon_{r_c} \cdot E_2^2 \cdot dV}_{\text{stray field}} + \tag{54}$$

$$\underbrace{\int_{V_c} \epsilon_{r_c} \cdot E_3^2 \cdot dV}_{\text{cavity}} + \underbrace{\int_{V_B} \epsilon_{r_B} \cdot E_4^2 \cdot dV}_{\text{bore}}$$

where ϵri and Ei were the relative permittivities and electric fields of the defined regions. The evaluation of the

---

*The general solution for the toroidal cavity also included a term associated with interaction of the cavity and stray fields:

$$2 \cdot \int_{V_c} \epsilon_{rc} \cdot E_2 \cdot E_3 \cdot \cos\{\angle E_2, E_3\} \cdot dV$$

Because of the axial symmetry of the cavity utilized in this study, this term was very small and was neglected.

first three integrals on the right hand side of equation 54 was done analytically; the last integral was evaluated by numerical methods. This was required due to the complicated nature of the dielectrics in the interaction region (see figure 34). The electric field between the pole tips was assumed to be uniform:

$$E_1 = \frac{U}{d} \tag{55}$$

where U is the voltage between the pole tips.

The relative energy integral* was determined to be:

$$\int_{V_P} \epsilon_{r_p} \cdot E_1^2 \cdot dV = \frac{U^2}{d} \cdot \pi \cdot \left(R_2^2 - R_1^2\right) \tag{56}$$

where the integration was performed over the volume between the pole tips, Vp. For the specific geometry utilized in the experiment and with U and ϵ_{rp} assumed to be unity:

$$\int_{V_P} \epsilon_{r_p} \cdot E_1^2 \cdot dV = 14.4 \text{ volt}^2\text{.cm} \tag{57}$$

The stray electric field in the cavity, set up by the pole tips, was assumed to be semicircular:

$$E_2 = \frac{U}{\pi \cdot x} \tag{58}$$

where x is the radius from the center of the gap. The

---

*Relative energy, since the permittivity of free space was not included.

relative energy integral of this field was determined to be:

$$\int_{V_c} \epsilon_{r_c} \cdot E_2^2 \cdot dV = 2 \cdot U^2 \cdot \left[R_2 \cdot LN\left\{ \frac{2 \cdot (R_3 - R_2)}{d} \right\} + \frac{2}{\pi} \cdot \left(R_3 - R_2 - \frac{d}{2} \right) \right] \quad (59)$$

where the integration was performed over the cavity volume, Vc. With the assumption of ϵ_{r_c} equal to unity:

$$\int_{V_c} \epsilon_{r_c} \cdot E_2^2 \cdot dV = 10.13 \text{ volt}^2 \text{.cm} \quad (60)$$

The electric field in the cavity was determined by applying a coaxial line approximation:

$$E_3(r,z) = \frac{1}{r} \cdot \frac{U \cdot SIN\left\{ K \cdot \left(\frac{h}{2} - z \right) \right\}}{2 \cdot LN\left\{ \frac{R_3}{R_2} \right\} \cdot SIN\left\{ K \cdot \left(\frac{h}{2} - \frac{d}{2} \right) \right\}} \quad (61)$$

The relative energy integral of this field was determined to be:

$$\int_{V_c} \epsilon_{r_c} \cdot E_3^2 \cdot dV = \frac{\pi}{4} \cdot U^2 \cdot \left[\frac{(h-d) - \left(\frac{1}{K} \right) \cdot SIN\{K \cdot (h-d)\}}{LN\left\{ \frac{R_3}{R_2} \right\} \cdot SIN^2\left\{ K \cdot \left(\frac{h}{2} - \frac{d}{2} \right) \right\}} \right] \quad (62)$$

where:

$$K = \frac{2 \cdot \pi}{\lambda_o} \quad (63)$$

The resonant wavelength, λ_o, for the cavity used in the experiment was 14.03 cm. Using this value, equation 62 was evaluated to be:

$$\int_{V_C} \epsilon_{r_C} \cdot E_3^2 \cdot dV = 1.115 \text{ volt}^2\text{.cm} \qquad (64)$$

The final integral of equation 54 was calculated by utilizing a relaxation technique to numerically solve Laplace's equation*. The outputs of the computer program were the potential and electric fields in the interaction volume. The square of the electric field multiplied by its associated relative permittivity was numerically integrated over the total bore volume, V_B, to provide the solution of the final integral of equation 54:

$$\int_{V_B} \epsilon_{r_B} \cdot E_4^2 \cdot dV = 25.69 \text{ volt}^2\text{.cm} \qquad (65)$$

The calculation was performed also for a bore volume without the dielectrics. The resulting integral was evaluated to be 8.482 volt^2cm. Therefore, the bore region with dielectrics contained considerable more energy than the one with an $\epsilon_r = 1$. This demonstrated the necessity of including the dielectrics in computing the bore region contribution to equation 54.

The solution of integral 65 did not include the contribution of the small quartz rod used as a light pipe to the photo-multiplier tube. This contribution was considered

---

*See Appendix A for a description of the computer program.

to be negligible since this rod occupied less than .13% of the cavity volume.

Figure 35 depicts the log of the square of the electric field for a bore region without the quartz tubes and the carbon tetrachloride. Figure 36 depicts the same with the inclusion of the dielectrics. Figure 37 is a cut of the mid-plane of figure 36. As depicted in figures 35 and 36, the dielectrics had a very pronounced and stepped effect on increasing the electric field in the bore of the cavity. In the plasma volume of the discharge tube, the highest coupling occurred at the circumference in the region of the cavity gap. The electric field did not fall off very rapidly in the radial, r, direction - indicating a weak dependence of microwave coupling on the electron density radial profile. The field did fall off rapidly in the axial, z, direction - indicating a good spatial resolution.

The final tabulation of the integrals on the right hand side of equation 54 resulted in a value of 51.34 volt^2 cm for the normalizing integral, 51.

The computation of the integral 52 was accomplished in a manner similar to the computation of the final integral of equation 54. The only difference was that the relative energy was integrated only over the bore region inside the inner discharge tube, V'. The integration was based on the following relation:

$$\int_{V'} N_e \cdot E^2 \cdot dV = N_{eo} \int_{V'} F(r) \cdot E^2(r,z) \cdot dV \qquad (66)$$

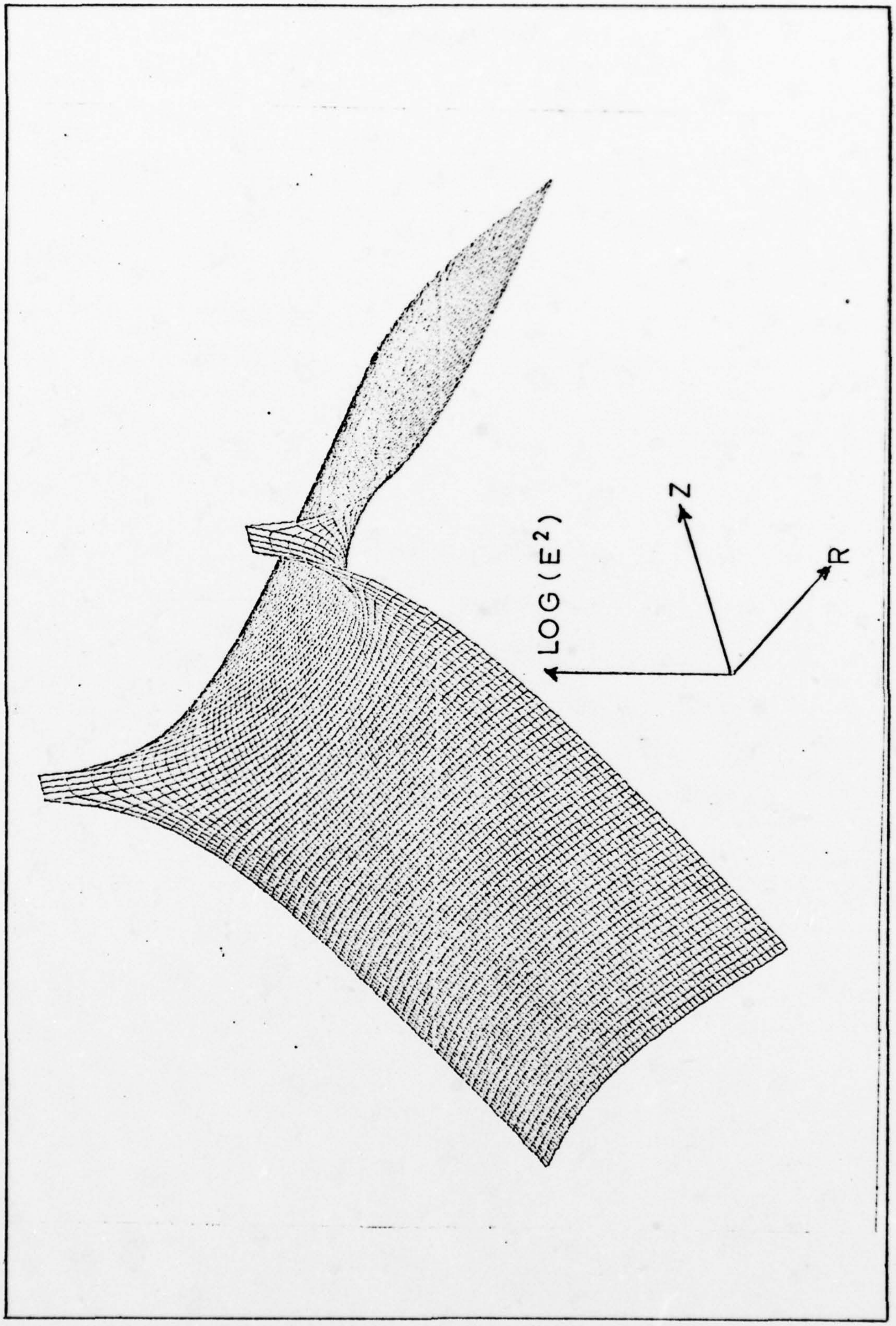

Figure 35. Cavity Electric Field without Dielectrics

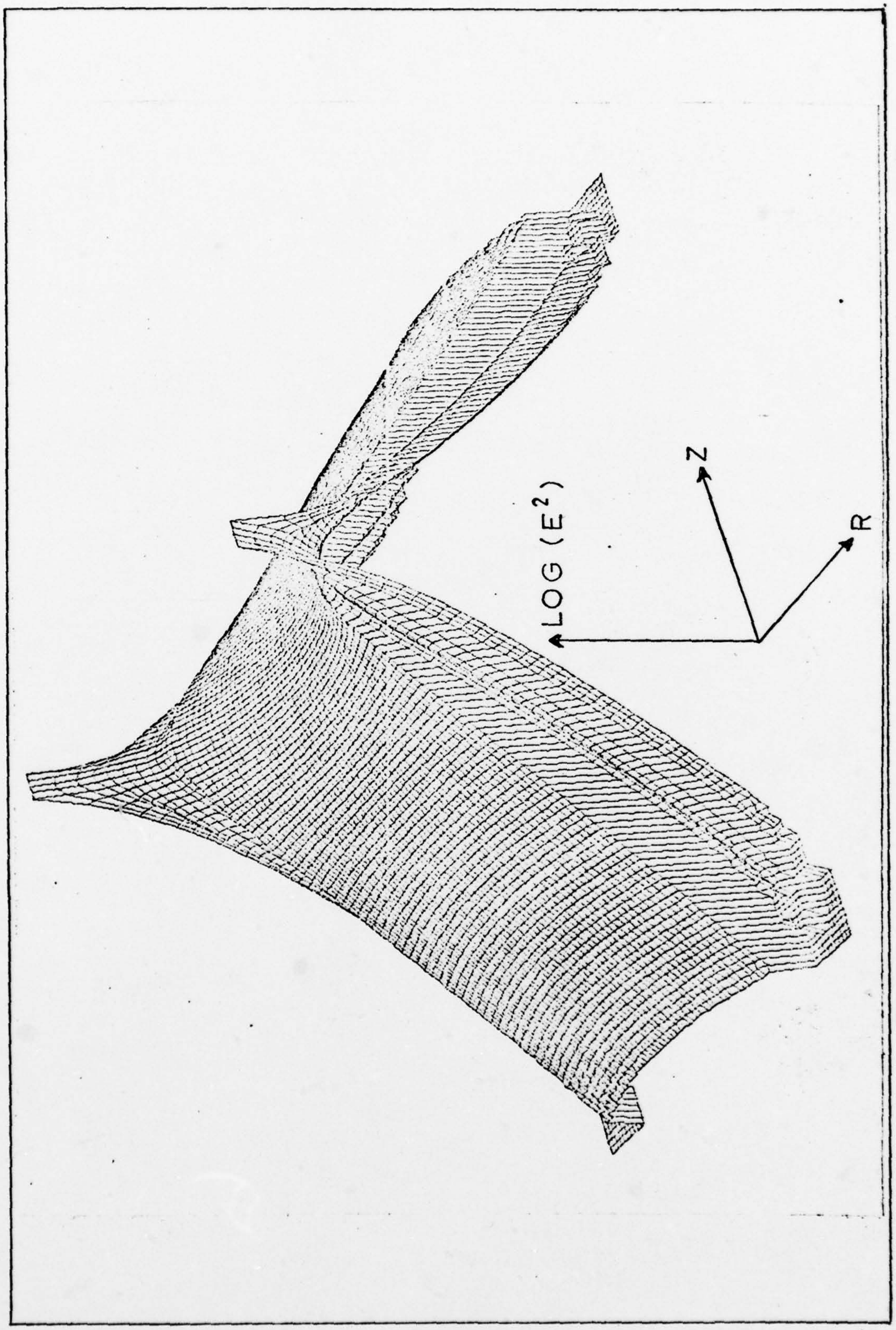

Figure 36. Cavity Electric Field with Dielectrics

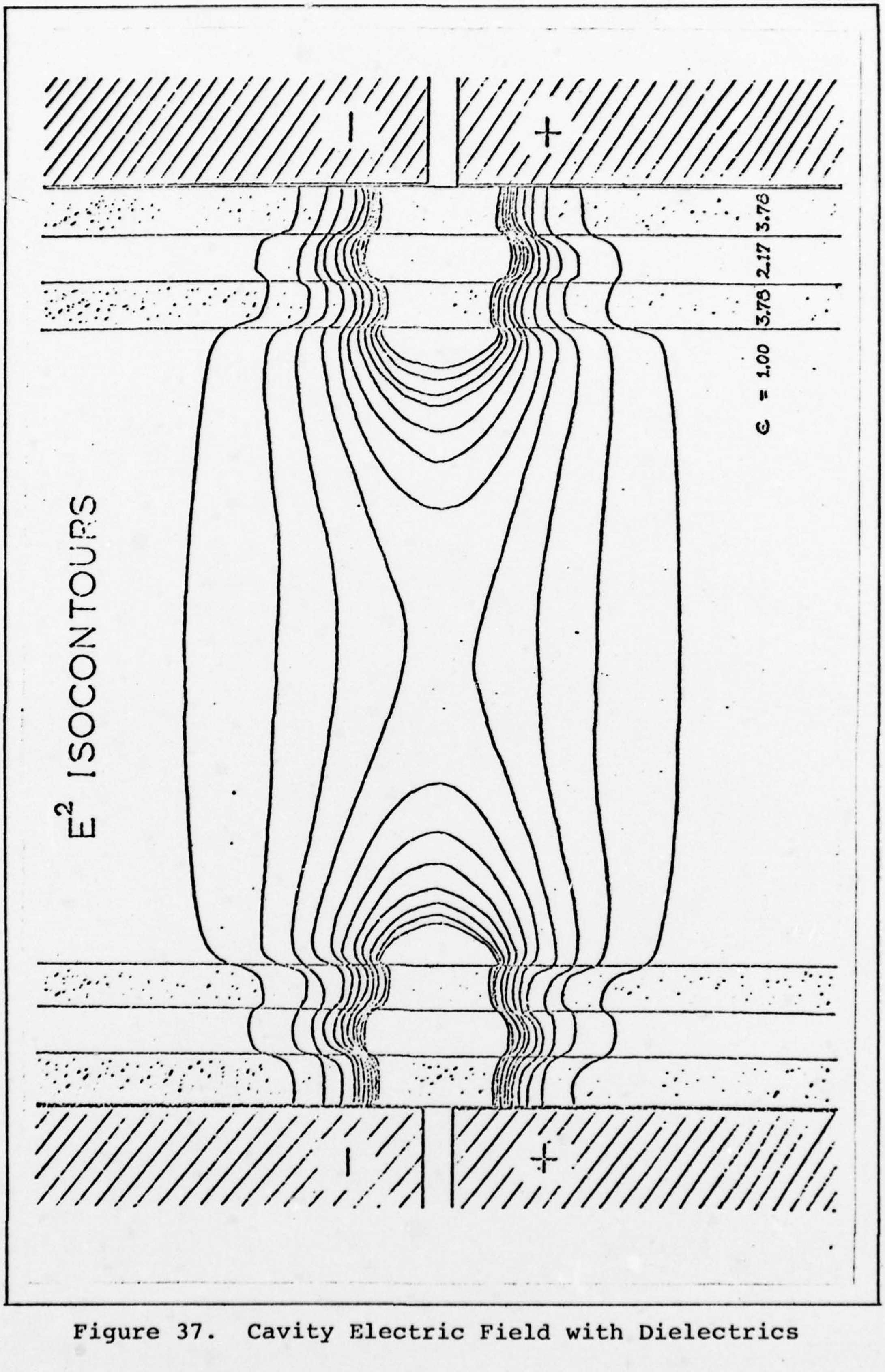

Figure 37. Cavity Electric Field with Dielectrics

where the density profile, F(r), was assumed to be either a Bessel (equation 53) or uniform profile. The results of the computation were linear solutions of the integral for the two profiles:

$$N_{eo} \cdot \int_{V'} J_o\left\{\frac{2.4 \cdot r}{R_o}\right\} \cdot E^2(r,z) \cdot dV = 0.611 \cdot N_{eo} \ \text{volt}^2.\text{cm} \qquad (67)$$

for the Bessel profile.

$$N_{eo} \int_{V'} E^2(r,z) \cdot dV = 1.717 \cdot N_{eo} \ \text{volt}^2.\text{cm} \qquad (68)$$

for the uniform profile.

Figure 38 depicts the axial response of the toroidal cavity for the uniform electron density profile; the normalized contribution to the interaction integral is plotted as a function of position along the axis of the discharge tube.

The cavity computations were experimentally checked by inserting dielectric rods along the axis of the cavity. Four different dielectric rods were used, two of quartz and two of pyrex. Table I lists the results of the experiments. In each case the relative dielectric constant used for the calculated resonant frequency shift was the published average value for that type of material (Ref 32:E-48). No attempt was made to independently determine the dielectric constant for the calibrating rods. The results indicated an average agreement of 13.3% between the measured and

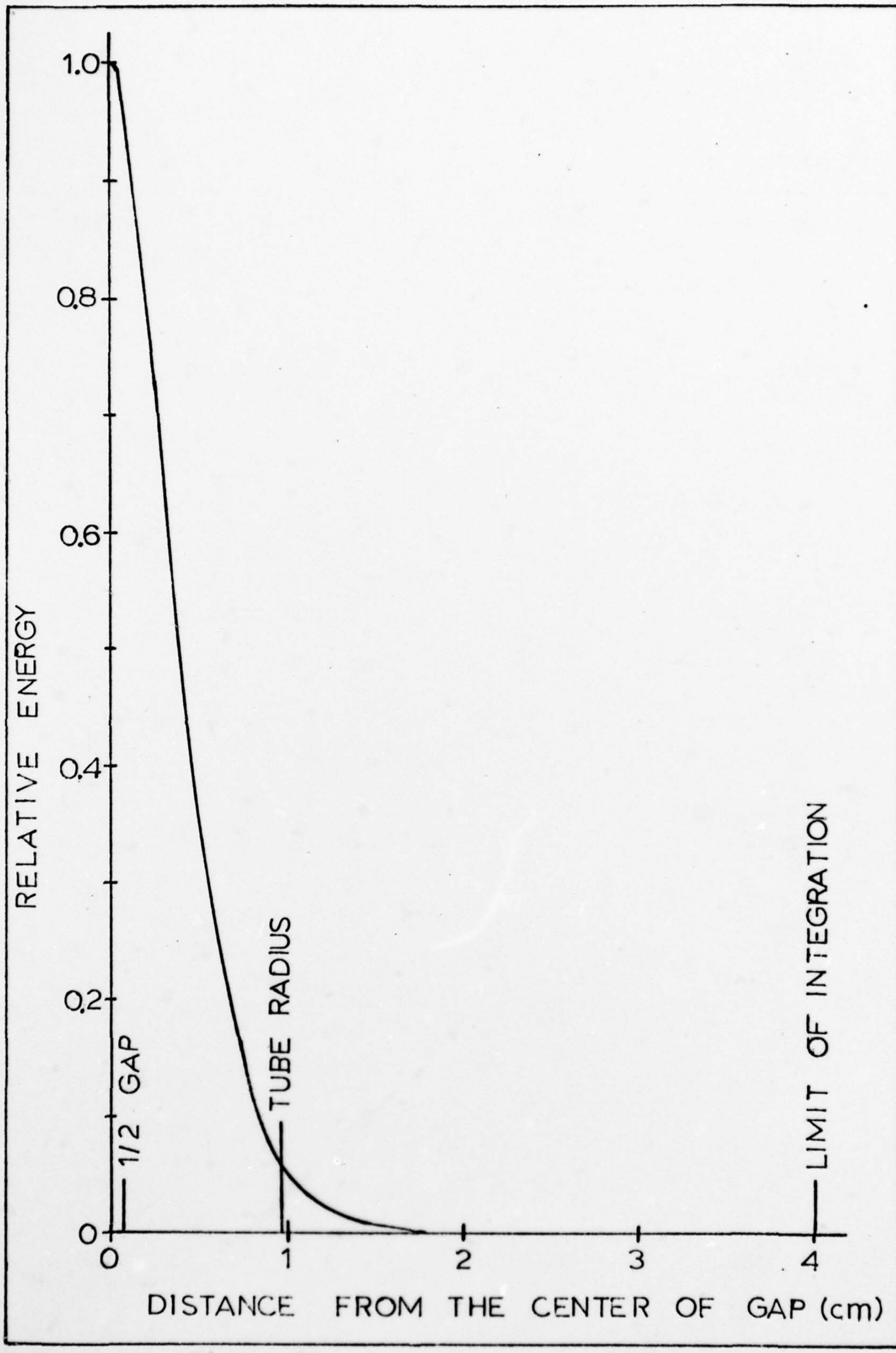

Figure 38. Response of Toroidal Cavity

calculated resonant frequency shifts. Also, the larger the diameter of the calibration rod, the better the agreement was. The experimental determination of cavity performance was merely used to validate the model; the results of the experiments were not used to modify the calculated factors.

Table I. Cavity Performance

Material	Radius (cm)	ϵ_r	Δf Measured	Δf Calculated	% Difference
Quartz	.150	3.93	1.90	1.56	-17.9
Pyrex	.250	4.74	6.50	5.64	-13.2
Quartz	.313	3.93	8.10	7.01	-13.5
Pyrex	.365	4.74	13.40	12.34	- 7.9

Experimental Results

Figures 39 through 44 depict the measured centerline electron densities as functions of the discharge current for pressures between 2 and 7 torr. For the high field form of the discharge, the Bessel profile coupling factor (equation 67) was used in reducing the data. For the low field form both the Bessel and the uniform profile coupling factors (equations 67 and 68) were used.

Electron densities were calculated for all of the runs using the electron drift velocity, tube current, electric field and pressure. The results of these calculations are depicted as dashed lines in figures 39 through 44. The

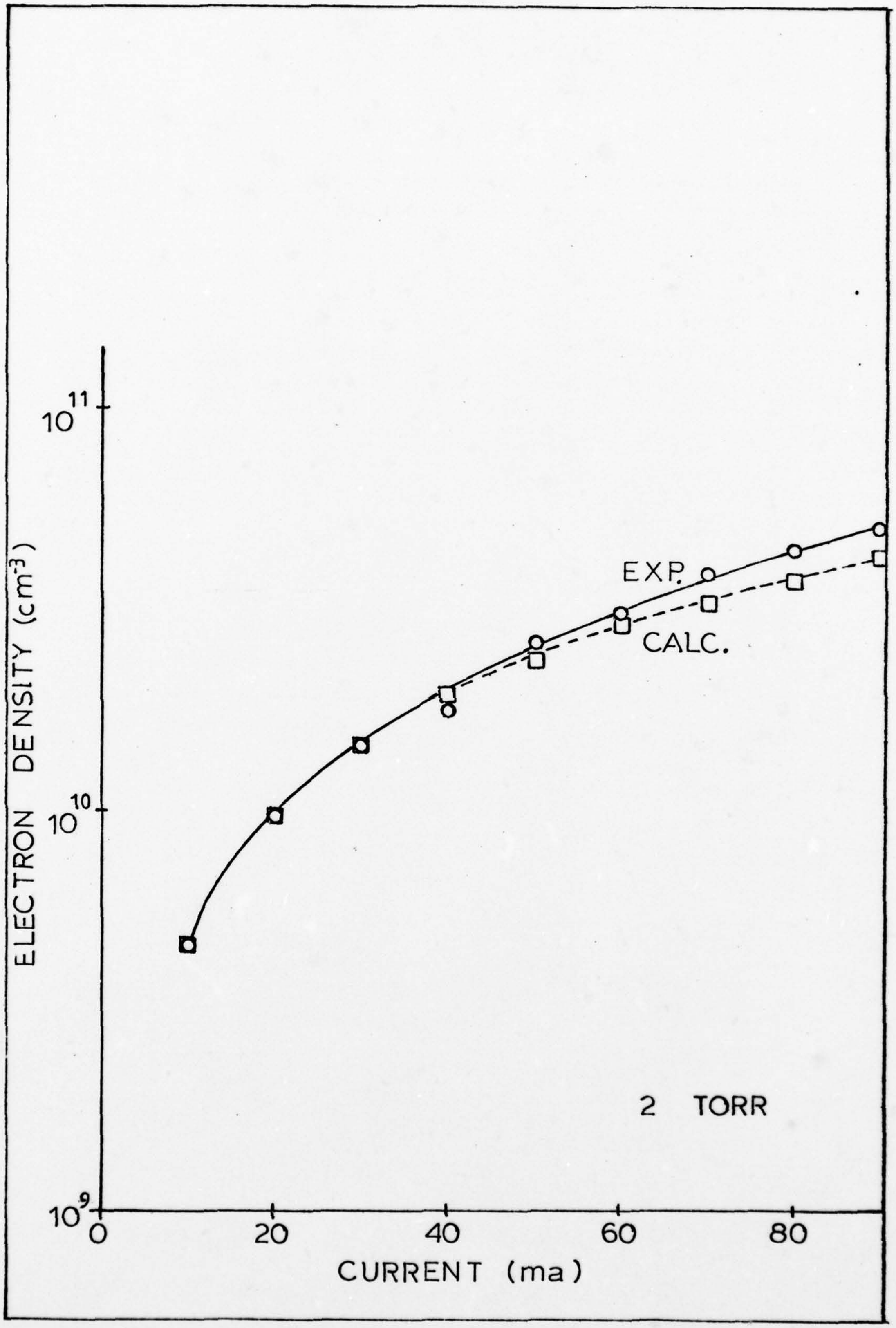

Figure 39. Electron Density at 2 Torr

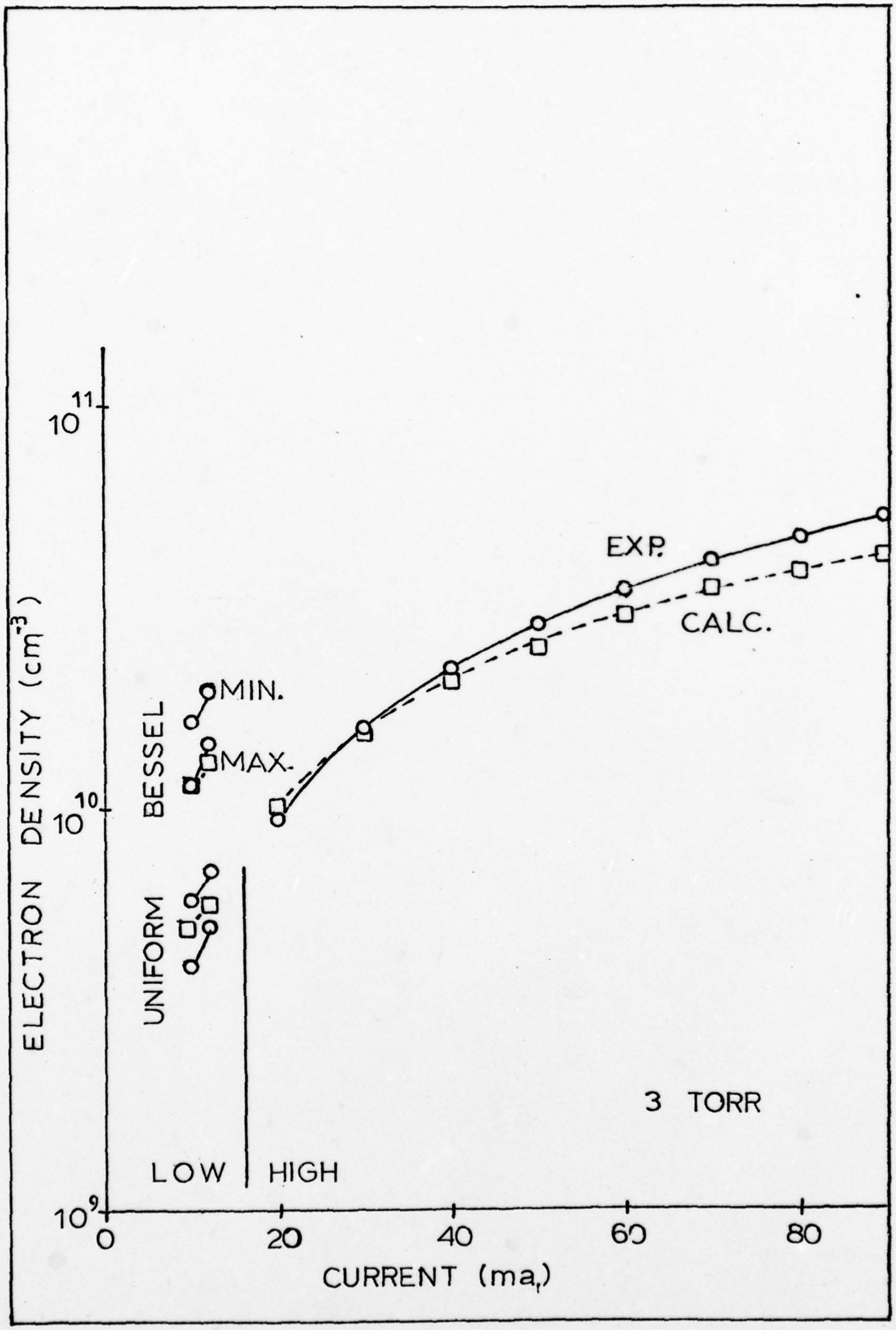

Figure 40. Electron Density at 3 Torr

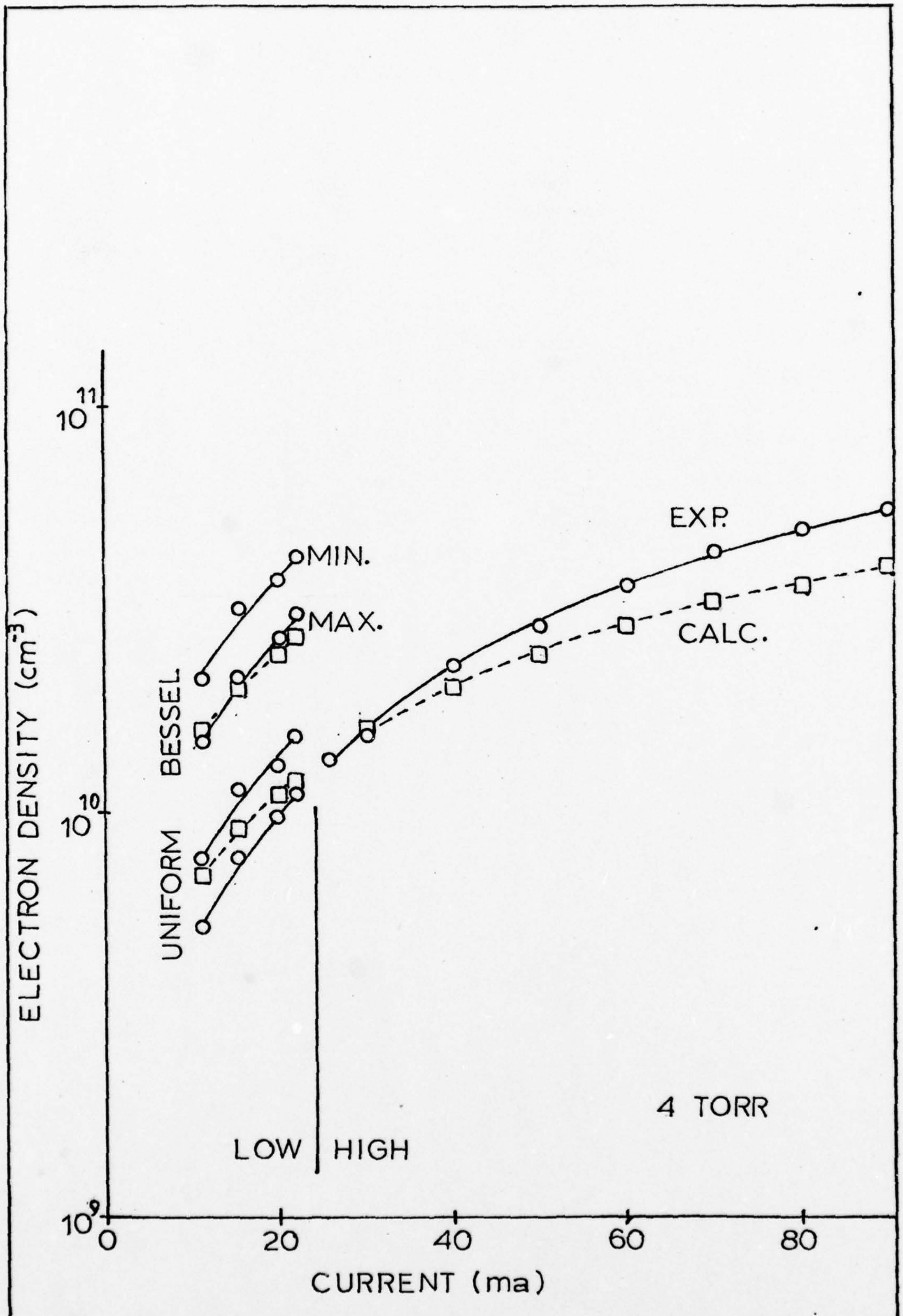

Figure 41. Electron Density at 4 Torr

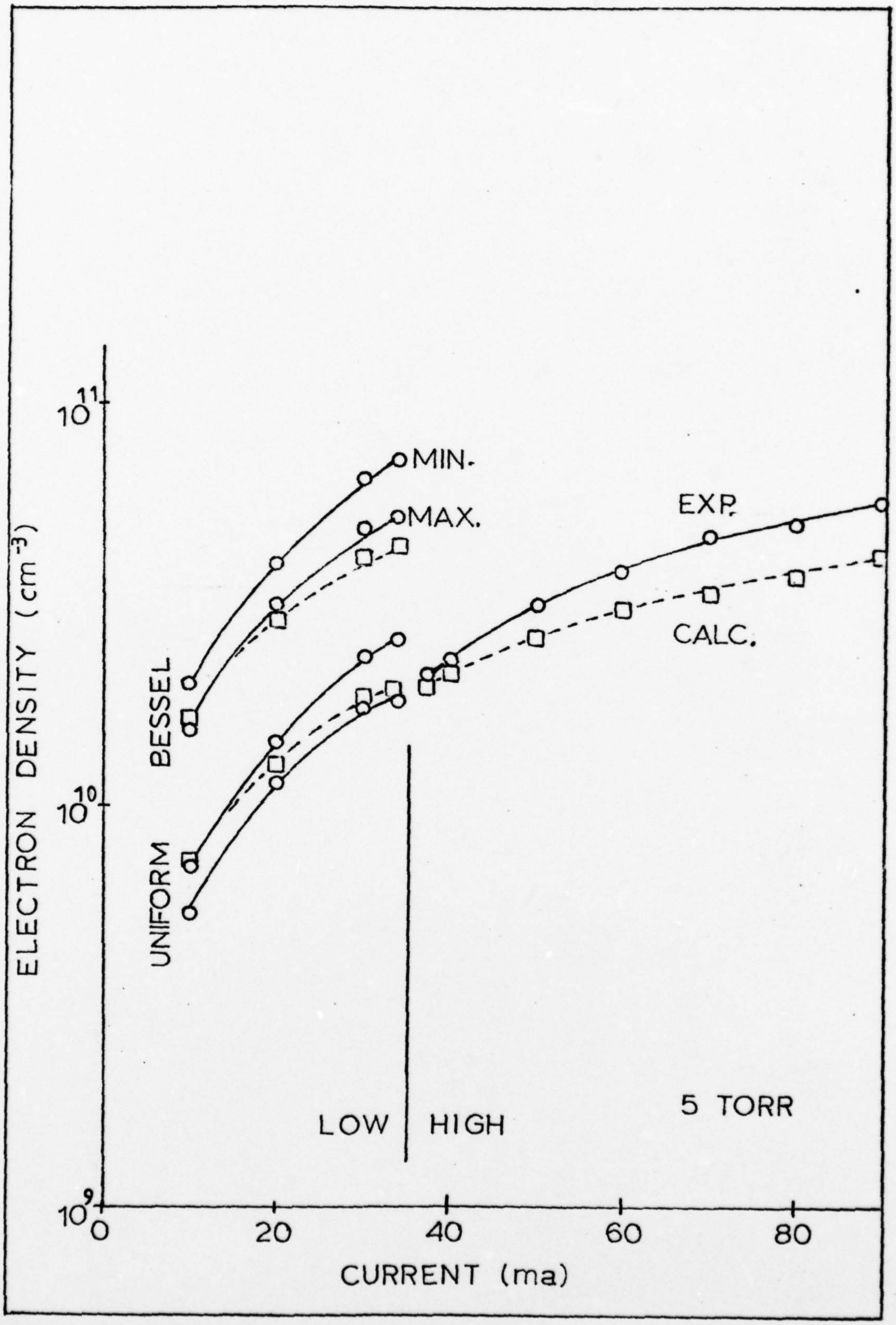

Figure 42. Electron Density at 5 Torr

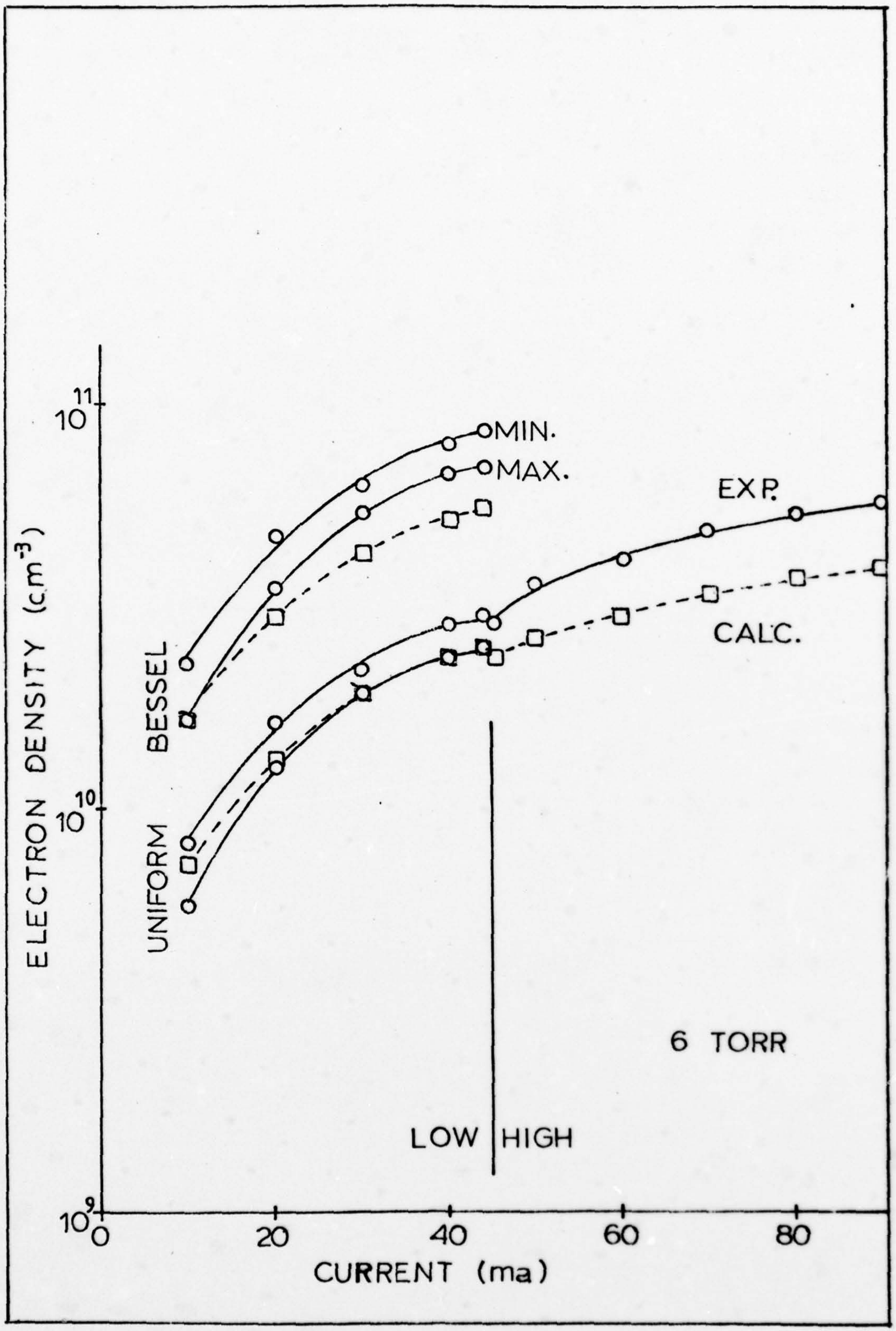

Figure 43. Electron Density at 6 Torr

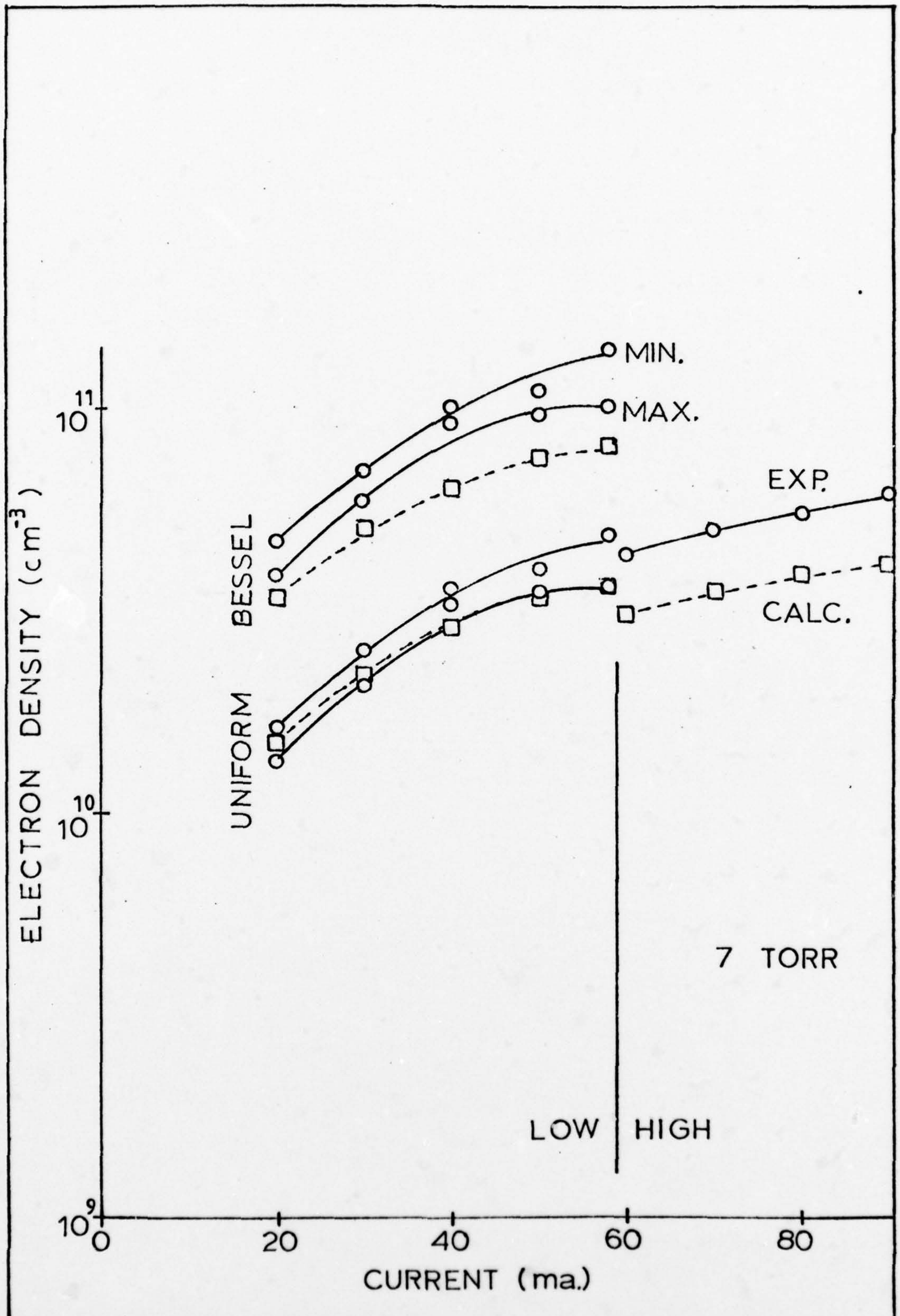

Figure 44. Electron Density at 7 Torr

calculations were performed using the following equation:

$$N_{eo} = \frac{I}{q \cdot \int_0^{R_o} \frac{N_e(r)}{N_{eo}} \cdot V_D\left(\frac{E}{N}\right) \cdot 2 \cdot \pi \cdot r \cdot dr} \tag{69}$$

For the Bessel profile:

$$N_e(r) = N_{eo} \cdot J_o \left\{ \frac{2.4 \cdot r}{R_o} \right\} \tag{70}$$

and for the uniform profile:

$$N_e(r) = N_{eo} \tag{71}$$

Using the Boltzmann code results of Chapter VIII (figures 51 and 56), the drift velocity was assumed to vary as:

$$V_D = A \cdot \left(\frac{E}{N}\right)^B \tag{72}$$

where the coefficients A and B were determined by regression analysis over the applicable E/N ranges.

Table II. Drift Velocity Coefficients

Discharge Form	E/N Range	A	B
Low	6-20TD	9.38×10^5	0.551
High	40-60TD	5.32×10^5	0.754

E/N is assumed to be a function of electric field, pressure, temperature rise and radius - in accordance with the following equation:

$$\frac{E}{N} = \frac{E}{P} \cdot 1.035 \times 10^{-12} \cdot \left[290 + \Delta T - \Delta T \cdot \left(\frac{r}{.95} \right)^2 \right] \qquad (73)$$

where the number density was calculated using the ideal gas law and a parabolic approximation for temperature as a function of radius (equation 22).

For the high field form of the discharge there was good agreement between the experimental and calculated electron densities at low pressures and low discharge currents. At higher currents and pressures the two results tended to diverge. This was probably due to the extrapolation required to determine the discharge gas temperature. As presented in Chapter IV, the gas temperature was experimentally measured only for low values of power input; high power temperatures were extrapolations. Since the electron density was calculated from the drift velocity which was E/N dependent, the accuracy of the calculated values was dependent on an accurate knowledge of the gas temperature to determine the neutral species number density.

For the low field form of the discharge, experimental and calculated values are depicted for both Bessel and uniform electron density profiles. These results provide upper and lower limits for the electron density. Thompson has demonstrated that for discharges in which the negative ion densities were greater than the electron densities, the electron density profile tended to be uniform. Since the low field form of the oxygen discharge has been shown to be rich in negative ions, the actual electron densities probably were very close to the uniform profile results. These results showed very good correlation between experimental and calculated values.

For each of the low field profiles, two experimentally determined electron density curves are depicted - one for the maximum of the oscillation and one for the minimum. The minimum of the oscillations corresponded to the higher of the electron density curves. This was consistent with current continuity considerations since the drift-velocity, number-density product for both the maximum and minimum points must be equal. Since the electric field* of the minimum point was lower than that of the maximum, the minimum point electron density was required to be higher.

The electron number density of the maximum of the oscillation in the low field form was underestimated. This was due to the fact that the electric field pulse of the discharge oscillation was so short that there was spatial averaging due to the cavity gap and temporal averaging due to the measuring electronics. The number density of the minimum of the oscillation should have been accurate since it was measured over a rather flat minimum of the electric field oscillation.

---

*And thus the drift velocity.

VII. Mass Spectra

The initial objective of the mass spectral experiments was to determine the relative densities of the neutral, positively ionized and negatively ionized species as functions of pressure and current. Of particular interest was the negative ion spectra, since the negative ions play such an important role in the low field form of the oxygen plasma. Due to equipment problems, only the neutral spectra were measured. The results of these neutral species' measurements were useful in the validation of the discharge modeling.

In the first section of this chapter the experimental setup is described. This is followed by a description of the calibration of the mass spectrometer. Finally, the experimental results are presented.

Experimental Setup

With the exception of the discharge tube, the general experimental setup described in Chapter II was utilized. Figure 45 depicts the discharge tube used in the mass spectra experiments. The length and cross section measurements of the tube were identical to those of the tube used in the previous experiments. However, the mass spectra tube was constructed without electric-field probe-ports and utilized pyrex glass instead of quartz. These differences were dictated by the critical construction and mounting requirements

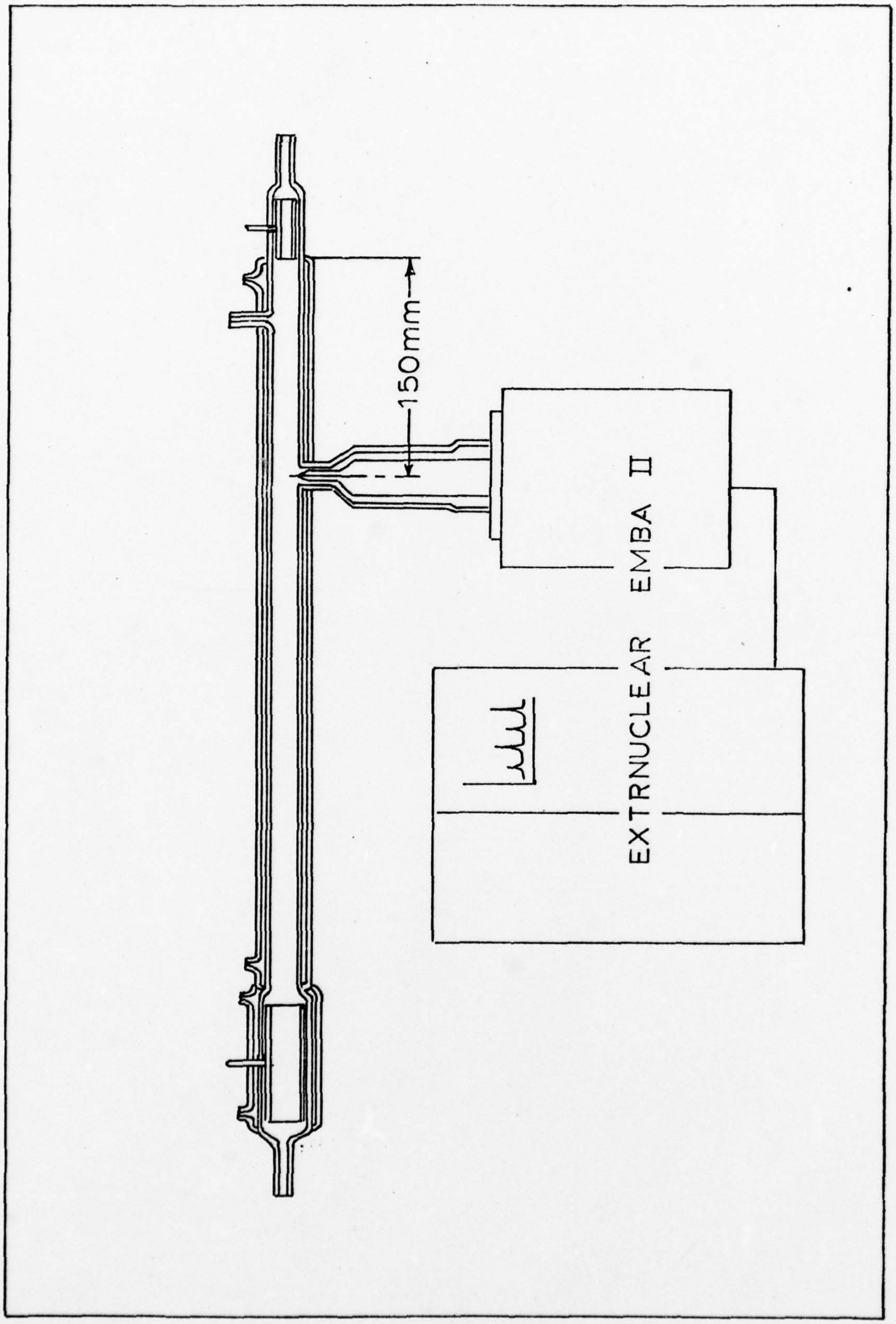

Figure 45. Mass Spectrometer Setup

imposed by the necessity of attaching the tube to the mass spectrometer. A sampling port was mounted in the side of the tube at a location that corresponded to half the distance between electric field ports three and four of the previous tube. A stainless steel sampling tube was inserted through this port; this tube extended to the edge of the discharge. Through this tube samples of the discharge plasma were drawn into the mass spectrometer.

Figure 46 illustrates the electrical setup for the experiment. The sampling tube was referenced to ground potential, and the discharge tube anode and cathode were allowed to "float." In order to utilize grounded current and voltage indicators, a laboratory designed and constructed isolator was used. This unit employed high voltage optical isolators to protect the indicators from damage.

The mass spectrometer utilized was an Extranuclear EMBA II. This system used a 22-centimeter quadrupole to provide a $M/\Delta M$ discrimination better than 1500. Sensitivity of the system was enhanced by the modulation of the sample beam by a tuning-fork-chopper prior to its entrance into the ionizer and subsequently using a Princeton Applied Research HR-8 Lock-In Amplifier for synchronous detection of the signal from the electron multiplier. This scheme allowed the effect of the background gases in the spectrometer to be minimized. The output of the mass spectrometer was recorded on a Hewlett Packard Model 7004 x-y plotter.

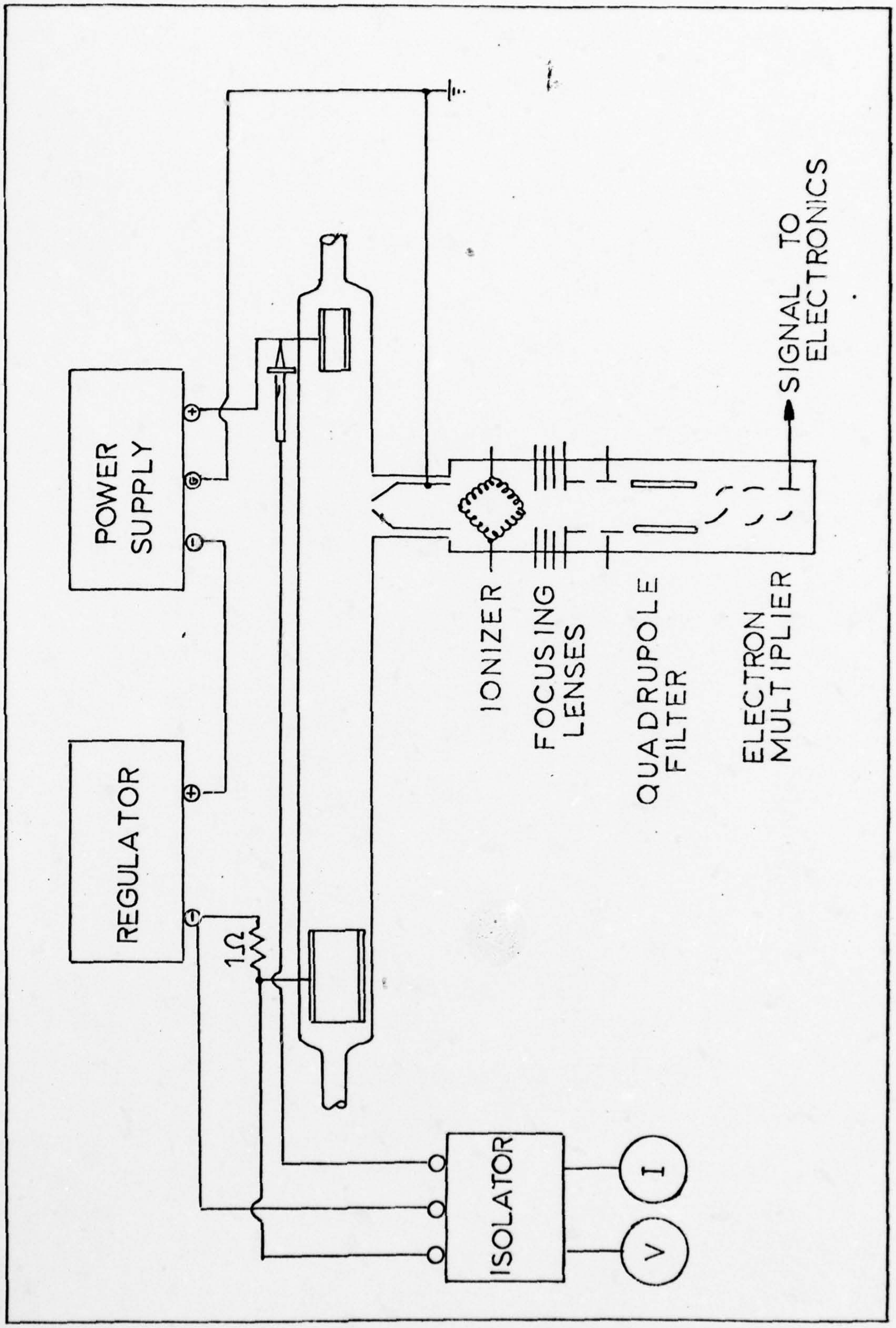

Figure 46. Mass Spectrometer Electrical Setup

System Calibration

In order to be able to measure the atomic oxygen concentration of the plasma, it was necessary to operate the ionizer at a potential which would not cause a significant dissociative ionization of the molecular oxygen but would still provide a strong ionization of atomic oxygen. To determine this ionizer potential the mass spectrometer was tuned to atomic oxygen, and its output was recorded as the ionizer potential was varied. Runs were accomplished with both the discharge on and off. The results of these runs are depicted in figure 47. An ionizer potential of 21 volts was chosen for the remaining runs.

Setting the ionizer at 21 volts did not result in 21 ev ionizing electrons; the work function of the filament had to be accounted for. In order to determine this offset the mass spectrometer was tuned to molecular oxygen; and with the discharge off, the system output was recorded as a function of the ionizer potential. Specifically of interest was the behavior in the potential interval near the threshold of ionization. A linear extrapolation of the slope of the ionization curve intercepted the ionizer potential axis at 18.4 volts*. However, this had to correspond to the ionization potential of 12.1 ev for molecular oxygen. Therefore, the offset potential for the system was determined to be 6.3 volts.

---

*See the inset of figure 28.

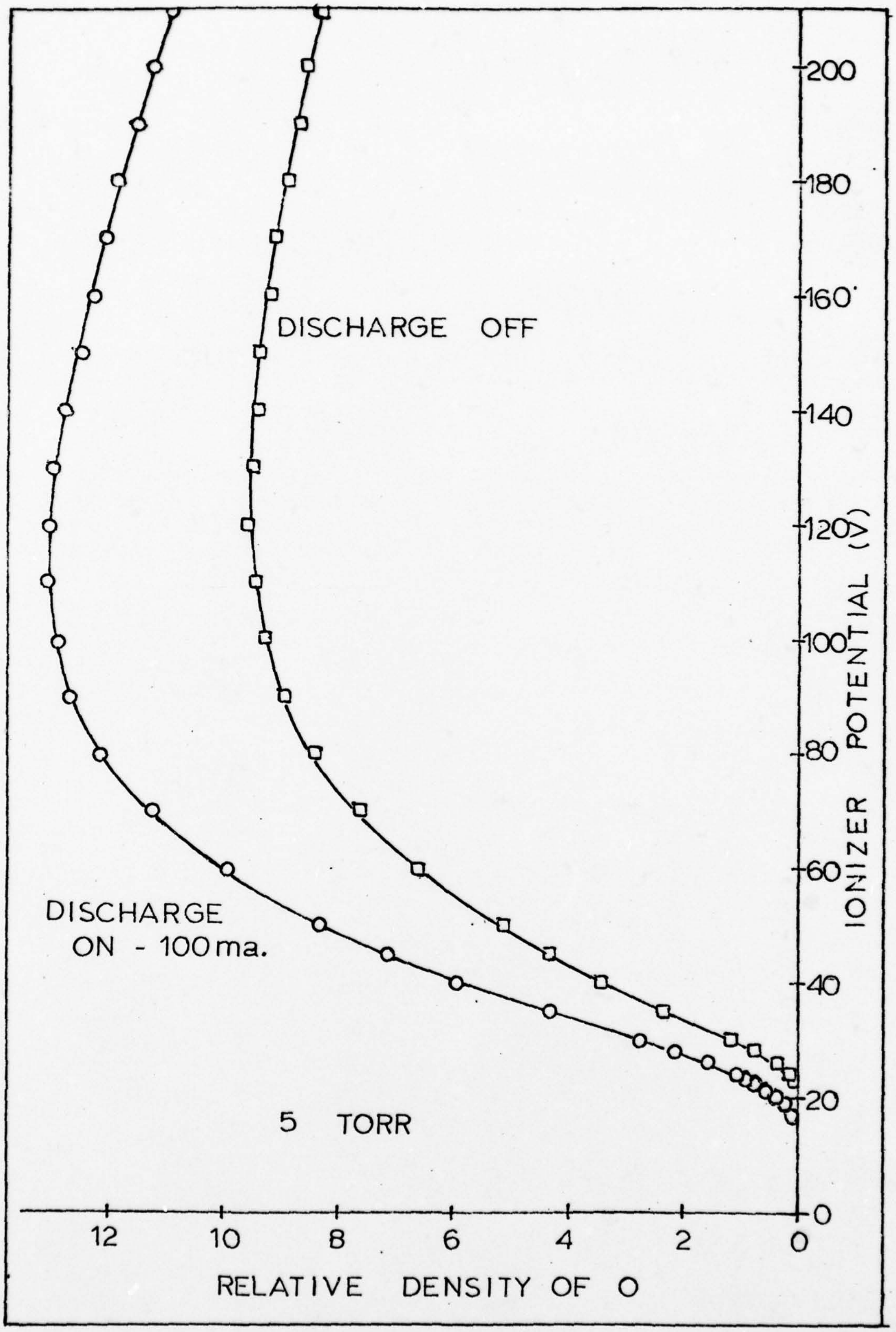

Figure 47. Ionizer Performance with Atomic Oxygen

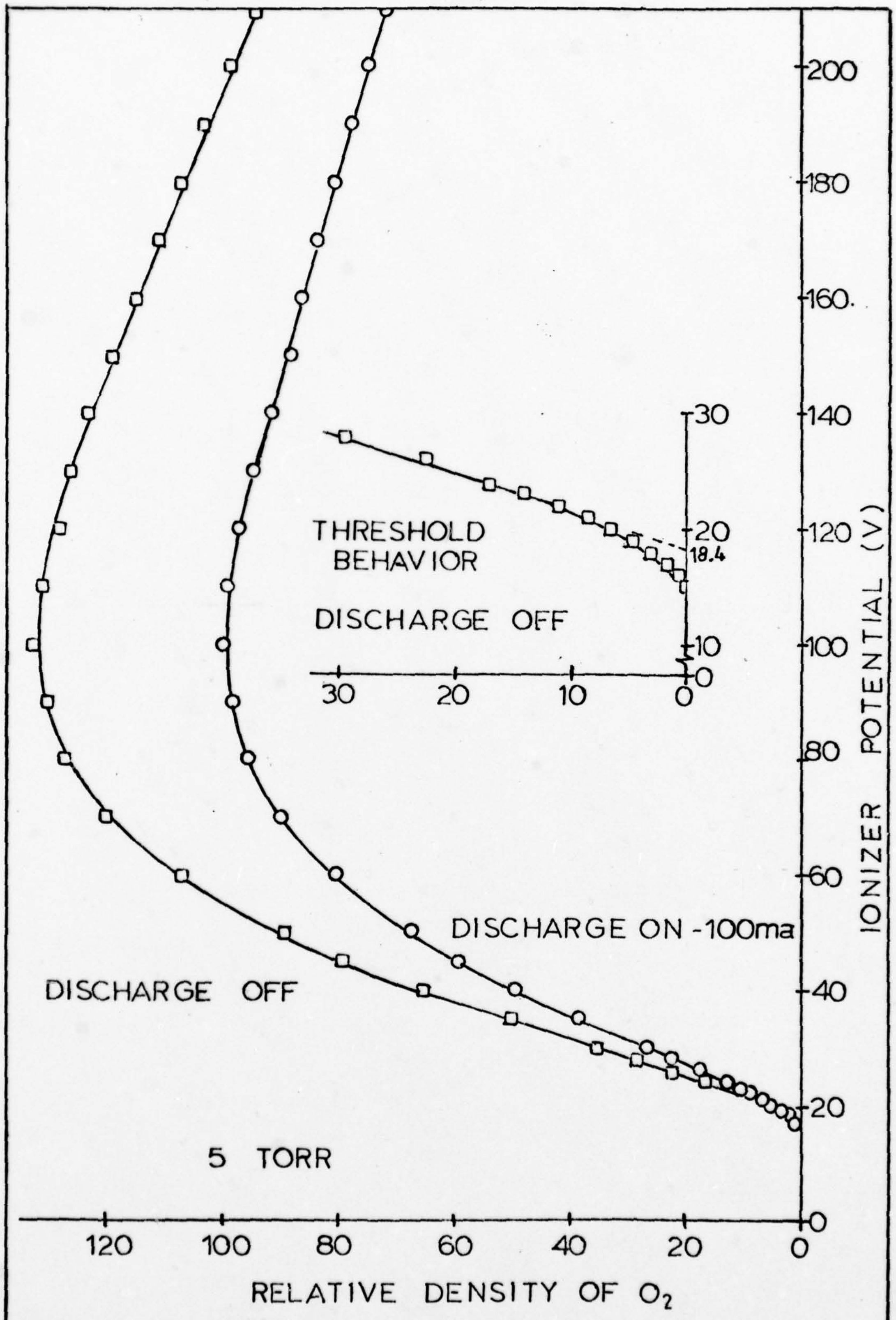

Figure 48. Ionizer Performance with Molecular Oxygen

Experimental Results

Figure 49 depicts mass spectral scans for different discharge tube currents at a pressure of 5 torr. Of interest was the sudden increase in the atomic oxygen output as the discharge transitioned from the low to high field forms between 40 and 50 ma. Also, there was a lack of measurable neutral ozone in the discharge. The signals at 18(H_2O), 28(N_2), and 44(CO_2) represented background gases of atmospheric origin. Although there were undoubtedly small leaks in the discharge tube portion of the experiment, the background in the spectra was the result primarily of a very small leak in the back chambers of the mass spectrometer. This was determined by observing the discharge tube gas flow and pressure effects on the background. The background peaks were a function of discharge tube pressure and not of the rate of gas flow into the discharge tube.

Figure 50 depicts the variations of molecular and atomic oxygen with discharge current. The experimental runs were made at a pressure of 5 torr. It was noted that when tuned to molecular oxygen, the mass spectrometer exhibited a long-term drift phenomenon; the signal output decreased as a function of time. This drift effect was not noticed when observing other species and was therefore assumed to be caused by an oxidation of the detector electrodes. The molecular oxygen curve of figure 50 was corrected for this effect by assuming a linear drift and requiring the low current start and end points to coincide.

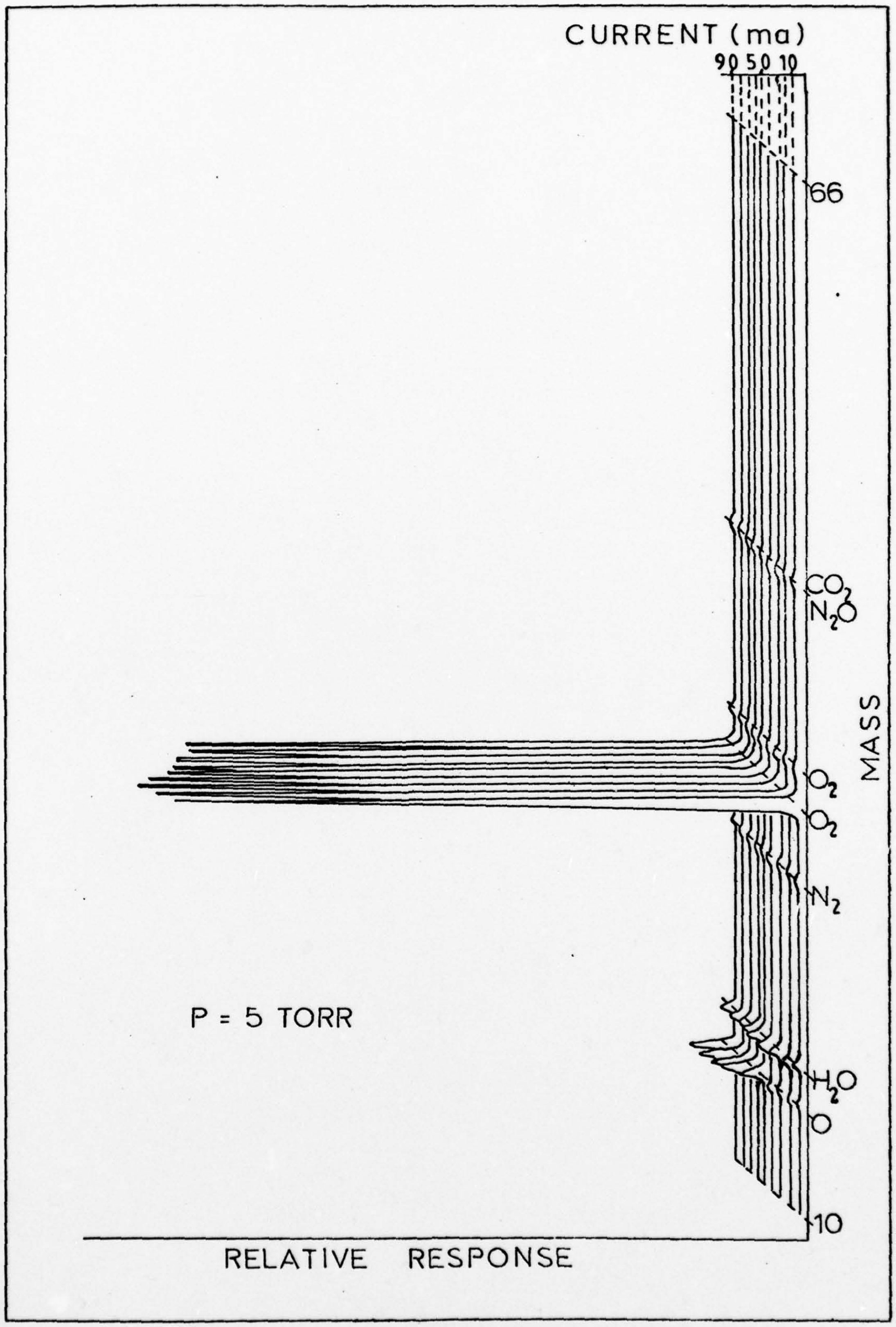

Figure 49. Mass Scans

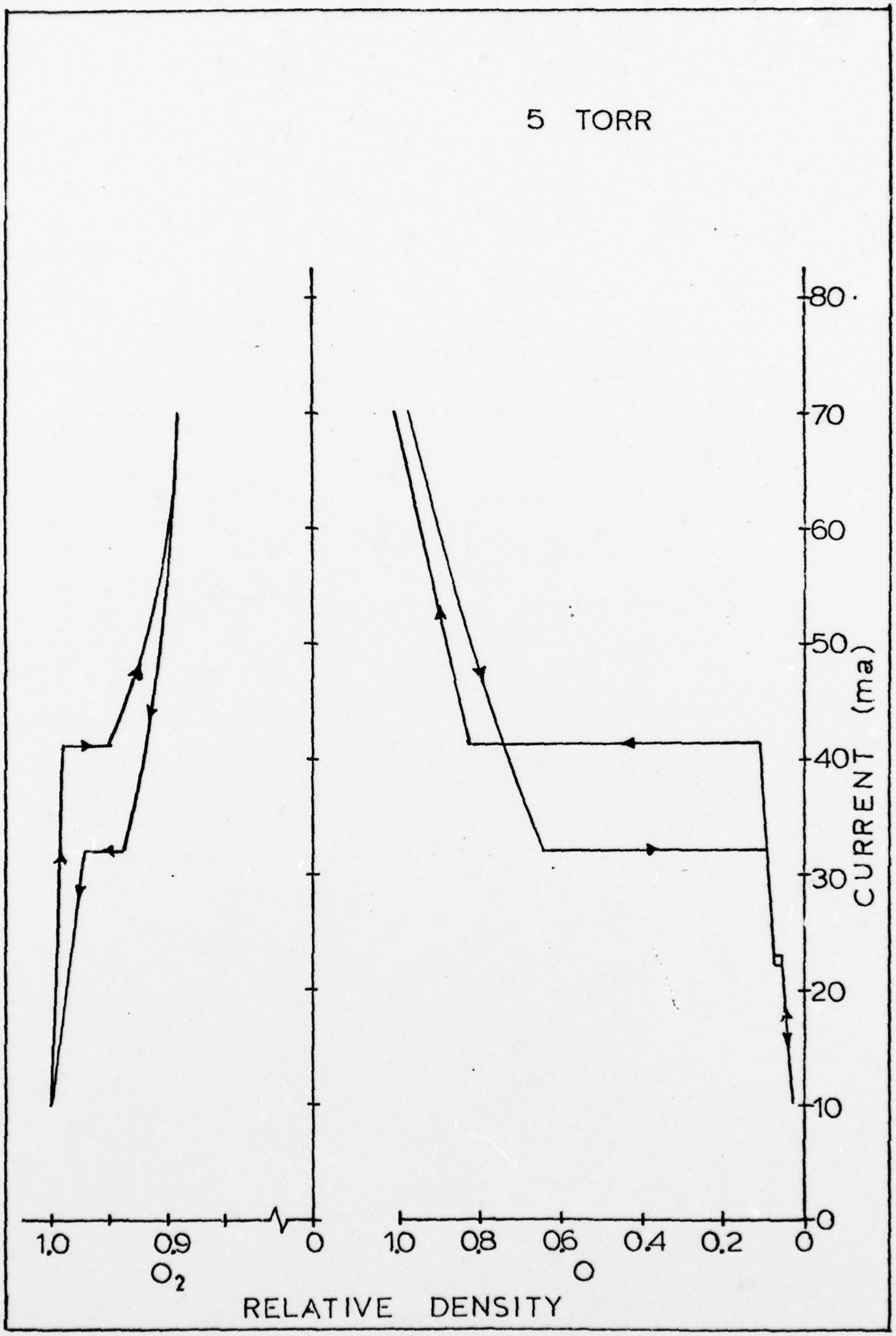

Figure 50. 0_2 and 0 Density Variations with Current

VIII. Electron Energy Distribution

In order to develop a mathematical model of the oxygen plasma, it was necessary to know the transport properties of the electrons and the reaction rates between the electrons and the other species. The reaction rates determine the generation of many of the species that contribute to the properties of the plasma, for example: the excited species, the ions, and the electrons themselves. In this study the Boltzmann equation was used for the numerical calculation of the electron energy distribution function, and from it the electron transport properties and reaction rates were calculated.

The chapter starts with a brief explanation of the theory associated with the use of the Boltzmann equation. Next, selected results of the calculations are validated by comparison to experiments reported in the literature. Finally, all of the results used in other portions of this study are presented.

Theory

The fundamental kinetic description of a plasma is provided by expressions for the velocity distributions of each constituent specie. Because of the relatively high pressure, low fields and approximately equal masses, the distribution functions for the ions, atoms and molecules were assumed in this study to be Maxwellian with a characteristic temperature equal to that of the gas*. The electron velocity distribution was not Maxwellian and was not in thermodynamic equilibrium with the other species. The electron velocity distribution was determined by a numerical solution of the Boltzmann transport equation.

Solutions of the Boltzmann equation provided descriptions of how the electrons were distributed in phase space** and in time. The inputs to the Boltzmann equation were the externally applied forces and the characteristics of the background gas which affected the collision-induced changes to the distribution function; the output of the equation revealed how the electrons were distributed in velocity and position. The Boltzmann equation is a very general mathematical relation; however, it was difficult to solve without involking simplifying assumptions. In the absence of a magnetic field the Boltzmann equation for the electrons can be written as (Ref 42:34):

$$\frac{\partial f_e}{\partial t} + \overline{V_e} \cdot \overline{\nabla_x f_e} - \frac{q}{m_e} \cdot \left(\overline{E} \cdot \overline{\nabla_v f_e}\right) = \left(\frac{\partial f_e}{\partial t}\right)_{\text{Collisions}} \qquad (74)$$

f_e = distribution function of electrons such that

$n_e f dv_x dv_y dv_z dx dy dz$ denotes the average number of electrons in the volume between x and x + dx, y and y + dy,

---

*Assumed to be 300°K.

**Phase space is a six-dimensional space in which each particle is represented by both position and velocity coordinates.

z and z + dz and with velocity components between v_x and $v_x + dv_x$, v_y and $v_y + dv_y$; and v_z and $v_z + dv_z$ and $f dv_x dv_q dv_z dx dy dz = 1$.

$\overline{X}_e = x, y, z$ = position coordinates in six-dimensional phase space.

$\overline{V}_e = v_x, v_y, v_z$ = velocity coordinates in six-dimensional phase space.

∇x = Del operator with respect of position.

∇v = Del operator with respect to velocity.

$\overline{E}$ = applied electric field.

Since the plasma studied was weakly ionized, only the collisions between electrons and neutral particles were considered. The collision term of equation 74 can then be written as (Ref 8:122):

$$\left(\frac{\partial f_e}{\partial t}\right)_{\text{Collisions}} = \int_{-\infty}^{\infty}\int\int\int_{0}^{2\pi}\int_{0}^{\pi}\left(\tilde{f}_e \cdot \tilde{f}_N - f_e \cdot f_N\right) \cdot g \cdot S(\chi) \cdot \text{SIN}\{\chi\} \cdot d\chi \cdot d\psi \cdot d^3 V_N \qquad (75)$$

where $f_e, \tilde{f}_e$ = electron velocity distribution functions before and after a collision.

$f_N, \tilde{f}_N$ = neutral species velocity distribution functions before and after a collision.

g = relative speed between the electron and neutral particle.

$S(\chi)$ = differential scattering cross section.

χ = scattering angle.

ψ = azimuth angle.

d^3V_N = velocity differential volume for the neutral particles.

Equations 74 and 75, when combined, form the general form of the Boltzmann equation. No closed form solution to the general equation was known; therefore, an approximate solution was obtained. An external electric field causes the electrons to acquire a drift velocity opposite to the direction of the field. This directed velocity component has the effect of causing the electron velocity distribution function to be anisotropic. For low values of electric field strength the drift velocity is small compared to the random velocity of the electrons. Therefore, the electric field effects were treated as a perturbation, and the electron velocity distribution was expressed as the sum of the first two terms of a spherical harmonic expansion (Ref 7: 274):

$$f_e = f_e^{(0)} + \frac{\overline{V}_e}{V_e} \cdot f_e^{(1)} \qquad (76)$$

where $fe^{(0)}$ is the isotropic distribution function and $fe^{(1)}$ is the directed distribution function.

Equations 74, 75 and 76 were combined into a computer program titled EED for solution of the Boltzmann equation*.

---

*Program EED was developed by William Bailey and William Long for use by the personnel of the Plasma Physics Laboratory of the Aerospace Research Laboratories.

The program, as listed in Appendix C, was used in this study to calculate the isotropic and directed electron velocity distribution functions, the electron transport parameters, and the electron-other species energy dependent reaction rates. The required inputs to the program were the reduced electric field (E/N) and the various electron collision cross sections (Appendix B). Both elastic collision cross sections, in which the internal energies and identities of the target particles remained unchanged, and inelastic collision cross sections, in which the state and/or identity of the target particles were changed, were provided to the program. For the inelastic collisions the electron energy after the collision was decreased by an amount equal to the threshold energy for the collision. For ionizing collisions the secondary electrons were considered to be created with zero energy.

The computer program EED calculated the electron energy distribution components, $f_e^{(0)}$ and $f_e^{(1)}$, and utilized them to calculate the electron transport parameters from the following moments (Ref 43:2):

$$\langle u \rangle_e = \int_0^\infty f_e^{(0)}(u_e) \cdot u_e \cdot du_e \tag{77}$$

where $\langle u \rangle_e$ is the mean electron energy.

$$V_{ed} = 10^2 \cdot \left(\frac{2 \cdot q}{m_e}\right)^{\frac{1}{2}} \cdot \int_0^\infty f_e^{(1)}(u_e) \cdot u_e^{\frac{1}{2}} \cdot du_e \tag{78}$$

where V_{ed} is the drift velocity of the electrons.

$$D_e = 10^2 \cdot \left(\frac{2 \cdot q}{m_e}\right)^{\frac{1}{2}} \cdot \int_0^\infty \frac{U_e^{\frac{1}{2}}}{Q_M} \cdot f_e^{(0)}(U_e) \cdot dU_e \qquad (79)$$

where De is the diffusion coefficient for the electrons and Qm is the momentum transfer cross section.

$$U_{e\text{-}CHAR} = \frac{D_e}{V_{ed}} \cdot \frac{E}{N} \qquad (80)$$

where $U_{e\text{-}CHAR}$ is the characteristic energy of the electrons. The program used the calculated electron energy distribution functions to calculate the electron-heavy particle reaction rates for each of the cross sections input to the program. These calculations were performed by the relation (Ref 9:42):

$$R_{12} = 10^2 \cdot \left(\frac{2 \cdot q}{m_e}\right)^{\frac{1}{2}} \cdot \int_0^\infty f_e^{(0)}(U_e) \cdot Q_{12}(U_e) \cdot U_e^{\frac{1}{2}} \cdot dU_e \qquad (81)$$

where R_{12} is the reaction rate for the process:

$$e + S_1 \xrightarrow{R_{12}} e + S_2$$

Q_{12} is the cross section for the above process and was assumed to be isotropic.

Comparison with Experiment

The Boltzmann code, EED, was run for input reduced electric fields, E/N, ranging from 1 Td to 100 Td. To validate the low energy end of the results, the calculated drift velocities were compared with the results of drift tube measurements. Figure 51 depicts the results of this comparison. Experimental data from Brown and Nelson were used for the comparison (Ref 44:91; Ref 45:4081). Figure 51 indicates the close correlation between the calculated and experimental values.

To validate the high energy portion of the results, a comparison was made between the calculated molecular ionization rates and the experimental rates of Corbin (Ref 46:81). In order to make a direct comparison the code parameters of E/N and ionization rate were converted to the parameters reported by Corbin, P_{20}/E and α_i/P_{20} . This conversion was made using the following relations:

$$\frac{P_{20}}{E} = \frac{N \cdot R \cdot T_{20}}{E} = \frac{3.03 \times 10^{-17}}{E/N} \tag{82}$$

$$\frac{\alpha_i}{P_{20}} = \left(\frac{N \cdot R_i}{V_{ed}}\right) \cdot \frac{1}{N \cdot R \cdot T_{20}} = 3.3 \times 10^{16} \cdot \frac{R_i}{V_{ed}} \tag{83}$$

where P_{20} = pressure reduced to 20°C (torr)

R = Universal Gas Constant

αi = Townsends first ionization coefficient (cm^{-1})

T_{20} = 293°K

Ri = ionization rate (cm^3 sec^{-1})

The comparison included the drift velocities calculated by EED at the high energy inputs. Again, as in the case of the

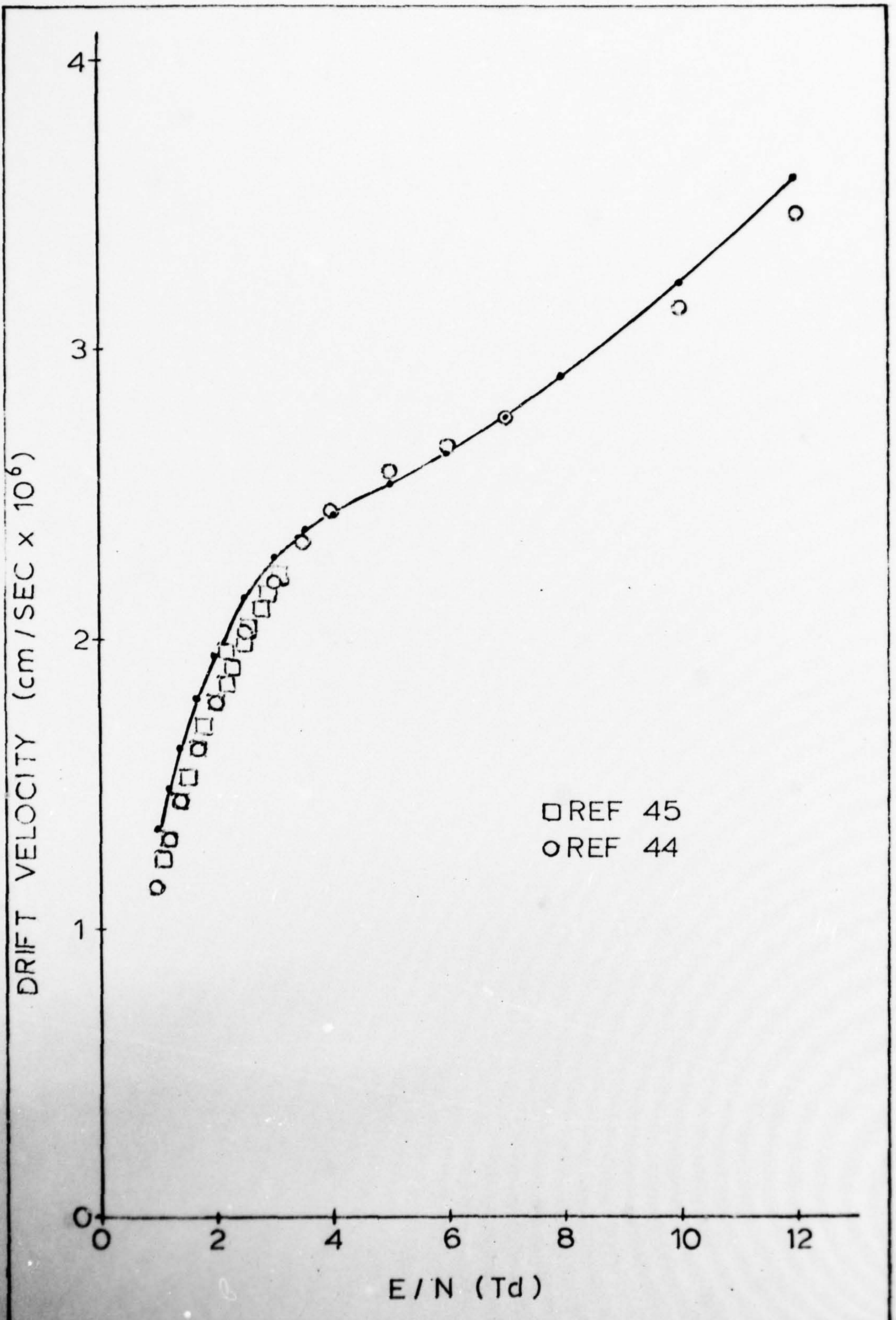

Figure 51. Comparison of Low Energy Drift Velocity

low energy results, the comparison indicated a close correlation between the EED results and experiments, as depicted in figure 52.

The electron energy distribution, $f_e^{(o)}$, at an E/N of 70 Td was compared to the experimental result of Rundle for an E/P of 25.6 v/cm torr* (Ref 47:147). Rundle's experiment indicated an exponential dropoff in the distribution of $-.0608E^{1.62}$; an analytic fit to the distribution of the present study resulted in a dropoff of $-.0745E^{1.75}$. Both experiment and theory, therefore, indicated the distribution was neither Maxwellian (E^1) nor Druyvesteyn (E^2) but occupied a position inbetween. The comparison is shown in figure 53.

<u>Results</u>

Figures 54 and 55 depict the isotropic, $f_e^{(o)}(u_e)/U_e^{\frac{1}{2}}$, and directed, $f_e^{(1)}(u_e)/U_e^{\frac{1}{2}}$, energy distribution functions for various values of reduced electric field, E/N**. Since the Boltzmann equation was solved by EED for the steady state condition, the depicted distribution functions apply only to the high field form of the discharge.

Figure 56 is a plot of the electron drift velocity as a function of the reduced electric field. Figure 57 presents

---

*At 273^{o}K an E/P of 25.6 v/cm torr equals an E/N of 72.4 Td.

**These plots are a function of energy and not of velocity; also, a factor of the square root of the energy, , has been divided out of the distributions.

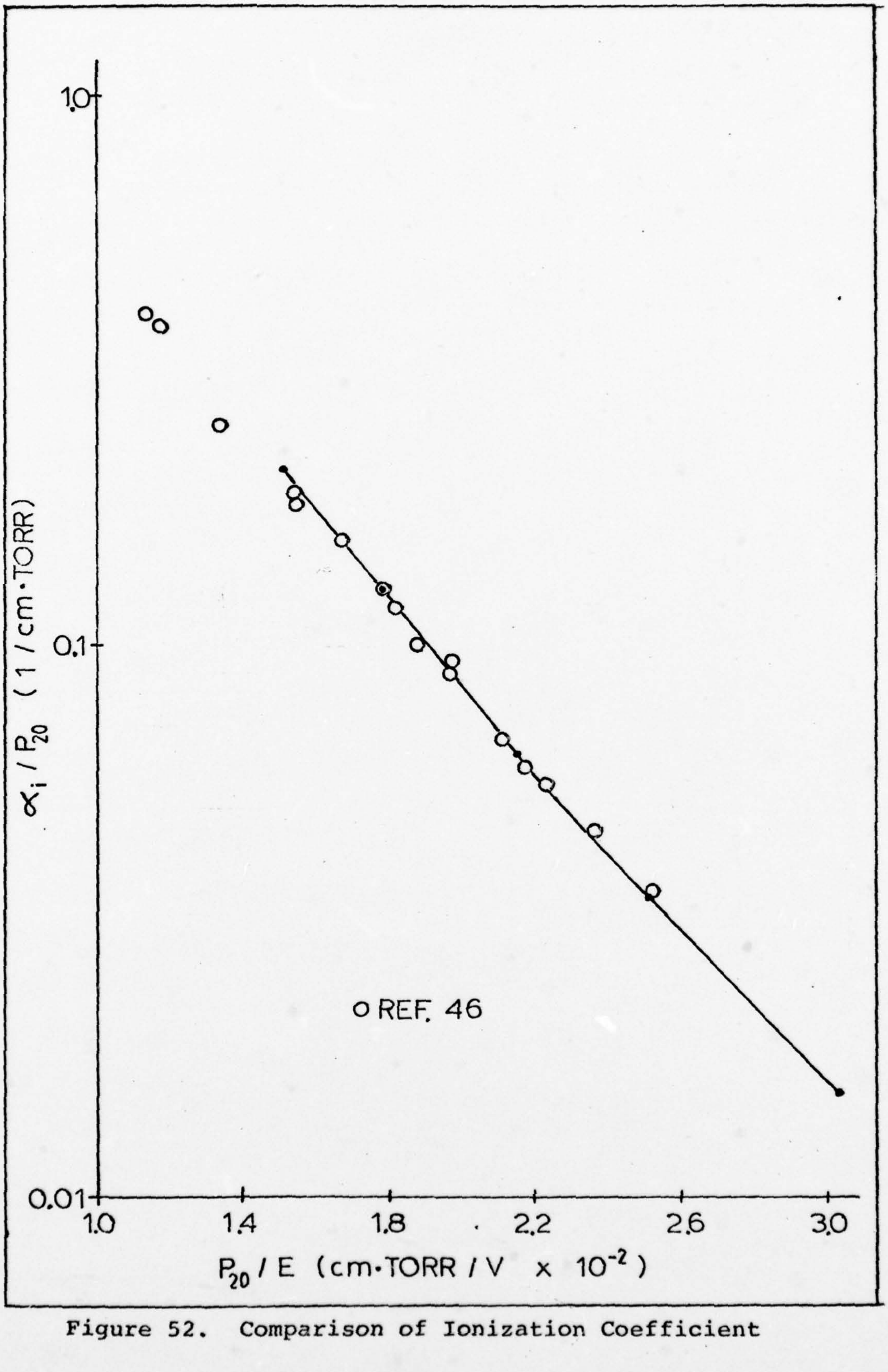

Figure 52. Comparison of Ionization Coefficient

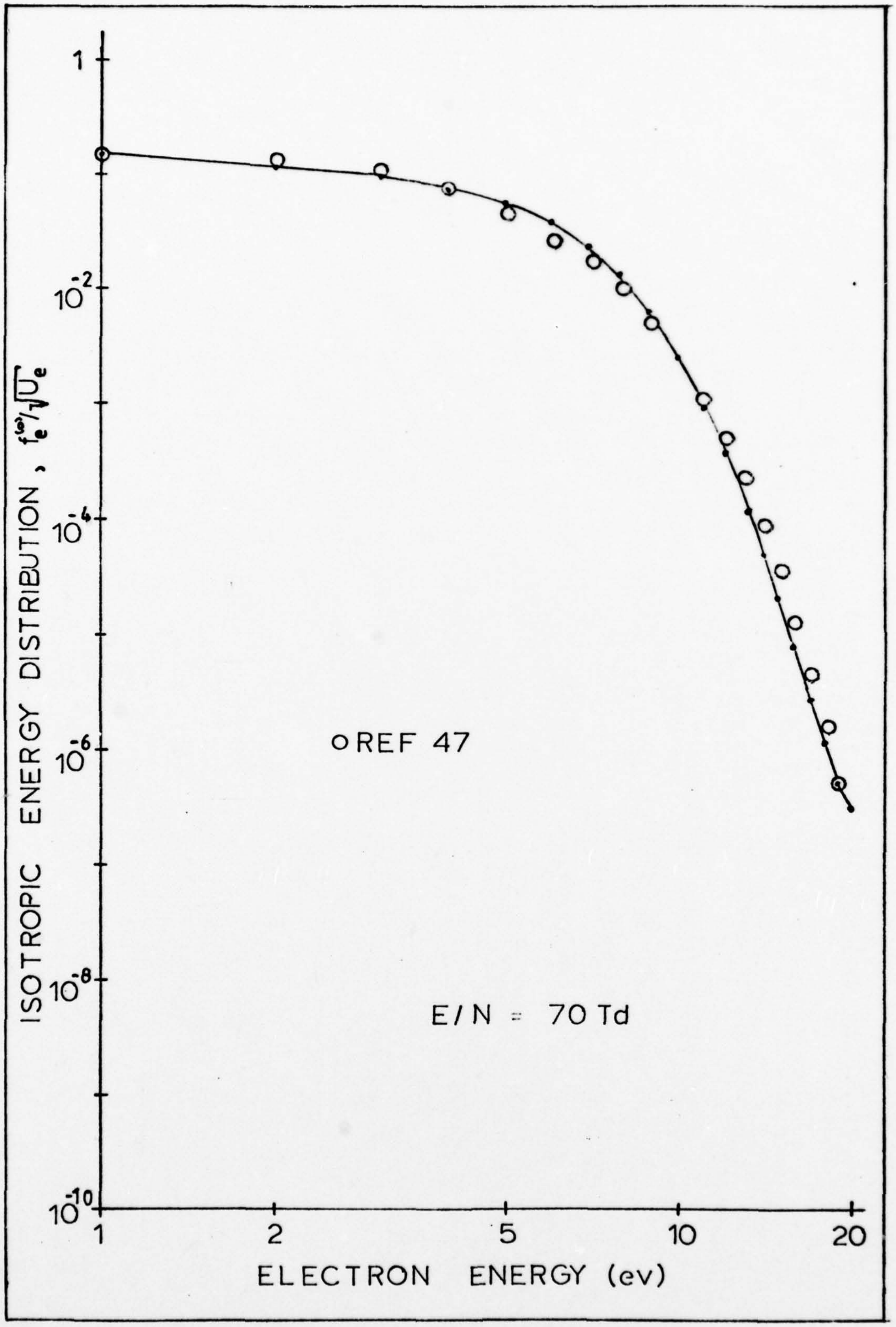

Figure 53. Analytic Approximation of the Isotropic Distribution

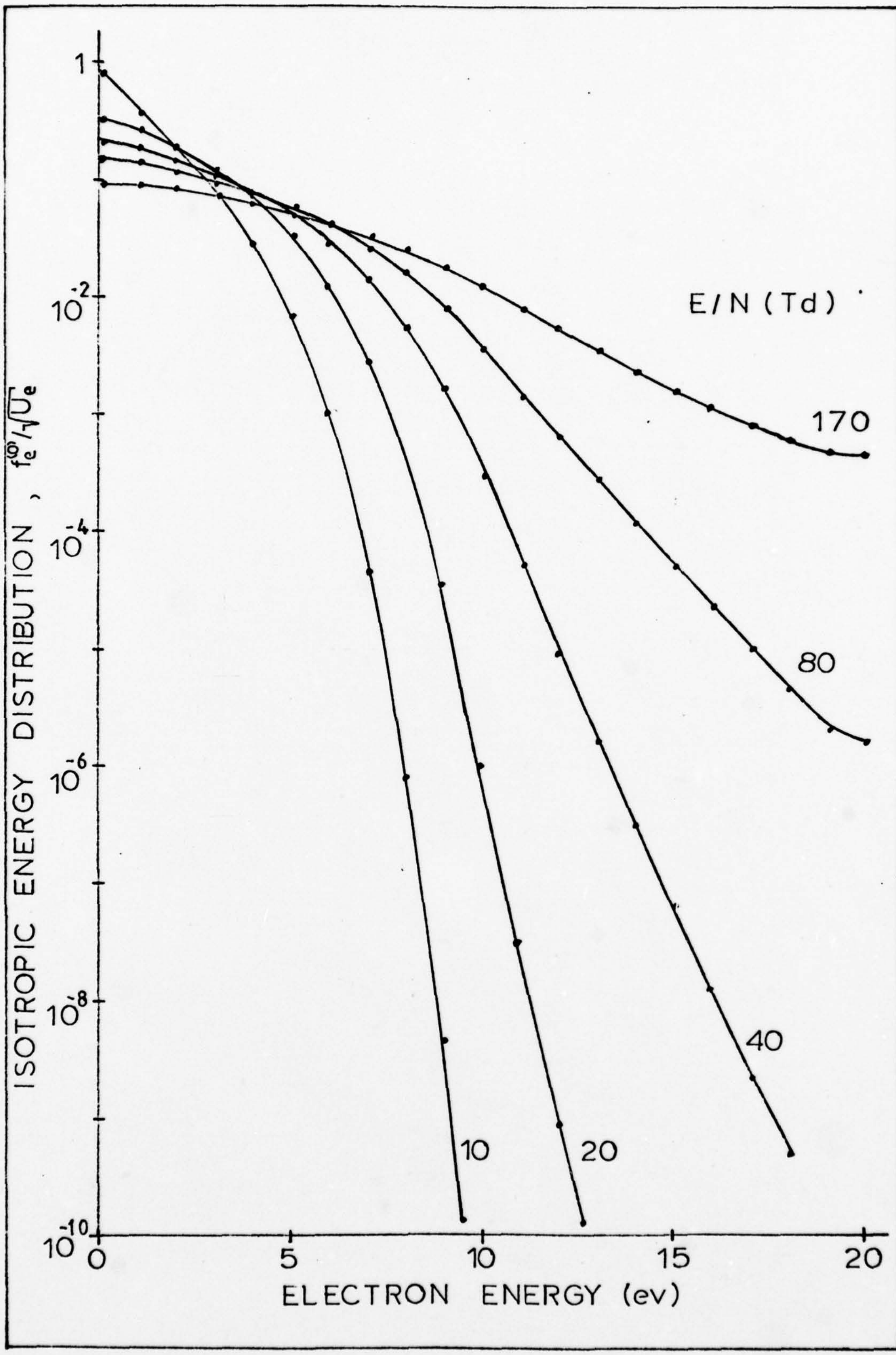

Figure 54. Isotropic Distribution

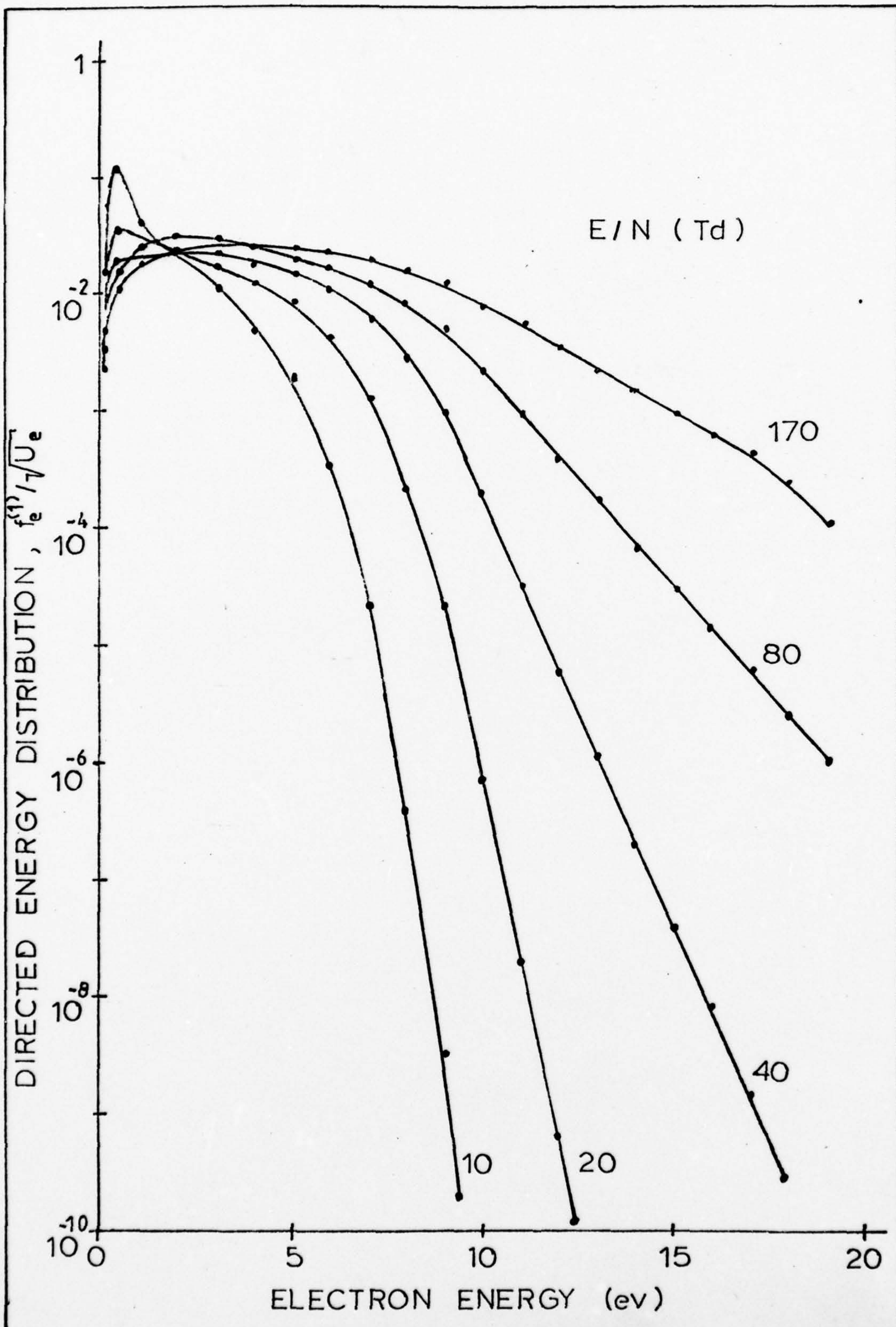

Figure 55. Directed Distribution

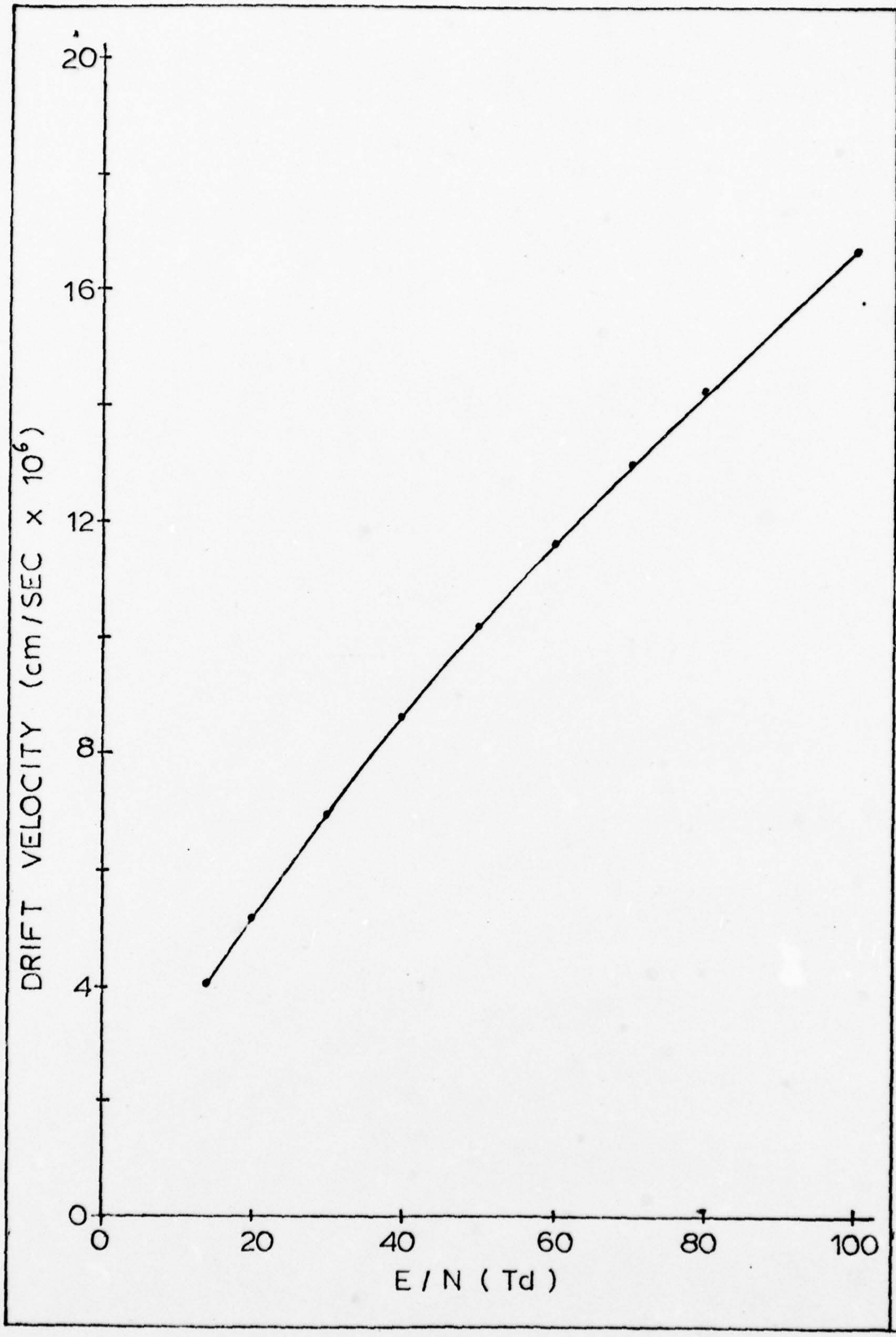

Figure 56. Drift Velocity

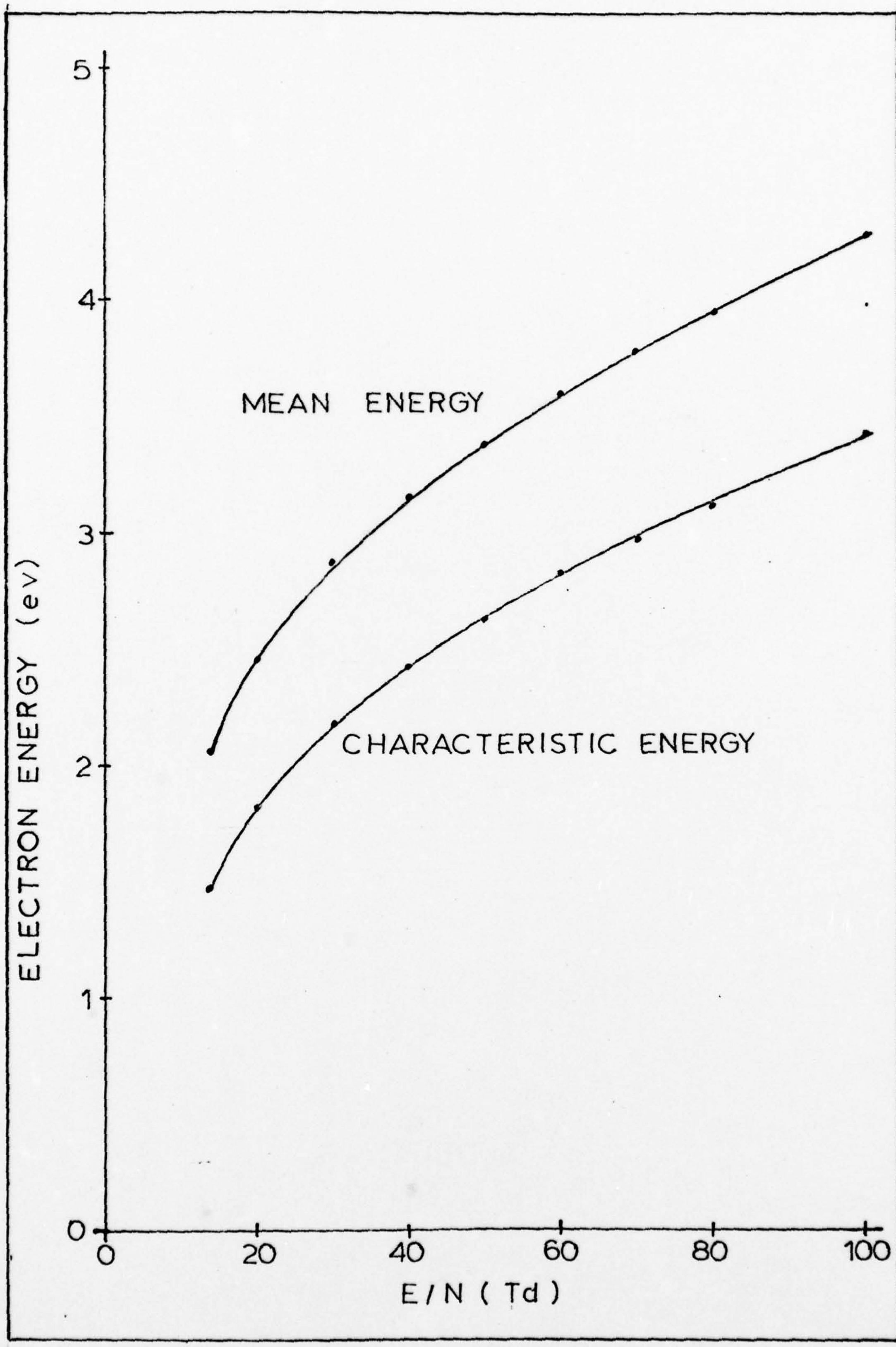

Figure 57. Mean and Characteristic Energies

the mean and characteristic energies as functions of E/N.

Figures 58 through 62 depict examples of various excitation, ionization, and attachment rates*. The examples chosen for presentation are those which were utilized later in the calculations of the plasma chemistry**.

Figure 63 is an estimate of the dissociation rate of molecular oxygen. It was determined by summing the rates associated with the pumping of the 6.0 and 8.4 electronic excitation levels. The cross sections associated with these excitations are reasonably well known; however, the physical transitions they correspond to are still in doubt. There is general agreement that the 8.4 ev cross section leads to the $B^3\Sigma_u^-$ electronic level of molecular oxygen; however, the Franck Condon principal indicates that this transition leads to a dissociative electronic-vibrational level which results in a breakup of the molecule. Both the 4.5 and 6.0 ev cross sections have been suggested to be associated with the excitation of the $c^1\Sigma_u^-$ electronic level. Of these two, the 6.0 ev cross section was postulated to lead to a dissociative level (Ref 48). Normally the $c^1\Sigma_u^-$ excitation would be represented by a single cross section. However, to separate the results of the collisions into those which would

---

*Refer to Appendix B for a further explanation of the cross sections that lead to these rates.

**Refer to Chapter IX and Appendix E for a description of the chemistry calculations.

result in excited molecules and those that would result in dissociation, the single cross section was broken into two.

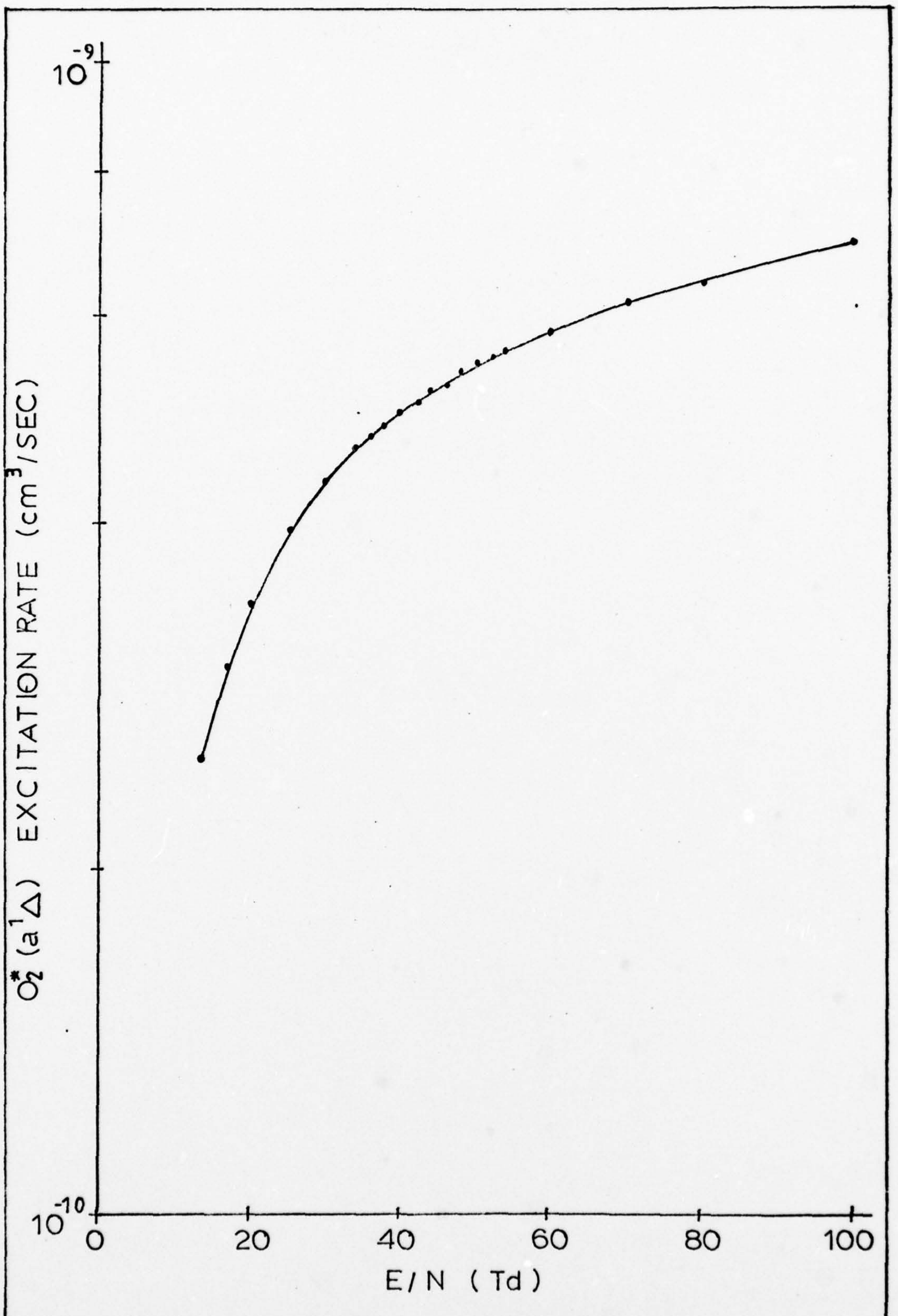

Figure 58. $0_2^*(a'\Delta)$ Excitation Rate

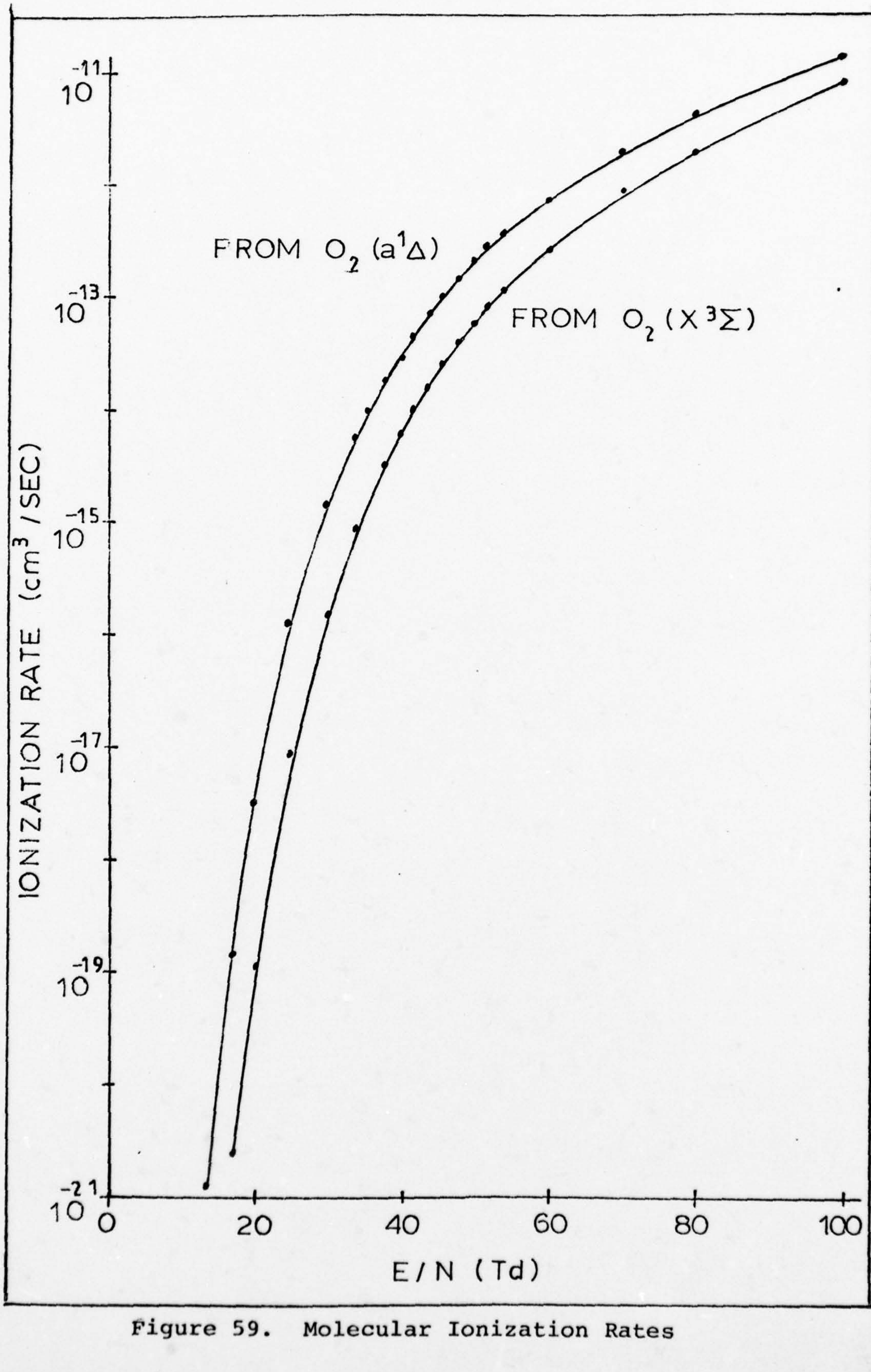

Figure 59. Molecular Ionization Rates

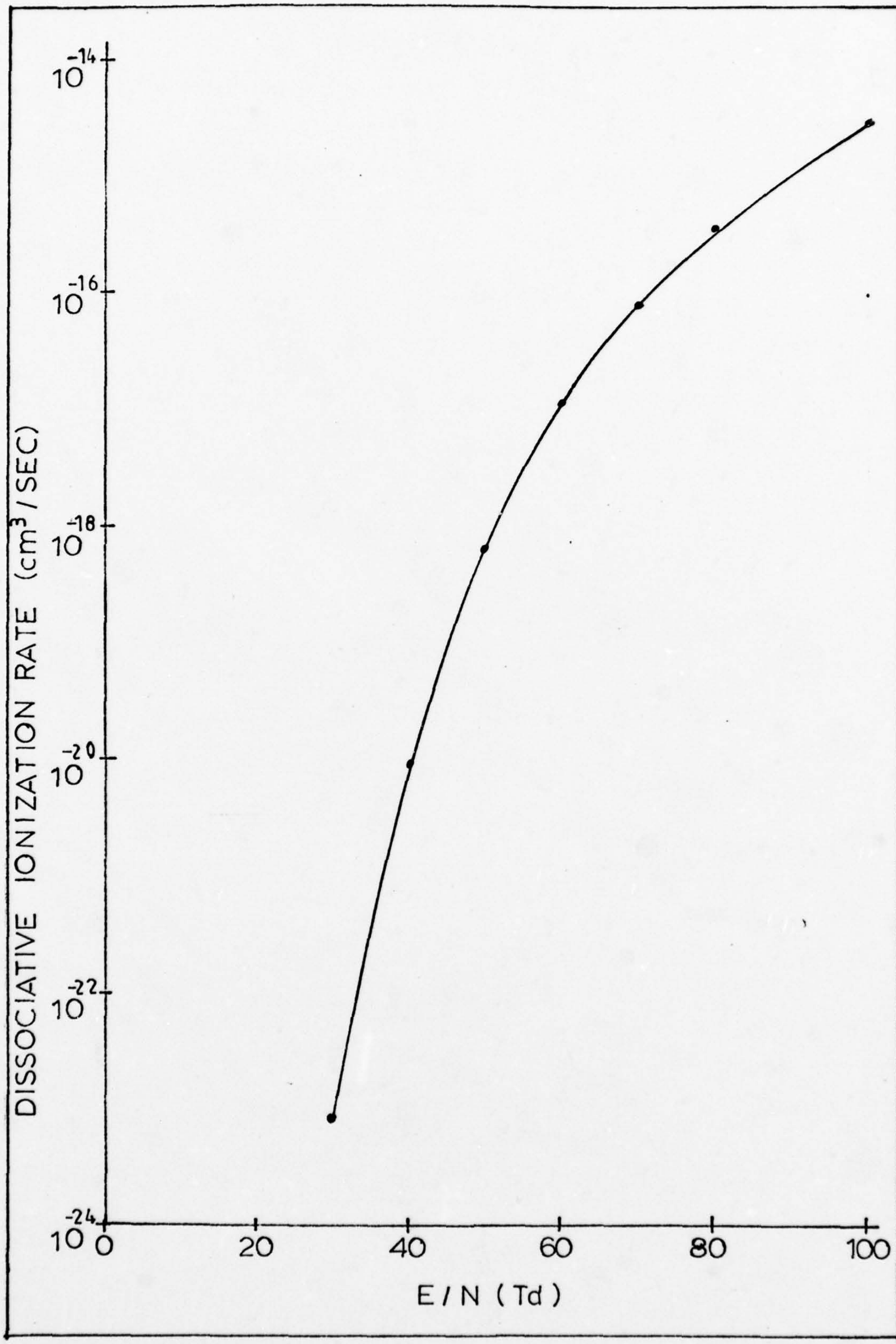

Figure 60. Dissociative Ionization Rate

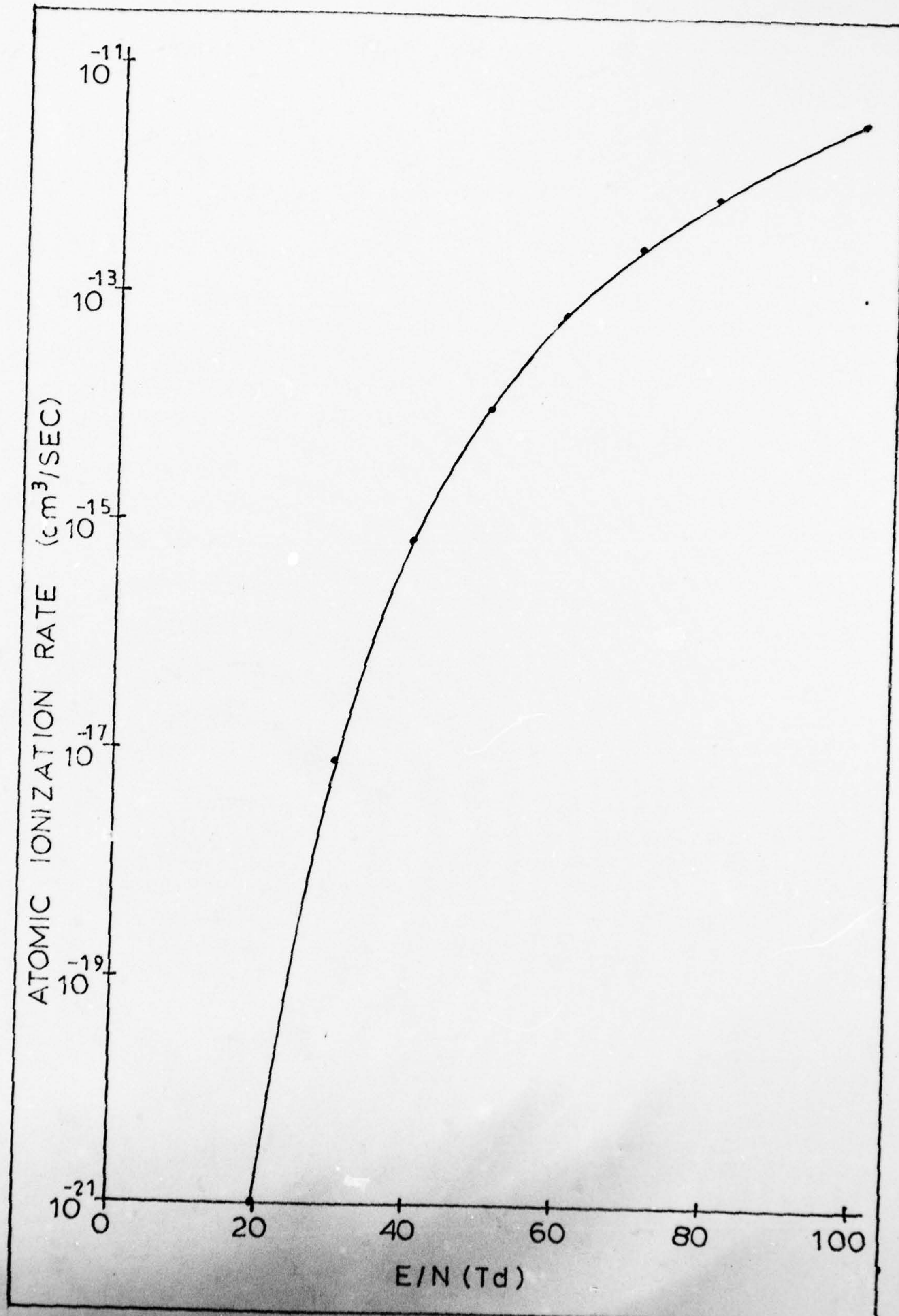

Figure 61. Atomic Ionization Rate

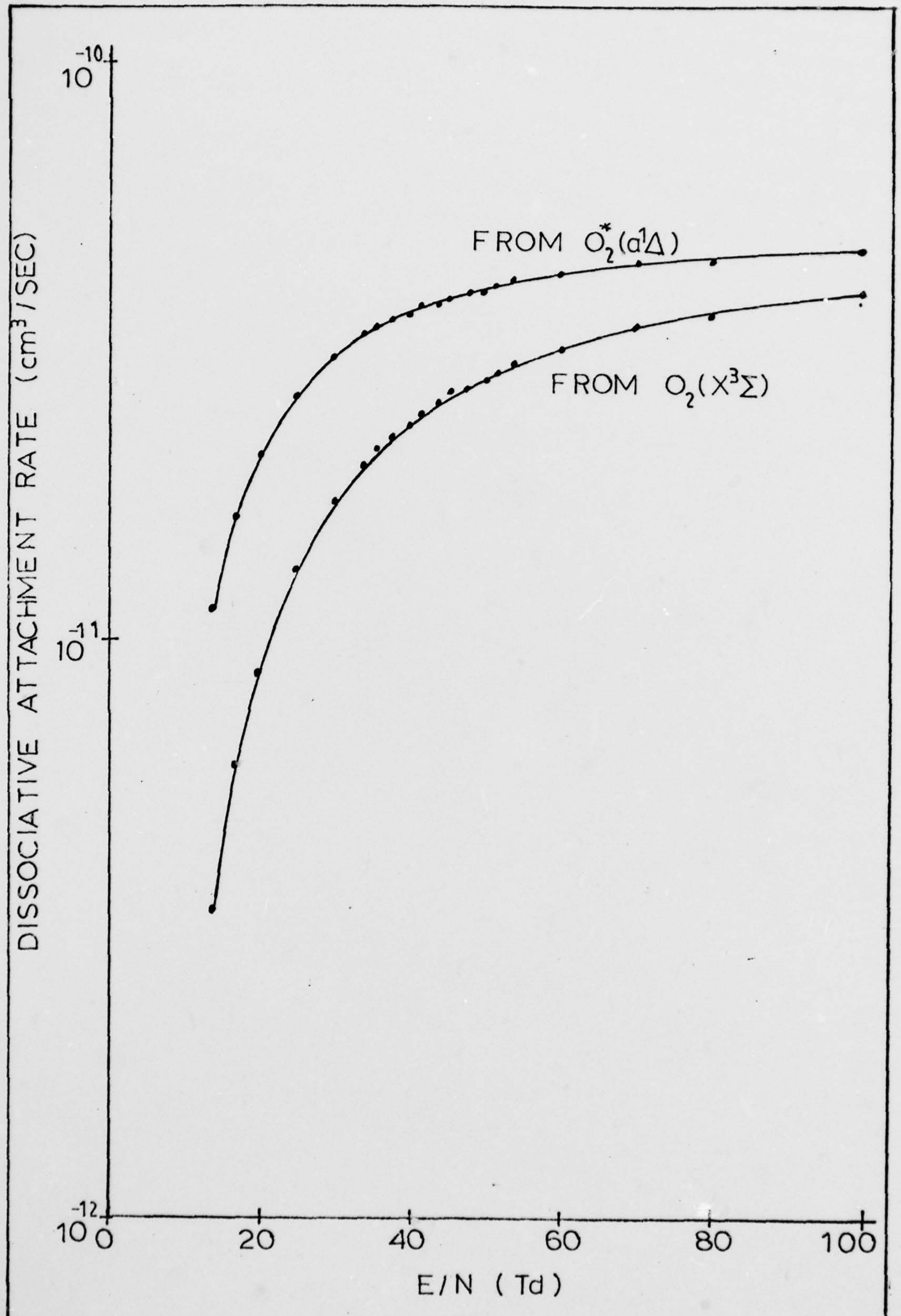

Figure 62. Dissociative Attachment Rates

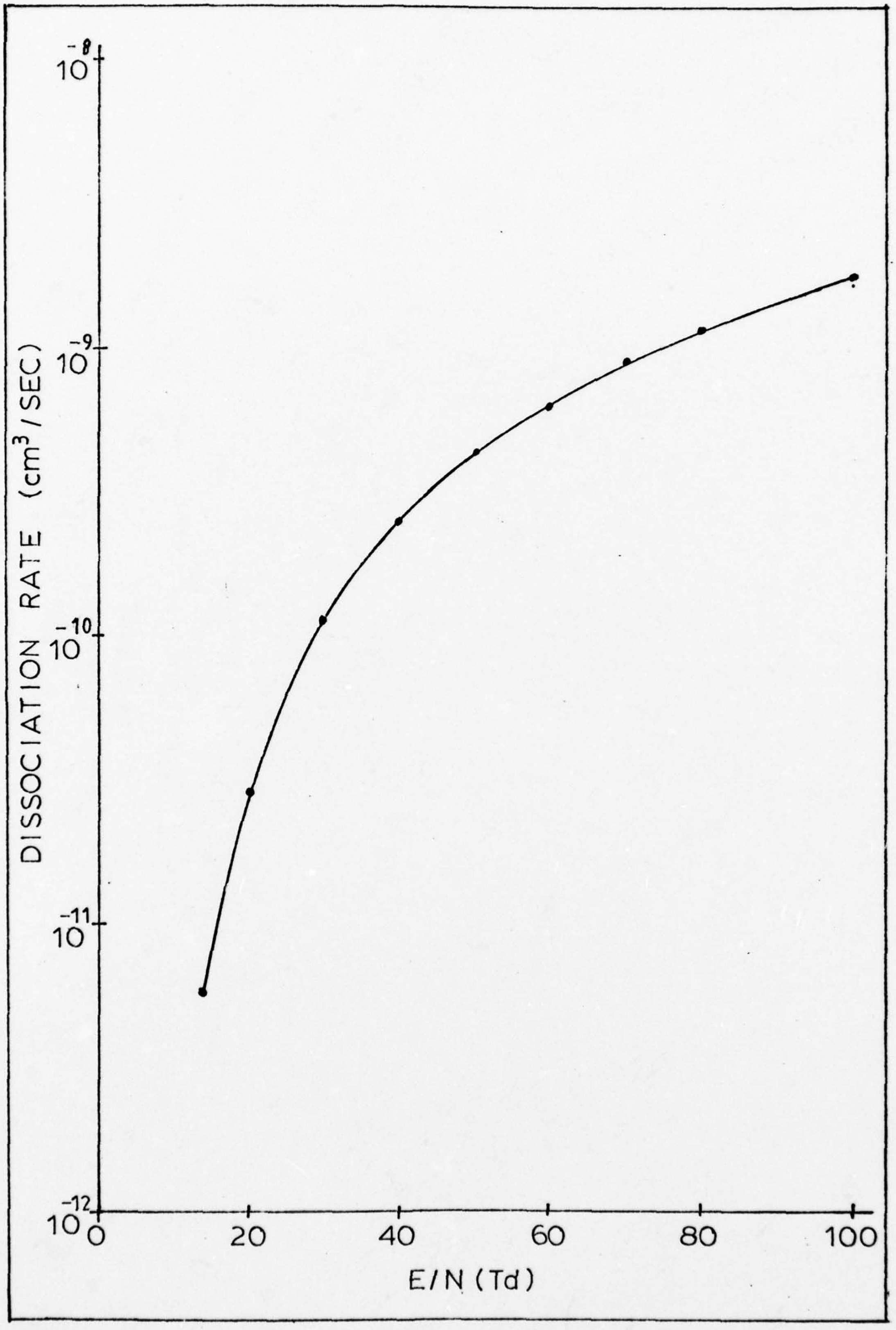

Figure 63. Dissociation Rate

IX. Plasma Chemistry

In a molecular gas plasma various physical and chemical processes occur and generate a large number of other species. Positive and negative ions are created; free electrons are generated; molecular bonds are broken down, creating atomic species and other molecules; species associate to form clusters; and species are raised in energy to various excitation levels. In order to understand the phenomena occurring in the oxygen discharge, it is important to be able to determine the concentrations of the various species and their excitation levels as functions of the applied electric field; the gas pressures, temperature, and flow; and the physical geometry. This chapter presents the results of a chemistry code, titled Chemco, which was used to calculate the species concentrations and selected excitation levels of the oxygen plasma under electrical discharge conditions corresponding to the high field experiments.

Chemco incorporated reaction rates between the various species, the transport parameters of the various species, and the effects of the discharge tube geometry. The inputs to Chemco included the initial oxygen molecular density entering the tube, N; the reduced electric field, E/N; the E/N dependent reaction rates; and the gas flow. The effects of temperature and pressure were taken into account by specifying N. The non-E/N-dependent reaction rates were taken from the open literature. The E/N-dependent rates were taken from the results of the Boltzmann Code, EED, computations*. Since EED and Chemco were not coupled, any single Chemco run was valid for only the chosen value of E/N. This limited the application of the results to the steady, or high field form, of the oxygen discharge.

Output from Chemco were various charged, neutral, and excited species densities and the effects of each of the included processes as functions of E/N and N. These outputs were used to provide additional insights into the oxygen plasma and to draw conclusions regarding the causes of the observed phenomena.

The chapter starts out with a description of the chemistry code-Chemco. This is followed by the results of a large number of calculations using the code. Some conslusions are presented with the results; however, the major conclusions are presented in Chapter X along with the conclusions from other chapters.

Chemco Description

General Approach. The basic equations of Chemco were the differential rate equations of each of the included species. These equations were simultaneously integrated as functions of time rather than being directly solved for their steady state solutions. This method was chosen because the coupled nonlinear algebraic equations that resulted

---

*See Chapter VIII.

from a steady state analysis were very difficult to solve for the number of species and degree of coupling between equations. For each run the calculations continued for a time equivalent to the residence time of the gas in the discharge tube. It was found, however, that the species concentrations for the conditions of interest reached equilibrium in a very short period of time.

Chemco is a one-dimensional code; the only dimension considered is time or the equivalent distance along the axis of the tube. The radial distributions of the species are not specifically calculated; however, assumed-radial-profile effects are taken account of in calculating the diffusion losses. Throughout the Chemco runs, total mass and charge are calculated and checked to assure conservation.

Chemco, as used, incorporated a total of 69 chemical and physical reactions between the various species. These reactions were considered to be the dominant ones over the pressure and electron density ranges of this study. Initial selection was made from a list of 130 potential reactions*. Nonutilized reactions were rejected because they either involved a species not carried in the code, had a low reaction rate in an absolute sense, had a low reaction rate relative to another channel with the same net reaction, or were determined by early Chemco runs to be insignificant.

In addition to chemical and physical reactions, Chemco

---

*See Appendix D.

includes the effects of ambipolar radial diffusion of all the charged species; radial diffusion of the neutral species with the exception of ozone, O_3; gas flow effects for all species; and axial drift effects for all charged species.

The general differential rate equation that is iteratively solved in Chemco for each of the species is:

$$\frac{dN_s}{dt} = \begin{array}{l}\text{Gains due to collisions - Losses}\\ \text{due to collisions - Diffusion}\\ \text{Losses - Flow Losses - Drift}\\ \text{Losses}\end{array} \qquad (84)$$

Species Included in Chemco. The inclusion of all possible neutral, charged and excited species present in an oxygen plasma is not practical. The number of species that can be tracked is limited by the size of the computer, the computer time available, and the current state of knowledge of the species reaction rates. Therefore, only the ten dominant neutral species and important ions present in the plasma are tracked in Chemco: O, O_2, $O_2(a'\Delta)$, O_3, e, O^-, O^-_2, O^-_3, O^+, and O^+_2.

It is well known that the oxygen molecule readily forms negative ions by attachment processes. The negative molecular ions included in Chemco are O_2^- and O_3^-. The negative atomic ion, O^-, is most readily formed by dissociative attachment; it is included in Chemco. The only positive molecular ion included is O_2^+. The observation of ionized ozone, O_3^+, has not been reported in the literature and was therefore expected to be unimportant in the ion balance;

thus, it is not included in Chemco. The positive atomic ion, O^+, is generated by direct ionization of the atom and by dissociative ionization of the molecule; it is included. Neutral atomic oxygen is predominantly produced by electron impact dissociation and dissociative attachment in the discharge; it is included in the model. Neutral ozone, O_3, is produced by several chemical reactions and has been observed to occur in the discharge; it is included in the code. The only electronically excited state included is the metastable $O_2^*(a'\Delta)$; it is produced primarily by electron collision with ground state O_2. Finally, the code includes the primary constituents: molecular oxygen and electrons.

Species Gain and Loss Processes. The gain and loss processes incorporated in Chemco for each of the included species are listed in Tables III through XXII. The letter M in the tables refers to an unspecified specie in a three-body collisional process. For reference and utilization in future studies a complete listing of all the included and nonincluded rates and their source references is presented in Appendix D.

Table III. Atomic Oxygen (O) Gains

Process Number/Symbol	Process
8	$O^- + O^+ \rightarrow 2O$
9	$O^- + O_2^+ \rightarrow O + O_2$
13	$O^- + O_3 \rightarrow O + O_3^-$
18	$e + O_3 \rightarrow O + O_2^-$
19	$e + O_2^+ \rightarrow 2O$
22	$e + O^+ + M \rightarrow O + M$
23	$O_2^- + O^+ \rightarrow O + O_2$
24	$O_3^- + O^+ \rightarrow O + O_3$
29	$O_2^- + O_2^+ \rightarrow 2O + O_2$
39	$O^+ + O_2 \rightarrow O + O_2^+$
51	$e + O^- \rightarrow O + 2e$
52	$e + O_2 \rightarrow 2O + e$
53	$e + O_2 \rightarrow O + O^-$
54	$e + O_3 \rightarrow O + O_2 + e$
55	$O_3 + O_2 \rightarrow O + 2O_2$
88	$e + O_2 \rightarrow O + O^+ + 2e$
93	$2e + O^+ \rightarrow O + e$
114	$O^- + O_2 \rightarrow O + O_2^-$
119	$O_2^* + O_3 \rightarrow O + 2O_2$
124	$O_2^* + O^- \rightarrow O + O_2^-$
136	$O_2^* + O^+ \rightarrow O + O_2^+$
138	$e + O_2^* \rightarrow 2O + e$
139	$e + O_2^* \rightarrow O + O^-$

Table III. Atomic Oxygen (0) Gains (Continued)

Process Number/Symbol	Process
140	$e + O_2^* \rightarrow O + O^+ + 2e$
$L_{DO}{}^-$	Diffusion Losses of O^-
$L_{DO}{}^+$	Diffusion Losses of O^+
$L_{MO}{}^-$	Drift Losses of O^-

Table IV. Atomic Oxygen (O) Losses

Process Number/Symbol	Process
1	$O + e \rightarrow O^+ + 2e$
3	$O + O^- \rightarrow O_2 + e$
5	$O + e \rightarrow O^-$
7	$O + O_2 + e \rightarrow O^- + O_2$
16	$O + O_2^- \rightarrow O_3 + e$
26	$O + O_2^- \rightarrow O^- + O_2$
28	$2O + O_2 \rightarrow 2O_2$
30	$O + O^+ + M \rightarrow O_2^+ + M$
31	$2O + M \rightarrow O_2 + M$
32	$O + 2O_2 \rightarrow O_3 + O_2$
33	$2O + O_2 \rightarrow O_3 + O$
34	$O + O_3 \rightarrow 2O_2$
35	$O + O_3^- \rightarrow O_2^- + O_2$
104	$O + O_3 \rightarrow O_2^* + O_2$
123	$O + O_3^- \rightarrow 2O_2 + e$
127	$O + O_2^* + e \rightarrow O^- + O_2^*$
132	$2O + O_2^* \rightarrow O_2 + O_2^*$
134	$2O + O_2^* \rightarrow O_3 + O$
L_{DO}	Diffusion Losses
L_{VO}	Flow Losses

Table V. Molecular Oxygen (O_2) Gains

Process Number/Symbol	Process
3	$O^- + O \rightarrow O_2 + e$
6	$e + O_3 \rightarrow O_2 + O^-$
9	$O^- + O_2^+ \rightarrow O_2 + O$
11	$O^- + O^+ + O \rightarrow O_2 + O$
23	$O_2^- + O^+ \rightarrow O_2 + O$
26	$O_2^- + O \rightarrow O_2 + O^-$
28	$O_2 + 2O \rightarrow 2O_2$
29	$O_2^- + O_2^+ \rightarrow O_2 + 2O$
31	$2O + M \rightarrow O_2 + M$
34	$O + O_3 \rightarrow 2O_2$
35	$O + O_3^- \rightarrow O_2 + O_2^-$
36	$O_2 + O_2^- \rightarrow 2O_2 + e$
38	$O_2^+ + M + e \rightarrow O_2 + M$
43	$O_2^+ + O_2^- \rightarrow 2O_2$
45	$O_2^- + O_3 \rightarrow O_2 + O_3^-$
54	$e + O_3 \rightarrow O_2 + O + e$
55	$O_2 + O_3 \rightarrow 2O_2 + O$
71	$O_2 + O_2^* \rightarrow 2O_2$
82	$2O_2^* \rightarrow O_2 + O_2^{**}$
94	$O_2^+ + 2e \rightarrow O_2 + e$
100	$O_2^* \rightarrow O_2$
104	$O + O_3 \rightarrow O_2 + O_2^*$
105	$e + O_2^* \rightarrow O_2 + e$

Table V. Molecular Oxygen (O_2) Gains (Continued)

Process Number/Symbol	Process
107	$O_2^* + O \rightarrow O_2 + O$
108	$O_2^* + O_3 \rightarrow O_2 + O_3$
118	$O_2^- + O_2^* \rightarrow 2O_2 + e$
119	$O_2^* + O_3 \rightarrow 2O_2 + O$
123	$O_3^- + O \rightarrow 2O_2 + e$
132	$2O + O_2^* \rightarrow O_2 + O_2^*$
$L_{DO_2^+}$	Diffusion Losses of O_2^+
$L_{DO_2^-}$	Diffusion Losses of O_2^-
$L_{DO_2^*}$	Diffusion Losses of O_2 (a'Δ)
$L_{VO_2^*}$	Flow Losses of O_2(a'Δ)
$L_{MO_2^+}$	Drift Losses of O_2^+
$L_{MO_2^-}$	Drift Losses of O_2^-
L_{VO}	Flow Losses of O
L_{MO^+}	Drift Losses of O^+
L_{VO_3}	Flow Losses of O_3
L_{DO}	Diffusion Losses of O

Table XI. Molecular Oxygen (O_2) Losses

Process Number/Symbol	Process
2	$O_2 + e \rightarrow O_2^+ + 2e$
4	$O_2 + O^- \rightarrow O_3 + e$
15	$O_2 + O^- + M \rightarrow O_3^- + M$
21	$O_2 + O + e \rightarrow O_2^- + O$
32	$2O_2 + O \rightarrow O_2 + O_3$
33	$O_2 + 2O \rightarrow O_3 + O$
39	$O_2 + O^+ \rightarrow O_2^+ + O$
41	$2O_2 + e \rightarrow O_2 + O_2^-$
52	$O_2 + e \rightarrow 2O + e$
53	$O_2 + e \rightarrow O^- + O$
88	$O_2 + e \rightarrow O + O^+ + 2e$
112	$O_2 + e \rightarrow O_2^* + e$
114	$O_2 + O^- \rightarrow O^- + O$
137	$O_2 + O_2^* + e \rightarrow O_2^- + O_2^*$

Table VII. Ozone (O_3) Gains

Process Number/Symbol	Process
4	$O^- + O_2 \rightarrow O_3 + e$
12	$O^- + O_2^+ + M \rightarrow O_3 + M$
16	$O_2^- + O \rightarrow O_3 + e$
24	$O_3^- + O^+ \rightarrow O_3 + O$
32	$O + 2O_2 \rightarrow O_3 + O_2$
33	$2O + O_2 \rightarrow O_3 + O$
117	$O^- + O_2^* \rightarrow O_3 + e$
134	$2O + O_2^* \rightarrow O_3 + O$
$L_{DO_3^-}$	Diffusion Losses of O_3^-
$L_{MO_3^-}$	Drift Losses of O_3^-

Table VIII. Ozone (O_3) Losses

Process Number/Symbol	Process
6	$O_3 + e \rightarrow O^- + O_2$
13	$O_3 + O^- \rightarrow O_3^- + O$
18	$O_3 + e \rightarrow O_2^- + O$
34	$O_3 + O \rightarrow 2O_2$
45	$O_3 + O_2^- \rightarrow O_3^- + O_2$
54	$O_3 + e \rightarrow O_2 + O + e$
55	$O_3 + O_2 \rightarrow 2O_2 + O$
104	$O_3 + O \rightarrow O_2^* + O_2$
119	$O_3 + O_2^* \rightarrow 2O_2 + O$
L_{VO_3}	Flow Losses

Table IX. Electron (e) Gains

Process Number/Symbol	Process
1	$e + O \rightarrow 2e + O^+$
2	$e + O_2 \rightarrow 2e + O_2^+$
3	$O^- + O \rightarrow e + O_2$
4	$O^- + O_2 \rightarrow e + O_3$
16	$O_2^- + O \rightarrow e + O_3$
36	$O_2^- + O_2 \rightarrow e + 2O_2$
51	$e + O^- \rightarrow 2e + O$
88	$e + O_2 \rightarrow 2e + O + O^+$
117	$O^- + O_2^* \rightarrow e + O_3$
118	$O_2^- + O_2^* \rightarrow e + 2O_2$
123	$O_3^- + O \rightarrow e + 2O_2$
126	$e + O_2^* \rightarrow 2e + O_2^+$
140	$e + O_2^* \rightarrow 2e + O + O^+$
L_{MO^-}	Drift Losses of O^-
$L_{MO_2^-}$	Drift Losses of O_2^-
$L_{MO_3^-}$	Drift Losses of O_3^-

Table X. Electron (e) Losses

Process Number/Symbol	Process
5	$e + O \rightarrow O^-$
6	$e + O_3 \rightarrow O^- + O_2$
7	$e + O + O_2 \rightarrow O^- + O_2$
18	$e + O_3 \rightarrow O_2^- + O$
19	$e + O_2^+ \rightarrow 2O$
21	$e + O + O_2 \rightarrow O_2^- + O$
22	$e + O^+ + M \rightarrow O + M$
38	$e + O_2^+ + M \rightarrow O_2 + M$
41	$e + 2O_2 \rightarrow O_2^- + O_2$
53	$e + O_2 \rightarrow O + O^-$
93	$2e + O^+ \rightarrow e + O$
94	$2e + O_2^+ \rightarrow e + O_2$
127	$e + O + O_2^* \rightarrow O^- + O_2^*$
130	$e + O + O_2^* \rightarrow O_2^- + O$
137	$e + O_2 + O_2^* \rightarrow O_2^- + O_2^*$
139	$e + O_2^* \rightarrow O^- + O$
141	$e + O_2^* + O_2 \rightarrow O_2^- + O_2$
142	$e + O_2^* + O_2^* \rightarrow O_2^- + O_2^*$
L_{De}	Diffusion Losses
L_{MO^+}	Drift Losses of O^+
$L_{MO_2^+}$	Drift Losses of O_2^+

Table XI. Atomic Negative Ion (O^-) Gains

Process Number/Symbol	Process
5	$e + O \rightarrow O^-$
6	$e + O_3 \rightarrow O^- + O_2$
7	$e + O + O_2 \rightarrow O^- + O_2$
26	$O_2^- + O \rightarrow O^- + O_2$
53	$e + O_2 \rightarrow O^- + O$
127	$e + O + O_2^* \rightarrow O^- + O_2^*$
139	$e + O_2^* \rightarrow O^- + O$

Table XII. Atomic Negative Ion (O^-) Losses

Process Number/Symbol	Process
3	$O^- + O \rightarrow O_2 + e$
4	$O^- + O_2 \rightarrow O_3 + e$
8	$O^- + O^+ \rightarrow 2O$
9	$O^- + O_2^+ \rightarrow O + O_2$
11	$O^- + O^+ + O \rightarrow O_2 + O$
12	$O^- + O_2^+ + M \rightarrow O_3 + M$
13	$O^- + O_3 \rightarrow O_3^- + O$
15	$O^- + O_2 + M \rightarrow O_3^- + M$
51	$O^- + e \rightarrow O + 2e$
114	$O^- + O_2 \rightarrow O_2^- + O$
117	$O^- + O_2^* \rightarrow O_3 + e$
124	$O^- + O_2^* \rightarrow O_2^- + O$
L_{DO^-}	Diffusion Losses
L_{MO^-}	Drift Losses
L_{VO^-}	Flow Losses

Table XIII. Molecular Negative Ion (O_2^-) Gains

Process Number/Symbol	Process
18	$e + O_3 \rightarrow O_2^- + O$
21	$e + O + O_2 \rightarrow O_2^- + O$
35	$O + O_3^- \rightarrow O_2^- + O_2$
41	$e + 2O_2 \rightarrow O_2^- + O_2$
114	$O^- + O_2 \rightarrow O_2^- + O$
124	$O^- + O_2^* \rightarrow O_2^- + O$
130	$e + O + O_2^* \rightarrow O_2^- + O$
137	$e + O_2 + O_2^* \rightarrow O_2^- + O_2^*$
141	$e + O_2 + O_2^* \rightarrow O_2^- + O_2$
142	$e + 2O_2^* \rightarrow O_2^- + O_2^*$

Table XIV. Molecular Negative Ion (O_2^-) Losses

Process Number/Symbol	Process
16	$O_2^- + O \rightarrow O_3 + e$
23	$O_2^- + O^+ \rightarrow O_2 + O$
26	$O_2^- + O \rightarrow O^- + O_2$
29	$O_2^- + O_2^+ \rightarrow O_2 + 2O$
36	$O_2^- + O_2 \rightarrow 2O_2 + e$
43	$O_2^- + O_2^+ \rightarrow 2O_2$
45	$O_2^- + O_3 \rightarrow O_3^- + O_2$
118	$O_2^- + O_2^* \rightarrow 2O_2 + e$
$L_{DO_2^-}$	Diffusion Losses
$L_{MO_2^-}$	Drift Losses
$L_{VO_2^-}$	Flow Losses

Table XV. Ozone Negative Ion (O_3^-) Gains

Process Number/Symbol	Process
13	$O^- + O_3 \rightarrow O_3^- + O$
15	$O^- + O_2 + M \rightarrow O_3^- + M$
45	$O_2^- + O_3 \rightarrow O_3^- + O_2$

Table XVI. Ozone Negative Ion (O_3^-) Losses

Process Number/Symbol	Process
24	$O_3^- + O^+ \rightarrow O_3 + O$
35	$O_3^- + O \rightarrow O_2^- + O_2$
123	$O_3^- + O \rightarrow 2O_2 + e$
$L_{DO_3^-}$	Diffusion Losses
$L_{MO_3^-}$	Drift Losses
$L_{VO_3^-}$	Flow Losses

Table XVII. Atomic Positive Ion (O^+) Gains

Process Number/Symbol	Process
1	$e + O \rightarrow O^+ + 2e$
88	$e + O_2 \rightarrow O^+ + O + 2e$
140	$e + O_2^* \rightarrow O^+ + O + 2e$

Table XVIII. Atomic Positive Ion (O^+) Losses

Process Number/Symbol	Process
8	$O^+ + O^- \rightarrow 2O$
11	$O^+ + O^- + O \rightarrow O_2 + O$
22	$O^+ + e + M \rightarrow O + M$
23	$O^+ + O_2^- \rightarrow O_2 + O$
24	$O^+ + O_3^- \rightarrow O_3 + O$
30	$O^+ + O + M \rightarrow O_2^+ + M$
39	$O^+ + O_2 \rightarrow O_2^+ + O$
93	$O^+ + 2e \rightarrow O + e$
136	$O^+ + O_2^* \rightarrow O_2^+ + O$
L_{DO^+}	Diffusion Losses
L_{MO^+}	Drift Losses
L_{VO^+}	Flow Losses

Table XIX. Molecular Positive Ion (O_2^+) Gains

Process Number/Symbol	Process
2	$e + O_2 \rightarrow O_2^+ + 2e$
30	$O^+ + O + M \rightarrow O_2^+ + M$
39	$O^+ + O_2 \rightarrow O_2^+ + O$
126	$e + O_2^* \rightarrow O_2^+ + 2e$
136	$O^+ + O_2^* \rightarrow O_2^+ + O$

Table XX. Molecular Positive Ion (O_2^+) Losses

Process Number/Symbol	Process
9	$O_2^+ + O^- \rightarrow O + O_2$
12	$O_2^+ + O^- + M \rightarrow O_3 + M$
19	$O_2^+ + e \rightarrow 2O$
29	$O_2^+ + O_2^- \rightarrow O_2 + 2O$
38	$O_2^+ + e + M \rightarrow O_2 + M$
43	$O_2^+ + O_2^- \rightarrow 2O_2$
94	$O_2^+ + 2e \rightarrow O_2 + e$
$L_{DO_3^+}$	Diffusion Losses
$L_{MO_2^+}$	Drift Losses
$L_{VO_2^+}$	Flow Losses

Table XXI. Molecular Metastable (O_2^* (a'Δ)) Gains

Process Number/Symbol	Process
104	$O + O_3 \rightarrow O_2^* + O_2$
112	$e + O_2 \rightarrow O_2^* + e$

Table XXII. Molecular Metastable ($O_2^*(a'\Delta)$) Losses

Process Number/Symbol	Process
71	$O_2^* + O_2 \rightarrow 2O_2$
82	$2O_2^* \rightarrow O_2^* + O_2$
100	$O_2^* \rightarrow O_2$
105	$O_2^* + e \rightarrow O_2 + e$
107	$O_2^* + O \rightarrow O_2 + O$
108	$O_2^* + O_3 \rightarrow O_2 + O_3$
117	$O_2^* + O^- \rightarrow O_3 + e$
118	$O_2^* + O_2^- \rightarrow 2O_2 + e$
119	$O_2^* + O_3 \rightarrow 2O_2 + O$
124	$O_2^* + O^- \rightarrow O_2^- + O$
126	$O_2^* + e \rightarrow O_2^+ + 2e$
130	$O_2^* + O + e \rightarrow O_2^- + O$
134	$O_2^* + 2O \rightarrow O_3 + O$
136	$O_2^* + O^+ \rightarrow O_2^+ + O$
138	$O_2^* + e \rightarrow 2O + e$
139	$O_2^* + e \rightarrow O + O^-$
140	$O_2^* + e \rightarrow O^+ + O + 2e$
141	$O_2^* + O_2 + e \rightarrow O_2^- + O_2$
142	$2O_2^* + e \rightarrow O_2^* + O_2^-$
$L_{DO_2^*}$	Diffusion Losses
$L_{VO_2^*}$	Flow Losses

Diffusion Losses of the Charged Species. In a plasma in which there is a multiplicity of charged species of differing mobilities and diffusion coefficients, there is an initial tendency for these species to diffuse out of the plasma at differing rates. The charge separation that results sets up an electric field which retards the diffusion of the faster diffusing species and enhances the diffusion of the slower species. The resulting coupling, which tends to cause all species to diffuse at some intermediate rate, is termed ambipolar diffusion. Classical ambipolar diffusion theory treats only two species: electrons and a single specie of positive ions. For the oxygen plasma a multiplicity of species must be considered, including electrons and both negative and positive ions: e, O^-, O_2^-, O_3^-, O^+, and O_2^+. A three-species solution to the coupled ambipolar diffusion equations, as derived by Thompson, is used for the chemistry code* (Ref 24:818-819). In order to utilize Thompson's solution, the five ionic species carried in Chemco were reduced to two by combining all of the negative ions into an averaged negative ion and all of the positive ions into an averaged positive ion**.

---

*For this study Thompson's derivation was accepted as presented in the reference. Attempts at an independent derivation were unsuccessful.

**As will be shown later the mobilities of the different ions are sufficiently close together to allow this approximation to be reasonable.

For any species, S, the radial diffusion equation is (Ref 8:187):

$$\bar{\Gamma}_s = D_s \cdot \overline{\nabla N}_s + N_s \cdot \mu_s \cdot \bar{E} \tag{85}$$

where $\bar{\Gamma}_s$ is the flux density,

D_s is the diffusion coefficient;

N_s is the number density;

μ_s is the mobility;

$\bar{E}$ is the space charge electric field.

Charge neutrality within the plasma requires that:

$$N_+ = N_- + N_e \tag{86}$$

while at the boundary:

$$\bar{\Gamma}_+ = \bar{\Gamma}_- + \bar{\Gamma}_e \tag{87}$$

Combining 85, 86, and 87 so as to eliminate the electric field term:

$$\bar{\Gamma}_s = -D_{AS} \cdot \overline{\nabla N}_s \tag{88}$$

where D_{AS} are the ambipolar diffusion coefficients, defined as:

$$D_{A+} = D_+ \cdot \left[\frac{(1+\gamma+2\cdot\alpha\cdot\gamma) \cdot \left(1 + \frac{\alpha\cdot\mu_-}{\mu_e}\right)}{(1+\alpha\cdot\gamma)\cdot\left\{1+\mu_+\cdot\left(\frac{1+\alpha}{\mu_e}\right) + \frac{\alpha\cdot\mu_-}{\mu_e}\right\}} \right] \tag{89}$$

$$D_{A-} = D_+ \cdot \left[\left(\frac{\mu_-}{\gamma \cdot \mu_e} \right) \cdot \frac{(1+\gamma+2\cdot\alpha\cdot\gamma)}{\left\{ 1 + \frac{\mu_+ \cdot (1+\alpha)}{\mu_e} + \frac{\alpha \cdot \mu_-}{\mu_e} \right\}} \right] \quad (90)$$

$$D_{Ae} = D_+ \cdot \left[\frac{1+\gamma+2\cdot\alpha\cdot\gamma}{1 + \frac{\mu_+ \cdot (1+\alpha)}{\mu_e} + \frac{\alpha \cdot \mu_-}{\mu_e}} \right] \quad (91)$$

α and γ are defined:

$$\alpha = \frac{N_-}{N_e} \quad (92)$$

and:

$$\gamma = \frac{\mathcal{E}_e}{\mathcal{E}_i} \quad (93)$$

where: $\mathcal{E}_e$ is the electron characteristic energy in ev.

$\mathcal{E}_i$ is the ion temperature in ev*.

For a T_i of $300^{\circ}K$: $\mathcal{E}_i = 3.88 \times 10^{-2}$ ev

and:

$$\gamma = 25.8 \cdot \mathcal{E}_e \quad (94)$$

The total positive ion density consists of the sum of the 0^+

---

*All ions are assumed to be at the same temperature.

AD-A066 196 AIR FORCE INST OF TECH WRIGHT-PATTERSON AFB OHIO SCH--ETC F/G 7/2
DISCHARGE PROCESSES IN THE OXYGEN PLASMA.(U)
DEC 78 J W DETTMER

UNCLASSIFIED AFIT/DS/PH/78-3 NL

3 OF 4

AD
A066196

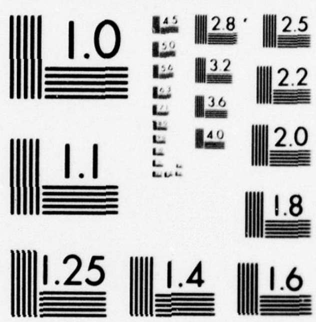

MICROCOPY RESOLUTION TEST CHART

NATIONAL BUREAU OF STANDARDS-1963-A

and O_2^+ densities:

$$N_+ = N_{O_2^+} + N_{O^+} \tag{95}$$

Similarly, the total negative ion density is described as:

$$N_- = N_{O^-} + N_{O_2^-} + N_{O_3^-} \tag{96}$$

Since ion mobility is the dominant factor in determining the diffusion rate, it is the factor that is averaged by weighting the mobilities of the constituents of N^+ and N^-:

$$\mu_+ = \frac{\mu_{O^+} \cdot N_{O^+} + \mu_{O_2^+} \cdot N_{O_2^+}}{N_+} \tag{97}$$

$$\mu_- = \frac{\mu_{O^-} \cdot N_{O^-} + \mu_{O_2^-} \cdot N_{O_2^-} + \mu_{O_3^-} \cdot N_{O_3^-}}{N_-} \tag{98}$$

For each of the basic species the mobility is (Ref 49:6):

$$\mu_s = \frac{760 \cdot T}{273 \cdot P} \cdot \mu_{os} \tag{99}$$

Where μ_{os} is the reduced mobility, T and P are the temperature and pressure of the background gas in ^oK and Torr respectively. In terms of the number density of the background gas, equation 99 becomes:

$$\mu_s = \frac{2.69 \times 10^{19}}{N} \cdot \mu_{os} \tag{100}$$

where N is the background gas density in CM^{-3}. For oxygen ions in their own background gas (Ref 50:477-487):

$$\mu_{oo^-} = 3.20 \ CM^2 \ Volt^{-1} \ SEC^{-1}$$

$$\mu_{oo_2^-} = 2.16 \ CM^2 \ Volt^{-1} \ SEC^{-1}$$

$$\mu_{oo_2^+} = 2.24 \ CM^2 \ Volt^{-1} \ SEC^{-1}$$

$$\mu_{oo_3^-} = 2.55 \ CM^2 \ Volt^{-1} \ SEC^{-1}$$

The mobility of the 0^+ ions is not listed. For this study it was assumed to have the same value as the 0^- ions*. Combining the reduced mobility values with equations 97, 98, and 99:

$$\mu_+ = \frac{2.69 \times 10^{19}}{N \cdot N_+} \cdot \left(3.2 \cdot N_{O^+} + 2.24 \cdot N_{O_2^+}\right) \quad (101)$$

$$\mu_- = \frac{2.69 \times 10^{19}}{N \cdot N_-} \cdot \left(3.2 \cdot N_{O^-} + 2.16 \cdot N_{O_2^-} + 2.55 \cdot N_{O_3^-}\right) \quad (102)$$

The electron mobility, μ_e, was determined by the Boltzmann equation code (EED) and was read into Chemco as a function of E/N.

The averaged diffusion coefficient is related to the

---

*This was a reasonable assumption since reduced mobility is inversely proportional to the mass of the ion and its collision cross section with the background gas, both of which should be approximately the same for the O^- and 0^+ ions.

averaged mobility by the Einstein relation (Ref 8:186):

$$D_S = \frac{\mu_S \cdot k \cdot T_S}{q} \tag{103}$$

For ion temperatures of $300^{\circ}K$:

$$D_{\pm} = 2.59 \times 10^{-2} \cdot \mu_{\pm} \tag{104}$$

The diffusion loss rate for the averaged charged species is a function of the ambipolar diffusion coefficients calculated in the previous paragraphs and of the radial density profiles of the species. For the averaged ionic species the radial density profiles were assumed to be zero order Bessel functions. The assumption matches closely the experimental results reported by Thompson (Ref 20:514).

$$N_{\pm}(r) = N_{0\pm} \cdot J_0\left\{\frac{2.4 \cdot r}{R_0}\right\} \tag{105}$$

where $N_{0\pm}$ is the centerline density. The diffusion loss, L_{DS}, at the wall, per unit length, was calculated from:

$$L_{D\pm} = -\int_0^1\int_0^{2\pi} D_{A\pm} \cdot \frac{\partial N_{\pm}(r)}{\partial r} \cdot r \cdot d\Theta \cdot dz \tag{106}$$

evaluated at r = Ro:

$$L_{D\pm} = -2 \cdot \pi \cdot D_{A\pm} \cdot r \cdot \frac{\partial}{\partial r}\left[N_{o\pm} \cdot J_o\left\{\frac{2.4 \cdot r}{R_o}\right\}\right]\Bigg|_{r=R_o} \qquad (107)$$

$$L_{D\pm} = -2 \cdot \pi \cdot D_{A\pm} \cdot R_o \cdot \left[\frac{-2.4 \cdot N_{o\pm}}{R_o} \cdot J_1\{2.4\}\right] \qquad (108)$$

$$L_{D\pm} = 7.84 \cdot D_{A\pm} \cdot N_{o\pm} \qquad (109)$$

The mean, averaged ion density, $\langle N \rangle_{\pm}$, is related to the centerline density, $N_{o\pm}$, by:

$$\langle N \rangle_{\pm} = \frac{1}{\pi \cdot R_o^2} \cdot \int_0^{R_o} N_{o\pm} \cdot J_o\left\{\frac{2.4 \cdot r}{R_o}\right\} \cdot 2 \cdot \pi \cdot r \cdot dr \qquad (110)$$

$$\langle N \rangle_{\pm} = 0.434 \cdot N_{o\pm} \qquad (111)$$

The loss rates for the ionic species were assumed to be related to that of the averaged ions by:

$$L_{DS} = \frac{\mu_s}{\mu_{\pm}} \cdot L_{D\pm} \qquad (112)$$

The averaged loss rate from the volume is:

$$\langle L_D \rangle_s = \frac{1}{\pi \cdot R_o^2} \cdot L_{DS} \tag{113}$$

Combining equations 100, 109, 111, 112 and 113:

$$\langle L_D \rangle_{O^+} = \frac{5.48 \times 10^{20}}{N \cdot \mu_+} \cdot D_{A+} \cdot \langle N \rangle_{O^+} \tag{114}$$

$$\langle L_D \rangle_{O_2^+} = \frac{3.84 \times 10^{20}}{N \cdot \mu_+} \cdot D_{A+} \cdot \langle N \rangle_{O_2^+} \tag{115}$$

$$\langle L_D \rangle_{O^-} = \frac{5.48 \times 10^{20}}{N \cdot \mu_-} \cdot D_{A-} \cdot \langle N \rangle_{O^-} \tag{116}$$

$$\langle L_D \rangle_{O_2^-} = \frac{3.7 \times 10^{20}}{N \cdot \mu_-} \cdot D_{A-} \cdot \langle N \rangle_{O_2^-} \tag{117}$$

$$\langle L_D \rangle_{O_3^-} = \frac{4.37 \times 10^{20}}{N \cdot \mu_-} \cdot D_{A-} \cdot \langle N \rangle_{O_3^-} \tag{118}$$

The electron radial density profile varies from generally Bessel for small values of α to uniform with a rapid drop-off near the wall for large values of α (Ref 24:819-820). This functional relationship in the vicinity of the walls cannot be approximated analytically. Therefore, the electron diffusion losses are determined by assuming a zero net current flow to the wall.

$$\langle L_D \rangle_e = \langle L_D \rangle_{O^+} + \langle L_D \rangle_{O_2^+} - \langle L_D \rangle_{O^-} - \langle L_D \rangle_{O_2^-} - \langle L_D \rangle_{O_3^-} \quad (119)$$

<u>Diffusion Losses of the Neutral Species</u>. The net flux of the neutral species to the wall is (Ref 51:19):

$$\Gamma_s = \frac{R_{ws} \cdot N_s \cdot \langle c \rangle_s}{4 \cdot (1 - \frac{R_{ws}}{2})} \quad (120)$$

where Rws is the deactivation or recombination coefficient and $\langle c \rangle_s$ is the mean speed of the species.

$$\langle c \rangle_s = \left(\frac{8 \cdot k \cdot T_s}{\pi \cdot m_s} \right)^{\frac{1}{2}} \quad (121)$$

The average loss per unit volume is related to the net flux by:

$$\langle L_D \rangle_s = \frac{2 \cdot \pi \cdot R_o}{\pi \cdot R_o^2} \cdot \Gamma_s \quad (122)$$

For $O_2^*(a'\Delta)$ at 300^oK*:

$$R_{wO_2^*} = 2 \times 10^{-5} \; SEC^{-1}$$

---

*Refer to process number 73 in Appendix D for source reference.

$$\langle C \rangle_{O_2^*} = 4.46 \times 10^4 \ \frac{CM}{SEC}$$

Therefore: $$\langle L_D \rangle_{O_2^*} = 0.469 \cdot N_{O_2^*} \qquad (123)$$

For 0 at 300°K:

$$R_{WO} = 10^{-4}\ SEC^{-1} \ *$$

$$\langle C \rangle_{O} = 6.3 \times 10^4 \ \frac{CM}{SEC}$$

Therefore: $$\langle L_D \rangle_{O} = 3.32 \cdot N_O \qquad (124)$$

Flow and Drift Losses. Since the gas was flowing through the tube during the experiment, there was a loss of all the species due to the flow. Also, the ionic species drifted in the electric field to one of the electrodes where they were neutralized. At any incremental volume in the positive column the actual gain or loss of a specie due to flow or drift is the net between the number of that specie entering the volume and the number leaving. This value is impossible to calculate without knowing the axial variation of the species densities and the electric field. For a

---

*Refer to process number 75 in Appendix D for source reference.

perfectly uniform positive column the losses would be zero except at the anode and cathode boundaries of the column. For this study the overall flow and drift losses for the discharge are calculated and are assumed to be distributed throughout the volume of the positive column. This assumption represents an upper limit on these losses in the column.

Assuming a gas temperature of 300°K, the experimental flow rate was kept constant at 31 cm/sec. This equates to a flow loss rate, per unit volume, of:

$$L_{FS} = \frac{V_F}{L} \cdot N_S \tag{125}$$

For a column length of 50 cm:

$$L_{FS} = 0.62 \cdot N_S \tag{126}$$

The loss of each of the species is returned to the plasma as molecular oxygen in order to conserve mass. This corresponds to a replacement of the species flowing out of the downstream end of the column by gas flowing in at the upstream end.

The drift velocity of a specie S, V_{DS}, is related to the electric field by:

$$V_{DS} = \mu_S \cdot E \tag{127}$$

The mobility of a specie S, μ_s, is related to its reduced mobility, μ_{os}, by:

$$\mu_s = \frac{2.69 \times 10^{19}}{N_s} \cdot \mu_{os} \qquad (128)$$

Combining equations 127 and 128:

$$V_{DS} = 2.69 \times 10^{19} \cdot \mu_{os} \cdot \frac{E}{N} \qquad (129)$$

Using the reduced mobilities listed in Reference 50,

$$V_{DO^+} = V_{DO^-} = 8.6 \times 10^{19} \cdot \frac{E}{N} \qquad (130)$$

$$V_{DO_2^-} = 5.8 \times 10^{19} \cdot \frac{E}{N} \qquad (131)$$

$$V_{DO_2^+} = 6.02 \times 10^{19} \cdot \frac{E}{N} \qquad (132)$$

$$V_{DO_3^-} = 6.85 \times 10^{19} \cdot \frac{E}{N} \qquad (133)$$

The drift loss rate per unit volume of the ionic species is:

$$L_{MS} = \frac{V_{DS}}{L} \cdot N_s \qquad (134)$$

$$L_{MS} = \frac{V_{DS}}{50} \cdot N_s \qquad (135)$$

Actually, in Chemco the drift and flow losses are combined for the ionic species. Due to experimental geometry in which the cathode was at the downstream end of the column, the net loss to the positive ions is the sum of the flow and drift losses; the net loss of the negative ions is the difference between the flow and drift losses.

Results of Calculations

Electron Density. Chemco was run for initial molecular densities between 3.2×10^{16} and 5.6×10^{17} oxygen molecules per cubic centimeter and for reduced field values, (E/N), between 14 and 100 Townsends. The electron densities determined by these calculations are depicted in Figures 64 and 65. It should be emphasized that any particular code calculation was performed at a fixed value of E/N and is therefore applicable only to the stable form of the discharge, the high field form. The rapid decrease of electron density with E/N, as illustrated in figure 64, would appear to be the transition of the discharge from a stable to a nonself-sustaining form. This corresponds to the experimentally observed transition between the high field and low field forms of the discharge.

Figures 64 and 65 represent calculations in which two-step ionization through the $O_2^*(a^1\Delta)$ level was included. In order to determine the magnitude of the effect of the two-step ionization on the electron density, a comparison calculation was made in which the population of the $O_2^*(a^1\Delta)$

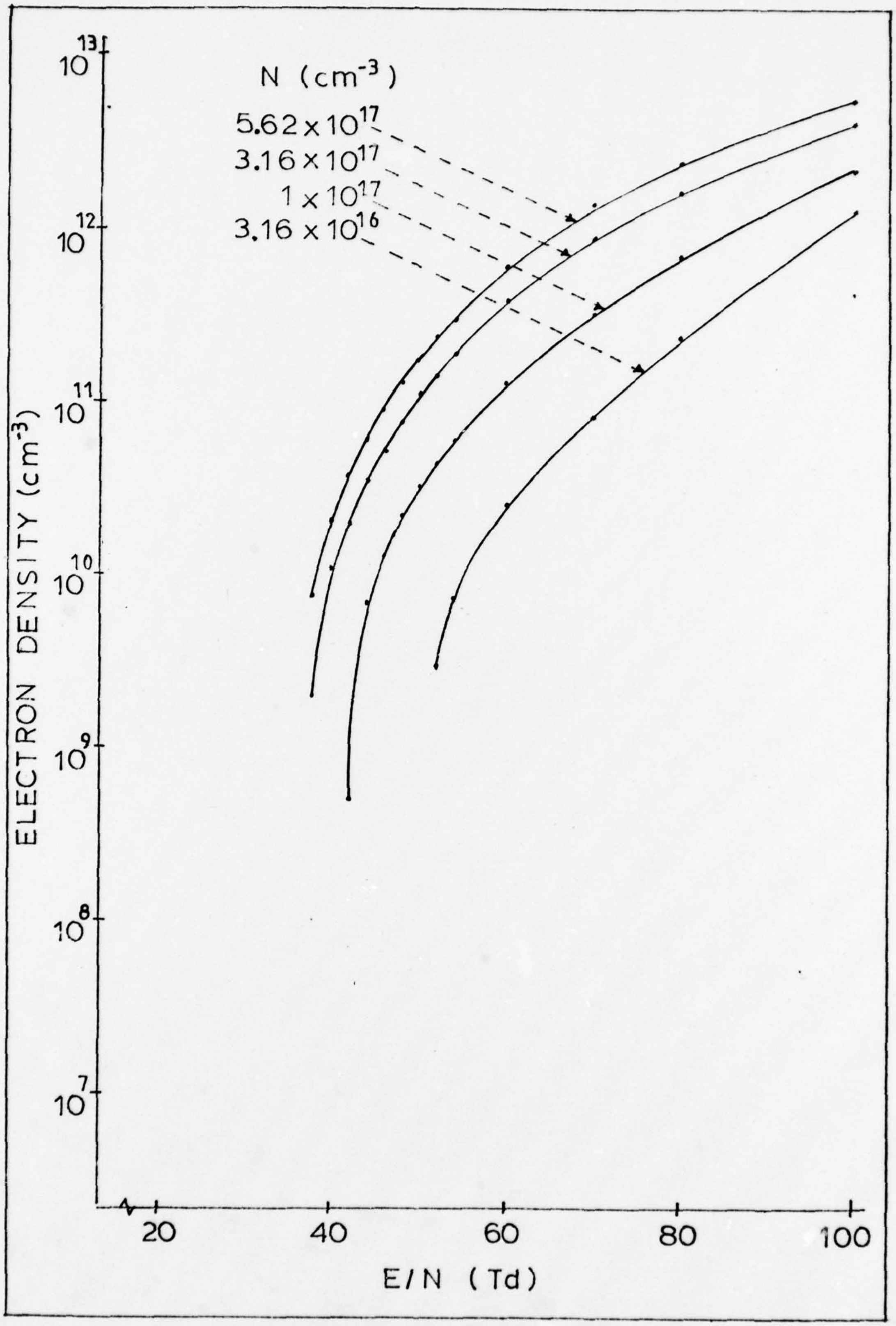

Figure 64. Electron Density

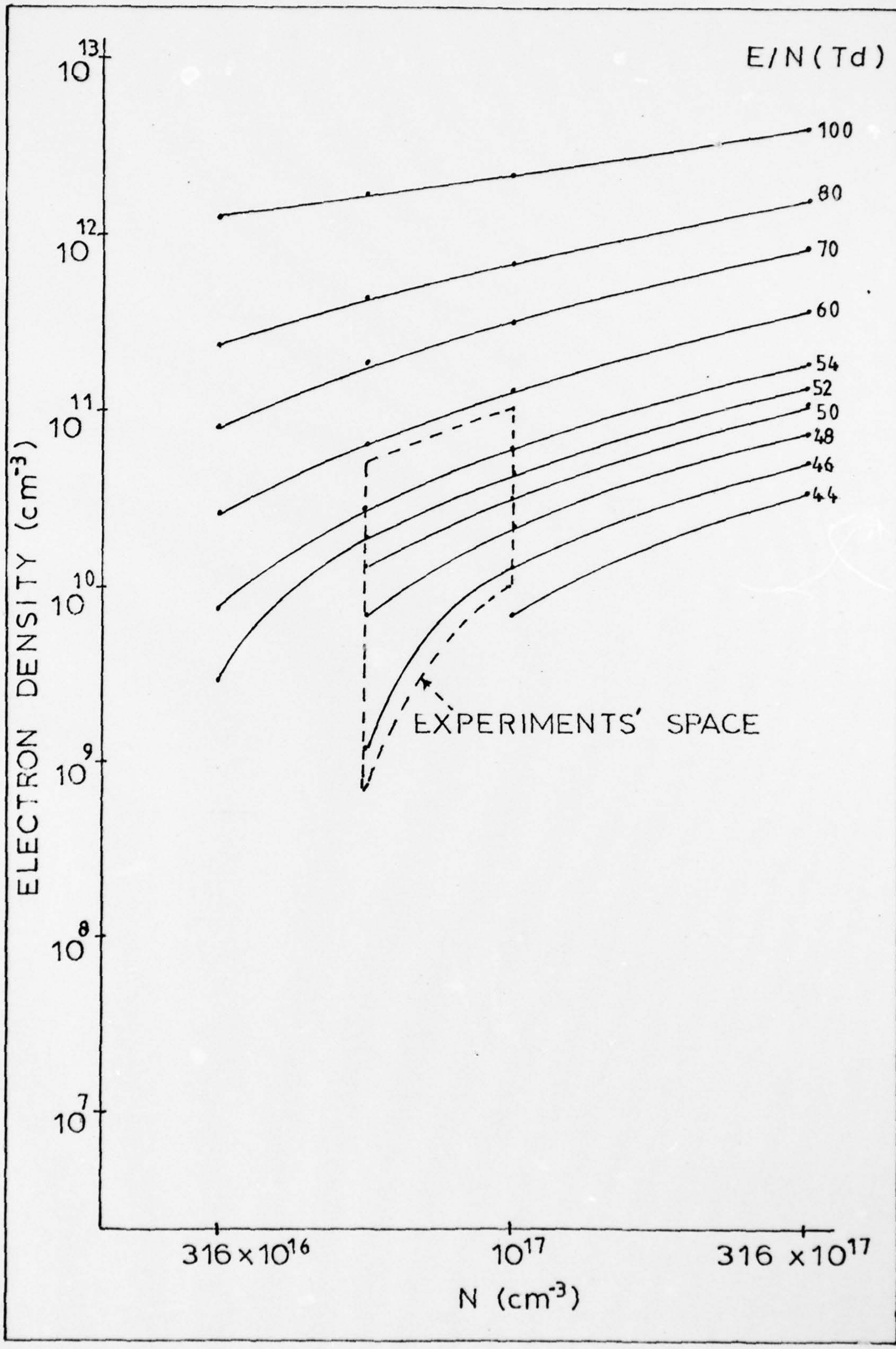

Figure 65. Electron Density

level was set at zero. This calculation was made for an initial molecular density of 1 x 10^{17} oxygen molecules per cubic centimeter. The results of this calculation are depicted along with the two-step ionization results in figure 66. Over the range of the experimental results (40 to 60 TD), it was found that two-step ionization is an important process in determining the electron density. At higher values of E/N, the two-step process becomes less important due to a decrease in the $O_2^*(a^1\Delta)$ and due to the lower ionization threshold of the metastable becoming less important.

Figures 67 and 68 compare the results of Chemco with experiments and with electron current continuity calculations. The experimental results were obtained from the microwave cavity experiments reported in Chapter VI. The current continuity calculations were determined from equation 69. The chemistry code values were calculated using an E/N taken from experiments. In determining the experimental E/N, the electric field was measured directly; the number density was calculated by determining the average of the radial temperature profile (equation 22) and using the results in equation 28:

$$\langle N \rangle = \frac{9.7 \times 10^{18} \cdot P}{\left(\frac{2 \cdot \Delta T_c}{3} + 290\right)} \qquad (136)$$

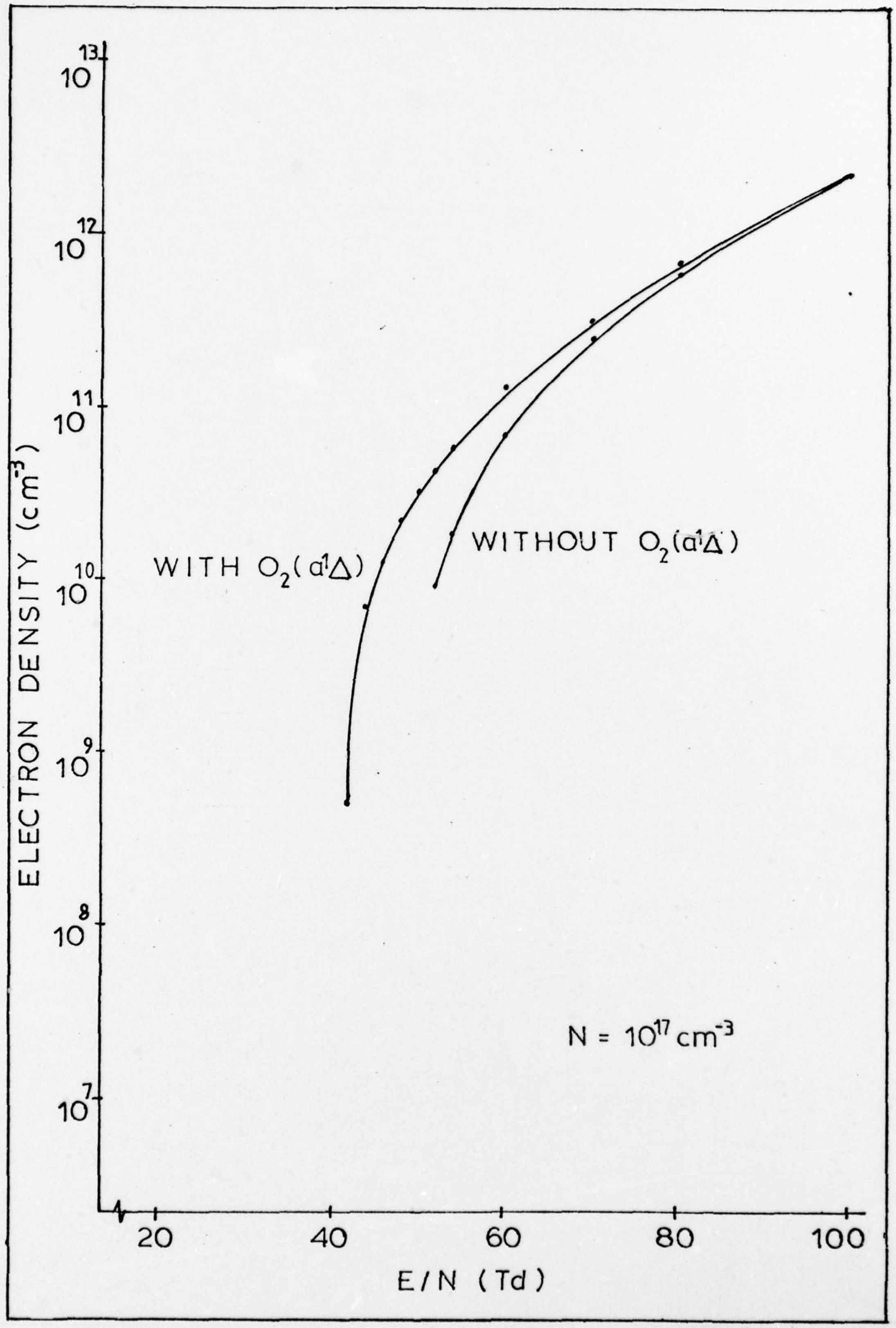

Figure 66. Effect of 0_2*(a'Δ) on Electron Density

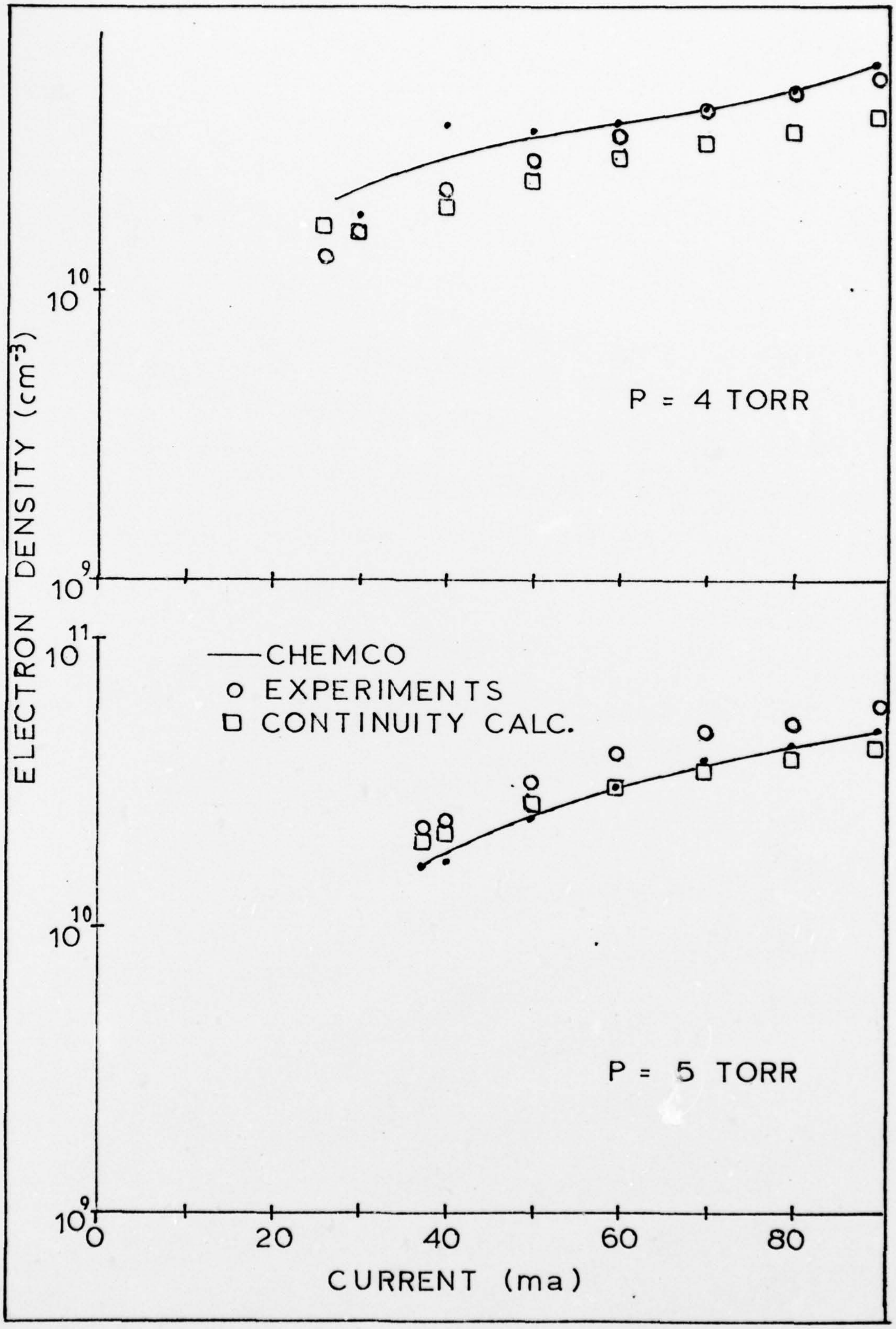

Figure 67. Electron Density Comparisons at 4 and 5 Torr

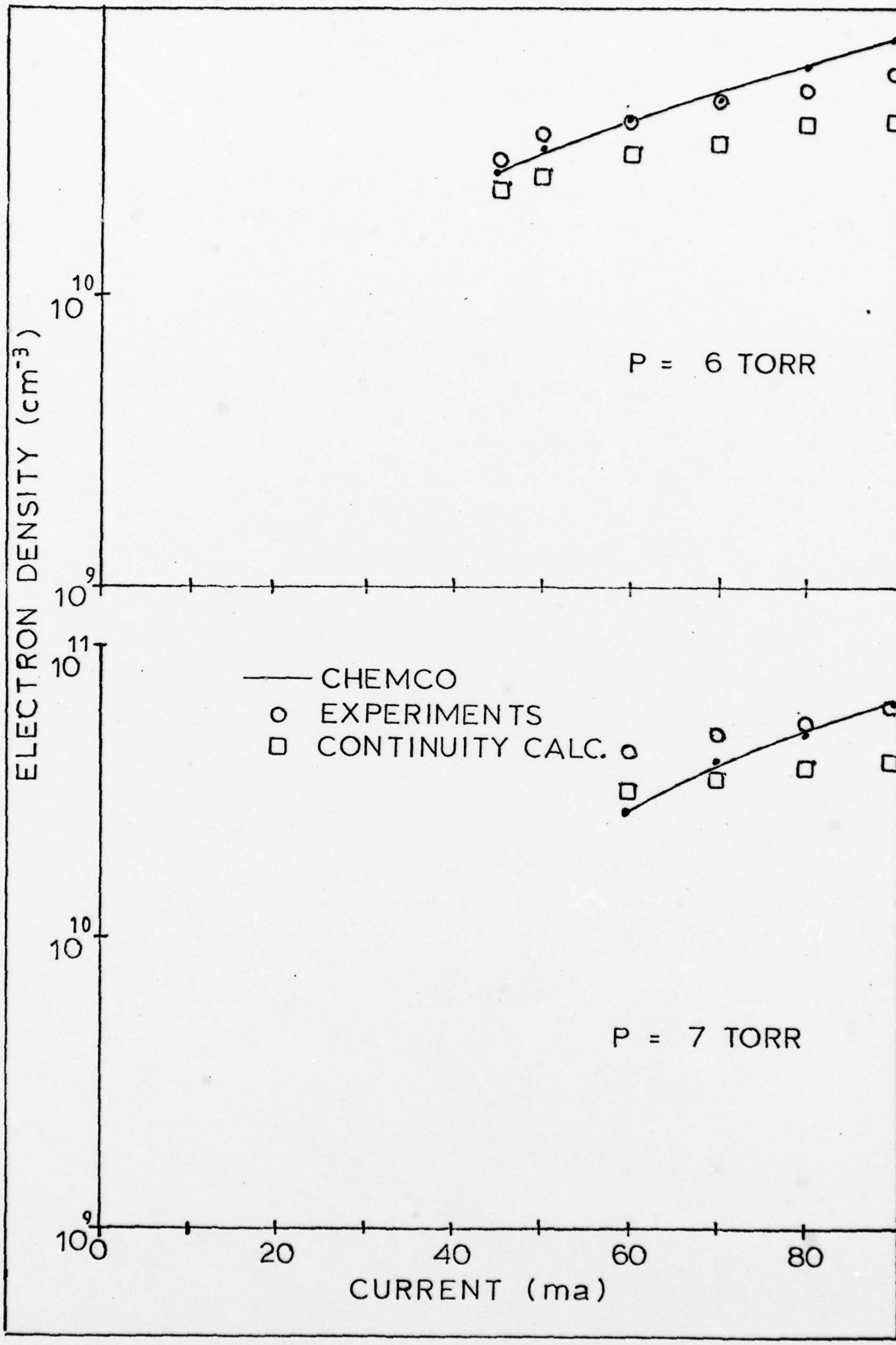

Figure 68. Electron Density Comparisons at 6 and 7 Torr

where ΔT_c is the temperature difference between the tube wall and the center of the discharge, in degrees centigrade*. The results of Chemco were interpolated or extrapolated using the average N and E/N to determine an average electron density. This average density was then multiplied by 1.64 to obtain the centerline electron density; 1.64 is the peak to average ratio for a Bessel profile.

The comparison of the results of Chemco to other calculations and to experiment is limited by two factors. A primary limitation is the comparison of a one dimensional time or axial variation code to a two-dimensional time or axial variation and radial variation experiment**. The code calculations were for values of E/N which do not vary in position or time. The stable-field experimental data did not change as a function of time, but it is expected that the quantities are functions of radial position. The second limitation is the linking of the results of the code and experiment through the reduced field, E/N. The experimental evaluation of this critical parameter required the accurate determination of the temperature of the gas in the discharge plasma. As discussed in Chapter IV, this measurement was difficult; and for the comparison regime, the values used were extrapolations of measurements made at lower values of

---

*Equation 24 with ΔT_C = To-Tw.

**The plasma parameters were assumed to be symmetric around the tube axis.

input power. Despite these approximations the results of the Chemco calculations compare well with the results from electron current continuity calculations and with the microwave experimental data.

Ion Densities. Figures 69, 70, and 71 depict the calculated charged species densities as functions of reduced electric field for three different values of initial molecular oxygen density. For the experimental parameter space of this study, the dominant positive ion was calculated to be O_2^+. This result agrees with the experimental observations of Thompson and Keren (Ref 12:52, Ref 19:8-9, Ref 24:820). The dominant negative ion is O^-, as previously measured by Thompson, Lunt, and Sabadil (Ref 24:820, Ref 25:1068, Ref 26:299-308). However as the value of E/N is lowered toward the point of transition between the stable and unstable forms, the negative molecular ions, O_2^- and O_3^-, become significant, especially as the neutral number density is increased. In fact, at a molecular density of 3.16 x 10^{17} molecules per cubic centimeter, the negative molecular densities are approximately the same as the atomic ion at the transition point.

Neutral Densities. Figures 72, 73, and 74 depict the calculated neutral species densities as functions of E/N at three different initial molecular densities. Of note is the relatively low E/N at which the $O_2^*(a^1\Delta)$ density reaches a maximum. At E/Ns above this value the density of $O_2^*(a^1\Delta)$ decreases, reducing the importance of two-step ionization

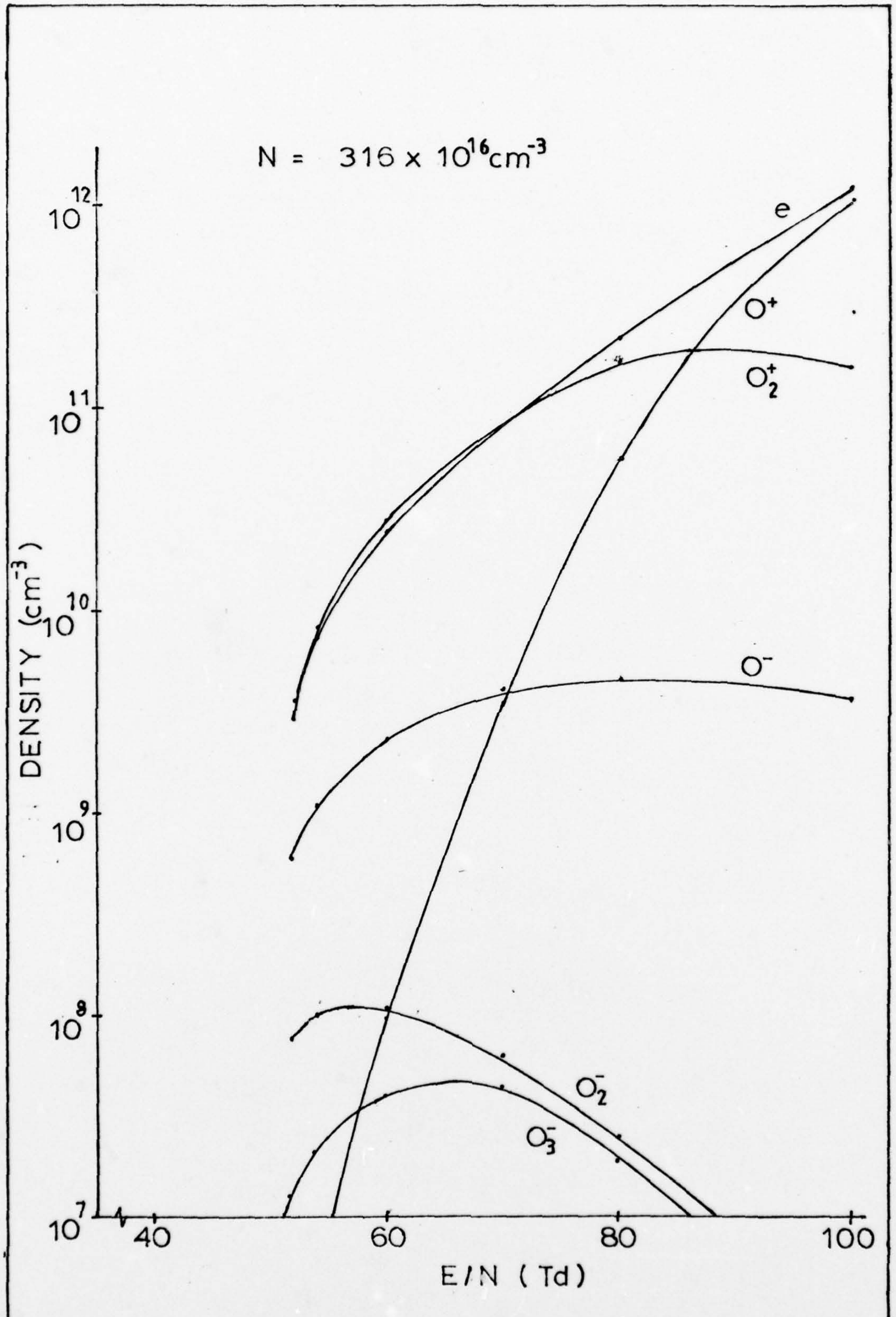

Figure 69. Charged Particle Densities at $N=3.16X10^{16}cm^{-3}$

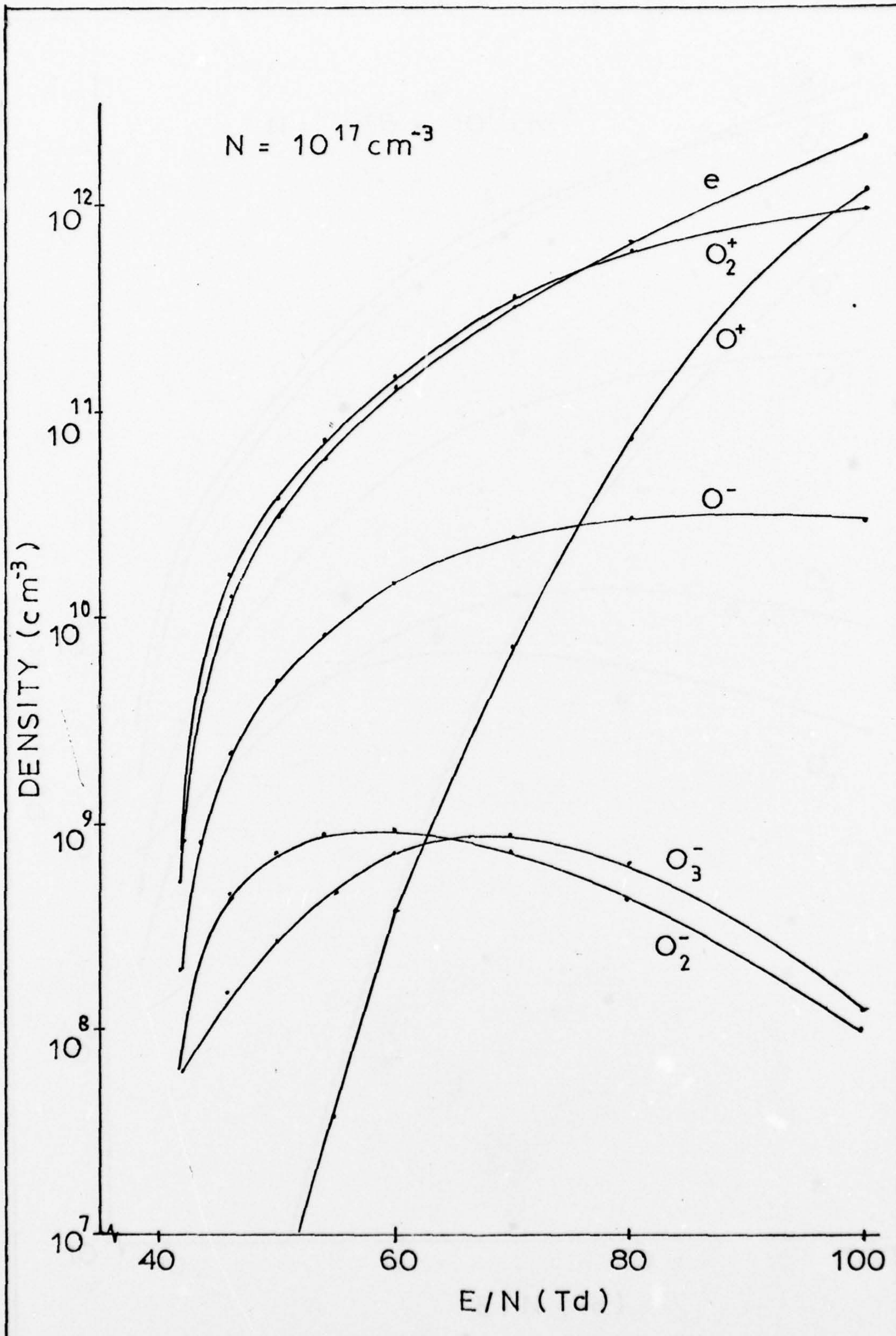

Figure 70. Charged Particle Densities at $N=1X10^{17} cm^{-3}$

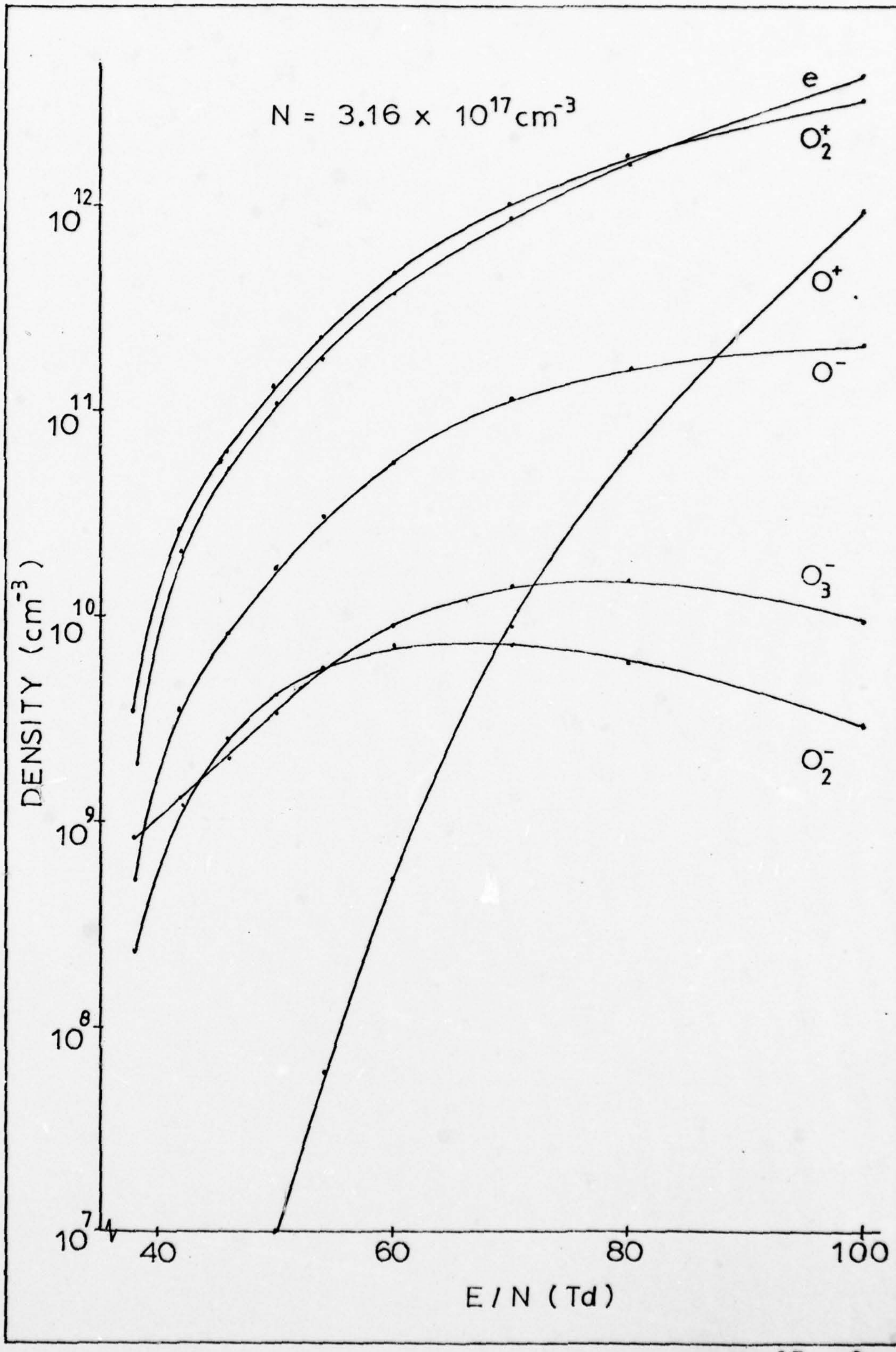

Figure 71. Charged Particle Densities at $3.16X10^{17} cm^{-3}$

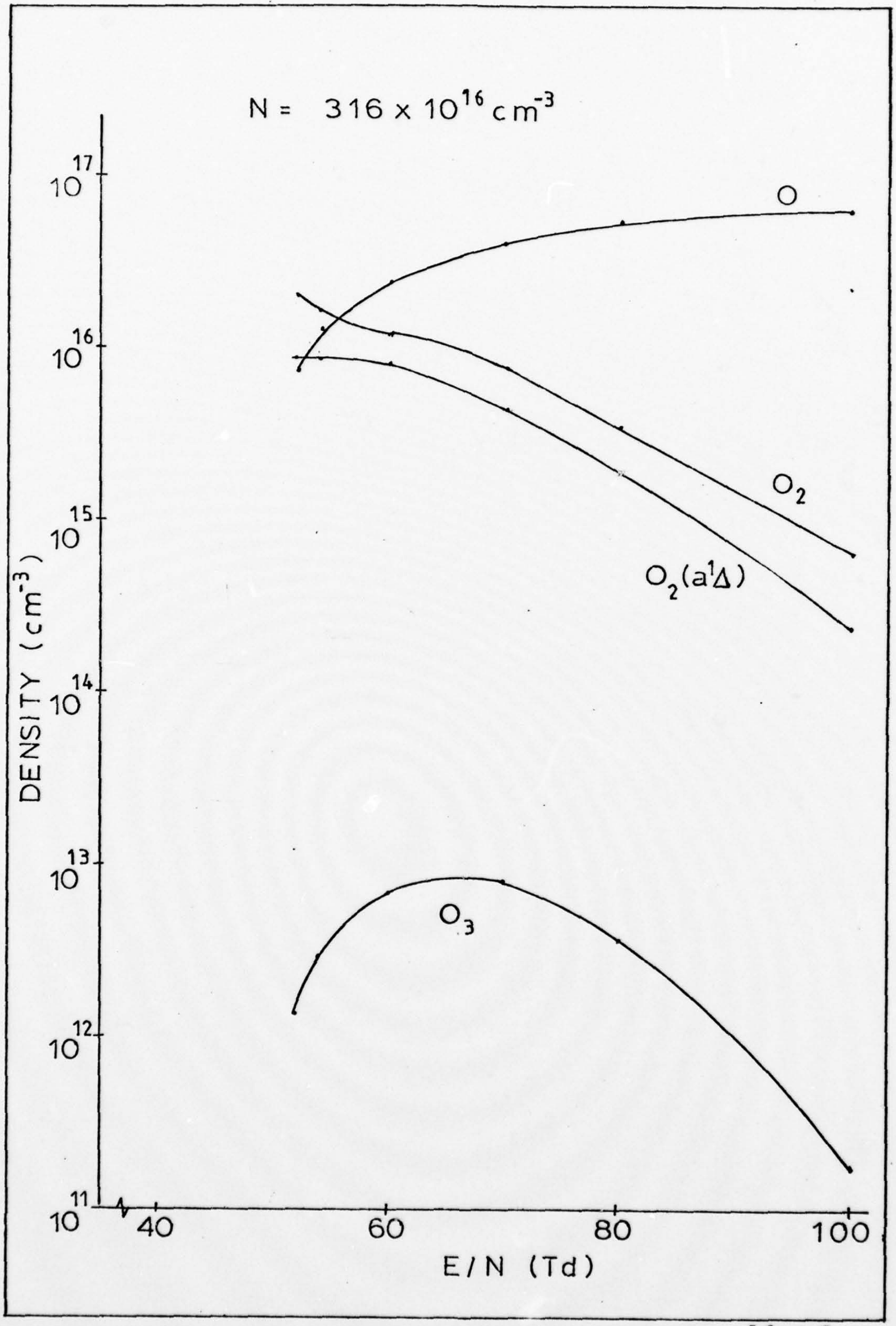

Figure 72. Neutral Species Densities at $3.16 \times 10^{16} cm^{-3}$

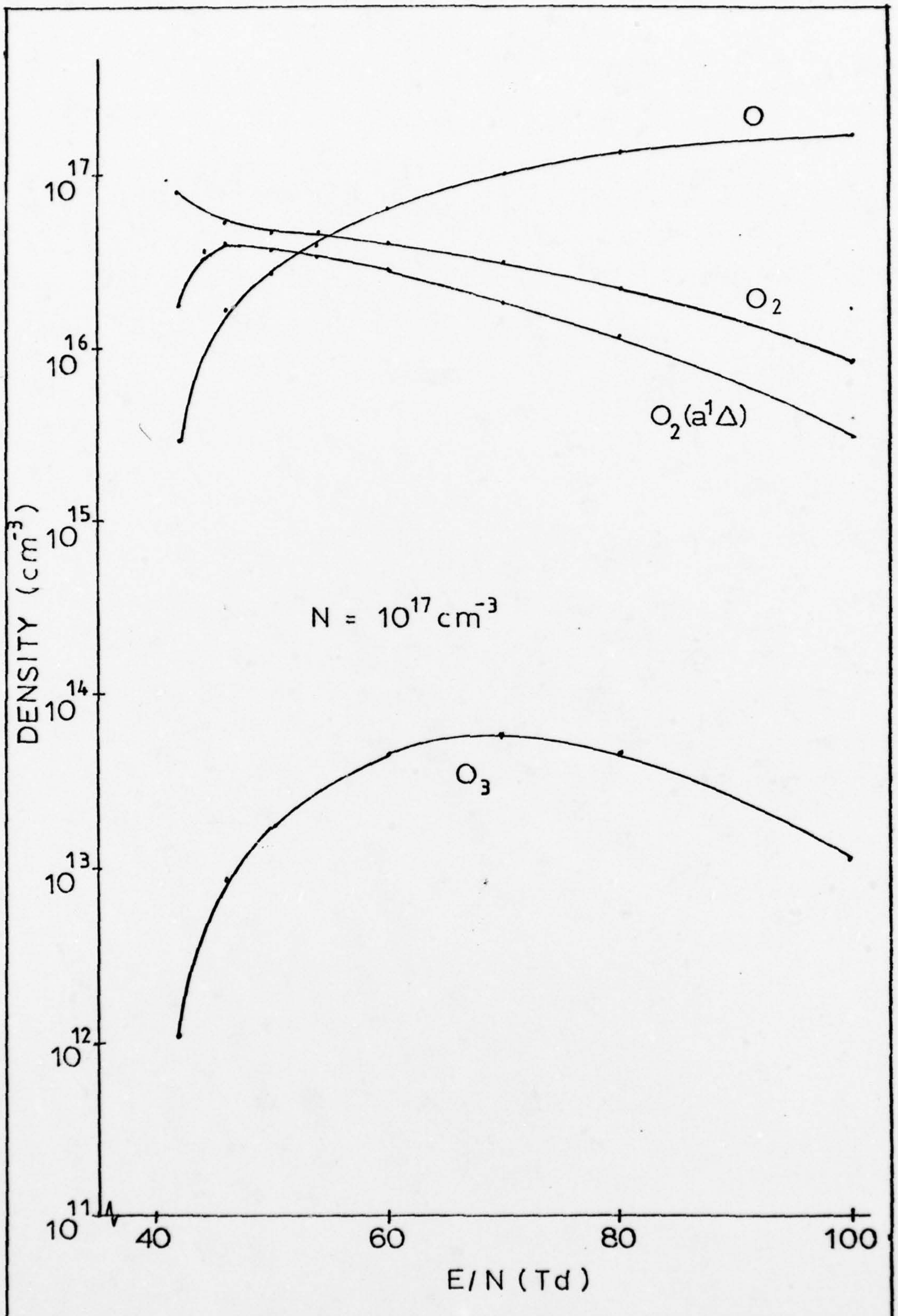

Figure 73. Neutral Species Densities at $1X10^{17}cm^{-3}$

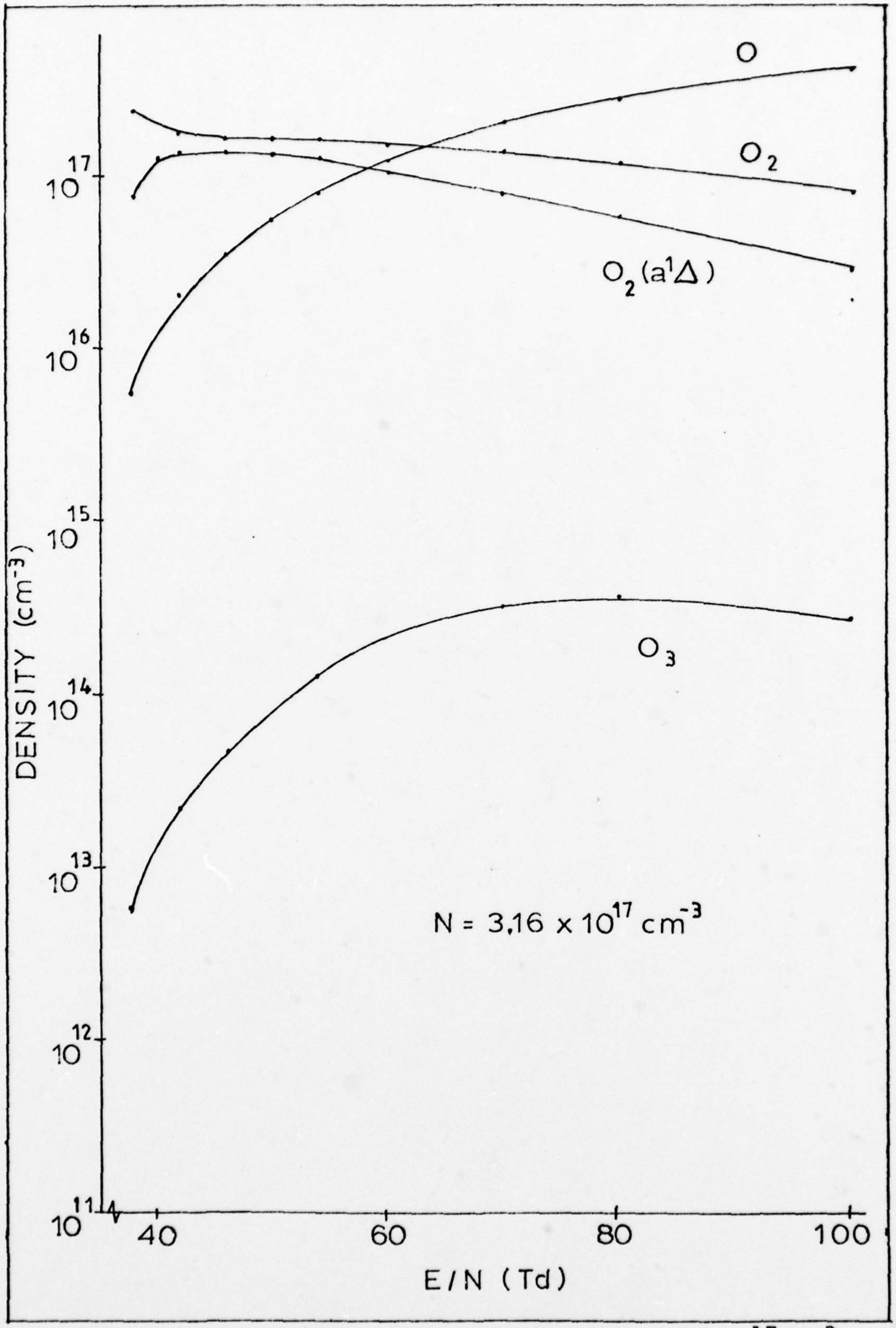

Figure 74. Neutral Species Densities at $3.16X10^{17}cm^{-3}$

at high E/N values. The O_3 density was calculated to be several orders of magnitude lower than that of the other neutral species. This is consistent with the mass spectrometer experiments during which O_3 was not observed within the two orders of magnitude range of the neutral spectra plots*.

The change of atomic oxygen density with discharge tube current is compared with experiment in figure 75. An absolute calibration of the atomic oxygen density was not made during the mass spectrometry experiments. However, a calibration using the results of Chemco indicated a maximum dissociation of 20% for the 5 torr experimental run.

Principal Electron Processes. Figures 76 through 81 depict the principal electron gain and loss processes at three different initial molecular oxygen densities. The rates are normalized to either the total gain or total loss rate to show relative importance. The principal gains for the electrons are from detachment processes from the atomic and molecular negative ions. The major detaching specie is the $O_2^*(a^1\Delta)$ excited molecule. Atomic oxygen plays a minor role as a detacher**. The principal loss mechanisms for the electrons are dissociative attachment from the $O_2^*(a^1\Delta)$ and

---

*Reference Chapter VII.

**Chemco runs in which the $O_2^*(a^1\Delta)$ population is set at zero results in the same high to low transition phenomenon. However, in those cases, the detaching specie is only atomic oxygen; and the transition occurs at a much higher value of E/N, as depicted in figure 84.

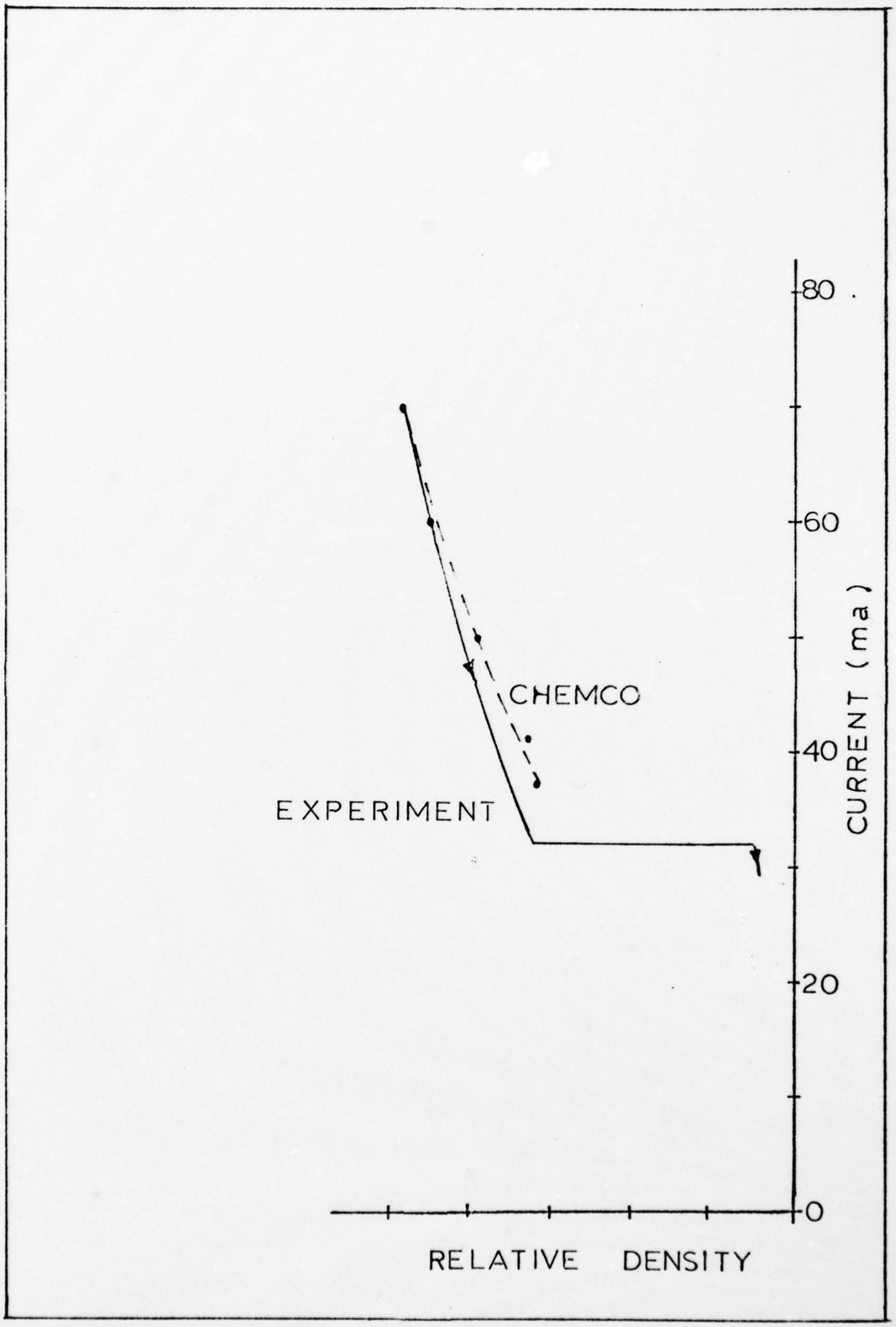

Figure 75. Atomic Oxygen Comparison

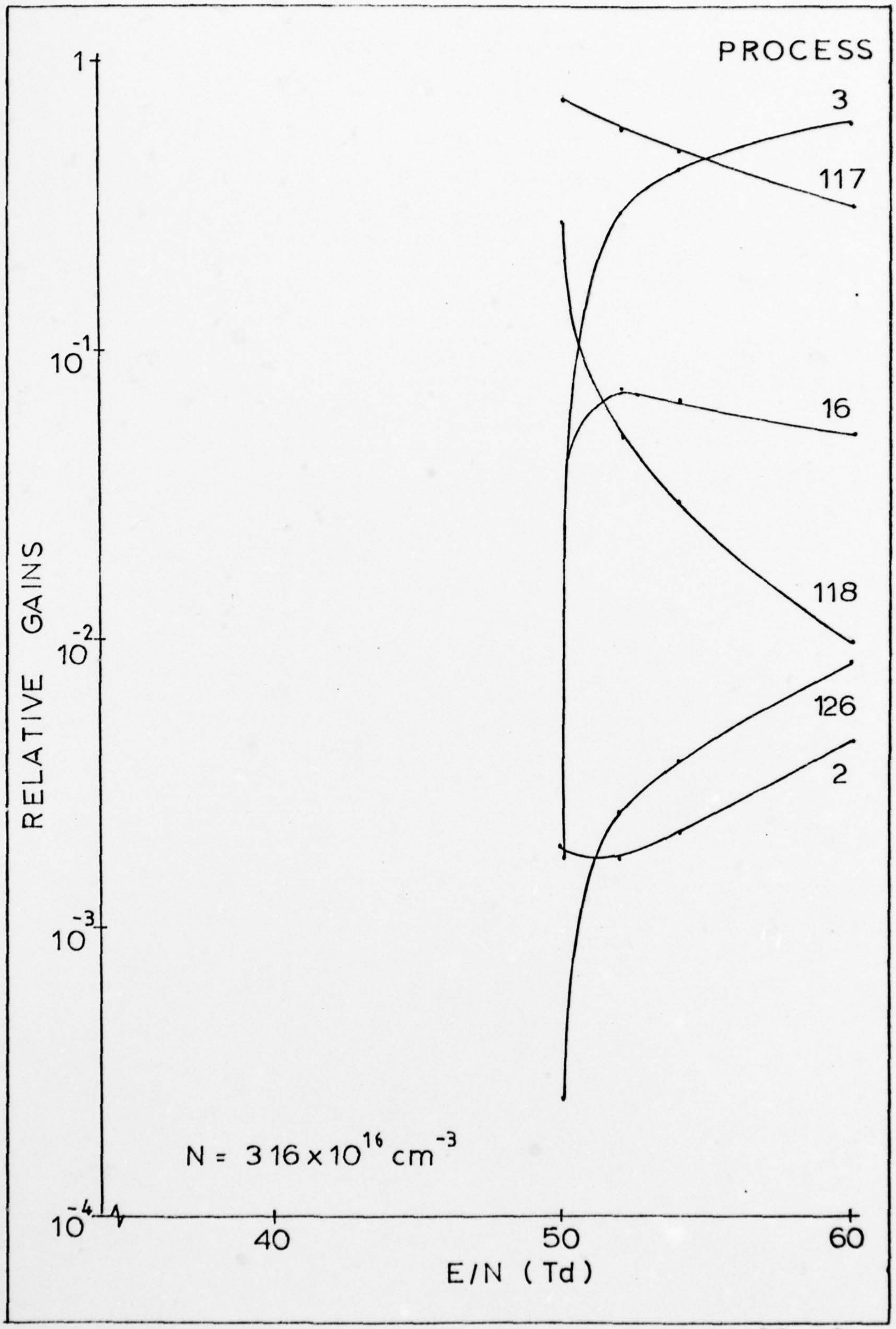

Figure 76. Principal Electron Gains at $3.16X10^{16}cm^{-3}$

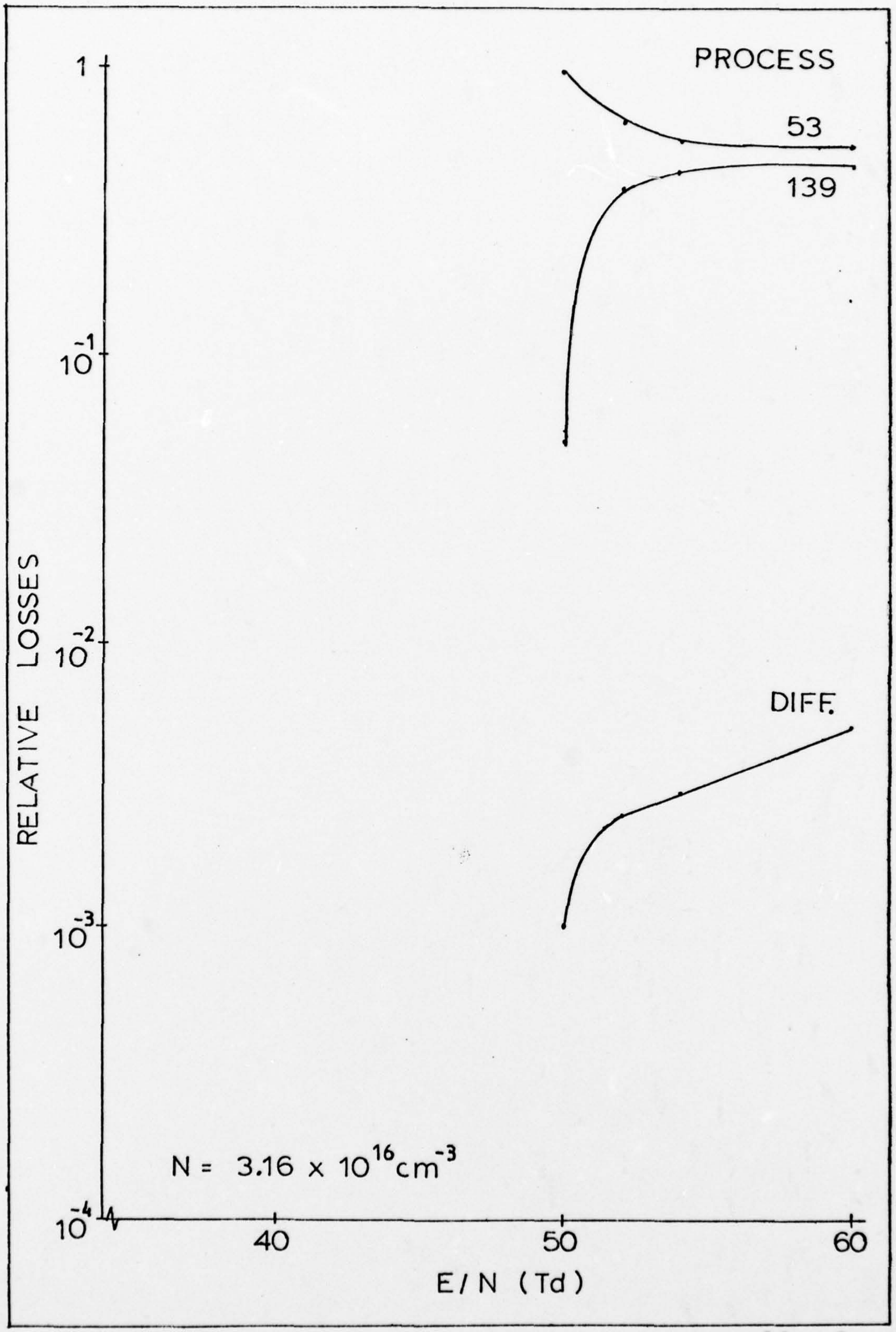

Figure 77. Principal Electron Losses at $N=3.16X10^{16}cm^{-3}$

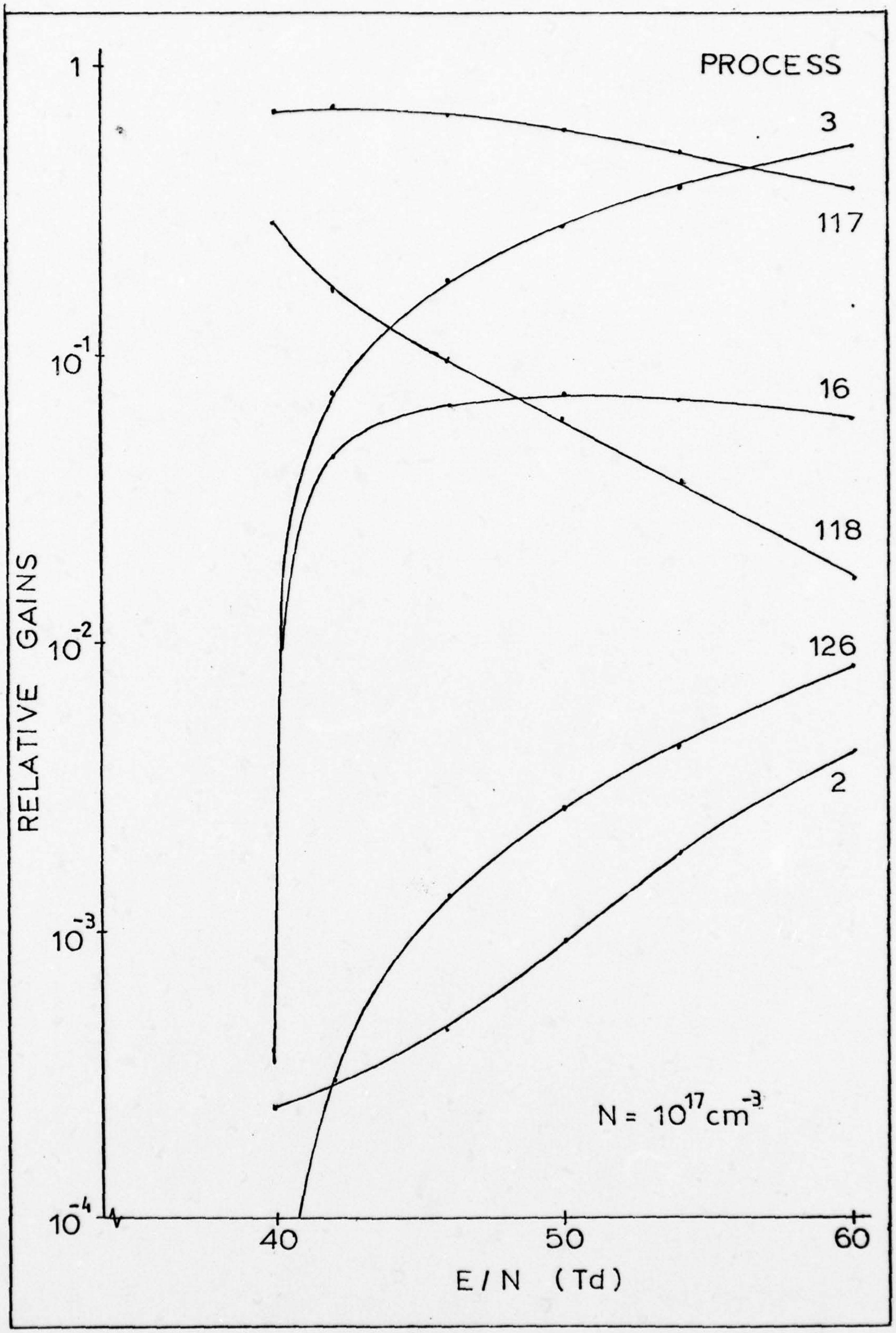

Figure 78. Principal Electron Gains at $N=1X10^{17} cm^{-3}$

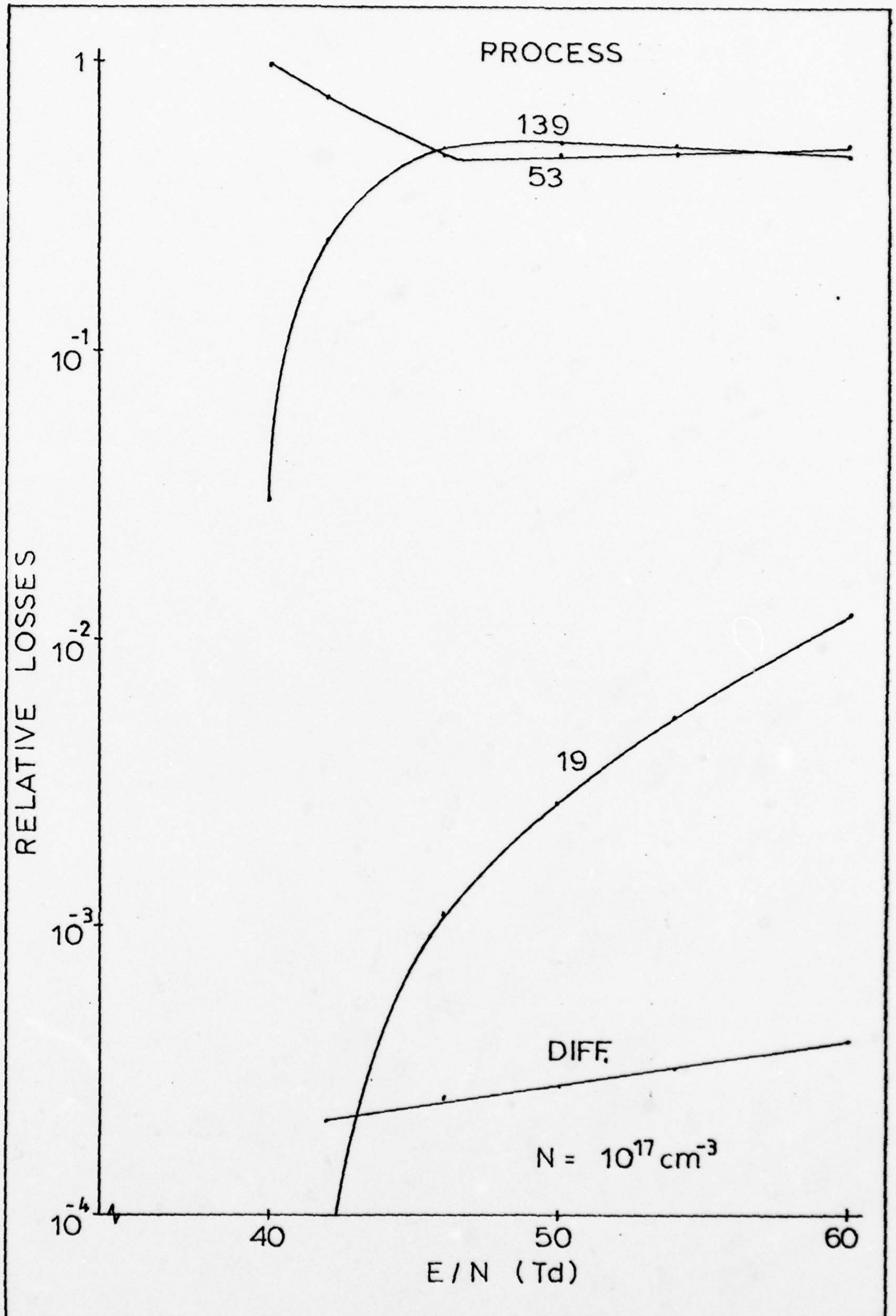

Figure 79. Principal Electron Losses at $N=1X10^{17} cm^{-3}$

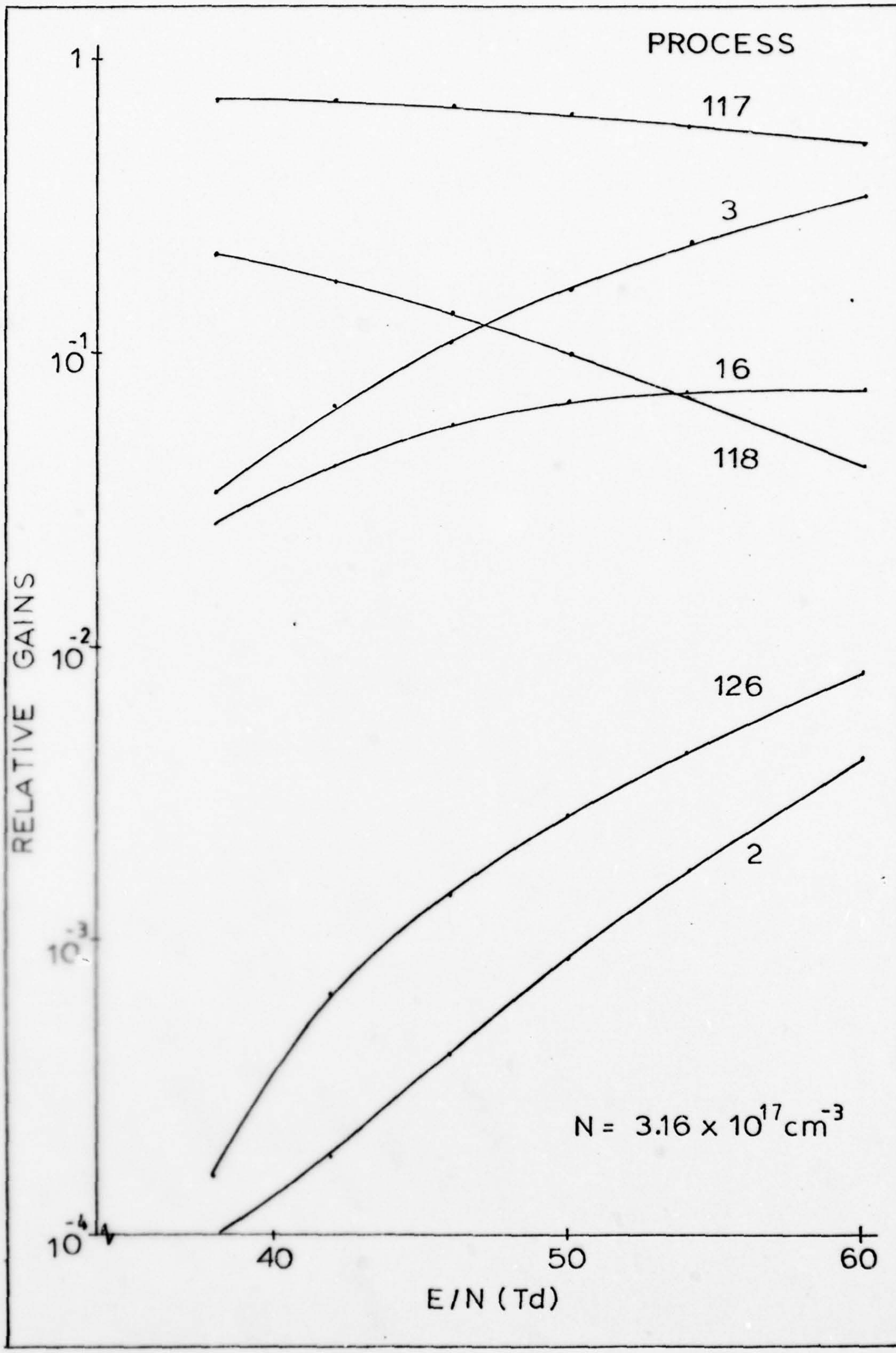

Figure 80. Principal Electron Gains at $N=3.16X10^{17}cm^{-3}$

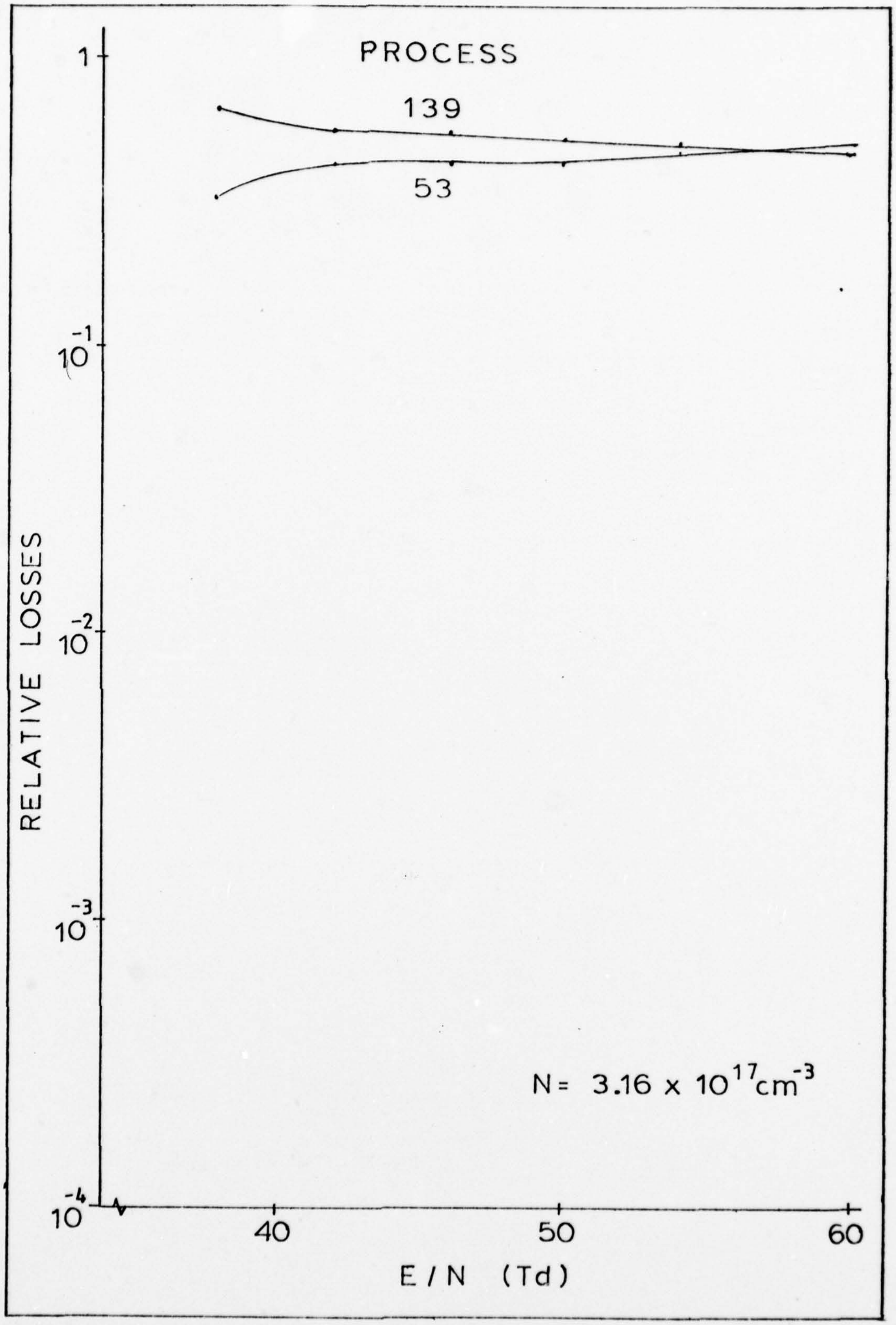

Figure 81. Principal Electron Losses at $N=3.16X10^{17} cm^{-3}$

ground states of the molecule.

As the point of transition is approached by the lowering of the reduced field, the relative effect of direct molecular ionization from the $O_2^*(a^1\Delta)$ and ground states becomes numerically insignificant to the other processes. The attachment/detachment processes numerically dominate the electron losses and gains. However, these processes merely transfer electrons back and forth from bound to unbound states; and any true losses to other processes are balanced by ionization. Therefore, although numerically insignificant near transition, the ionization process is key to the maintenance of the stable discharge. As the ionization process rapidly decreases near the point of transition, the electrons stored in the attachment/detachment processes become depleted through other loss processes; and the discharge becomes nonself-sustaining. Due to the presence of negative ions, the diffusion process is insignificant with respect to the attachment processes in the range of initial molecular densities considered in Chemco. However, the diffusion loss is comparable to the recombination and flow losses.

X. Discussion and Conclusions

Chapters III through VII of this study reported on the results of the experimental observations of the oxygen discharge. Chapters VIII and IX presented a computer model of the discharge and compared that model with the experiments. In this chapter the results of these previous chapters are used to explain the phenomena associated with the oxygen plasma. Specifically, the discussion focuses on the high field form of the discharge and the transition from the high field form to the low field form. Quantitative data are used to draw conclusions regarding these topics. Some qualitative discussion and conclusions are also presented regarding the low field form and the transition from the low field form to the high field form.

It is believed that the results developed in this study are much more comprehensive than those previously developed for the oxygen plasma. However, there still remains a significant amount of work that must be accomplished to fully understand the phenomena. In addition to oxygen, it is believed that the experimental and modeling approaches presented in this study are also useful in the investigation of other electro-negative plasmas.

Discussion

High Field Form. Throughout the region of the experimental investigation the high field form, though stable, is nevertheless a plasma in which the negative ions play important roles. As the point of transition between stable and unstable forms is approached, the attachment-detachment processes dominate the electron gains and losses, leading to a situation in which attachment is approximately balanced by detachment (Ref 30:11).

$$N_e \cdot K_a = N_- \cdot K_d \qquad (137)$$

where Ka is the attachment processes, Kd is the detachment processes. The dominant* attachment and detachment processes for values of E/N between 60 Td and the transition points and for initial molecular densities between 3.16×10^{16} and $3.17 \times 10^{17} cm^{-3}$ are listed in table XXIII**. Equation 137 was satisfied very closely throughout the E/N range of this investigation for the processes of table XXIII.

Although not the primary source of electrons, ionization is important for replenishing the electrons lost by processes other than attachment. For a stable discharge, ionization balances these other losses.

$$K_I \cdot N_{O_2} \cdot N_e = K_r \cdot N_+ \cdot N_e + K_{DF} \cdot N_e + K_v \cdot N_e \qquad (138)$$

---

*Within two orders of magnitude.

**Refer to figures 76 through 81 for a graphical description of the dominant processes. Equation 137 is true only when the attachers and detachers are the same species: in this case $O_2^*(a^1\Delta)$ dominates close to the point of transition.

where Ki is the ionization coefficient, Kr is the recombination coefficient, Kdf is the diffusion loss coefficient, and Kv is the drift loss coefficient. The dominant* ionization and nonattachment loss processes are listed in table XXIV.

Table XXIII. Dominant Attachment and Detachment Processes

Attachment	Process Number*	Func. Dep.	Typical Rates (30 to 60 TD)
$e + O_2 \rightarrow O + O^-$	53	E/N	1.7×10^{-11} to 3.2×10^{-11}
$e + O_2^* \rightarrow O + O^-$	139	E/N	3.1×10^{-11} to 4.2×10^{-11}
$e + 2O_2 \rightarrow O_2^- + O_2$	41	None	1.9×10^{-30}
$e + O_2^* + O_2 \rightarrow O_2^- + O_2$	141	None	1.9×10^{-30}
Detachment			
$e + O^- \rightarrow e + O_2$	3	None	1.9×10^{-10}
$O^- + O_2^* \rightarrow O_3 + e$	117	None	3×10^{-10}
$O_2^- + O \rightarrow O_3 + e$	16	None	3.3×10^{-10}
$O_2^- + O_2^* \rightarrow 2O_2 + e$	118	None	2×10^{-10}

*Processes listed in descending order of importance at $N = 1 \times 10^{17} cm^{-3}$.

---

*Within two orders of magnitude.

Table XXIV. Dominant Ionization and Loss Processes

Ionization	Process Number*	Func. Dep.	Typical Rates (30 to 60 TD)
$e + O_2^* \rightarrow O_2^+ + 2e$	126	E/N	1.4×10^{-15} to 7.5×10^{-13}
$e + O_2 \rightarrow O_2^+ + 2e$	2	E/N	1.6×10^{-15} to 2.7×10^{-13}
$e + O \rightarrow O^+ + 2e$	1	E/N	7.8×10^{-18} to 6.8×10^{-14}
$N_- +$ Electrode $\rightarrow N + e$	Drift	E/N	-
Non-Attachment Losses			
$e + O_2^+ \rightarrow 2O$	19	None	2.1×10^{-7}
$e + O_2^+ + M \rightarrow O_2 + M$	38	None	1×10^{-26}
$e + N_+ +$ Wall $\rightarrow N$	Diffusion	N_e/N	-
$e + N_+ +$ Electrode $\rightarrow N$	Drift	E/N	-

*Processes listed in descending order of importance at $N = 1 \times 10^{17} cm^{-3}$.

Using the processes of table XXIV, equation 138 was satisfied within $\pm$ 16% over the range of E/N values from 60 Td to the points of transition and for initial molecular densities between 3.16×10^{16} and $3.16 \times 10^{17} cm^{-3}$.

High Field-to-Low Field Transition

An electronegative molecular plasma can become unstable when two conditions are satisfied (Ref 30:23-26, Ref 52:1030-1031). The first condition requires that:

$$K_a \cdot \frac{\partial LN\{K_a\}}{\partial LN\{E/N\}} > K_i \cdot \frac{\partial LN\{K_i\}}{\partial LN\{E/N\}} \tag{139}$$

This is a necessary condition and requires that the attachment coefficient be an increasing function of E/N and of a magnitude comparable to the ionization coefficient. This relationship leads to a net loss of electrons during a positive fluctuation in E/N*. In order to maintain current continuity in such a plasma, the discharge must adjust itself to a higher E/N which further decreases the electron density. It is this feedback mechanism that leads to instability and runaway. Figure 82 depicts the ratio of the two quantities in equation 139 as a function of E/N and for the two limiting conditions where all of the ionization is from the $O_2^*(a^1\Delta)$ level or from the ground level. The data was taken from the Boltzmann Code results of Chapter VIII. Even with a highly populated $O_2^*(a^1\Delta)$ level, the necessary condition for instability is only satisfied for E/N values below 67.4 TD.

The second condition, a sufficient condition, requires that the negative ion concentration be significant compared

---

*From an experimental viewpoint in order for the electric field to change as a function of the changing nature of the plasma, the discharge must be connected to a constant current source.

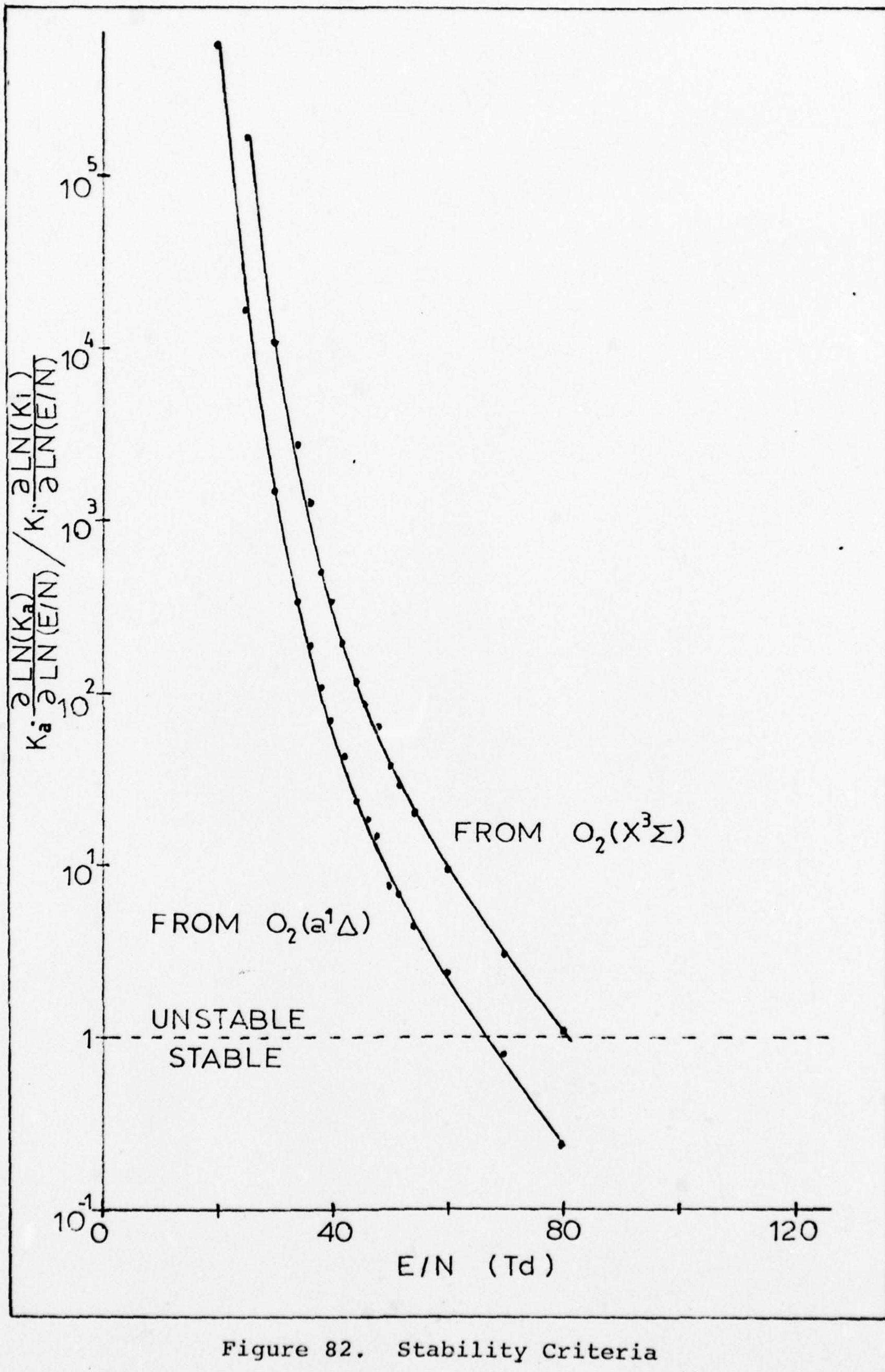

Figure 82. Stability Criteria

to that of the electrons. This is required so that negative ion and electron processes can couple during a disturbance in plasma properties. Specifically, this requires for instability that:

$$N_- \geq N_e \tag{140}$$

where it is assumed that in an electronegative multi-component plasma, a summation can be performed over all the negative ion species:

$$N_- = N_{O^-} + N_{O_2^-} + N_{O_3^-} \tag{141}$$

Figure 83 depicts the ratio of these parameters as functions of E/N and initial molecular density. The data was taken from the chemistry code results of Chapter IX. Using the equality of the electrons and negative ions as the sufficient condition for transition from stability to instability, the E/N values at the transition point are plotted on figure 84 as a function of initial molecular density. Also plotted on this figure are the data points taken from the experiments. There is considerable scatter in the experimental values, due to difficulty in determining the actual gas density. Even so, the data indicates that the calculated transition points are in reasonable agreement with experiments.

<u>Pressure Effects</u>. Since the more critical condition

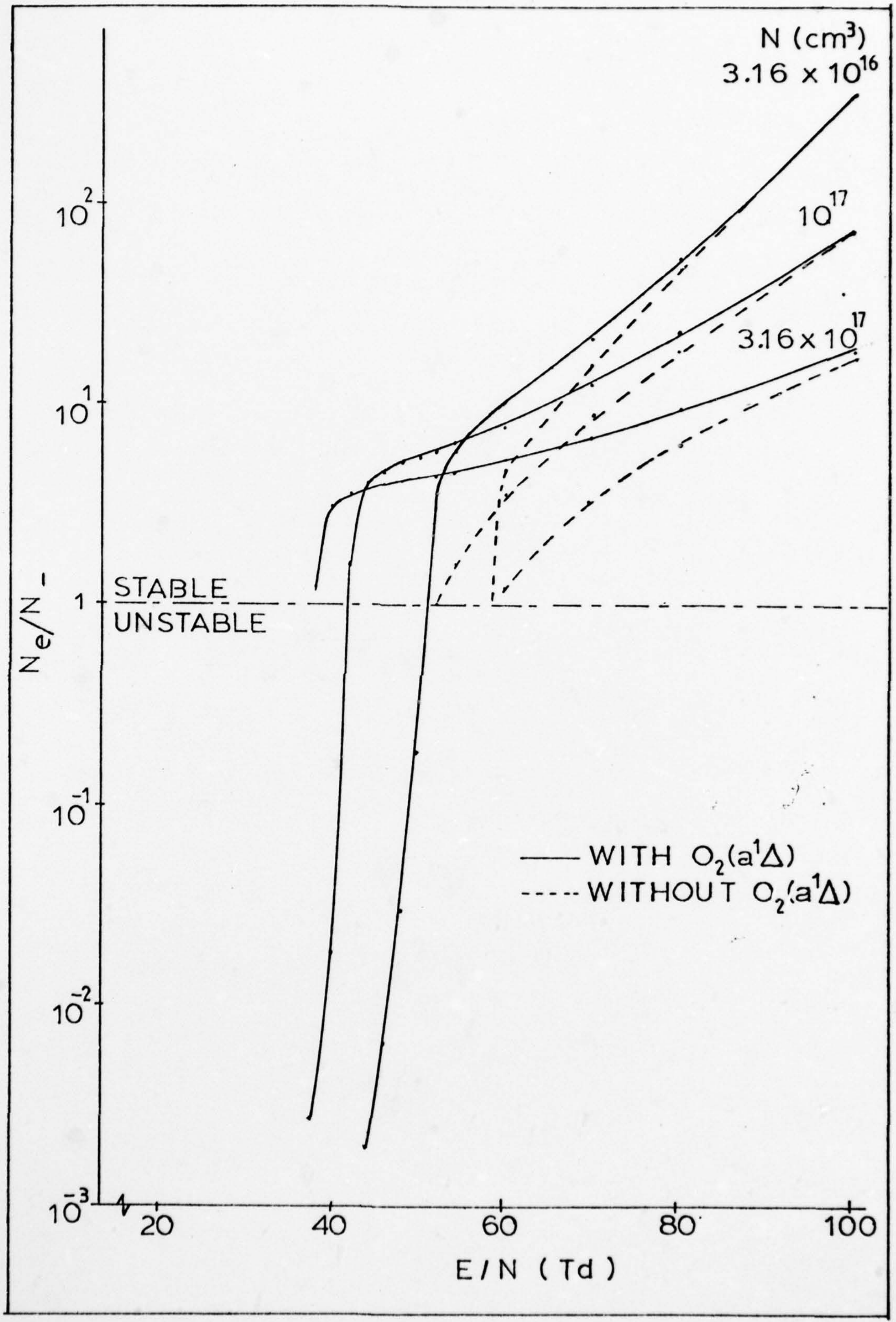

Figure 83. Electron-to-Negative Ion Ratio

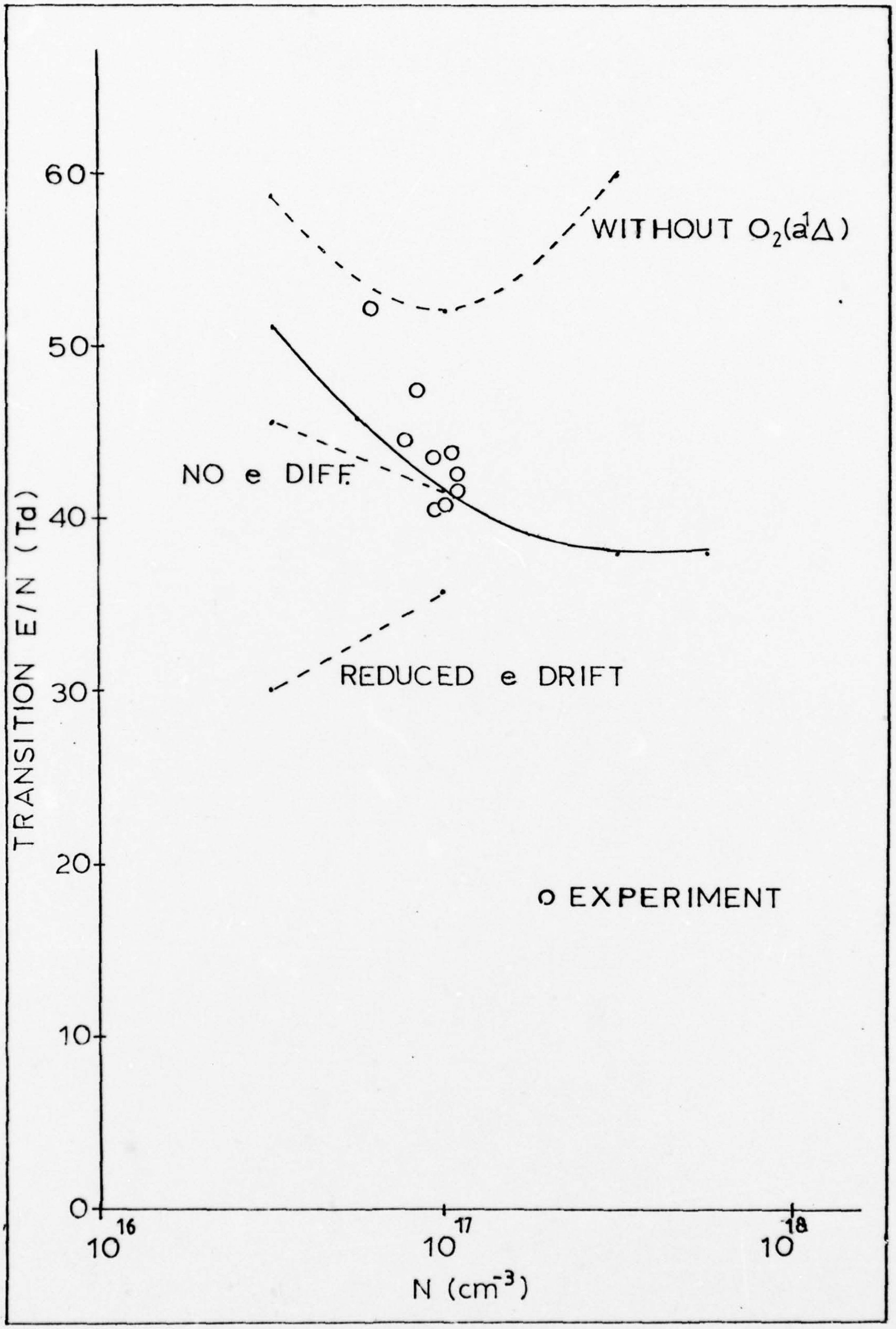

Figure 84. High-to-Low Transition Comparison

for the transition between the stable high field forms to the unstable low form of the discharge is the equivalence of the electron and negative ion densities, it is appropriate to study this relationship as a function of initial molecular density (pressure). As depicted in figure 84, the transition value of E/N is a decreasing function of the initial molecular density. This implies that the pressure effect is caused by processes which increase the electron density or decrease the negative ion densities as the initial molecular density is increased. Normally, this results from three-body collisional processes; however, there are no dominant three-body processes in Chemco which could cause the effect. There are, however, two noncollisional processes which can account for the pressure effects on the transition values - the diffusion and drift losses of the electrons.

In order to determine the effects of electron diffusion and drift losses, consider an expansion of equation 138:

$$K_i \cdot N_{O_2} \cdot N_e = K_r' \cdot N_e^2 \cdot N_{O_2} + K_{DF} \cdot N_e + K_v \cdot N_e \tag{142}$$

where $N_eN_{O_2}$ is substituted for N_+ and Kr takes on a new value, $-K_r'$. Equation 142 can be simplified to:

$$N_e = \frac{K_i}{K_r'} - \frac{K_v}{K_r' \cdot N_{O_2}} - \frac{K_{DF}}{K_r' \cdot N_{O_2}} \tag{143}$$

The only pressure sensitive terms in equation 143 are the diffusion and drift terms. As the pressure increases, these terms decrease; and the transition point values of E/N decrease. In order to determine the magnitude of the effect of these terms on the transition point, Chemco was modified to neglect the electron diffusion* and to compensate for the pressure effects of the electron drift**. The results of these modifications are illustrated in figure 84. As shown, the electron diffusion only has a minor effect on the transition point pressure dependence; the major effect is due to the drift loss. In fact, the particular compensation term that was used overcorrected the functional dependence and resulted in a change in the slope of the curve. No attempt was made to determine a better compensation term since the objective was only to determine the pressure dependent processes in Chemco.

<u>Effect of $O_2^*(a^1\Delta)$</u>. For many years one of the unknown aspects of the oxygen discharge has been the role $O_2^*(a^1\Delta)$ plays in determining the characteristics of the discharge. Although no direct measurement was made of the density of $O_2^*(a^1\Delta)$ during the experimental phase of this investigation***,

---

*Actually all of the charged particle diffusion terms were neglected. The negative ion diffusion losses are so low as to have negligible effect on the electron to negative ion ratio.

**Compensation term: $Vs' = \dfrac{N}{3.16 \times 10^{17}} \cdot Vs$

***The $O_2^*(a^1\Delta)$ densities that were predicted by the calculations were approximately equal to those reported by other experimenters for similar discharge conditions (Ref 53).

a comparison between the experimentally observed characteristics of the discharge and the results of the model of the discharge which includes $O_2^*(a^1\Delta)$ indicates that $O_2^*(a^1\Delta)$ plays a prominent role in the discharge. It affects the characteristics of the stable high field form in two different ways: first, two-step ionization is required* to achieve the electron densities observed during the experiments; and second, the detaching effect of $O_2^*(a^1\Delta)$ is required to match the high-to-low E/N transition values seen in the experiments.

Low Field Form. The unstable low field form of the discharge was studied experimentally in this investigation but was not modeled. A considerable expansion of the chemistry code would have been required to allow a time varying value of E/N and a fixed electrical current. The results of the high field model can be used, however, to draw inferences as to the processes involved in the low field form. At the point of transition between forms, it was shown that the attachment and detachment processes are very strong, and indeed dominated the gain and loss of the electrons. The logarithmic derivative of the attachment coefficient with respect to the reduced electric field is greater than that of the ionization coefficient. It is reasonable to assume, therefore, that as E/N is further decreased and the discharge becomes unstable, the instability can be characterized as

*In addition to direct ionization.

an ionization-attachment-detachment instability (Ref 54).

In such an instability, as a local variation in E/N takes place, the strong attachment rate* causes a local decrease in electron density. In order to maintain a constant discharge current, the value of E/N must decrease. This process continues until either the ionization rate dominates or until there is a sufficient buildup in detaching species to recover the electrons through the detachment process. The study of the stable discharge showed that the latter process occurs at a lower value of E/N than the former. Once the detachers are produced, they have a rather long life**; and during the time they are removing free electrons from the negative ions, the reduced field returns to a low value. Once the electrons are detached and/or the detachers have decayed or have chemically combined, the process starts over again.

Low-to-High Field Transition. The transition from the unstable low field form to the stable high field form is postulated to occur when the detacher specie density has increased to the point where the electron density is continuously greater than the negative ion density. The fact that the low-to-high and high-to-low transitions exhibit hysterisis phenomena indicates that different physical processes could be involved in triggering the transitions. For the

---

*Compared to ionization.

**Especially the $O_2^*(a^1\Delta)$.

low-to-high transition, a preliminary study (Ref 55) of the changes to the electron energy distribution function that occurs with dissociation indicates a shifting of energy into the high energy "tail" of the distribution. This was studied by inserting cross sections for atomic oxygen into the Boltzmann Equation Code and running the code for various percentages of dissociation. A study of the forward rates that were developed from the code runs indicated that dissociation could change the electron energy distribution function sufficiently to be initially self-enhancing. This process, therefore, could provide a positive feedback for the generation of atomic oxygen. Atomic oxygen is a good detacher but is not considered to be the prime detacher near the point of transition; $O_2^*(a^1\Delta)$ is. At the transition values of E/N the effect of the changing electron energy distribution function on the generation of $O_2(a^1\Delta)$ is small.

Conclusions

The following are the conclusions from the experimental and computational portions of the study. For the most part, this summary is qualitative only. Since the quantitative results are generally dependent on many variables, the reader should refer to the appropriate portion of the study report for the numerical results.

A summary of the major conclusions is presented first. This is followed by a more detailed listing of the results derived from the experimental and modeling phases of the study. All significant observations are listed. Some of these have been previously reported by other investigators and are listed here as corroboration. Other results are original with this study and are identified by asterisks.

Summary of Major Conclusions. The primary emphasis of this study was the development and experimental verification of a model of the stable, high-field form of the oxygen discharge. This model was then used to determine the characteristics of the stable discharge and the criteria for transition to the unstable, low-field form of the discharge.

The chemistry of the stable high-field form of the oxygen discharge is dominated by attachment and detachment processes. Electrons are continuously attached to and detached from the negative ions. The principle negative ion is O^-; however, the molecular negative ions O_2^- and O_3^- become significant as the pressure is increased. Both the metastable molecule, $O_2(a^1\Delta)$, and the atom, O, act as electron detachers. The former, however, was determined to be the predominant detacher. Although the negative ion densities are high in the stable discharge, their combined density is smaller than that of the electrons. With the exception of very high values of E/N, the positive molecular ion, O_2^+, dominates the atomic ion, O^+.

Although attachment/detachment processes dominate the electron chemistry, they tend to only transfer the electrons from bound to free states; any permanent electron losses must be balanced by ionization. In the stable discharge, the ionization processes are sufficiently strong to dominate recombination and other nonattachment losses. Two-step ionization from the ground level, $O_2(X^3\Sigma)$, through the metastable level, $O_2(a^1\Delta)$, of the molecule is an important source of electrons in the stable discharge.

The transition from the stable to the unstable form of the discharge occurs when the reduced electric field value, E/N, is lowered to the point where the logarithmic derivative of attachment with respect to E/N is greater than that of ionization and the combined negative ion densities equals that of the electrons. Pressure sensitive processes which directly or indirectly affect the electron density also affect the point of transition between the stable and unstable forms. The electron diffusion and drift losses cause a decrease in the value of the transition E/N as the pressure is increased. Also, the addition to the discharge of another detaching specie, CO, decreases the value of E/N at which the transition occurs.

Detailed Conclusions from the Experiments. The oxygen discharge was observed to exist in two forms, the high field form and the low field form. The transition between the forms is a function of pressure and current. The high field form generally exists at high currents and low pressures. The low field form was observed at low currents and high pressures. There is also evidence of a high field form that exists at very low currents and is not a function of pressure*.

The transition between forms exhibits a hysteresis effect. The discharge tends to persist in its form as the current is swept from high-to-low or low-to-high values.

Near the point of transition between forms, both forms tend to simultaneously exist in the positive column with the high field form on the anode side of the interface between forms and the low field form on the cathode side. The interface between forms usually occurs at a discontinuity in the discharge tube geometry, such as an electric field probe.

The impedances of the high and low field forms do not change as a function of gas flow velocity*. The transition point between forms does change however; as the flow velocity is increased, the transitions occur at lower currents; and hysterisis becomes more pronounced*.

The additive of an inert gas, argon, does not change the impedances of the high and low field forms*. The point of transition between forms is only slightly affected by the addition of argon; the transition current increases as argon is added*.

The addition of an electron detaching gas, carbon monoxide, (CO), to the discharge has marked effects on the discharge characteristics*. The addition of CO increases the low field impedance to the point where the difference between forms essentially ceases to exist; the impedance of

*Original observation.

the high field form is not affected*. As CO is added the transition point between forms decreases to lower currents, and the hysteresis effects become less pronounced*.

The high field form of the discharge was observed to be stable, with no perceivable oscillations or noiselike behavior.

The low field form of the discharge was observed to be nonstable, exhibiting either periodic or aperiodic, noiselike oscillatory behavior. The periodic oscillations exist only for certain frequencies or modes*. The discharge impedance is a function of the oscillation frequency*. The optical output from the periodic low field form is highly modulated. The photomultiplier output indicates very short pulses of light with relatively long dark periods between pulses. Electron density measurements indicate that the electron density is at a maximum during the dark period and at a minimum during the light pulses*. The oscillation frequency ranges from 20KHz to 90KHz. The oscillations exhibit a small amount of normal dispersion with phase velocities between 2.6×10^5 and 3.5×10^5 cm/sec and group velocities between 2.5×10^5 and 3.1×10^5 cm/sec.

The temperature of the discharge is represented by an analytic function of pressure and power input to the discharge*.

---

*Original observation.

Mass spectra data indicates that atomic oxygen concentration increases suddenly and significantly as the discharge transitions from the low-to-high field forms of the discharge*. In both forms there is a lack of measurable ozone.

Detailed Conclusions from the Modeling. The isotropic portion of the electron energy distribution exhibits a roll-off characteristic intermediate between that of Maxwellian and Druyvesteyn distributions.

For the range of E/N's that correspond to the experiments, the dominant positive ion was calculated to be O_2^+. At high values of E/N the O^+ density becomes dominant*.

The dominant negative ion was calculated to be O^-. As the E/N is lowered toward the point of transition from the high-to-low forms of the discharge, the number densities of the O_2^- and O_3^- ions become significant - especially at the higher values of initial molecular density (pressure)*.

The calculated atomic oxygen density indicates a high level of dissociation, especially at high values of E/N*.

The ozone density was calculated to be several orders of magnitude lower than the other neutral species carried in Chemco*.

The metastable $O_2^*(a^1\Delta)$ density was calculated to reach a maximum at relatively low values of E/N and then decrease as the E/N is increased*.

Over the range of 40-60 TD, it was determined that

---

*Original observation.

two-step ionization through the $O_2^*(a^1\Delta)$ state is an important contributor in matching calculated to experimental electron densities*. At higher values of E/N the two-step process becomes less important due to a decrease in the $O_2^*(a^1\Delta)$ density and due to the lower ionization threshold of the metastable becoming less important*.

The principal electron gain processes are electron detachment from the negative ions*. Both $O_2^*(a^1\Delta)$ and O act as the detachers with the predominate process involving the metastable molecule detaching the electron from the negative atomic ion*.

The principal electron losses are by attachment processes, both from the ground state and the metastable molecules.

Since the attachment/detachment processes only transfer electrons back and forth from bound to free states, any permanent losses are balanced by ionization. As the ionization decreases with decreasing E/N, these other loss processes eventually lead to a nonself-sustaining discharge (transition from high-to-low field forms).

One of the conditions for instability - the dominance of the derivative of the attachment coefficient with respect to E/N over that of the ionization coefficient - is satisfied for values of E/N below 67.4 TD*.

The other condition for instability - the equivalence

---

*Original observation.

of the negative ion and electron number densities - predicts reasonably well the experimentally determined transitions from the high-to-low field forms*. Calculations were made using both $O_2^*(a^1\Delta)$ and O as the dominant detacher. The $O_2^*(a^1\Delta)$ calculations provide the better match to experiments*.

The pressure effect of the transition between forms was determined to be due to the electron diffusion and drift loss processes*. As the pressure is increased, these processes have the tendency of increasing the electron density and thus decreasing the value of E/N at which the transition takes place*.

---

*Original observation.

XI. Limitations of the Study

and

Recommendations for Future Work

Limitations of the Study

Throughout this report the limitations associated with the experiments and with the model have been specified. It is appropriate at this point to summarize those limitations in order to provide an introduction into the recommendations for further work.

Experiments. The major limitation of the experimental portion of the study was the difficulty in determining the gas density exactly. Temperatures could be measured only at low values of input power. The gas densities at high input power were determined by an extrapolation process.

Models. The major limitations with the models were:

1. The electron energy distribution code was run only for the ground state molecular oxygen cross sections. It did not include the effects of other atomic and molecular species on the electron energy distribution function. The two species which were present in the discharge in large numbers were the metastable oxygen molecule, $O_2^*(a^1\Delta)$, and the oxygen atom. The inclusion of these in the Boltzmann Code could affect the transport and forward generation rates at the high E/N values where their densities were relatively significant.

For the E/N values at which the model was compared to the experiments, the rates calculated by EED would probably not change greatly in magnitude. Since the Chemco code only modeled steady conditions, the results would not change significantly with minor changes in the rates. A time varying code, however, could be affected by a minor but rapid change in the rates.

2. The rates utilized in the chemistry model were for one value of reduced field. Once the E/N was set on a particular run, it could not vary and thus model the oscillatory mode of the discharge or take into account external circuit effects. Therefore, only the steady state discharge was fully modeled.

3. The chemistry model did not include calculations of the radial distribution of the energies and densities of the different species. Radial density profiles were assumed in order to estimate diffusion losses. Calculations of the radial distributions and energies would lead to a more exact determination of diffusion losses.

Recommendations for Future Work

Experiments. Additional experimentation is required to fully compare the oxygen positive column with mathematical models and validate the models. Specifically, experiments should be repeated using a more exact method of determining the gas density. This is important because the model and experiment are linked through the E/N and N parameters.

Also, it would be extremely beneficial to be able to determine the absolute densities of the negative ions, atomic oxygen, and the $O_2^*(a^1\Delta)$ metastable molecules, since these species are important in the discharge in the region of transition.

Models. The chemistry model should be upgraded to include the calculation of the radial distributions of the species and their energies. The model should also allow for the species concentrations to feedback through a solution of the Boltzmann equation into a determination of the electron energy distribution function and thus the forward generation rates. This should allow the chemistry code to model the unstable form of the discharge in addition to the stable form. Each of these recommendations would have a very large impact on the size of the computer program and on the amount of computer time required to make a run.

If one is interested in high-pressure electron-beam sustained discharges, the chemistry code would have to be modified to model them. Two changes would be required: different chemical reactions would have to be included, and provisions would have to be made to incorporate a constant source of high energy electrons. The chemical reactions chosen for Chemco were the ones that were dominant for the pressure range of the study. For higher pressures the dominant rates would have to be re-established using the listing of Appendix D.

Bibliography

1. Djeu, Nicholas I. CW Atomic Oxygen Laser at 4.56. ARPA Order No. 660. Washington: Advanced Research Projects Agency, 1970.

2. Hubner, Gunter and Curt Wittig. "Some New Infrared Laser Transitions in Atomic Oxygen and Sulfur." Journal of the Optical Society of America, Vol. 61, No. 3:415-416

3. Rockwood, Stephen D. Mechanisms for Achieving Lasing on the 5577A Line of Atomic Oxygen. LA-VR-73-1031. Los Alamos, N.M.: Los Alamos Scientific Laboratory, 1973.

4. Ali, A.W. "N_2^+ Meinel and O_2^+ Second Negative Bands Laser Theory." Applied Optics, Vol. 12, No. 10:2243-2245 (October 1973).

5. Pirkle, Robert J., et al. "Production of Electronically Excited Iodine Atoms, $I(^2P_{1/2})$, Following Injection of HI Into a Flow of Discharged Oxygen." IEEE Journal of Quantum Electronics, Vol. QE-11, No. 10:834-838 (October 1975).

6. Fournier, Gerard, et al. Singlet Oxygen and Ozone Generation by an Electron-Beam-Controlled Discharge in Pure Oxygen. Preprint provided by the author to Dr. Garscadden. 1977.

7. Tanenbaum, B. Samuel. Plasma Physics. New York: McGraw-Hill Book Co., 1967.

8. Holt, E.H. and R.E. Haskell. Foundations of Plasma Dynamics. New York: The Macmillan Company, 1965.

9. Mitchner, M. and Charles H. Kruger Jr. Partially Ionized Gases. New York: John Wiley and Sons, 1973.

10. Cobine, James Dillon. Gaseous Conductors. New York: Dover Publications, Inc., 1958.

11. Von Engel, A. Ionized Gases (Second Edition). London: Oxford University Press, 1965.

12. Thompson, J.B. "The Ion Balance of the Oxygen D.C. Glow Discharge." Proceeding of the Royal Society (London), A262:519-528 (1961).

13. Guntherschulze, A. "Der Gradient in der Positiven Saule der Glimmentladung. II Sauerstoff, Luft, Wasserdampf, Helium, Argon, Krypton, Xenon, Queckoilber." Zeitschrift Fur Physik, 42:763 (1927). (In German).

14. Seeliger, Von R. and A. Wichman. "Untersuchungen uber die positive Saule der Glimmentladung in Sauerstoff. I." Annalen der Physik 6. Folge Band 9:235-244 (1951). (In German. Translated verbally by Dr. Wolgang Braun).

15. Pekark, L. "The Connection Between Low Gradient Form of the Positive Column in Oxygen and Moving Striations." Czechoslovakian Journal of Physics, B-10:749-753 (1960).

16. Sabadil, H. "Stratification Phenomena in the Positive Column of a Low Pressure Oxygen Discharge." Beitrage aus der Plasma Physik, Vol. 6, No. 5:305-317 (1966). (Original in German. Translated by Foreign Technology Division of AFSC, FTC-HC-23-1385-74, 25 June 74).

17. Edgley, P.D. and A. von Engel. "The Positive Column in Oxygen." Proceedings of the 10th Ionization Conference at Oxford:3.1.5.1 (1971).

18. Deckers, J.M. Energy Distribution in Flames and Electrical Discharges. Final Report, AFOSR Grant 375-64. Toronto, Ontario: Lash Miller Chemical Laboratories, University of Toronto, 1966. (AD638678).

19. Keren, H., et al. Positive Ion Mass Spectra of a Glow Discharge in Oxygen. Report submitted to Journal of Applied Physics. Jerusalem, Israel: The Racah Institute of Physics, The Hebrew University of Jerusalem, 1975.

20. Thompson, J.B. "Electron Energy Distributions in Plasma, IV Oxygen and Nitrogen." Proceedings of Royal Society (London), A262:503-518 (1961).

21. Koroleva, E.A. and L.E. Khvorostovskaya. "Deactivation Coefficients of the $O(^1D)$ and $O(^1S)$ Metastable Atoms in the Glow Discharge in Oxygen." Optical Spectroscopy, Vol. 35, No. 1:11-93 (July 1973).

22. Sabadil, H. "The Effect of Current Pulse on the Electric Field in the Column of A.D.C. Discharge in O_2." XI International Conference on Phenomena in Ionized Gases, Conference Abstracts: 3.1.5.9, 1973.

23. Sabadil, H. "On the Radial Structure of the Diffusion Designated Positive Column of Oxygen Discharge at Low-Gas Pressure." Beitrage Aus der Plasma Physik, Vol. 13, No. 4:235-251 (1973). (In German. Translated by Foreign Technology Division of AFSC, FTC-HC-23-2824-74, 21 October 74).

24. Thompson, J.B. "Negative Ions in the Positive Column of the Oxygen Discharge." Proceedings Physics Society, 73:818-821 (1959).

25. Lunt, R. Winstanley and A.H. Gregg. "The Occurrence of Negative Ions in the Glow Discharge through Oxygen and Other Gases." Transactions of the Faraday Society, 36:1062-1072 (1940).

26. Sabadil, Heinz. "Gunn Instabilities in the Positive Column of Oxygen Discharge." Beitrage Aus der Plasma Physik, Vol. 8, No. 4:299-308 (1968). (In German. Translated by the Foreign Technology Division of AFSC. FTD-HC-23-1387-74).

27. Sabadil, H. "On the Mechanism of the Homogeneous Positive Column in Oxygen Low Pressure Discharge." Beitrage Aus der Plasma Physik, Vol. 11, No. 1:53-66 (1971). (In German. Translated by the Foreign Technology Division of AFSC. FTD-HC-23-1387-74).

28. Grosu, D. and X. Grosu. "Comparative Study of the Electrical Oscillations in Positive and Negative Column in a D.C. Glow Discharge." Studii Si Cercetari de Fizica, Vol. 22, No. 4:409-420 (1970). (Translated by the Foreign Technology Division of AFSC. FTD-HC-23-1340-74).

29. Deckers, J.M. Energy Distribution in Flames and Electrical Discharges, Final Report, AFOSR Grant 375-65. Toronto, Ontario: Lash Miller Chemical Laboratories, University of Toronto, 1966.

30. Nighan, W.L. and W.J. Wiegand. The Influence of Negative Ion Processes on the Stability of Molecular Gas Discharges. UAR - N23. East Hartford, Conn.: United Aircraft Research Laboratories, 1974.

31. Mauer, J.L. and G.J. Schulz. "Associative Detachment of O^- with CO, H_2, and O_2." Physical Review A, Vol. 7, No. 2:593-605 (1973).

32. Weast, Robert C. Handbook of Chemistry and Physics (53rd) Edition). Cleveland, Ohio: The Chemical Rubber Co., 1972.

33. Shkarofsy, I.P. and A. Bonnier. Electrostatic Probes in Plasmas. Research Report No. FXc66-2. Quebec, Canada: RCA Research Laboratories, 1974.

34. Terman, Frederick E. Radio Engineering (Third Edition). New York: McGraw-Hill Book Company, 1947.

35. Buchsbaum, S.J. and Sanborn C. Brown. "Microwave Measurements of High Electron Densities." Physical Review, Vol. 106, No. 2:196-199 (April 15, 1957).

36. Slater, J.C. "Microwave Electronics." Review of Modern Physics, Vol. 18:441 (1946).

37. Ernst, W.P. A Survey of Microwave Electron Density Measuring Systems Used in Controlled Fusion Research. AEC Research and Development Report MAtt-871. Princeton, New Jersey: Princeton University Plasma Physics Laboratory, November 1971.

38. Garscadden, Alan. Time-Space Resolved Cavity Resonance Measurements. Plasma Physics Laboratory Internal Report. Wright-Patterson AFB, Ohio: Aerospace Research Laboratories, 1966.

39. Sicha, M., et al. "Characteristics of a Toroidal Resonator for Plasma Diagnostics." Canadian Journal of Physics, Vol. 45:3979-3989 (1967).

40. Sicha, M., et al. "A Contribution to the Measurement of the Electron Density of Discharge Plasma by Means of a Toroidal Resonator." Czechoslovakian Journal of Physics, B17:48-66 (1967).

41. Sicha, M. and V. Vesely. "Measurement of Electron Concentration of Plasma in Toroidal Resonator." Czechoslovakian Journal of Physics, B8:256 (1958).

42. Uman, Martin A. Introduction to Plasma Physics. New York: McGraw-Hill Book Co., 1964.

43. Long, William. Program EED. Plasma Physics Laboratory Internal Working Paper. Wright-Patterson AFB, Ohio: Aerospace Research Laboratories, 1974.

44. Brown, S.C. Basic Data of Plasma Physics. Boston, Massachusetts: MIT Press, 1967.

45. Nelson, D.R. and F.J. Davis. "Thermal and Near-Thermal Electron Transport coefficients in O_2 Determined with a Time-of-Flight Swarm Experiment Using a Drift-Dwell-Drift Technique." The Journal of Chemical Physics, Vol. 57, No. 10:4079 (15 Nov 1972).

46. Corbin, Robert J. A Time Resolved (Drift Tube) Study of Electron Avalanches in Oxygen. PhD Dissertation. Austin, Texas: The University of Texas at Austin, August 1973.

47. Rundle, H.W., et al. "Electron Energy Distribution Functions in an O_2 Glow Discharge." Canadian Journal of Physics, Vol. 51:144-148 (1973).

48. Phelps, Arthur V. Private Correspondence with Dr. Alan Garscadden of Plasma Physics Laboratory of Aerospace Research Laboratories. Boulder, Colorado: Joint Institute for Laboratory Astrophysics, 1975.

49. McDaniel, Earl W. and Edward A. Mason. The Mobility and Diffusion of Ions in Gases. New York: John Wiley and Sons, 1973.

50. Snuggs, R.M., et al. "Mobilities and Longitudinal Diffusion Coefficients of Mass-Identified Potassium Ions and Positive and Negative Oxygen Ions in Oxygen." Physics Review A, Vol. 3, No. 1:477-487 (1971).

51. Black, Graham et al. De-excitation of Metastables at Plasma Boundaries. ARL 73-0182. Wright-Patterson AFB, Ohio: Aerospace Research Laboratories, December 1973.

52. Haas, Roger A. "Plasma Stability of Electric Discharges in Molecular Gases." Physical Review A, Vol. 8, No. 2:1017-1043 (August 1973).

53. Foner, S.N. and R.L. Hudson. "Metastable Oxygen Molecules Produced by Electrical Discharges." Journal of Chemical Physics, Vol 25:601 (1956).

54. Hirsh, Merle N. and H.J. Oskam. Gaseous Electronics, Volume 1/Electrical Discharges. New York: Academic Press, Inc., 1978.

55. Private Correspondence between the Author and Dr. Alan Garscadden and Major William Bailey of the High Power Branch of the Aerospace Propulsion Laboratory. Dayton, Ohio: Wright-Patterson AFB, 1977.

56. Hake, R. and A. Phelps. "Momentum-Transfer and Inelastic Collision Cross Sections for Electrons in O_2, CO, and CO_2." Physical Review, Vol. 158, No. 1:70-84 (1967).

57. Veatch, G.E., et al. "Measurements of Electron-Collision Frequency for Momentum Transfer in Oxygen." Bulletin American Physical Society, 11:496 (1966).

58. Gerjuoy, E. and S. Stein. "Rotational Excitation by Slow Electrons." Physical Review, Vol. 97, No. 6:1671-1679 (1955).

59. Linder, F. and H. Schmidt. "Experimental Study of Low Energy e-O_2 Collision Processes." Z. Naturfarsch, A, 26:1617-1625 (1971).

60. Takayanagi, Kazuo and Tau Takahashi. "Collision Cross Sections between Oxygen Molecules and Low-Energy Electrons." Tokyo Daigaku Uche Koku Kenkyusho Hokoku, Vol. 3, No. 3:217-243 (Jouly 1967). (In Japanese. Translated by NASA, NASA TT F-15, 011, July 1973).

61. Wong, S.F., et al. "Vibrational Excitation of O_2 by Electron Impact above 4 eV." Physical Review Letters, Vol. 31, No. 16:969-972 (October 1973).

62. Trajmar, S., et al. "Differential and Integral Cross Sections for the Electron-Impact Excitation of the $a^1{}_g$ and $b^1{}_g^+$ States of O_2." Physical Review A, Vol. 4, No. 4:1482-1492 (October 1971).

63. Rapp, Donald and Donald D. Briglia. "Total Cross Sections for Ionization and Attachment in Gases by Electron Impact. II. Negative-Ion Formations." The Journal of Chemical Physics, Vol. 43, No. 5:1480-1489 (September 1965).

64. Rapp, Donald and Paula Englander-Golden. "Total Cross Sections for Ionization and Attachment in Gases by Electron Impact. I. Positive Ionization." The Journal of Chemical Physics, Vol. 43, No. 5:1463-1479. (September 1965).

65. Englander-Golden, P. and D. Rapp. Total Cross Sections for Ionization of Atoms and Molecules by Electron Impact. LMSC 6-74-64-12, Palo Alto, Calif.: Lockheed Missiles and Space Company, Dept. 52-10, 1965.

66. Rothe, E.W. et al. "Electron Impact Ionization of Atomic Hydrogen and Atomic Oxygen." Physics Review, 125:582 (1962).

67. Ferguson, Eldon E. "Laboratory Measurements of Ionospheric Ion-Molecule Reaction Rates." Reviews of Geophysics and Space Physics, Vol. 12, No. 4:703-713 (November 1974).

68. Bortner, M.H. and T. Baurer. Defense Nuclear Agency Reaction Rate Handbook (Second Edition). Santa Barbara, Calif.: DASIAC DOD Nuclear Information and Analysis Center General Electric, TEMPO, March 1972.

69. Niles, Franklin E. Survey of Two-Body and Three-Body Reaction-Rate Coefficients for the Ionized Stratosphere and Mesosphere. Report No. 1702. Aberdeen Proving Ground, Maryland: USA Ballistics Research Laboratories, March 1974.

70. Niles, Franklin E. "Airlike Discharges with CO_2, NO, NO_2 and N_2) as Impurities." Journal of Chemical Physics, 52:408 (1970).

71. Tisone, G.C. and L.M. Branscomb. "Detachment of Electrons from H^- and O^- Negative Ions by Electron Impact." Physics Review, 170:169 (1968).

72. Nighan, W. and J. Bennett. "Electron Energy Distribution Functions and Vibrational Excitation Rates in CO_2 Laser Mixtures." Applied Physics Letters, 14:240 (1969).

73. Schofield, K. "An Evaluation of Kinetic Rate Data for Reactions of Neutrals of Atmospheric Interest." Planetary and Space Science, 15:643 (1967).

74. Burrow, P.D. "Dissociative Attachment from the $O_2(a^1\ _g)$ State." Journal of Chemical Physics, Vol. 59, No. 9: 4922-4931 (November 1973).

75. Reaction Rate Data, No. 41. Santa Barbara, Calif.: DASIAC DOD Nuclear Information and Analysis Center. General Electric, TEMPO, July 1973.

76. Stone, E.J. and E.C. Zipf. "Electron-Impact Excitation of the $^3S^o$ and $^5S^o$ States of Atomic Oxygen." Journal of Chemical Physics, Vol. 60, No. 11:4238-4243 (June 1974).

77. Geltman, S. "Free-Free Radiation in Electron-Neutral Atom Collisions." Journal Quantum Spectroscopy, 13: 601 (1973).

78. Harrison, L. and I.L. Moruzzi. "Ion Mobilities and Ion-Molecule Reaction Rates in Oxygen." Journal of Physics, D: Applied Physics, Vol. 5:1239-1248 (1972).

79. Gilmore, Forrest. "Potential Energy Curves for N_2, NO, O_2 and Corresponding Ions." Journal of Quantitative Spectroscopy and Radiative Transfer, Vol. 5:369-389 (1965).

Appendix A

Microwave Cavity Program

The program listing presented in Table A - I was the one utilized to compute the electric field in the bore and interaction regions of the microwave cavity described in Chapter VI. The solution involved the utilization of a relaxation technique to solve Laplace's equation for the potential field. The electric field was then determined by numerically taking the spatial derivative of the potential field. The program was developed in collaboration with Captain M.R. Stamm of the Plasma Physics Laboratory* of the Aerospace Research Laboratories.

The geometry of figure A-1 was utilized in setting up the program:

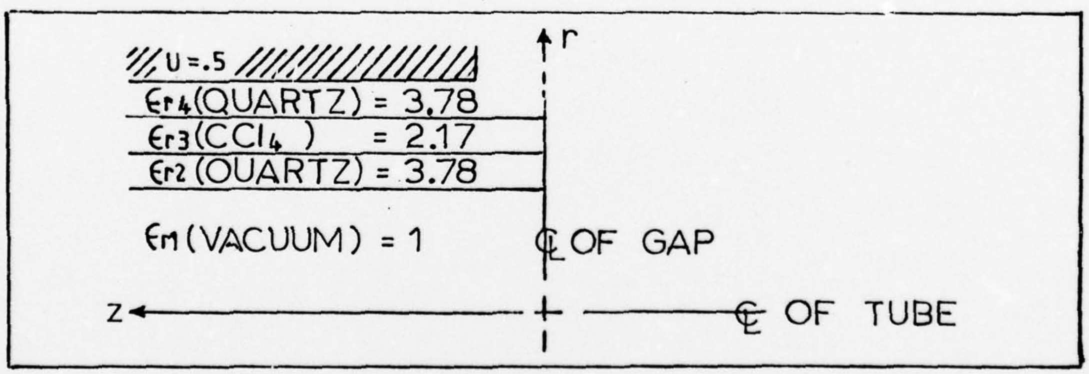

Figure A-1. Bore Region

---

*Now the High Power Branch of the A.F. Aero Propulsion Laboratory.

Cylindrical symmetry was assumed around the axis of the tube, and mirror symmetry was assumed on either side of the gap. Therefore, the problem was reduced from three to two dimensions in order to simplify its solution. The mesh was constructed of 71 divisions in the radial direction (1.4 cm) and 101 divisions in the z direction (4 cm). This resulted in a cell size of approximately .02 cm x .04 cm. The boundary condition on the pole was assumed to be .5 volt, corresponding to a U of 1 volt. The boundary along the $z = 0$ axis was assumed to be zero. The boundary across the gap was assumed to have a linear variation between 0 and .5 volt. The boundary at $z = 4$ cm was assumed to be zero. The $z = 0$ boundary was adjusted such that the first mesh point on the negative-r side of the z axis corresponded in value to the last mesh point on the positive-r side of the axis, for all values of z. Only one mesh point was carried on the negative-r side of the z axis. Values at each of the mesh points were calculated by successive solutions of Laplace's equation. The calculation was terminated when the maximum change in the successive values at any mesh point was less than the specified minimum of 5×10^{-9} volt.

Table A - I   Microwave Cavity Program

```
H S
      PROGRAM LAPLACE(INPUT,OUTPUT,PUNCH)
C
C     PROGRAM CONTROL CARDS
C     ******************************************************************
      DIMENSION A(71,101),B(71,101),EP(71,101)
      DR = .02
      DZ = .15875/4.
      IB = 71
      JB = 101
      IW = 18
      JW = 3
      V = .5
      DELMAX = 1.E-8*V
      MAXCNT = 500
      NEP1 = .975/DR + 1.5
      NEP2 = 1.10/DR + 1.5
      NEP3 = 1.25/DR + 1.5
      NEP4 = IB
C     ******************************************************************
C
C     AUXILARY VARIABLES
      F = (DR/DZ)**2
      X=SIN(3.14159/AMINO(IB,JB))
      W=2./(1.+X)
      JBM=JB-1
      IBM=IB-1
      IWM=IW-1
      JWM=JW-1
      NEP1P = NEP1 + 1
      NEP2P = NEP2 + 1
      NEP3P = NEP3 + 1
      PRINT 900, NEP1,NEP2,NEP3,NEP4
900   FORMAT(1X, *NEP1=*,I5*NEP2=*I5*NEP3=*I5*NEP4=*I5)
C
C     ESTABLISHING THE DIELECTRIC
      DO 16 J=1,JB
      DO 13 I=1,NEP1
13    EP(I,J) = 1.
      DO 14 I=NEP1P,NEP2
14    EP(I,J) = 3.78
      DO 15 I=NEP2P,NEP3
15    EP(I,J) = 2.17
      DO 16 I=NEP3P,NEP4
16    EP(I,J) = 3.78
C
      DO 9 I=IW,IB
      DO 9 J=JW,JB
      A(I,J)=V
9     B(I,J)=0.
      N=JBM
```

Table A - I   Microwave Cavity Program (continued)

```
      DO 1 I=1,IB
      A(I,1)=0.
      A(I,JW)=V
      A(I,JB)=V
      IF(I.GE.IW) N=JW-1
      DO 1 J=2,N
1     A(I,J)=.5*V
      DO 2 J=JW,JBM
      A(IW,J)=V
2     A(IB,J)=V
      ICOUNT=0
C
C     UPDATING THE POTENTIAL, A, AT EACH MESH POINT
11    N=JBM
      DEL=0.
      ICOUNT=ICOUNT+1
      DO 3 I=2,IBM
      IF(I.GE.IW) N=JW-1
      DO 3 J=2,N
      R = FLOAT(I-1)*DR
      AIJ = A(I,J)
      AIP = A(I+1,J)
      AIM = A(I-1,J)
      AJP = A(I,J+1)
      AJM = A(I,J-1)
      RES = (.5/(1.+F))*((.5*(AIP-AIM)*DR/R + (AIP-2.*AIJ+AIM)
     1  + F*(AJP-2.*AIJ+AJM)) + (.25/EP(I,J))*((EP(I+1,J)-EP(I-1,J))*
     2  (AIP-AIM) + F*(EP(I,J+1)-EP(I,J-1))*(AJP-AJM)))
      DEL=AMAX1(DEL,ABS(RES))
3     A(I,J)=A(I,J)+W*RES
      DO 4 J=2,JBM
      RES = (.5/(1.+F))*(2.*(A(2,J)-A(1,J)) + F*(A(1,J+1)-2.*A(1,J)
     1  +A(1,J-1)) + F*.25/EP(1,J)*(EP(1,J+1)-EP(1,J-1))
     2  *(A(1,J+1)-A(1,J-1)) )
4     A(1,J)=A(1,J)+W*RES
C     CONSTANT FIELD AT THE SLIT
      DO 5 J=2,JWM
5     A(IB,J) = V*FLOAT(J-1)/FLOAT(JWM)
C
      IF(DEL.LT.DELMAX)  GO TO 12
      IF(ICOUNT.GE.MAXCNT) GO TO 12
      GO TO 11
C
C     PRINT AND PLOT STATEMENTS
12    PRINT*, ICOUNT,DEL
C
C     COMPUTING THE SQUARE OF THE FIELD, B, AT EACH MESH POINT
      N=JBM
      DO 6 I=2,IBM
      IF(I.GE.IW) N=JW-1
```

Table A - I   Microwave Cavity Program (continued)

```
      DO 6 J=2,N
6     B(I,J)=((A(I+1,J)-A(I-1,J))**2+F*(A(I,J+1)-A(I,J-1))**2)/DR**2/4.
      DO 7 I=1,IB
      B(I,1)=A(I,2)**2/DZ**2
      IF(I.LT.IW) B(I,JB)=(A(I,JB)-A(I,JBM))**2/DZ**2
7     IF(I.GT.IW) B(I,JW)=(A(I,JW)-A(I,JWM))**2/DZ**2
      DO 8 J=2,JBM
      B(1,J)=(A(1,J+1)-A(1,J-1))**2/4./DZ**2
      IF(J.GT.JW) B(IW,J)=(A(IW,J)-A(IWM,J))**2/DR**2
8     IF(J.LT.JW) B(IW,J)=(A(IB,J+1)-A(IB,J-1))**2/4./DZ**2
      B(IW,JB)=0.
      B(IW,JW)=((A(IW,JW)-A(IW,JWM))**2)/DZ**2
C
C     CALCULATE ENERGY
      TOTAL = 0.
      DO 34 I=1,49
      ENERG = 0.
      DO 30 J = 1 , 100
      EN = 1.
33    DELTA=.3926990818*DR**2*DZ*(2.*I-1.)*(B(I,J)+B(I+1,J)+B(I,J+1)
     I +B(I+1,J+1)) * EN
30    ENERG = ENERG + DELTA * 8.
      TOTAL = TOTAL + ENERG
      ZR = DR * FLOAT(I)
34    PRINT 36, ZR,TOTAL
36    FORMAT (1X, F10.7, E15.5)
      STOP
      END
```

Appendix B

Electron Impact Cross Sections

In this appendix the electron impact cross sections utilized in the Boltzmann equation program, EED*, are presented. All of the cross sections, with the exception of rotational excitation, were determined from experimental data. The rotational excitation cross section was derived from a theoretical development. Dr. Arthur Phelps' consultation was extremely helpful in choosing the set of electron impact processes to include in the Bolzmann code and in determining the values of the cross sections (Ref 45). The information Dr. Phelps provided was based on his experiences in running Boltmann codes and matching experimental transport parameters.

Momentum Transfer Cross Section (Figure B-1)

The momentum transfer cross section was taken from Reference 56:72. The listing was for the data without the 4.5 ev resonance. At energies below 1 electron volt, the cross section was reduced slightly in order to agree with the microwave data of Reference 57 and the drift velocity data of Reference 45.

---

*Refer to Appendix C.

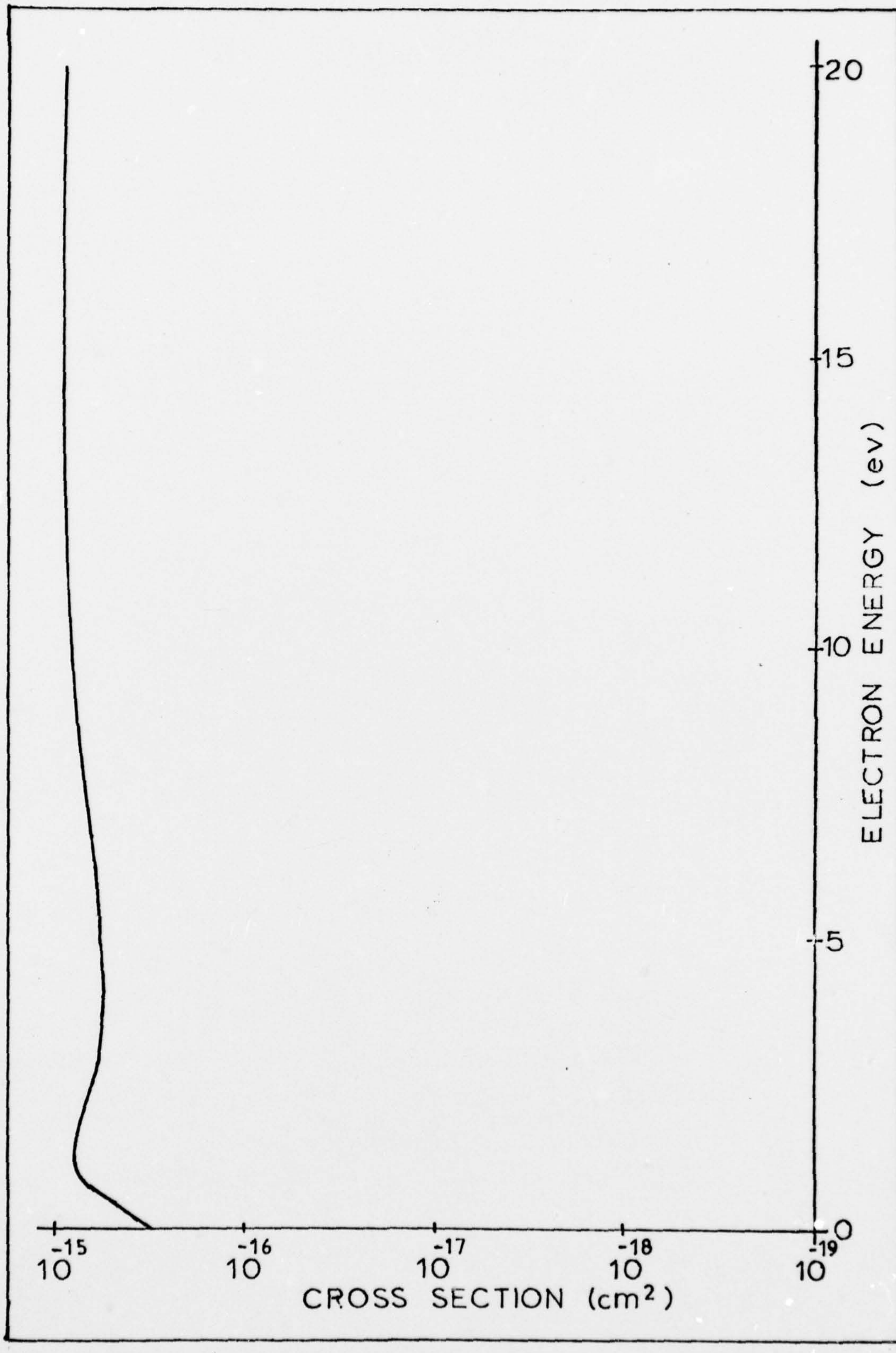

Figure B-1. Momentum Transfer Cross Section

Rotational Excitation

A rotational cross section of $.15 \times 10^{-16} cm^2$ was used with a threshold of .001 ev (Ref 58:1674).

Low Energy Vibrational Excitation Cross Sections (Figure B-2)

Low energy vibrational excitation is accomplished primarily by resonance scattering from the vibrationally-excited, temporary, negative-ion states. Direct excitation of the vibrational levels of the ground-state, neutral molecule is roughly on the order of 1% of the excitation through the resonance channels (Ref 59:1619, 1621). The data used for the low energy vibrational excitation cross sections were taken from Reference 59. Since the cross sections were so narrow, their magnitudes were adjusted to make their energy-integrated values match. Once this was accomplished, the cross sections were doubled to allow the low energy transport parameters calculated by the program EED to match experimental values. This adjustment was recommended by Dr. Phelps (Ref 48) and was also confirmed by adjusting a cross-section multiplication factor, running the program EED and then comparing the drift velocity against drift tube data.

The thresholds for the vibrational excitations were taken from Reference 60: $\nu = 0 \rightarrow 1$, 1190 ev; $\nu = 0 \rightarrow 2$, .380 ev; $\nu = 0 \rightarrow 3$, .570 ev; and $\nu = 0 \rightarrow 4$, .750 ev.

High Energy Vibrational Excitation Cross Sections (Figure B-3)

The low energy vibrational excitation cross sections were via the ground state, temporary negative-ion resonance.

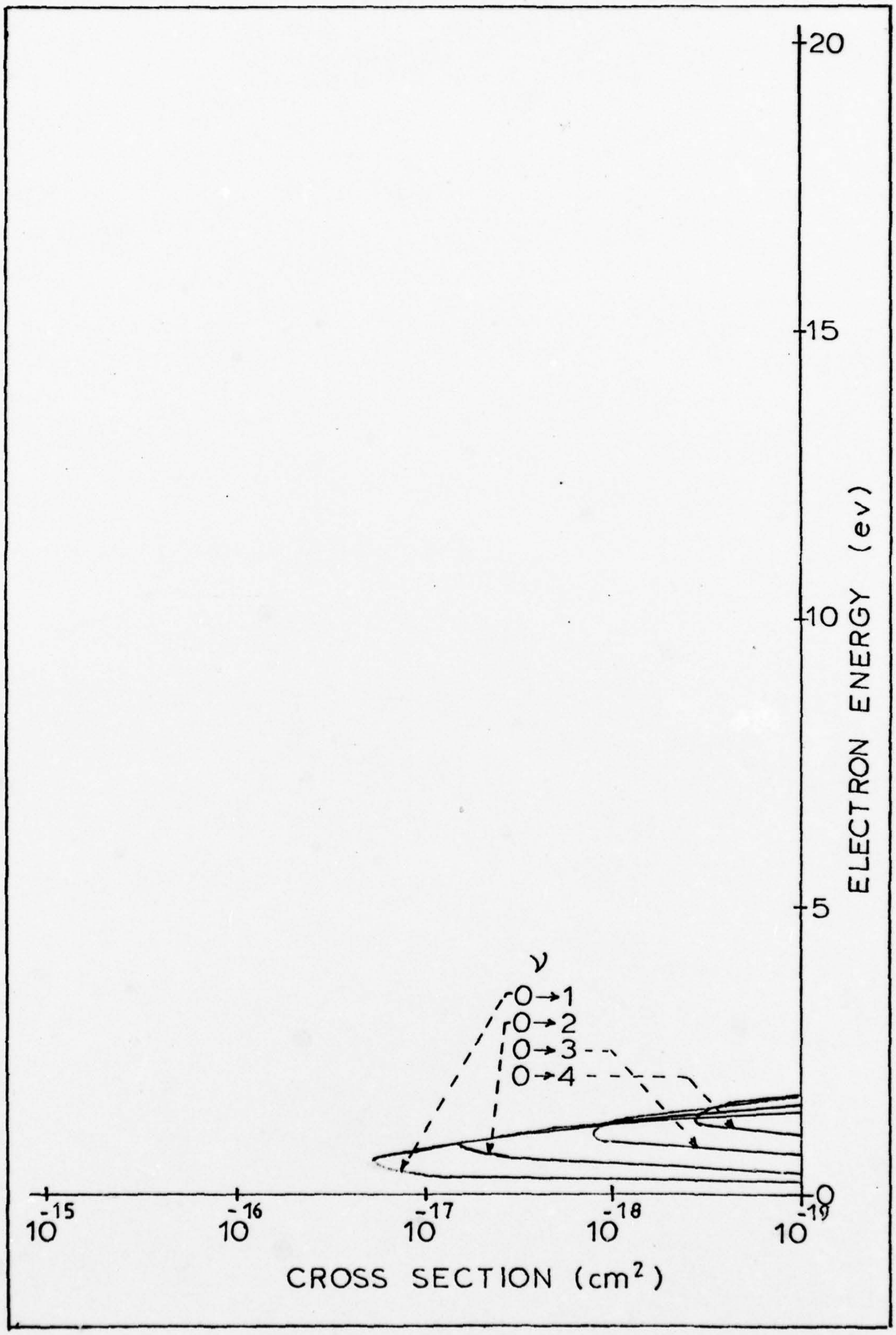

Figure B-2. Low Energy Vibrational Excitation Cross Sections

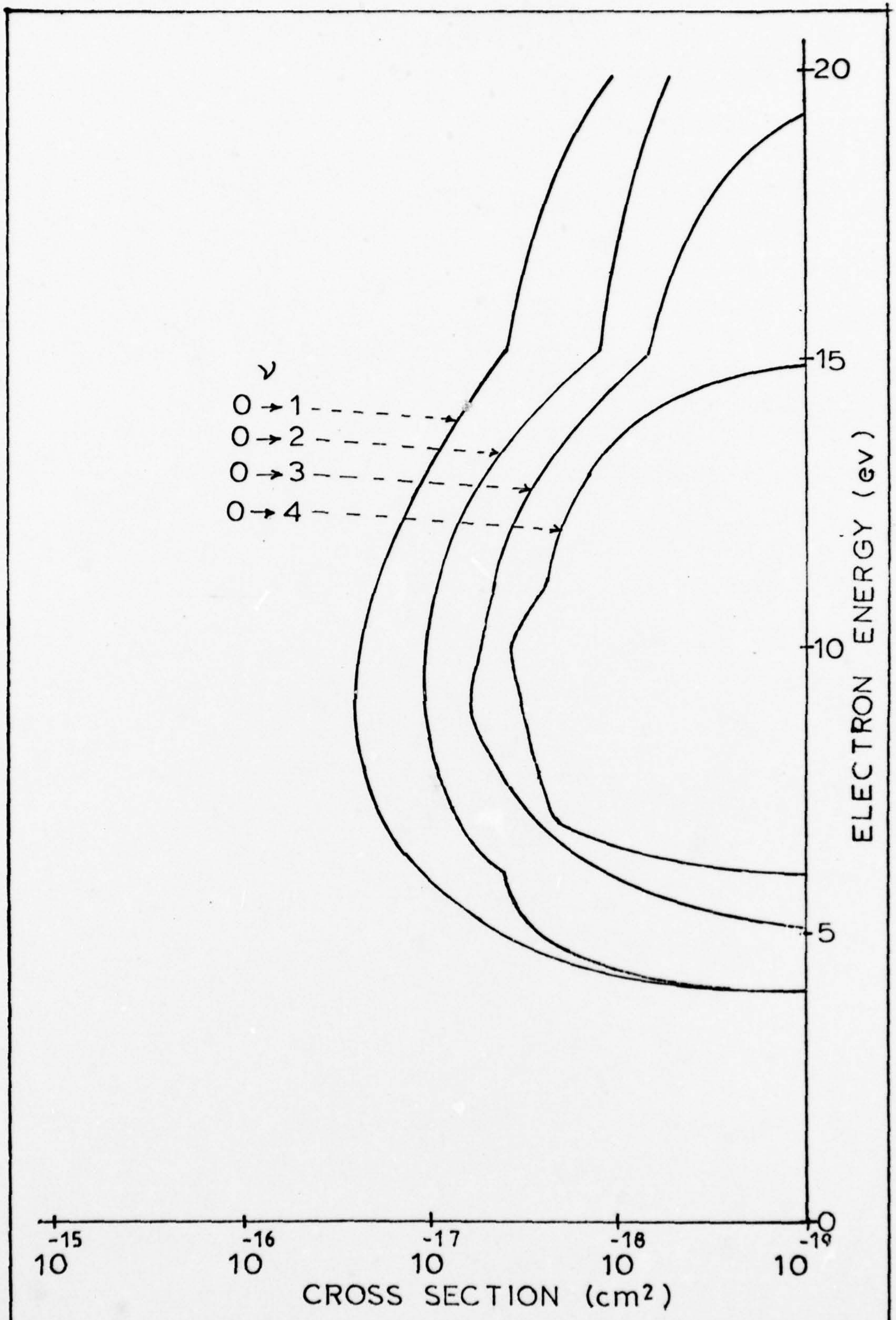

Figure B-3. High Energy Vibrational Excitation Cross Sections

Vibrational excitation of the ground state neutral molecule has been observed to also occur via electronically excited, temporary, negative-ion resonances. The data for these high energy vibrational cross sections were provided by Dr. Phelps (Ref 48). He derived the values by normalizing the differential cross sections of Reference 61:970 to the integrated values provided by Reference 62.

The energy losses for these cross sections were the same as used for the corresponding low energy vibrational excitations.

Electronic Metastable Excitation Cross Sections (Figure B-4)

The cross sections for excitation of the ground state molecule, $O_2(X^3\Sigma_g^-)$, to the two low metastable levels, $O_2^*(a^1\Delta_g)$ and $O_2^*(b^1\Sigma_g^+)$, were taken from Reference 62:1491.

The threshold used for the $O_2^*(a^1\Delta_g)$ excitation was .980 ev; for the $O_2^*(b^1\Sigma_g^+)$ excitation, 1.672 ev.

Electronic Excitation Cross Sections (Figure B-5)

The cross sections for the 4.5, 6.0, and 8.4 ev threshold excitations were provided by Dr. Phelps (Rev 48).

Dissociative Attachment (Figure B-6)

The cross section for dissociative attachment* from the ground level state was taken from Reference 63:1486.

In the absence of measured data, the cross section for

---

*$e + O_2(X^3\Sigma_g^-) \rightarrow O + O^-$

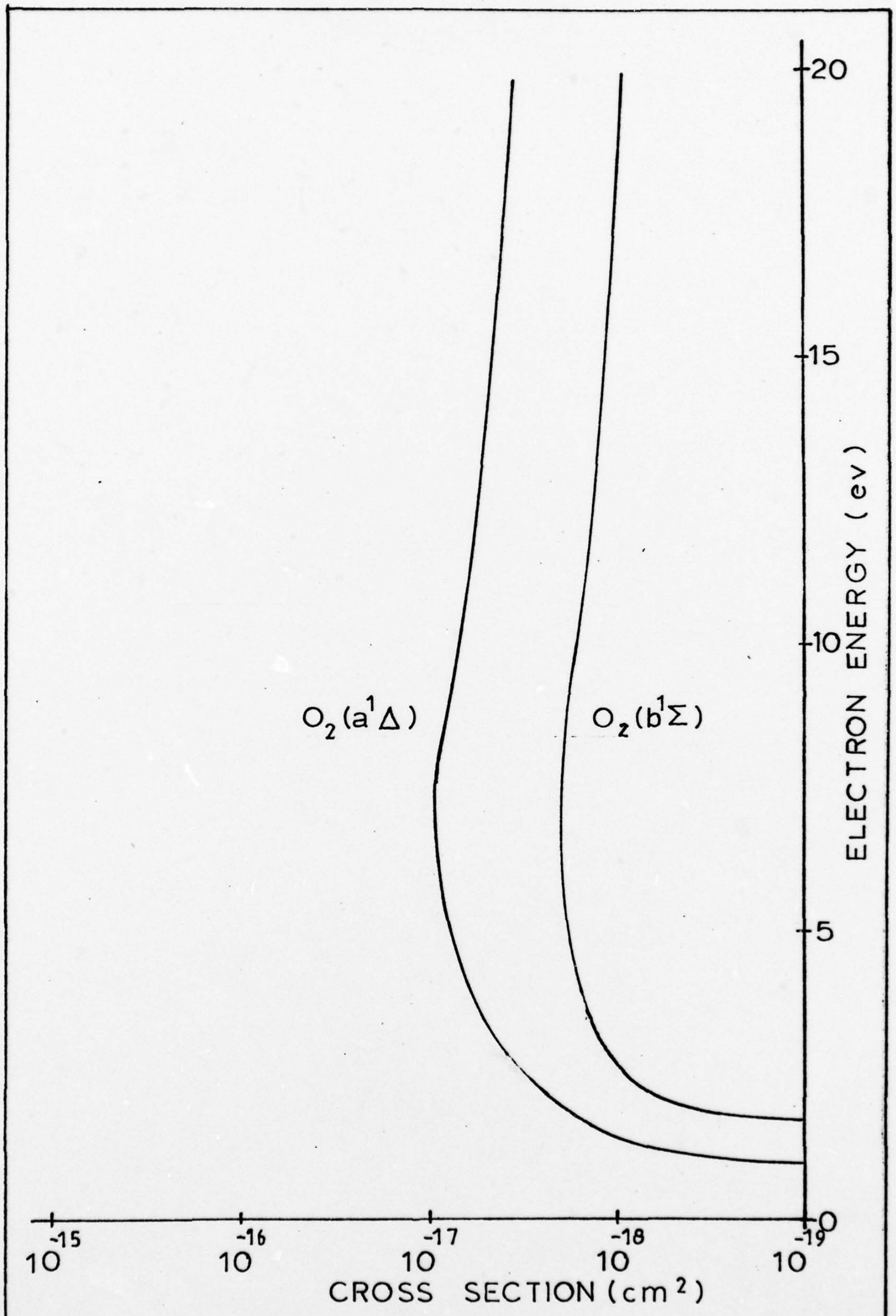

Figure B-4. Electronic Metastable Excitation Cross Sections

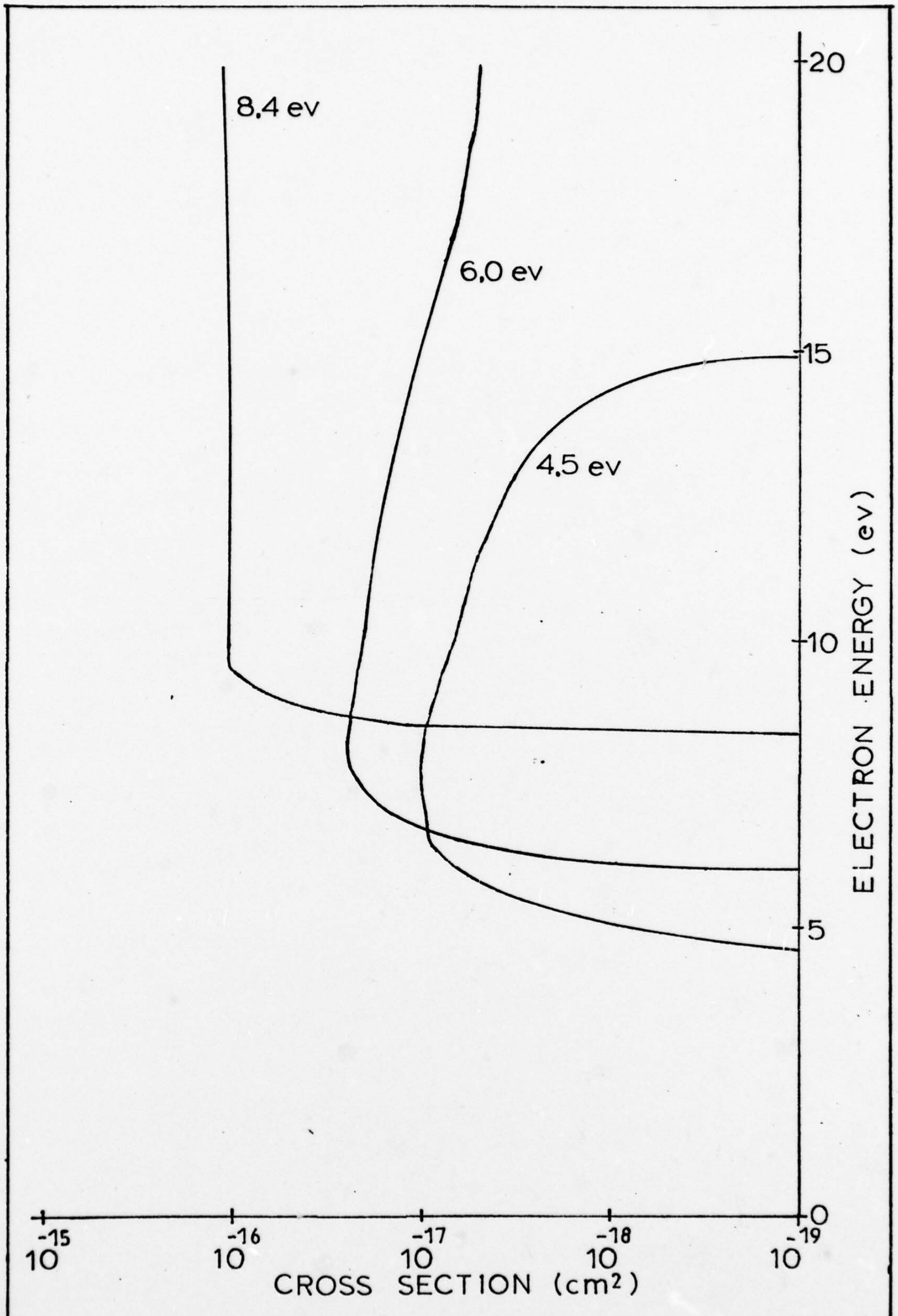

Figure B-5. Electronic Excitation Cross Sections

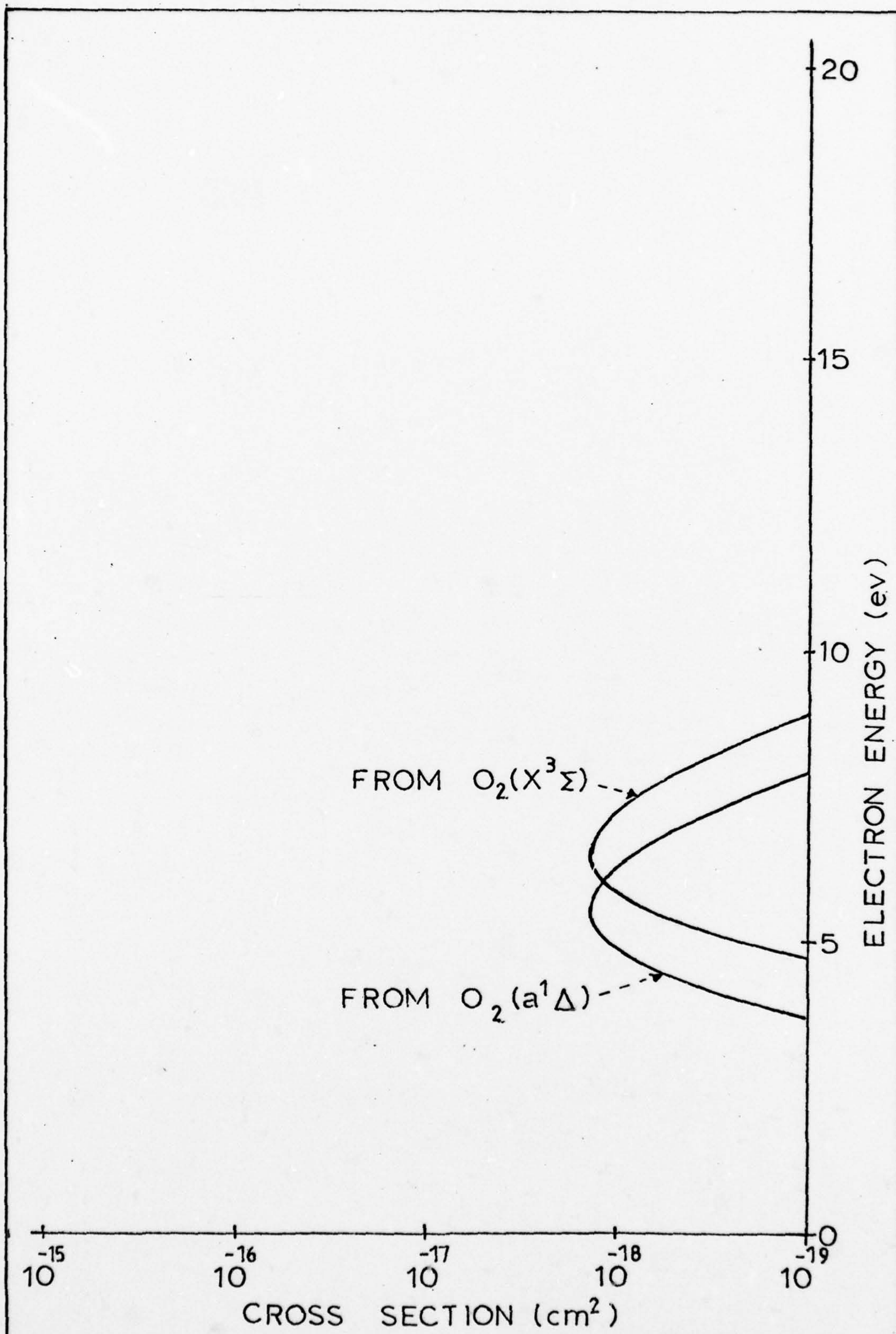

Figure B-6. Dissociative Attachment Cross Sections dissociative attachment from the $O_2^*(a^1\Delta_g)$ state was assumed to be the same shape and magnitude as the process from the ground state. However, the energy values were shifted down by .98 ev, the difference in energy between the two states. This assumption was based on the similiarity of the potential energy curves for the two states. In order to avoid having the dissociative attachment cross section from the $a^1\Delta_g$ state influence the electron energy distribution calculation, the cross section values were decreased by two orders of magnitude when they were entered into EED; the reaction rates that were calculated by the program for the process were then increased by two orders of magnitude to compensate. The influence of the excited state dissociative attachment cross section on the distribution function was eliminated due to a lack of knowledge of the relative population of the excited level. If this population were known, the cross section would have been included; and a more exact calculation of the distribution function would have been possible.

The threshold for the ground state process was 4.400 ev; for the excited state process, it was 3.420 ev.

Molecular Ionization (Figure B-7)

The molecular ionization cross section for the ground state process was taken from Reference 64:1471-1472.

The cross section for the excited state process was derived and handled in a manner similar to that discussed

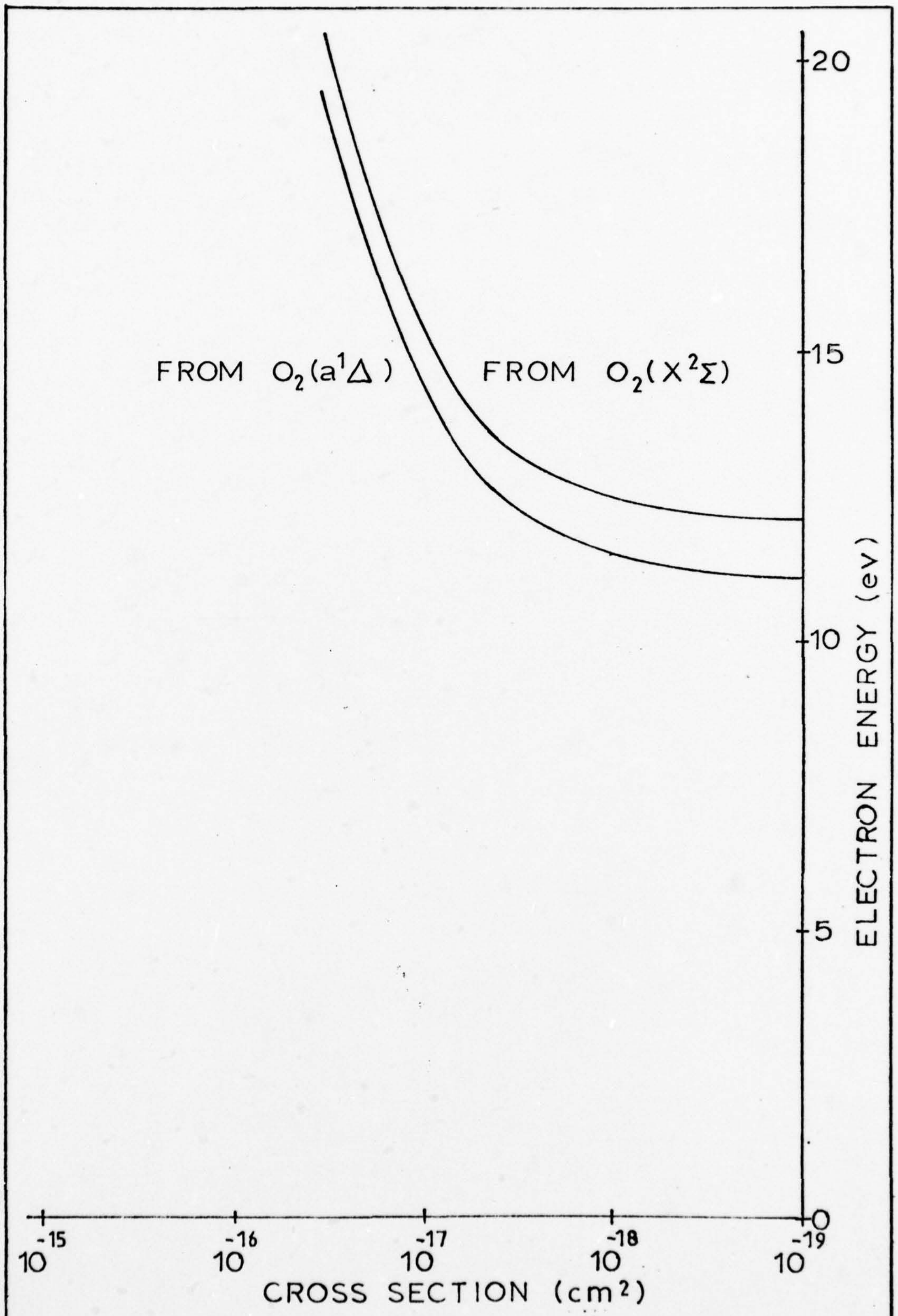

Figure B-7. Molecular Ionization Cross Sections for the dissociative attachment process.

The threshold for the ground state ionization was 12.200 ev; for the excited state process, it was 11.220 ev.

Dissociative Ionization (Figure B-8)

The dissociative ionization cross section was taken from Reference 65.

The threshold energy for the process was 18.5 ev.

Atomic Ionization (Figure B-8)

The atomic ionization cross section was taken from Reference 66. The cross section values utilized in the EED program were decreased by two orders of magnitude to avoid influencing the distributions. The ionization rates that came out of the code runs were increased by two orders of magnitude to compensate. The reason for the de-emphasis of the cross section is the same as for the dissociative attachment from the $O_2^*(a^1\Delta_g)$ state.

The threshold energy for the atomic ionization process was 13.618 ev.

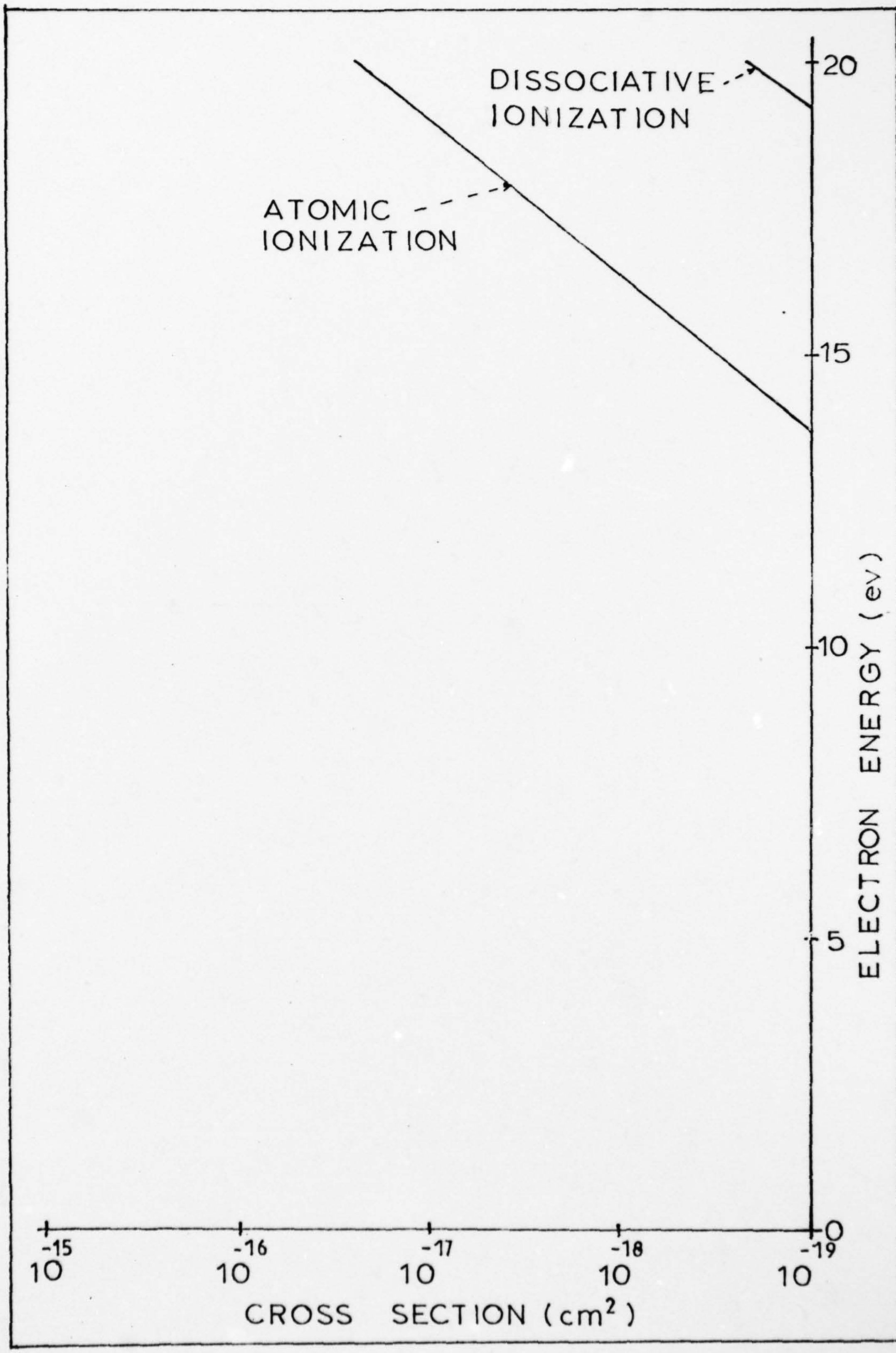

Figure B-8. Atomic Ionization Cross Sections

Appendix C

Boltzmann Equation Program, EED

The program listing presented in Table C - I was the one utilized to calculate the electron energy distributions, transport properties, and reaction rates described in Chapter VIII. The program was developed by William Bailey and William Long for use by the personnel of the Plasma Physics Laboratory* of the Aerospace Research Laboratories. The only portion of the program provided by the author was the consistent set of cross sections described in Appendix B.

---

*Now the High Power Branch of the A.F. Aero Propulsion Laboratory.

Table C - I   Boltzmann Equation Program, EED

```
      PROGRAM  EED (INPUT,OUTPUT,PUNCH,DATA,TAPE5=DATA,PLOT)
      DIMENSION XR(30)
      COMMON/CROSS/ A(5),INX(5),ING
      COMMON/FUN/ ETA(200,30),QR(200),DF(200),EOVRN,XMR,ID(30),
     $  DEP(30),Q(200),ITP,IOV,DU,TG,TV,F,XNU(30),XNV(30),IVO,IVI,AN
      COMMON/SUN/ BTA(200),DOF(200),DEL(200),RT(50),ITV(30)
      COMMON/SCALER/LX,LY,XP(5),NAME(5)
      DATA IPRT,IPN/1,0/
      DATA F,TV,TG/0.,0.,293./
C
C
C     ********   EED    *** NUMERICAL SOLUTION OF BOLTZMANN EQUATION ****
C
C       EED NUMERICALLY SOLVES THE COLLISIONAL BOLTZMANN EQUATION IN THE
C     P1 APPROXIMATION FOR THE ELECTRON ENERGY DISTRIBUTION FUNCTION.
C     FROM THIS IS CALCULATED THE MEAN ENERGY, DRIFT VELOCITY, AND
C     ENERGY LOSS RATES.
C
C     READ IN BASIC PARAMETERS
      READ*, NEN,IPRT,IPN
C1    NUMBER OF E/N,S TO BE CALCULATED
C3    PRINT OUT F0 AND F1             IPRT=1
C                                     IPRT=0  NOT REQUESTED
C5    PUNCH OPTION REQUESTED        IPN=1
C                                   IPN=0 NO PUNCH
C
      XMR=1.09E-3
      CALL CROSS
      MOM=200
      IOV=MOM
      DO 46 I=1,MOM
46    DOF(I)=1.
      DO 42 INU=1,NEN
      PRINT99,IPRT
   99 FORMAT(I1)
      PRINT100,(XP(IR)*100.,NAME(IR),IR=1,ING)
  100 FORMAT(5(1X,F10.2,*%*,3X,A10))
C
C     READ E/N VALUES
C     ************************************************************
      READ*,EOVRN,F,TV,TG
C     EOVRN=EOVRN/3.54
      IF(TV.GT.10.) TV=TV/11605.4
      IF(TG.GT.10.) TG=TG/11605.4
      DO 13 J=1,30
      XNU(J)=1.
   13 XNV(J)=0.
      IF(TV.GT.0.) CALL VIB
      CALL INTGRAL
C
```

Table C - I Boltzmann Equation Program, EED (continued)

```
C      CALCULATE NORMALIZATION CONSTANT, MEAN ENERGY , AND F1
C      ****************************************************************
       EBR=0.
       DE=0.
       QLOSS=0.
       VD=0.
       XNERM=0.
       SIM=2./3.
       DO 400 I =1,IOV
       UX=FLOAT(I)*DU
       SIM=2.-SIM
       XNERM=XNERM+DF(I) *UX**.5*DU *SIM
       EBR=EBR+DF(I) *UX**1.5*DU*SIM
       DE=DE+DF(I)*UX*DU*SIM/QR(I)
       QLOSS=QLOSS+Q(I)*XMR*UX**2*(DF(I)-TG*QR(I)*BTA(I)/EOVRN)*SIM*DU
       VD =VD +BTA(I)*UX*DU*SIM
400    CONTINUE
       EBR=EBR/XNERM
       DE=DE*5.9E7/XNERM/3.
       QLOSS=QLOSS*5.929E-9/XNERM
       VD=VD*5.929E7/XNERM/3.
       DO 14 I=1,MOH
       BTA(I)=BTA(I)/XNERM
       DF(I)=DF(I)/XNERM
14     CONTINUE
       PRINT 503, EOVRN*1.E-16,F*XNERM
  503 FORMAT (1X ,*    E/N*,1PE12.2,*  V-CM2*,10X,*FRACTIONAL IONIZATION*
     $,1PE12.2)
C      PRINT 503, EOVRN*3.54   ,F*XNERM
C 503 FORMAT (1X ,*    E/P*,1PE12.2,*  V/CM/TORR*,10X,*FRACTIONAL IONIZAT
C    $ION*,1PE12.2)
       PRINT 504, TV*11605.4,TG*11605.4
  504 FORMAT (1X,*   VIBRATIONAL TEMPERATURE*,F12.2,* K*,10X,*GAS TEMPER
     $ATURE*,F12.2,* K*)
       IF(IPRT.EQ.0) GO TO 9
       PRINT 507
  507 FORMAT(1H0,* NORMALIZED DISTRIBUTION FUNCTION F0*)

C      WRITE F0 AND F1
C      ****************************************************************
       PRINT 8, (DF(I),I=1,IOV)
       IF(IPN.EQ.1) PUNCH 666,    (DF(I),I=1,IOV)
       PRINT 604
604    FORMAT(1H0,* F1 COMPONENT OF DISTRIBUTION*)
       PRINT 8, (BTA(I),I=1,IOV)
8      FORMAT(1P,(1X,10E12.4))
       PRINT 50, DU
50     FORMAT (1H0,* ENERGY STEP =*,F5.3)
  666 FORMAT (1X,5E12.4)
       XON=0.
```

Table C - I Boltzmann Equation Program, EED (continued)

```
C       WRITE OUT PUMPING RATES AND ENERGY LOSSES FOR ADDED GASES
C       ****************************************************************
9       XJE=0.
        EIN=VD*EOVRN*1.E-16
        PRINT 490, QLOSS/EIN
  490   FORMAT(1H0,  * FRACTIONAL RECOIL ENERGY LOSS*,F12.4)
        EE=0.
        IBT=1
        DO 848 ITM=1,ING
        ITP=INX(ITM)-1+IBT
        DO 846 J=IBT,ITP
        XR(J)=0.
        IF(ID(J).GE.MOM-1) GO TO 846
        P=DEP(J)/DU-FLOAT(ID(J))
        XR(J)=ETA(ID(J)+1,J)*(XNU(J)*DOF(ID(J)+1)-XNV(J)*DOF(1))*(1.-P/2.)
        ILO=ID(J)+2
        DO 845 I=ILO,MOM
        U=FLOAT(I)*DU
        XR(J)=XR(J)+ETA(I,J)*(XNU(J)*DOF(I)-XNV(J)*(P*DOF(I-ID(J)-1)+(1.-
       $P)*DOF(I-ID(J))))
  845   CONTINUE
  846   XR(J)=XR(J)*5.929E-9/XP(ITM)*DU/XNERM
        PRINT 505,NAME(ITM)
  505   FORMAT(1X,     * NET PUMPING RATES   CM3/SEC   FOR *,A10)
        PRINT 8,     (XR(I),I=IBT,ITP)
        DO 847 J=IBT,ITP
        BTA(J)=XR(J)*DEP(J)*XP(ITM)
        EE=EE+BTA(J)
847     CONTINUE
        PRINT 511,NAME(ITM)
  511   FORMAT(1X,* FRACTIONAL ENERGY DEPOSITION FOR *,A10)
        PRINT 10, (BTA(J)/EIN,J=IBT,ITP)
   10   FORMAT(1X,10F12.4)
        IBT=ITP+1
848     CONTINUE
        EE=EE+QLOSS
        PRINT 492, EBP,DE*1.E16
  492   FORMAT (1H0, * MEAN ENERGY*,F12.3,* EV*,10X,*DIFFUSION COEFFICIENT
       $*,1PE12.4,* 1/CM/SEC*)

C       WRITE DRIFT VELOCITY AND CURRENT DENSITY
        ECH=EOVRN*DE/VD
        PRINT 510,    VD,ECH
  510   FORMAT(1X,1P, * DRIFT VELOCITY*,E12.4,* CM/SEC*,10X,*CHARACTERISTI
       $C ENERGY*,0PF12.3,* EV*)
        ERR =    (EE-EIN)/EIN*100.
        PRINT 512, ERR
  512   FORMAT(/ *  ENERGY BALANCE*,F10.2,* %*)
42      CONTINUE
        END
```

Table C - I   Boltzmann Equation Program, EED (continued)

```
      SUBROUTINE CROSS
      COMMON/CROSS/ A(5),INX(5),ING
      COMMON/FUN/ ETA(200,30),QR(200),DF(200),EOVRN,XMR,ID(30),
     $ DEP(30),Q(200),ITP,IOV,DU,TG,TV,F,XNU(30),XNV(30),IVO,IVI,AN
      COMMON/SUN/ BTA(200),DOF(200),DEL(200),RT(50),ITV(30)
      COMMON/SCALER/LX,LY,XP(5),NAME(5)
      DATA SCALE,EGRID/1.,0./
      READ*,ING,UMAX
      DU=UMAX/200.
      DO 10 I=1,200
      Q(I)=0.
   10 QR(I)=0.
      ITP=0
      DO 40 IR=1,ING
      NVO=0
      READ*, NAME(IR),XP(IR),A(IR),INX(IR),NVO,NVI,AN
      IF(NVO.EQ.0) GO TO 11
      IVO=NVO+ITP-1
      IVI=NVI+ITP-1
   11 IP=INX(IR)
      INX(IR)=IP-1
      DO 40 IN=1,IP
      READ*,LABEL,EL,SCALE,EGRID
      IF(EGRID.EQ.0.) GO TO 15
      READ*,(DF(I),I=2,200),DUM
      DF(1)=DF(2)
      DOF(1)=0.
      DO 12 I=2,200
      DOF(I)=EGRID*FLOAT(I-1)
      IF(EL.GT.0.) DF(I)=DF(I)/DOF(I)
   12 CONTINUE
      GO TO 16
   15 READ*,(DOF(I),DF(I),I=1,200)
   16 DO 30 IX=1,199
      IF(DF(IX).NE.0.) RTJ=DOF(IX+1)
      ILO=IFIX(DOF(IX)/DU)+1
      IHI=IFIX(DOF(IX+1)/DU+.001)
      IF(ILO.GT.IHI) GO TO 30
      IF(IHI.GT.200) IHI=200
      SLOPE=(DF(IX+1)-DF(IX))/(DOF(IX+1)-DOF(IX))
      DO 20 I=ILO,IHI
      U=FLOAT(I)*DU
   20 DEL(I)=(DF(IX)+SLOPE*(U-DOF(IX)))*SCALE
      IF(IHI.EQ.200) GO TO 35
   30 CONTINUE
   35 IQ=IX+1
      IF(IQ.GT.200) IQ=200
      IF(EL.GT.0.) GO TO 37
      PRINT101, LABEL,SCALE,(DOF(I),DF(I),I=1,IQ)
```

Table C - I   Boltzmann Equation Program, EED (continued)

```
      DO 36 I=1,200
      Q(I)=Q(I)+XP(IR)*DEL(I)/A(IR)
   36 QR(I)=QR(I)+XP(IR)*DEL(I)
      GO TO 40
   37 ITP=ITP+1
      DEP(ITP)=EL
      ID(ITP)=IFIX(EL/DU)
      RT(ITP)=RTJ
      PRINT102, LABEL,EL,SCALE,(DOF(I),DF(I),I=1,IQ)
      DO 39 I=1,200
      U=FLOAT(I)*DU
   39 ETA(I,ITP)=DEL(I)*U*XP(IR)
   40 CONTINUE
      DO 50 I=1,200
      U=FLOAT(I)*DU
      DO 50 K=1,ITP
   50 QR(I)=QR(I)+ETA(I,K)/U
  101 FORMAT(1H0,A10,3X,*MOMENTUM TRANSFER CROSS SECTION*,
     $32X,*SCALE FACTOR=*,F6.2/
     $(1X,5(F6.2,3X,F8.4,6X)))
  102 FORMAT(1H0,A10,3X,*INELASTIC PROCESS WITH ENERGY LOSS=*,F7.3,*EV*,
     $20X,*SCALE FACTOR=*,F6.2/
     $(1X,5(F6.2,3X,F8.4,6X)))
      RETURN
      END
      SUBROUTINE INTGRAL
      COMMON/FUN/ ETA(200,30),QR(200),DF(200),EOVRN,XMR,ID(30),
     $  DEP(30),Q(200),ITP,IOV,DU,TG,TV,F,XNU(30),XNV(30),IVO,IVI,AN
      COMMON/SUN/ BTA(200),DOF(200),DEL(200),RT(50),ITV(30)
      ICOUNT=0
      Y=3.27E4*F*10.
      FEM=1.
      SGNO=-1.
2     DEFM=0.
      ICOUNT=ICOUNT+1
      SUM=0.
      EE1=.5*DOF(1)*DU**1.5
      EE2=EE1*DU
      EE3=.5*DOF(1)*DU
      DO 1 I=2,IOV
    1 EE3=EE3+DOF(I)*DU
      BTA(200)=DOF(1)
      DO 10 I=1,IOV
        U=FLOAT(I)*DU
        A=XMR*Q(I)*U**2
        B=0.
        DO 8 J=1,ITP
          IF(ID(J).EQ.0) GO TO 6
      IF(ID(J).GE.199) GO TO 8
      IF(U.GT.RT(J)) GO TO 8
```

Table C - I Boltzmann Equation Program, EED (continued)

```
      IF(DOF(I)/DOF(ID(J)).LT.1.E-10)   GO TO 11
          XL=0.
          YL=0.
          IP=I+ID(J)
          UP=U+DEP(J)
      IM=I-ID(J)-1
3         P=UP/DU-FLOAT(IP)
      IF(I.GT.1) GO TO 20
          XH=ETA(IP+1,J)*DOF(IP+1)*P**2+ETA(IP,J)*DOF(IP)*(1.+P*(1.-P))
      YH=ETA(IP+1,J)*(P*DOF(I)+(1.-P)*DOF(I+1))*P**2+ETA(IP,J)*DOF(I)*
     $(1.+P*(1.-P))
          DEL(J)=0.
      GO TO 5
   20 XH=0.
      YH=0.
          IF(IP.GE.200) GO TO 4
          XH=ETA(IP-1,J)*DOF(IP-1)*(1.-P)**2+ETA(IP+1,J)*DOF(IP+1)*P**2
     $        +ETA(IP,J)*DOF(IP)*(1.+2.*P*(1.-P))
      YH=ETA(IP-1,J)*(P*DOF(I-2)+(1.-P)*DOF(I-1))*(1.-P)**2+ETA(IP,J)*(P
     $*DOF(I-1)+(1.-P)*DOF(I))*(1.+2.*P*(1.-P))+ETA(IP+1,J)*(P*DOF(I)+(1
     $.-P)*DOF(I+1))*P**2
    4 IF(I.LE.ID(J)) GO TO 5
      IF(I.EQ.ID(J)+1) GO TO 21
          XL=(ETA(I-1,J)*DOF(I-1)+ETA(I,J)*DOF(I))
      YL=ETA(I-1,J)*(P*DOF(IM-1)+(1.-P)*DOF(IM))+ETA(I,J)*(P*DOF(IM)+(1.
     $-P)*DOF(IM+1))
      GO TO 5
   21 XL=ETA(I,J)*DOF(I)*(1.-P)
      YL=ETA(I,J)*(P*DOF(IM)+(1.-P)*DOF(IM+1))*(1.-P)
    5 DEL(J)=DEL(J)+(XH-XL)*XNU(J)-(YH-YL)*XNV(J)
          B=B+DEL(J)
          GO TO 8
6         A=A+DEP(J)*ETA(I,J)
8       CONTINUE
      C=3./U*(A+.5*B*DU/DOF(I)+.5*Y*EE1)/(EOVRN**2/QR(I)
     $+Y*(EE2/U+EE3*U**.5)+3.*A*TG/U)
    9 SUM=SUM+C*DU/2.
        IF(SUM.GT.30.) GO TO 11
        DF(I)=EXP(-SUM)
      SUM=SUM+C*DU/2.
      DEF=ABS(DOF(I)-DF(I))/AMIN1(DOF(I),DF(I))
      IF(DEFM.GE.DEF) GO TO 13
      DEFM=DEF
      SGN=SIGN(1.,DF(I)-DOF(I))
   13 BTA(I)=C*DF(I)*EOVRN/QR(I)
      IF(F.LT.1.E-15) GO TO 10
      EE3=EE3-(DOF(I)+DOF(I+1))*DU/2.
      EE2=EE2+(DOF(I)*U**1.5+DOF(I+1)*(U+DU)**1.5)*DU/2.
      EE1=EE1+(DOF(I)*U**.5+DOF(I+1)*(U+DU)**.5)*DU/2.
10    CONTINUE
```

Table C - I   Boltzmann Equation Programm, EED (continued)

```
 11 IOV=I-1
    IF(IOV.LE.1) STOP2
    IF(ICOUNT.EQ.30) GO TO 16
    IF(DEFM.LT..01) GO TO 16
    S=1.
    IF(SGN*SGNO.LT.0.) FEM=FEM*.5
    SGNO=SGN
    DEFL=ALOG10(DEFM+1.)
    IF(DEFL.GT.FEM) S=DEFL/FEM
    DO 12 I=1,IOV
 12 DOF(I)=DOF(I)**(1.-1./S)*DF(I)**(1./S)
    SLOPE=DOF(IOV)/DOF(IOV-1)
    DO 14 I=IOV,199
14  DOF(I+1)=DOF(I)*SLOPE
    IOV=200
    GO TO 2
 16 RETURN
    END
    SUBROUTINE VIB
    COMMON/FUN/ ETA(200,30),QR(200),DF(200),EOVRN,XMR,ID(30),
   $ DEP(30),Q(200),ITP,IOV,DU,TG,TV,F,XNU(30),XNV(30),IVO,IVI,AN
    E1=DEP(IVO)
    E2=AN*E1/(1.-2.*DE)
    VMIN=80.
    IF(AN.NE.0.) VMIN=E1*TG/(2.*E2*TV)+.5
    XNORM=0.
    XNERM=0.
    YNU=0.
    DO 10 I=1,80
    V=FLOAT(I-1)
    EV=V*(E1-(V-1.)*E2)
    IF(V.GT.VMIN) GO TO 5
    XV=EXP(-V*E1/TV+V*(V-1.)*E2/TG)
    GO TO 6
  5 XV=(VMIN+1.)/(V+1.)*EXP(-VMIN**2*E2/TG)
  6 XNORM=XNORM+XV
    XNERM=XNERM+XV*EV
    IF(I.GT.8) GO TO 10
    YNU=YNU+XV
    IF(I.EQ.1) GO TO 10
    JMAX=MIN0(IVO+I-2,IVI)
    DO 9 J=IVO,JMAX
  9 XNV(J)=XNV(J)+XV
 10 CONTINUE
    DO 12 I=IVO,IVI
    XNU(I)=YNU/XNORM
 12 XNV(I)=XNV(I)/XNORM
    PRINT 8, (XNV(I),I=IVO,IVI),XNERM/XNORM
  8 FORMAT(1P,(1X,10E12.4))
    RETURN
    END
```

Appendix D

Chemistry Rates

Table D - I is a listing of the chemical and physical reaction rates collected during the course of this study. The last column in the table specifies the reactions utilized in Chemco (See Chapter IX). Nonutilized reactions were rejected because they did not involve species carried in the code, were slow in an absolute sense, were slow relative to another channel with the same net reaction, or were determined by early Chemco runs to be insignificant. The letter M in the reaction column refers to an unspecified specie in a three-body collisional process.

The rate dimensions for single body processes are sec^{-1}; for two-body processes, cm^3sec^{-1}; and for three-body processes, cm^6sec^{-1}.

Table D - I. Reaction Rates

Reaction #	Reaction	Rate	Ref.*	Notes	Used in Chem. Code
1	$e + O \rightarrow O^+ + e + e$	From Boltz. Code	EED	1	X
2	$e + O_2 \rightarrow O_2^+ + e + e$	From Boltz. Code	EED	1	X
3	$O^- + O \rightarrow O_2 + e$	1.9×10^{-10}	67:711		X
4	$O^- + O_2 \rightarrow O_3 + e$	5×10^{-15}	68:24-13		X
5	$e + O \rightarrow O^- + h\nu$	1.3×10^{-15}	69:63		X
6	$e + O_3 \rightarrow O^- + O_2$	9×10^{-12}	68:24-13		X
7	$e + O + O_2 \rightarrow O^- + O_2$	1×10^{-31}	70		X
8	$O^- + O^+ \rightarrow O + O$	2.7×10^{-7}	69:82		X
9	$O^- + O_2^+ \rightarrow O + O_2$	9.6×10^{-8}	69:81		X
10	$O^- + O^+ + M \rightarrow O_2 + M$	2×10^{-25}	69:82		
11	$O^- + O^+ + O \rightarrow O_2 + O$	2×10^{-25}	69:82		X
12	$O^- + O_2^+ + M \rightarrow O_3 + M$	2×10^{-25}	69:82		X
13	$O^- + O_3 \rightarrow O_3^- + O$	5.3×10^{-10}	67:711		X
14	$O^- + O_2 \rightarrow O_3^- + h$	1×10^{-17}	68:24-28		
15	$O^- + O_2 + M \rightarrow O_3^- + M$	1.1×10^{-30}	69:68		X

Table D - I. Reaction Rates (Continued)

Reaction #	Reaction	Rate	Ref.*	Notes	Used in Chem Code
16	$O_2^- + O \rightarrow O_3 + e$	3.3×10^{-10}	67:711		X
17	$O_4^- + O \rightarrow O_3^- + O_2$	4×10^{-10}	69:70		
18	$e + O_3 \rightarrow O_2^- + O$	1.3×10^{-30}	68:24-13		X
19	$e + O_2^+ \rightarrow O + O('D)$	2.1×10^{-7}	69:60		X
20	$e + O^+ \rightarrow O + h\nu$	3.5×10^{-12}	69:62		
21	$e + O + O_2 \rightarrow O_2^- + O$	1×10^{-31}	68:24-11		X
22	$e + O^+ + M \rightarrow O + M$	1×10^{-26}	70		X
23	$O_2^- + O^+ \rightarrow O_2 + O$	1×10^{-7}	69:82		X
24	$O_3^- + O^+ \rightarrow O_3 + O$	1×10^{-7}	69:82		X
25	$O_3^- + O_2^+ \rightarrow O_3 + O + O$	1×10^{-7}	70		
26	$O_2^- + O \rightarrow O^- + O_2$	3.3×10^{-10}	69:69		X
27	$O^+ + O \rightarrow O_2^+ + h$	1×10^{-17}	70		
28	$O + O + O_2 \rightarrow O_2 + O_2$	7.4×10^{-33}	69:93		X
29	$O_2^- + O_2^+ \rightarrow O_2 + O + O$	1×10^{-7}	70		X
30	$O^+ + O + M \rightarrow O_2^+ + M$	1×10^{-29}	70		X

Table D - I. Reaction Rates (Continued)

Reaction #	Reaction	Rate	Ref.*	Notes	Used in Chem Code
31	$O + O + M \rightarrow O_2 + M$	7.4×10^{-33}	69:93		X
32	$O + O_2 + O_2 \rightarrow O_3 + O_2$	6×10^{-34}	69:93		X
33	$O + O + O_2 \rightarrow O_3 + O$	6×10^{-34}	69:93		X
34	$O + O_3 \rightarrow O_2 + O_2$	4.7×10^{-15}	69:93		X
35	$O + O_3^- \rightarrow O_2^- + O_2$	1×10^{-11}	69:73		X
36	$O_2^- + O_2 \rightarrow O_2 + O_2 + e$	2.2×10^{-18}	68:25-12		X
37	$e + O_2 \rightarrow O_2^- + h\nu$	2×10^{-19}	69:63		
38	$e + O_2^+ + M \rightarrow O_2 + M$	1×10^{-26}	70		X
39	$O^+ + O_2 \rightarrow O_2^+ + O$	2×10^{-11}	69:44		X
40	$O_2^- + O_2^+ + M \rightarrow O_2 + O_2 + M$	2×10^{-25}	69:82		
41	$e + O_2 + O_2 \rightarrow O_2^- + O_2$	1.9×10^{-30}	69:60		X
42	$e + O_2^+ \rightarrow O_2 + h\nu$	4×10^{-12}	68:24-5		
43	$O_2^+ + O_2^- \rightarrow O_2 + O_2$	4.2×10^{-7}	69:81		X
44	$O_2^+ + O_3^- \rightarrow O_2 + O_3$	2×10^{-7}	69:81		
45	$O_2^- + O_3 \rightarrow O_3^- + O_2$	4×10^{-10}	69:69		X
46	$O_2^+ + O_2 + M \rightarrow O_4^+ + M$	2.8×10^{-30}	69:46		

Table D - I. Reaction Rates (Continued)

Reaction #	Reaction	Rate	Ref.*	Notes	Used in Chem Code
47	$O_2^- + O_2 + M \rightarrow O_4^- + M$	3.5×10^{-31}	69:69		
48	$O_2^- + O^+ + M \rightarrow O_3 + M$	2×10^{-25}	69:82		
49	$e + O_3 \rightarrow O_3^- + h\nu$	1×10^{-17}	69:63		
50	$e + O_4^+ \rightarrow O_2 + O_2$	2×10^{-6}	69:60		
51	$e + O^- \rightarrow O + e + e$	1×10^{-8}	71		X
52	$e + O_2 \rightarrow O + O + e$	From Boltz. Code	EED	1	X
53	$e + O_2 \rightarrow O + O^-$	From Boltz. Code	EED	1	X
54	$e + O_3 \rightarrow O_2 + O + e$	1×10^{-8}	72		X
55	$O_3 + O_2 \rightarrow O_2 + O_2 + O$	1.5×10^{-13}	73		X
56	$e + O_2 \rightarrow O_2 + e$, (Rotational)	From Boltz Code	EED	2,3	
57	Not Used				
58	Not Used				
59	$e + O_2 \rightarrow O_2 + e$, (Elastic)	From Boltz Code	EED	2,4	
60	$e + O_2 \rightarrow O_2^* + e$, (4.5 Elect.)	From Boltz Code	EED	2,5	
61	$e + O_2 \rightarrow O_2^* + e$, (6.0 Elect.)	From Boltz Code	EED	2,5	
62	$e + O_2 \rightarrow O_2^* + e$, (8.4 Elect.)	From Boltz Code	EED	2,5	

Table D - I. Reaction Rates (Continued)

Reaction #	Reaction	Rate	Ref.*	Notes	Used in Chem Code
63	$e + O_2$ — O_2 ($\nu = 1$) + e, (Low Res.)	From Boltz Code	EED	2,6	
64	$e + O_2$ — O_2 ($\nu = 2$) + e, (Low Res.)	From Boltz Code	EED	2,6	
65	$e + O_2$ — O_2 ($\nu = 3$) + e, (Low Res.)	From Boltz Code	EED	2,6	
66	$e + O_2$ — O_2 ($\nu = 4$) + e, (Low Res.)	From Boltz Code	EED	2,6	
67	$e + O_2$ — O_2 ($\nu = 1$) + e, (High Res.)	From Boltz Code	EED	2,7	
68	$e + O_2$ — O_2 ($\nu = 2$) + e, (High Res.)	From Boltz Code	EED	2,7	
69	$e + O_2$ — O_2 ($\nu = 3$) + e, (High Res.)	From Boltz Code	EED	2,7	
70	$e + O_2$ — O_2 ($\nu = 4$) + e, (High Res.)	From Boltz Code	EED	2,7	
71	$O_2\ (a^1\Delta g) + O_2 \rightarrow O_2 + O_2$	2.2×10^{-18}	69:85		X
72	$O_2\ (b^1\Sigma_g^+) + O_2 \rightarrow O_2 + O_2$	1.5×10^{-16}	74:4925		
73	$O_2\ (a^1\Delta g)$ + Pyrex $\rightarrow O_2$	2×10^{-5}	74:4924		
74	$O_2\ (b^1\Sigma_g^+)$ + Pyrex $\rightarrow O_2$	2×10^{-3}	74:4925		
75	$O + O$ + Pyrex $\rightarrow O_2$	1.1×10^{-4} (Single Body)	74:4925		
76	$O^+ + O \rightarrow O + O^+$ (Charge Ex.)	Cross Section	75:18	8	
77	$O^- + O \rightarrow O + O^-$ (Charge Ex.)	Cross Section	75:18	8	
78	$e + O \rightarrow O\ (^3S^\circ) + e$	Cross Section	76:4241	8	

AD-A066 196 AIR FORCE INST OF TECH WRIGHT-PATTERSON AFB OHIO SCH--ETC F/G 7/2
DISCHARGE PROCESSES IN THE OXYGEN PLASMA.(U)
DEC 78 J W DETTMER

UNCLASSIFIED AFIT/DS/PH/78-3 NL

4 OF 4

AD
A066196

END
DATE
FILMED
5-79
DDC

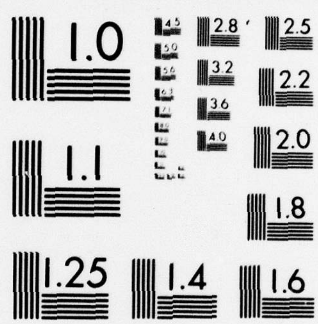

MICROCOPY RESOLUTION TEST CHART
NATIONAL BUREAU OF STANDARDS-1963-A

Table D - I. Reaction Rates (Continued)

Reaction #	Reaction	Rate	Ref.*	Notes	Used in Chem Code
79	$e + O \rightarrow O\,(^5S^0) + e$	Cross Section	76:4242	8	
80	$O\,(^1S) + O(^3P) \rightarrow O(^1D) + O(^1D)$	NA		9	
81	$O(^1D) + O_2 \rightarrow O_2(b^1\Sigma_g^+) + O(^3P)$	7.5×10^{-11}	69:85		
82	$O_2(a^1\Delta_g) + O_2(a^1\Delta_g) \rightarrow O_2(b^1\Sigma_g^+) + O_2$	2×10^{-18}	69:85		X
83	$O(^1D) + O_3 \rightarrow O_2 + O_2$	2.5×10^{-10}	69:85		
84	$O(^1S) + O_2 \rightarrow$	5×10^{-13}	21:11		
85	$O(^1S) + O_3 \rightarrow$	8×10^{-10}	21:11		
86	$O_2(b^1\Sigma_g^+) + O_3 \rightarrow O + O_2 + O_2$	2.5×10^{-11}	69:85		
87	Not Used				
88	$e + O_2 \rightarrow O^+ + O + e + e$	From Boltz Code	EED	1	X
89	$O_4^+ + M \rightarrow O_2^+ + O_2 + M$	2.9×10^{-14}	69:46		
90	$O_4^+ + O \rightarrow O_2^+ + O_3$	3×10^{-10}	69:47		
91	$O^+(^2D) + O_2 \rightarrow O_2^+(a,A) + O$	3×10^{-10}	69:55		
92	$O_2^+ + O + M \rightarrow O_3^+ + M$	1×10^{-29}	69:51		
93	$e + e + O^+ \rightarrow O + e$	1×10^{-19}	69:62		X
94	$e + e + O_2^+ \rightarrow O_2 + e$	1×10^{-19}	69:62		X

Table D - I. Reaction Rates (Continued)

Reaction #	Reaction	Rate	Ref.*	Notes	Used in Chem Code
95	$O_4^- + M \rightarrow O_2^- + O_2 + M$	1.4×10^{-14}	69:69		
96	$O_4^- + O_3 \rightarrow O_3^- + O_2 + O_2$	5×10^{-10}	69:70		
97	$O_2^+ + O_4^- \rightarrow O_2 + O_2 + O_2$	2×10^{-7}	69:81		
98	$O(^1D) \rightarrow O + h\nu$	6.8×10^{-3}	69:84		
99	$O(^1D) + O_2 \rightarrow O + O_2$	5×10^{-11}	69:85		
100	$O_2(a^1\Delta_g) \rightarrow O_2 + h\nu$	2.6×10^{-4}	69:85		X
101	Not Used				
102	$O_2(b^1\Sigma_g^+) \rightarrow O_2 + h\nu$	8.3×10^{-2}	69:85		
103	$O_2(b^1\Sigma_g^+) + O_2 \rightarrow O_2 + O_2$	1.5×10^{-16}	69:85		
104	$O + O_3 \rightarrow O_2(a^1\Delta_g) + O_2$	4.7×10^{-15}	69:93		X
105	$e + O_2(a^1\Delta_g) \rightarrow O_2 + e$	1×10^{-11}	69:93		X
106	$O(^1D) + O_2 \rightarrow O_2(a^1\Delta_g) + O$	1×10^{-12}	69:94		
107	$O_2(a^1\Delta_g) + O \rightarrow O + O_2$	1×10^{-16}	69:94		X
108	$O_2(a^1\Delta_g) + O_3 \rightarrow O_2 + O_3$	3×10^{-15}	69:94		X
109	$O + O \rightarrow O_2 + h\nu$	2.4×10^{-21}	69:96		
110	$O + O + O \rightarrow O(^1S) + O_2$	1.5×10^{-34}	69:101		

Table D - I. Reaction Rates (Continued)

Reaction #	Reaction	Rate	Ref.*	Notes	Used in Chem Code
111	$e + O \rightarrow O + e$, (Elastic)	Cross Section	77	8	
112	$e + O_2 \rightarrow O_2(a^1\Delta_g) + e$	From Boltz Code	EED		X
113	$e + O_2 \rightarrow O_2(b^1\Sigma_g^+) + e$	From Boltz Code	EED		
114	$O^- + O_2 \rightarrow O_2^- + O$	f(E/N)	78:1247	1	X
115	Not Used				
116	Not Used				
117	$O^- + O_2(a^1\Delta_g) \rightarrow O_3 + e$	3×10^{-10}	67:711		X
118	$O_2^- + O_2(a^1\Delta_g) \rightarrow O_2 + O_2 + e$	2×10^{-10}	67:711		X
119	$O_2(a^1\Delta_g) + O_3 \rightarrow O_2 + O_2 + O$	4×10^{-15}	68:24-33		X
120	$O^- + O_2 \rightarrow O_2 + O + e$	1×10^{-46}	68:24-12		
121	$O_2^- + O \rightarrow O_2 + O + e$	2.1×10^{-18}	68:24-12		
122	$O^- + O_3 \rightarrow O_2 + O_2 + e$	Slow	68:24-13		
123	$O_3^- + O \rightarrow O_2 + O_2 + e$	1×10^{-13}	70		X
124	$O^- + O_2(a^1\Delta_g) \rightarrow O_2^- + O$	1×10^{-10}	68:24-21		X
125	Not Used				
126	$e + O_2(a^1\Delta_g) \rightarrow O_2^+ + e + e$	From Boltz Code	EED	1,10	X

Table D - I. Reaction Rates (Continued)

Reaction #	Reaction	Rate	Ref.*	Notes	Used in Chem Code
127	$e + O + O_2(a^1\Delta_g) \rightarrow O^- + O_2(a^1\Delta_g)$	Same as 7	Assumed	11	X
128	Not Used				
129	Not Used				
130	$e + O + O_2(a^1\Delta_g) \rightarrow O_2^- + O$	Same as 21	Assumed	11	X
131	Not Used				
132	$O + O + O_2(a^1\Delta_g) \rightarrow O_2 + O_2(a^1\Delta_g)$	Same as 28	Assumed	11	X
133	Not Used				
134	$O + O + O_2(a^1\Delta_g) \rightarrow O_3 + O$	Same as 33	Assumed	11	X
135	Not Used				
136	$O^+ + O_2(a^1\Delta_g) \rightarrow O_2^+ + O$	Same as 39	Assumed	11	X
137	$e + O_2 + O_2(a^1\Delta_g) \rightarrow O_2^- + O_2(a^1\Delta_g)$	Same as 41	Assumed	11	X
138	$e + O_2(a^1\Delta_g) \rightarrow O + O + e$	Same as 52	Assumed	11	X
139	$e + O_2(a^1\Delta_g) \rightarrow O + O^-$	From Boltz Code	EED	1,10	X
140	$e + O_2(a^1\Delta_g) \rightarrow O^+ + O + e + e$	Same as 88	Assumed	11	X
141	$e + O_2(a^1\Delta_g) + O_2 \rightarrow O_2^- + O_2$	Same as 41	Assumed	11	X
142	$e + O_2(a^1\Delta_g) + O_2(a^1\Delta_g) \rightarrow O_2^- + O_2(a^1\Delta_g)$	Same as 41	Assumed	11	X

Notes:

*References 67, 68, 69, and 75 are compilations of rates and as such do not represent primary sources.

1 - Rate entered into Chemco as a function of E/N.

2 - Computed in EED but not entered in Chemco.

3 - Rotational excitation.

4 - Momentum transfer.

5 - Electronic excitation.

6 - Low energy vibrational excitation.

7 - High energy vibrational excitation.

8 - Cross section not used in EED or Chemco.

9 - No rate found.

10 - See Appendix B for cross section modification.

11 - Rate not available. Reaction assumed, so as to allow reactions involving $O_2(a^1\Delta_g)$ in Chemco.

Appendix E

Chemistry Code, Chemco

The program listing presented in Table E - I was the one utilized to calculate the species concentrations and relative reaction contributions described in Chapter IX. The basic program was developed by Michael Stamm for use by the personnel of the Plasma Physics Laboratory* of the Aerospace Research Laboratories. The portions of the program provided by the author were: the initial conditions; chemical rates and reactions; chemical difference equations; diffusion, flow and drift loss equations; and the input/output instructions.

---

*Now the High Power Branch of the A.F. Aero Propulsion Laboratory.

Table E - I Chemistry Program, CHEMCO

```
      PROGRAM CHEMCO (OUTPUT,INPUT)
C
      COMMON/XSK/O,O2,O2D,O3,E,ON,O2N,O3N,OP,O2P
      COMMON/XDOTSK/ODOT,O2DOT,O2DDOT,O3DOT,EDOT,ONDOT,O2NDOT,O3NDOT,
     1 OPDOT,O2PDOT
      COMMON/SCALII/ NX,NY,NXI,NYI,LINPIN,IGRID
      DIMENSION KCH(10),X(20),XDOT(20)
      COMMON/RATERK/R1,R93,R2,R94,R3,R53,R4,R6,R5,R7,R8,R9,R11,R12,
     1  R13,R15,R16,R18,R19,R21,R22,R23,R24,R25,R114,R28,R29,R30,
     2  R31,R32,R110,R33,R55,R34,R35,R36,R41,R38,R39,R43,R45,
     3  R51,R52,R54,R71,R82,R88,R100,R104,R105,
     4  R112,R107,R108,R117,R118,R123,R124,R126,R127,R128,R129,
     5  R130,R131,R132,R133,R134,R135,R136,R137,R138,R139,R140,RX,R141,
     6 RY,RZ
      COMMON/SSK/S1,S2,S3,S4,S5,S7,S8,S9,S11,S12,S13,S15,S16,
     1  S19,S21,S22,S23,S24,S26,S28,S29,S30,S31,S32,S33,S34,S35,S36,
     2  S38,S39,S43,S45,S51,S52,S54,S71,S82,S55,
     3  S88,S100,S104,S105,S107,S108,S117,S118,S123,S124,S126,S130,
     4  S134,S136,S138,S139,S140,SX,S141,S6,S18,S41,S53,S93,S94,S112,
     5  S114,S119,SY,SZ
      COMMON/PARAMK/P,EECHAR,XEM,DOP,DO2P,DON,DO2N,DO3N,DE,DO,DO2D,SN,
     1  EOVERN,VOP,VO2P,VON,VO2N,VO3N,VO,VO3,EXCITE,VE,VO2D,VF,ALFA
      DATA KCH/ 1H1, 1H2, 1H3, 1H4, 1H5, 1H6, 1H7, 1H8, 1H9, 1HA/
C
C   INITIAL CONDITIONS
      DELT = 1.E10
      CHEMMAX = 20.
      CYCMAX = 50000.
      FRACT = .02
      PRNTCY = 50001.
      FRACTPO = 1.
      PREP = 0.
      KK = 10
C
      READ*,SN,VF,XDTCH
C
      RX = XDTCH * SN * 6.E-10
      RY  = RX
      RZ = RX
      O = .26*SN
      ON = 1.E-8*SN
      OP = 1.E-9*SN
      O2N = 1.E-9*SN
      O2P = 1.E-7*SN
      O3 = 1.E-4*SN
      O3N = 1.E-10*SN
      O2D = 0.2*SN
      O2=SN-.5*(O+ON+OP)-O2D-O2N-O2P-1.5*(O3+O3N)
      R3 = 1.9E-10
      R4 = 5.E-15
```

Table E - I Chemistry Program, CHEMCO (continued)

```
R5 = 1.3E-15
R6 = 4.E-12
R7 = 1.E-31
R8 = 2.7E-7
R9 = 9.6E-8
R11 = 2.E-25
R12 = 2.E-25
R13 = 5.3E-10
R15 = 1.1E-30
R16 = 3.3E-10
R18 = 1.3E-30
R19 = 2.1E-7
R21 = 1.E-31
R22 = 1.E-26
R23 = 1.E-7
R24 = 1.E-7
R26 = 3.3E-10
R28 = 7.4E-33
R29 = 1.E-7
R30 = 1.E-29
R31 = 7.4E-33
R32 = 6.E-34
R33 = 6.E-34
R34 = 4.7E-15
R35 = 1.E-11
R36 = 2.2E-19
R38 = 1.E-25
R39 = 2.E-11
R41 =1.9E-30
R43 = 4.2E-7
R45 = 4.E-10
R51 = 1.E-8
R54 = 1.E-8
R55 = 1.5E-13
R71 = 2.2E-18
R92 = 2.E-18
R93 = 1.E-19
R94 = 1.E-19
R100 = 2.6E-4
R104 = 4.7E-15
R105 = 1.E-11
R107 = 1.E-16
R108 = 3.E-15
R117 = 3.E-10
R118 = 2.E-10
R119 = 4.E-15
R123 = 1.E-13
R124 = 1.E-10
R130 = R21
R134 = R33
```

Table E - I   Chemistry Program, CHEMCO (continued)

```
      R136 = R39
      R141 = R41
C
10    READ*,EOVERN,R112,R52,R53,R2,R1,R88,R114,FECHAR,XEM,R126,R139
      R138 = R52
      R140 = R88
      IF(EOVERN.EQ.0.) GO TO 1000
C
      O = O+10.
      O3 = O3+10.
      O2D = O2D + 10.
      ON = ON+10.
      O2N = O2N+10.
      O3N = O3N+10.
      OP = OP+20.
      O2P = O2P+20.
      O2 = O2-85.
      F = OP+O2P-ON-O2N-O3N
      XEM = XEM/SN
C
      CYCLES = 0.
      CYCMCYC = 0.
      CHEMDT = 0.
      CHEMT = 0.
      ISTOP = 0
      TIME = 0.
      TIMAX = 50./VF
C
      IF(AMOD(PPPP,5.) .LT. .1) PRINT 902
902   FORMAT(1H1)
      PRINT 925,VF,EOVERN,SN,XDTCH
      PRINT*,EOVERN,R112,R52,R53,R2,R1,R88,R114,FECHAR,XEM,R126,R139
925   FORMAT(1H1,*FLOW =*F9.0*    E/N =*F6.1*    SN =*F10.3*    DTCHR=*
     1    F6.3)
C
100   CONTINUE
C
      IFLAG = 0
      CALL MIKCHEM(DELT,FRACT,FRACTDD,CHEMDT,CHEMT,CHEMCYC,CHEMMAX,KK)
      TIME = TIME + CHEMT
      CYCLES = CYCLES + 1.
      IF(CYCLES.GT.CYCMAX)  ISTOP=1
      IF(TIME.GT.TIMAX)  ISTOP=1
C
C
900   CONTINUE
      X(1) = O
      X(2) = O2
      X(3) = O2D
      X(4) = O3
```

Table E - I   Chemistry Program, CHEMCO (continued)

```
      X(5) = E
      X(6) = ON
      X(7) = O2N
      X(8) = O3N
      X(9) = OP
      X(10) = O2P
      XDOT(1) = ODOT
      XDOT(2) = O2DOT
      XDOT(3) = O2DDOT
      XDOT(4) = O3DOT
      XDOT(5) = EDOT
      XDOT(6) = ONDOT
      XDOT(7) = O2NDOT
      XDOT(8) = O3NDOT
      XDOT(9) = OPDOT
      XDOT(10) = O2PDOT
C
      IF(ISTOP.EQ.1) GO TO 901
C
      IF(AMOD(CYCLES,PRNTCY).GT. .1)  GO TO 930
901   PRINT 905
      PPPP = PPPP +1.
905   FORMAT(/,4X,*TIME        **DT          **O          **O2         *
     C        *O2D        **O3        **E         **ON        *
     C        *O2N        **O3N       **OP        **O2P       ** ALPHA*)
      PRINT 910, TIME,CHEMT,(X(J), J=1,KK),ALFA
910   FORMAT(1X, 1P13E10.2)
      PRINT 915, (XDOT(J), J=1,KK)
915   FORMAT(21X,1P11E10.2)
C
      SOG=2.*S3+S9+S13+S18+2.*S19+S22+S23+S24+2.*S29+S39+S51+2.*S52+S53+
     1S54+S55+S98+S93+S114+S119+S124+S136+2.*S138+S139+S140+DON+DOP+VON
     2 + 1.
      SOL=S1+S3+S5+S7+S16+S26+2.*S28+S30+2.*S31+S32+S33+S34+S35+S104+
     1S123+S134+DO+VO
     2 + 1.
      SO2G=S3+S6+S9+S11+S23+S26+S28+S29+S31+2.*S34+S35+S36+S38+2.*S43+
     1S45+S54+S55+S71+2.*S82+S94+S100+S104+S105+S107+S108+2.*S118+
     22.*S119+2.*S123+DO2P+DO2N+DO2D+VO2D+VO2P+VO2N+.5*VO+.5*VOP+
     31.5*VO3+.5*DO
     4 +1.
      SO2L=S2+S4+S15+S21+2.*S32+S33+S39+S41+S52+S53+S88+S112+S114
     1 + 1.
      SO3G=S4+S12+S16+S24+S32+S33+S117+S134+DO3N+VO3N
     1 + 1.
      SO3L=S6+S13+S18+S34+S45+S54+S55+S104+S119+VO3
     1 + 1.
      SEG=S1+S2+S3+S4+S16+S36+S51+S88+S117+S118+S123+S126+S140+VON+VO2N+
     1VO3N
     2 + 1.
```

Table E - I Chemistry Program, CHEMCO (continued)

```
      SEL=S5+S6+S7+S18+S19+S21+S22+S38+S41+S53+S93+S94+S130+S139+S141+
     1S142+DF+VOP+VO2P
     2 + 1.
      SONG=S5+S6+S7+S26+S53+S139
     1 + 1.
      SONL=S3+S4+S8+S9+S11+S12+S13+S15+S51+S114+S117+S124+DON+VON
     1 + 1.
      SO2NG=S19+S21+S35+S41+S114+S124+S130+S141
     1 + 1.
      SO2NL=S16+S23+S26+S29+S36+S43+S45+S118+DO2N+VO2N
     1 + 1.
      SO3NG=S13+S15+S45
     1 + 1.
      SO3NL=S24+S35+S123+DO3N+VO3N
     1 + 1.
      SOPG=S1+S88+S140
     1 + 1.
      SOPL=S8+S11+S22+S23+S24+S30+S39+S93+S136+DOP+VOP
     1 + 1.
      SO2PG=S2+S30+S39+S126+S136
     1 + 1.
      SO2PL=S9+S12+S19+S29+S38+S43+S94+DO2P+VO2P
     1 + 1.
      SO2DG=S104+S112
     1 + 1.
      SO2DL=S71+2.*S82+S100+S105+S107+S108+S117+S118+S119+S124+S126+
     1S130+S134+S136+S138+S139+S140+S141+DO2D+VO2D
     2 + 1.
C
      OS8=2.*S8/SOG
      OS9=S9/SOG
      OS13=S13/SOG
      OS16=S16/SOG
      OS19=2.*S19/SOG
      OS22=S22/SOG
      OS23=S23/SOG
      OS24=S24/SOG
      OS29=2.*S29/SOG
      OS39=S39/SOG
      OS51=S51/SOG
      OS52=2.*S52/SOG
      OS53=S53/SOG
      OS54=S54/SOG
      OS55=S55/SOG
      OS82=S82/SOG
      OS93=S93/SOG
      OS114=S114/SOG
      OS119=S119/SOG
      OS124=S124/SOG
      OS136=S136/SOG
```

Table E - I Chemistry Program, CHEMCO (continued)

```
OS138=2.*S138/SOG
OS139=S139/SOG
OS140=S140/SOG
ODON=DON/SOG
ODOP=DOP/SOG
OVON=VON/SOG
OS1=S1/SOL
OS3=S3/SOL
OS5=S5/SOL
OS7=S7/SOL
OS16=S16/SOL
OS26=S26/SOL
OS28=2.*S28/SOL
OS30 = S30/SOL
OS31 =  2.*S31/SOL
OS32 = S32/SOL
OS33 = S33/SOL
OS34 = S34/SOL
OS35 = S35/SOL
OS104 = S104/SOL
OS123 = S123/SOL
OS134 = S134/SOL
ODO = DO/SOL
OVO = VO/SOL
O3S4 = S4/SO3G
O3S12 = S12/SO3G
O3S16 = S16/SO3G
O3S24 = S24/SO3G
O3S32 = S32/SO3G
O3S33 = S33/SO3G
O3S117 = S117/SO3G
O3S134 = S134/SO3G
O3DO3N = DO3N/SO3G
O3VO3N = VO3N/SO3G
O3S6 = S6/SO3L
O3S13 = S13/SO3L
O3S18 = S18/SO3L
O3S34 = S34/SO3L
O3S45 = S45/SO3L
O3S54 = S54/SO3L
O3S55 = S55/SO3L
O3S104 = S104/SO3L
O3S119 = S119/SO3L
O3VO3 = VO3/SO3L
ES1 = S1/SEG
ES2 = S2/SEG
ES3 = S3/SEG
ES4 = S4/SEG
ES16 = S16/SEG
ES36 = S36/SEG
```

Table E - I   Chemistry Program, CHEMCO (continued)

```
ES51 = S51/SEG
ES88 = S88/SEG
ES117 = S117/SEG
ES118 = S118/SEG
ES123 = S123/SEG
ES126 = S126/SEG
ES140 = S140/SEG
EVON = VON/SEG
EVO2N = VO2N/SEG
EVO3N = VO3N/SEG
ES5 = S5/SEL
ES6 = S6/SEL
ES7 = S7/SEL
ES18 = S18/SEL
ES19 = S19/SEL
ES21 = S21/SEL
ES22 = S22/SEL
ES38 = S38/SEL
ES41 = S41/SEL
ES53 = S53/SEL
ES93 = S93/SEL
ES94 = S94/SEL
ES130 = S130/SEL
ES139 = S139/SEL
ES141 = S141/SEL
EDE = DE/SEL
EVOP = VOP/SEL
EVO2P = VO2P/SEL
ONS5 = S5/SONG
ONS6 = S6/SONG
ONS7 = S7/SONG
ONS26 = S26/SONG
ONS53 = S53/SONG
ONS139 = S139/SONG
ONS3 = S3/SONL
ONS4 = S4/SONL
ONS8 = S8/SONL
ONS9 = S9/SONL
ONS11 = S11/SONL
ONS12 = S12/SONL
ONS13 = S13/SONL
ONS15 = S15/SONL
ONS51 = S51/SONL
ONS114= S114/SONL
ONS117 = S117/SONL
ONS124 = S124/SONL
ONDON = DON/SONL
ONVON = VON/SONL
O2NS18 = S18/SO2NG
O2NS21 = S21/SO2NG
```

Table E - I Chemistry Program, CHEMCO (continued)

```
O2NS35 = S35/SO2NG
O2NS41 = S41/SO2NG
O2N114 = S114/SO2NG
O2N124 = S124/SO2NG
O2N130 =  S130/SO2NG
O2N141 = S141/SO2NG
O2NS16 = S16/SO2NL
O2NS23 = S23/SO2NL
O2NS26 = S26/SO2NL
O2NS29 = S29/SO2NL
O2NS36 = S36/SO2NL
O2NS43 = S43/SO2NL
O2NS45 = S45/SO2NL
O2N118 = S118/SO2NL
O2ND2N = DO2N/SO2NL
O2NV2N = VO2N/SO2NL
O3NS13 = S13/SO3NG
O3NS15 = S15/SO3NG
O3NS45 = S45/SO3NG
O3NS24 = S24/SO3NL
O3NS35 = S35/SO3NL
O3N123 = S123/SO3NL
O3ND3N = DO3N/SO3NL
O3NV3N = VO3N/SO3NL
OPS1 = S1/SOPG
OPS98 = S98/SOPG
OPS140 = S140/SOPG
OPS8 = S8/SOPL
OPS11 = S11/SOPL
OPS22 = S22/SOPL
OPS23 = S23/SOPL
OPS24 = S24/SOPL
OPS30 = S30/SOPL
OPS39 = S39/SOPL
OPS93 = S93/SOPL
OPS136 = S136/SOPL
OPDOP = DOP/SOPL
OPVOP = VOP/SOPL
O2PS2 = S2/SO2PG
O2PS30 = S30/SO2PG
O2PS39 = S39/SO2PG
O2P126 = S126/SO2PG
O2P136 = S136/SO2PG
O2PS9 = S9/SO2PL
O2PS12 = S12/SO2PL
O2PS19 = S19/SO2PL
O2PS29 = S29/SO2PL
O2PS38 = S38/SO2PL
O2PS43 = S43/SO2PL
O2PS94 = S94/SO2PL
```

Table E - I   Chemistry Program, CHEMCO (continued)

```
      O2PD2P = DO2P/SO2PL
      O2PV2P = VO2P/SO2PL
      O2D104 = S104/SO2DG
      O2D112 = S112/SO2DG
      O2DS71 = S71/SO2DL
      O2DS82 = 2.*S82/SO2DL
      O2D100 = S100/SO2DL
      O2D105 = S105/SO2DL
      O2D107 = S107/SO2DL
      O2D108 = S108/SO2DL
      O2D117 = S117/SO2DL
      O2D118 =S118/SO2DL
      O2D119 = S119/SO2DL
      O2D124 = S124/SO2DL
      O2D126 = S126/SO2DL
      O2D130 = S130/SO2DL
      O2D134 = S134/SO2DL
      O2D136 = S136/SO2DL
      O2D138 = S138/SO2DL
      O2D139 = S139/SO2DL
      O2D140 = S140/SO2DL
      O2D141 = S141/SO2DL
      O2DD2D = DO2D/SO2DL
      O2DV2D = VO2D/SO2DL
C
      PRINT 801. O,SOG,SOL
801   FORMAT(1H0.*O =*1P1E10.2*  GAIN =*1P1E10.2*  LOSS =*1P1E10.2)
      PRINT 802
802   FORMAT(/,6X,*S8         S9         S13        S18        S19        S22
     1         S23        S24        S29        S39        S51        S52
     2 S53*)
      PRINT 916.OS8,OS9.OS13,OS18.OS19,OS22.OS23,OS24.OS29,OS39,OS51.
     1 OS52.OS53
      PRINT 803
803   FORMAT(/,6X,*S54        S55        S88        S93        S114       S11
     19        S124       S136       S138       S139       S140       DON
     2 DOP*)
      PRINT 916.OS54,OS55,OS88,OS93,OS114,OS119,OS124,OS136,OS138,OS139.
     1 OS140,ODON,ODOP
      PRINT 804
804   FORMAT (/.6X.*VON*)
      PRINT 916.OVON
      PRINT 805
805   FORMAT(/,6X,*S1         S3         S5         S7         S16        S26
     1         S28        S30        S31        S32        S33        S34
     2 S35*)
      PRINT 916.OS1.OS3.OS5.OS7.OS16,OS26.OS28,OS30.OS31.OS32.OS33,OS34.
     1 OS35
      PRINT 806
806   FORMAT(/,6X,*S104       S123       S134       DO         VO*)
```

Table E - I   Chemistry Program, CHEMCO (continued)

```
      PRINT 916,OS104,OS123,OS134,ODO,OVO
      PRINT 835, O2,SO2G,SO2L
835   FORMAT (1H0,*O2 =*1P1E10.2*  GAIN =*1P1E10.2*  LOSS =*1P1E10.2)
      PRINT 807,O3,SO3G,SO3L
807   FORMAT (1H0,*O3 =*1P1E10.2*  GAIN =*1P1E10.2*  LOSS =*1P1E10.2)
      PRINT 808
808   FORMAT(/,6X,*S4          S12         S16         S24         S32         S33
     1         S117        S134        DO3N        VO3N*)
      PRINT 916,O3S4,O3S12,O3S16,O3S24,O3S32,O3S33,O3S117,O3S134,O3DO3N,
     1O3VO3N
      PRINT 809
809   FORMAT(/,6X,*S6          S13         S18         S34         S45         S54
     1         S55         S104        S119        VO3*)
      PRINT 916,O3S6,O3S13,O3S18,O3S34,O3S45,O3S54,O3S55,O3S104,O3S119,O
     13VO3
      PRINT 810,E,SEG,SEL
810   FORMAT (1H0,*E =*1P1E10.2*  GAIN =*1P1E10.2*  LOSS =*1P1E10.2)
      PRINT 811
811   FORMAT(/,6X,*S1          S2          S3          S4          S16         S36
     1         S51         S88         S117        S118        S123        S126
     2 S140*)
      PRINT 916,ES1,ES2,ES3,ES4,ES16,ES36,ES51,ES88,ES117,ES118,ES123,ES
     1126,ES140
      PRINT 812
812   FORMAT(/,6X,*VON         VO2N        VO3N*)
      PRINT 916,EVON,EVO2N,EVO3N
      PRINT 813
813   FORMAT(/,6X,*S5          S6          S7          S18         S19         S21
     1         S22         S38         S41         S53         S93         S94
     2 S130*)
      PRINT 916,ES5,ES6,ES7,ES18,ES19,ES21,ES22,ES38,ES41,ES53,ES93,ES94
     1,ES130
      PRINT 814
814   FORMAT(/,6X,*S139        S141        DE          VOP         VO2P*)
      PRINT 916,ES139,ES141,EDE,EVOP,EVO2P
      PRINT 815,ON,SONG,SONL
815   FORMAT (1H0,*ON =*1P1E10.2*  GAIN =*1P1E10.2*  LOSS =*1P1E10.2)
      PRINT 816
816   FORMAT(/,6X,*S5          S6          S7          S26         S53         S13
     19*)
      PRINT 916,ONS5,ONS6,ONS7,ONS26,ONS53,ONS139
      PRINT 817
817   FORMAT(/,6X,*S3          S4          S8          S9          S11         S12
     1         S13         S15         S51         S114        S117        S124
     2 DON*)
      PRINT 916,ONS3,ONS4,ONS8,ONS9,ONS11,ONS12,ONS13,ONS15,ONS51,ONS114
     1 ,ONS117,ONS124,ONDON
      PRINT 818
818   FORMAT (/,6X,*VON*)
      PRINT 916,ONVON
```

THIS PAGE IS BEST QUALITY PRACTICABLE
FROM COPY FURNISHED TO DDC

Table E - I   Chemistry Program, CHEMCO (continued)

```
      PRINT 819,O2N,SO2NG,SO2NL
819   FORMAT (1H1,*O2N =*1P1E10.2*  GAIN =*1P1E10.2*  LOSS =*1P1E10.2)
      PRINT 820
820   FORMAT(/,6X,*S18          S21          S35          S41          S114          S12
     14          S130          S141*)
      PRINT 916,O2NS18,O2NS21,O2NS35,O2NS41,O2N114,O2N124,O2N130,O2N141
      PRINT 821
821   FORMAT(/,6X,*S16          S23          S26          S29          S36          S43
     1          S45          S118          DO2N          VO2N*)
      PRINT 916,O2NS16,O2NS23,O2NS26,O2NS29,O2NS36,O2NS43,O2NS45,O2N118,
     1O2ND2N,O2NV2N
      PRINT 822,O3N,SO3NG,SO3NL
822   FORMAT (1H0,*O3N =*1P1E10.2*  GAIN =*1P1E10.2*  LOSS =*1P1E10.2)
      PRINT 823
823   FORMAT(/,6X,*S13          S15          S45*)
      PRINT 916,O3NS13,O3NS15,O3NS45
      PRINT 824
824   FORMAT(/,6X,*S24          S35          S123          DO3N          VO3N*)
      PRINT 916,O3NS24,O3NS35,O3N123,O3ND3N,O3NV3N
      PRINT 825,OP,SOPG,SOPL
825   FORMAT (1H0,*OP =*1P1E10.2*  GAIN =*1P1E10.2*  LOSS =*1P1E10.2)
      PRINT 826
826   FORMAT(/,6X,*S1          S88          S140*)
      PRINT 916,OPS1,OPS88,OPS140
      PRINT 827
827   FORMAT(/,6X,*S8          S11          S22          S23          S24          S30
     1          S39          S93          S136          DOP          VOP*)
      PRINT 916,OPS8,OPS11,OPS22,OPS23,OPS24,OPS30,OPS39,OPS93,OPS136,OP
     1DOP,OPVOP
      PRINT 828,O2P,SO2PG,SO2PL
828   FORMAT (1H0,*O2P =*1P1E10.2*  GAIN =*1P1E10.2*  LOSS =*1P1E10.2)
      PRINT 829
829   FORMAT(/,6X,*S2          S30          S39          S126          S136*)
      PRINT 916,O2PS2,O2PS30,O2PS39,O2P126,O2P136
      PRINT 830
830   FORMAT(/,6X,*S9          S12          S19          S29          S38          S43
     1          S94          DO2P          VO2P*)
      PRINT 916,O2PS9,O2PS12,O2PS19,O2PS29,O2PS38,O2PS43,O2PS94,O2PD2P,O
     12PV2P
      PRINT 831,O2D,SO2DG,SO2DL
831   FORMAT (1H0,*O2D =*1P1E10.2*  GAIN =*1P1E10.2*  LOSS =*1P1E10.2)
      PRINT 832
832   FORMAT(/,6X,*S104          S112*)
      PRINT 916,O2D104,O2D112
      PRINT 833
833   FORMAT(/,6X,*S71          S82          S100          S105          S107          S10
     18          S117          S118          S119          S124          S126          S130
     2 S134*)
      PRINT 916,O2DS71,O2DS82,O2D100,O2D105,O2D107,O2D108,O2D117,O2D118,
     1O2D119,O2D124,O2D125,O2D130,O2D134
```

Table E - I   Chemistry Program, CHEMCO (continued)

```
      PRINT 934
834   FORMAT(/,6X,*S136        S138       S139       S140       S141        OO2
     1D        VO2D*)
      PRINT 916,O2D136,O2D138,O2D139,O2D140,O2D141,O2DD2D,O2DV2D
916   FORMAT(1X,1P13E10.2)
C
      CONSM = O/2.+O2+O2D+3.*O3/2.+ON/2.+O2N+3.*O3N/2.+OP/2.+O2P
      CONSC = OP+O2P-E-ON-O2N-O3N
      PRINT 920, CYCLES,CONSM,CONSC
920   FORMAT(/,1X,*CYCLE*,F10.2,*  MOLECULES=*,F11.5,*   CHARGE=*,F10.2)
930   CONTINUE
C
      IF(ISTOP.LT.1)  GO TO 100
C
998   CONTINUE
999   CONTINUE
      GO TO 10
1000  CONTINUE
      END
C
      SUBROUTINE MIKCHEM(DELT,FRACT,FRACTDD,CHEMDT,CHEMT,CHEMCYC,
     C        CHEMMAX,KK)
      COMMON/XBK/ CH(10)
      COMMON/XDOTBK/ CHDOT(10)
      DIMENSION OCH(20),OCHDOT(20),DELCH(20),DDELCH(20),DCH(20)
C
      CHEMCYC = 0.
      TIME = 0.
      DO 105 K=1,KK
      OCH(K) = CH(K)
105   CONTINUE
200   CONTINUE
C     SET TIME STEP
      DT = DELT-TIME
C
      CALL DERIV(CH,CHDOT)
      DO 214 K=1,KK
      DDELCH(K) = 1.E10
C
C     COMPUTING DELCH FROM MAXIMUM FRACTIONAL CHANGE OF EACH VARIABLE.
      DELCH(K) = ABS(FRACT*CH(K)/(CHDOT(K)+1.E-100))
      IF(CH(K).EQ.0.)  DELCH(K)=1.E10
      IF(DELCH(K)*FRACTDD.GE.(DELT-TIME))  GO TO 206
C
C     COMPUTE MINIMUM DDELCH.
      DCHDOT = OCHDOT(K)-CHDOT(K)
      DDELCH(K) = DCH(K)/(DCHDOT + 1.E-100)
      IF(DDELCH(K).LT.0.)  DDELCH(K)=1.E10
      IF(CHEMCYC.GE.CHEMMAX-1.)  DDELCH(K) = 1.E10
206   CONTINUE
```

Table E - I Chemistry Program, CHEMCO (continued)

```
      DT = AMIN1(DDELCH(K),DELCH(K),DT)
214   CONTINUE
C
C     UPDATE
      DO 220 K=1,KK
      OCH(K) = CH(K)
      OCHDOT(K) = CHDOT(K)
      DCH(K) = CHDOT(K)*DT
      CH(K) = CH(K) + DCH(K)
      IF(CH(K).LE..1) CH(K) = 0.
220   CONTINUE
      TIME = TIME + DT
C
      CHEMT = TIME
      CHEMDT = DT
      CHEMCYC = CHEMCYC + 1.
      IF(CHEMCYC.GE.CHEMMAX)  RETURN
      IF((1.+1.E-10)*TIME.LT.DELT)  GO TO 200
      RETURN
      END
C
      SUBROUTINE DERIV (X, XDOT)
C
      COMMON/GASEK/ E,H
C
C   DERIV TAKES THE VARIABLES AND RETURNS THEIR DERIVATIVES.
C
      DIMENSION X(10),XDOT(10)
      COMMON/RATERK/R1,R93,R2,R94,R3,R53,R4,R6,R5,R7,R8,R9,R11,R12,
     1  R13,R15,R16,R18,R19,R21,R22,R23,R24,R26,R114,R28,R29,R30,
     2  R31,R32,R119,R33,R55,R34,R35,R36,R41,R38,R39,R43,R45,
     3  R51,R52,R54,R71,R82,R88,R100,R104,R105,
     4  R112,R107,R108,R117,R118,R123,R124,R126,R127,R128,R129.
     5  R130,R131,R132,R133,R134,R135,R136,R137,R138,R139,R140,RX,R141,
     6 RY,RZ
      COMMON/SRR/S1,S2,S3,S4,S5,S7,S8,S9,S11,S12,S13,S15,S16,
     1  S19,S21,S22,S23,S24,S26,S28,S29,S30,S31,S32,S33,S34,S35,S36,
     2  S38,S39,S43,S45,S51,S52,S54,S71,S92,S55,
     3  S88,S100,S104,S105,S107,S108,S117,S118,S123,S124,S126,S130.
     4  S134,S136,S138,S139,S140,SX,S141,S6,S18,S41,S53,S93,S94,S112,
     5  S114,S119,SY,SZ
      COMMON/PARAM/P,EECHAR,XEM,DOP,DO2P,DON,DO2N,DO3N,DE,DO,DO2D,SN,
     1  EOVERN,VOP,VO2P,VON,VO2N,VO3N,VO,VO3,EXCITE,VE,VO2D,VF,ALFA
C
      O = X(1)
      O2 = X(2)
      O2D = X(3)
      O3 = X(4)
      E = X(5)
      ON = X(6)
```

Table E - I Chemistry Program, CHEMCO (continued)

```
      O2N = X(7)
      O3N = X(8)
      OP = X(9)
      O2P = X(10)
      OM = O+O2+O2D+O3
C
      S1 = R1*E*O
      S2 = R2*E*O2
      S3 = R3*O*ON
      S4 = R4*ON*O2
      S5 = R5*E*O
      S6 = R6*E*O3
      S7 = R7*E*O*(O2+O2D)
      S8 = R8*ON*OP
      S9 = R9*ON*O2P
      S11 = R11*ON*OP*O
      S12 = R12*ON*O2P*OM
      S13 = R13*ON*O3
      S15 = R15*ON*O2*OM
      S16 = R16*O2N*O
      S18 = R18*E*O3
      S19 = R19*E*O2P
      S21 = R21*E*O*O2
      S22 = R22*E*OP*OM
      S23 = R23*O2N*OP
      S24 = R24*O3N*OP
      S26 = R26*O2N*O
      S28 = R28*O*O*(O2+O2D)
      S29 = R29*O2N*O2P
      S30 = R30*OP*O*OM
      S31 = R31*O*O*OM
      S32 = R32*O*O2*O2
      S33 = R33*O*O*O2
      S34 = R34*O*O3
      S35 = R35*O*O3N
      S36 = R36*O2N*O2
      S38 = R38*E*O2P*OM
      S39 = R39*OP*O2
      S41 = R41*E*O2*(O2+O2D)
      S43 = R43*O2N*O2P
      S45 = R45*O2N*O3
      S51 = R51*ON*E
      S52 = R52*O2*E
      S53 = R53*E*O2
      S54 = R54*O3*E
      S55 = R55*O2*O3
      S71 = R71*O2*O2D
      S82 = R82*O2D*O2D
      S88 = R88*O2*E
      S93 = R93*E*E*OP
```

Table E - I Chemistry Program, CHEMCO (continued)

```
      S94 = R94*E*E*O2P
      S100 = R100*O2D
      S104 = R104*O3*O
      S105 = R105*O2D*E
      S107 = R107*O2D*O
      S108 = R108*O2D*O3
      S112 = R112*O2*E
      S114 = R114*ON*O2
      S117 = R117*ON*O2D
      S118 = R118*O2N*O2D
      S119 = R119*O2D*O3
      S123 = R123*O3N*O
      S124 = R124*O2D*ON
      S126 = R126*O2D*E
      S130 = R130*O2D*E*O
      S134 = R134*O2D*O*O
      S136 = R136*O2D*OP
      S138 = R138*O2D*E
      S139 = R139*O2D*E
      S140 = R140*O2D*E
      S141 = R141*O2D*(O2+O2D)*E
      SX = RX*ON
      SY = RY*O2N
      SZ = RZ*O3N
C
C     CALCULATION OF DIFFUSION LOSSES
      XP = OP+O2P
      XN = ON+O2N+O3N
      XPM = 2.687E19*(3.2*OP+2.24*O2P)/(XP*SN+1.E-100)
      XNM = 2.687E19*(3.2*ON+2.16*O2N+2.55*O3N)/(XN*SN+1.E-100)
      XPD = 2.59E-2*XPM
      GAMA = EFCHAR*25.79
      ALFA = XN/(E+1.E-100)
      AX1 = (1. +GAMA+2.*ALFA*GAMA)
      AX2 = XPM*(1.+ALFA)/XEM
      AX3 = ALFA*XNM/XEM
      DAP = XPD*AX1*(1.+AX3)/((1.+ALFA*GAMA)*(1.+AX2+AX3))
      DAN = XPD*XNM*AX1/(GAMA*XEM*(1.+AX2+AX3))
      DAE = XPD*AX1/(1.+AX2+AX3)
      DOP = 5.48E20*DAP*OP/(SN*XPM+1.E-100)
      DO2P = 3.94E20*DAP*O2P/(SN*XPM+1.E-100)
      DON = 5.48E20*DAN*ON/(SN*XNM+1.E-100)
      DO2N = 3.7E20*DAN*O2N/(SN*XNM+1.E-100)
      DO3N = 4.37E20*DAN*O3N/(SN*XNM+1.E-100)
      DF = DOP+DO2P-DON-DO2N-DO3N
      DO = 3.32*O
      DO2D = 0.47*O2D
C
C     CALCULATION OF VELOCITY LOSSES
      VOP = OF*(859.8*EOVERN+VF)/50.
```

Table E - I Chemistry Program, CHEMCO (continued)

```
      VO2P = O2P*(601.9*EOVERN+VE)/50.
      VON = ON*(850.8*EOVERN-VE)/50.
      VO2N = O2N*(580.4*EOVERN-VE)/50.
      VO3N = O3N*(685.2*EOVERN-VE)/50.
      VO = O*VE/50.
      VO3 = O3*VE/50.
      VO2D = O2D*VE/50.
      VE = VON + VO2N + VO3N - VOP - VO2P
C
      ODOT = -S1-S3-S5-S7+2.*S8+S9+S13-S16+S19+S22+S23+S24-S26
     1  -2.*S28+2.*S29-S30-2.*S31-S32-S33-S34-S35+S39+S51+2.*S52+S54+S88
     2  +S55-S104+S19 -S123+S124-DO+DOP+DON+VON-VO-S134+S136
     3  +2.*S138+S139+S140+S93+S53+S18+S114+S119
C
      O2DOT = -S2+S3-S4+S9+S11-S15-S21+S23+S26+S28+S29+S31-S32
     1  -S33+2.*S34+S35+S36+S38-S39+2.*S43+S45-S52-S41
     2 +S54+S71+2.*S82-S88+S100+S104+S105+S107+S108+S55 +2.*S118+2.*S123
     3  +DO2P+DO2N+VO2P+VO2N+.5*DO+.5*VO+1.5*VO3+.5*VOP+VO2D+DO2D
     4  +.5*SX+SY+1.5*S7+S94-S53+S6-S114+2.*S119-S112
C
      O3DOT = S4+S12-S13+S16+S24+S32+S33-S34-S45-S55-S54-S104+S134
     1  +S117+DO3N+VO3N-VO3-S6-S18-S119
      EDOT = S1+S2+S3+S4-S5-S7+S16-S19-S21-S22+S36-S38+S51+S88+S117
     1  +S118+S123-DE+VON+VO2N+VO3N-VOP-VO2P+S126-S130-S139+S140-S141
     2  +SX+SY+S7-S93-S94-S53-S6-S18-S41
C
      ONDOT = -S3-S4+S5+S7-S8-S9-S11-S12-S13-S15+S26-S51-S117-S124
     1  -DON-VON+S139+S53+S6-S114
     2  -SX
C
      O2NDOT = -S16+S21-S23-S26-S29+S35-S36-S43-S45-S118
     1  +S124-DO2N-VO2N+S130+S141-SY+S18+S114+S41
C
      O3NDOT = S13+S15-S24-S35+S45-S123-DO3N-VO3N-SZ
C
      OPDOT = S1-S8-S11-S22-S23-S24-S30-S39+S88-DOP-VOP-S136+S140-S93
C
      O2PDOT = S2-S9-S12-S19+S30-S38+S39-S43-DO2P+S126+S136
     1  -S25-VO2P-S94
C
      O2DDOT =     -S71-2.*S82-S100+S104-S105-S107-S108-S117-S118-S124
     1  -DO2D-S126-S130-S134-S136-S138-S139-S140-VO2D-S141-S119+S112
C
      XDOT(1) = ODOT
      XDOT(2) = O2DOT
      XDOT(3) = O2DDOT
      XDOT(4) = O3DOT
      XDOT(5) = EDOT
      XDOT(6) = ONDOT
      XDOT(7) = O2NDOT
```

Table E - I   Chemistry Program, CHEMCO (continued)

```
XDOT(8)  =  O3NDOT
XDOT(9)  =  OPDOT
XDOT(10)  =  O2PDOT
RETURN
END
```

Vita

John W. Dettmer was born on 27 September 1935 in Cincinnati, Ohio. He was graduated from Purcell High School in 1951 and attended the University of Cincinnati, receiving an Electrical Engineering Degree and a commission in the U.S. Air Force in 1956. He entered active duty on 17 December 1956 and attended pilot training. After being awarded his wings, he flew B-47Es for the Strategic Air Command from Davis-Monthan AFB, Arizona until December 1963. He then attended the air Force Institute of Technology where he received a Master of Science in Electronics Engineering in 1965. He then served as a Communications Engineer with the Ground Electronics Engineering and Installation Agency at Wheeler AFB, Hawaii until 1966, at which time he attended the Aerospace Test Pilot School at Edwards AFB. After receiving the Rest Pilot specialty in 1967, he was assigned to the Test Operations Division of the Manned Orbiting Laboratory Program located at Los Angeles A.F.S. In 1968 he was assigned as a Plans Officer with the Seventh Air Force Headquarters located at Tan Son Nhut, RVN. From 1969 until 1971 he served as a test pilot and operations officer for the Cargo Test Branch of the 4950 Test Wing at Wright-Patterson AFB, Ohio. In 1972 he again entered the Air Force Institute of Technology, becoming a Doctoral Candidate in 1973. He was then assigned to Aerospace Research Laboratories (ARL) to pursue his doctoral research. Upon disestablishment of the organization in 1975 until August 1978, he was again assigned to the 4950 Test Wing as the Assistant to the Commander for the Airborne Laser Laboratory (ALL) and as Commander of the Wing's Detachment at Kirtland AFB. He was then assigned to the Weapons Laboratory as Director of Test and Operations for the ALL. During the period after the disestablishment of ARL, he pursued his doctoral research on a part-time basis.

John W. Dettmer is a member of Eta Kappa Nu and the American Institute of Electronic and Electrical Engineers. He is married to the former Erin Lee Ross of Tucson, Arizona; and they have four children.

SECURITY CLASSIFICATION OF THIS PAGE (When Data Entered)

REPORT DOCUMENTATION PAGE

READ INSTRUCTIONS BEFORE COMPLETING FORM

1. REPORT NUMBER: AFIT/DS/78-3
2. GOVT ACCESSION NO.
3. RECIPIENT'S CATALOG NUMBER
4. TITLE (and Subtitle): Discharge Processes In The Oxygen Plasma
5. TYPE OF REPORT & PERIOD COVERED: Final
6. PERFORMING ORG. REPORT NUMBER
7. AUTHOR(s): John W. Dettmer, Colonel, USAF
Air Force Weapons Laboratory
Kirtland AFB, New Mexico 87117
8. CONTRACT OR GRANT NUMBER(s)
9. PERFORMING ORGANIZATION NAME AND ADDRESS: Air Force Institute of Technology
Wright Patterson AFB, Ohio 45433
10. PROGRAM ELEMENT, PROJECT, TASK AREA & WORK UNIT NUMBERS: N/A
11. CONTROLLING OFFICE NAME AND ADDRESS: Same as 9.
12. REPORT DATE: November 1978
13. NUMBER OF PAGES
14. MONITORING AGENCY NAME & ADDRESS (if different from Controlling Office): Same as 9.
15. SECURITY CLASS. (of this report): Unclassified
15a. DECLASSIFICATION/DOWNGRADING SCHEDULE
16. DISTRIBUTION STATEMENT (of this Report)

Approved for public release, distribution unlimited.

17. DISTRIBUTION STATEMENT (of the abstract entered in Block 20, if different from Report)
18. SUPPLEMENTARY NOTES

Oxygen

FEB 8 1979

APPROVED FOR PUBLIC RELEASE AFR 190-17.
JOSEPH P. HIPPS, Major, USAF
Director of Information

19. KEY WORDS (Continue on reverse side if necessary and identify by block number)

Oxygen discharge, glow discharge, unstable discharge, oxygen plasma, solutions to Boltzmann equation, plasma chemistry model, O_2 metastable, negative Ion, two step ionization.

20. ABSTRACT (Continue on reverse side if necessary and identify by block number)

The electric glow discharge in oxygen was experimentally studied and mathematically modeled for pressures of one to ten torr and current densities to 35 milliamperes per square centimeter. Experimentally it was observed that the oxygen discharge existed in either a high-electric-field or a low-electric-field form. The high field form was present at high currents and low pressures, the low field form at low currents and high pressures. The high field form exhibited stable characteristics while the low field form was oscillatory. Solutions of

DD FORM 1 JAN 73 1473 EDITION OF 1 NOV 65 IS OBSOLETE

SECURITY CLASSIFICATION OF THIS PAGE (When Data Entered)

20. ABSTRACT (continued)

the Boltzmann transport equation indicated that the electron energy distribu- function exhibited a characteristic intermediate between Maxwellian and Druyvesteyn. Chemistry model results showed the dominant positive ions to be O_2^+ and O^-. The transition from the stable to unstable forms was determined to be related to two criteria: the dominance of the derivative of the attachment coefficient with respect to E/N over that of the ionization coefficient and the equivalence of the negative ion and electron number densities. The chemistry model results indicated that two-step ionization from the metastable $O_2(a'\Delta)$ and collisions between the metastable and negative ions were important electron sources.